Dissertation

submitted to the
Combined Faculty of Natural Sciences and Mathematics
of the Ruperto-Carola-University
of Heidelberg, Germany
for the degree of
Doctor of Natural Sciences

Put Forward by
Patrick Dominik Rupprecht
born in Nürnberg

Oral examination: June 8th, 2022

Ultrafast Laser Control of Molecular Quantum Dynamics from a Core-Electron Perspective

Referees:

Prof. Dr. Thomas Pfeifer

Prof. Dr. Andreas Wolf

DON'T PANIC!

---

from *The Hitchhiker's Guide to the Galaxy*
by Douglas Adams

or *general advice if you are living in the 2020s.*

Ultraschnelle Laserkontrolle Molekularer Quantendynamik aus der Rumpfelektronen-Perspektive—Diese Arbeit führt zwei neue experimentelle Ansätze zur Kontrolle von Quantendynamik in Molekülen aus der Sicht der Rumpfelektronen ein. Hierfür wurde eine Laser-Quelle entwickelt, deren ultrakurze Pulse Zugang zu den Zeitskalen der Elektronen- und Strukturdynamik in Molekülen ermöglichen. Mit einer Dauer von nur wenigen optischen Zyklen im 1 µm bis 2 µm Spektralbereich kurzwelliger Infrarotstrahlung (SWIR) werden Pulsintensitäten von bis zu $10^{15}\,\mathrm{W/cm^2}$ erreicht. In Kombination mit einer Vakuumapparatur ermöglicht dieser experimentelle Aufbau die ultraschnelle Laserkontrolle von Molekül-Dynamik, welche durch Rumpfelektronen-Anregung mittels Röntgenabsorptionsspektroskopie (XAS) gemessen wird. Das erste Experiment untersucht die Manipulation der molekularen Elektronenstruktur. Dabei wird ein Puls im weichen Röntgenbereich (SXR) gleichzeitig zu einem SWIR Puls mit veränderlicher Intensität eingestrahlt. Die gemessene Absorption in SF_6 zeigt eine Intensitätsabhängigkeit und deckt damit eine Zunahme der effektiven Elektronen-Austauschwechselwirkungs-Energie auf. Diese Messung demonstriert erstmalig eine gezielte Änderung dieser rein quantenmechanischen Komponente der Elektron-Elektron-Wechselwirkung. In einem zweiten Experiment regt ein SWIR Puls kohärente Molekülvibrationen mit einer Amplitude des zehnfachen Kerndurchmessers an. Der zeitverzögerte SXR Puls misst die Bindungslängenänderung mittels Rumpfelektronen-Übergängen. Die dabei erreichte, bisher beispiellose Präzision von 14 Femtometern ebnet den Weg für Atom-spezifische Vibrationsmetrologie in Molekülen in der Gasphase. Insgesamt ermöglichen diese Ergebnisse eine ultraschnelle chemische Kontrolle auf der Quantenebene.

Ultrafast Laser Control of Molecular Quantum Dynamics from a Core-Level Perspective—This work introduces two experimental approaches to control quantum dynamics in molecules, employing core electrons as messengers. A laser source providing ultrashort pulses has been developed to access the timescale of electronic and structural dynamics inside molecules. Pulses of few-cycle durations in the 1 µm to 2 µm short-wavelength infrared (SWIR) spectral region provide intensities up to $10^{15}\,\mathrm{W/cm^2}$. In combination with a vacuum beamline, this experimental setup allows for ultrafast laser control of molecular dynamics probed by core-electron transitions via x-ray absorption spectroscopy (XAS). The first experiment investigates the manipulation of molecular electronic structure. Here, a soft x-ray (SXR) pulse probes simultaneously to an SWIR pulse of variable intensity. The measured intensity-

dependent absorbance changes in SF_6 reveal an increased effective electronic-exchange energy. This demonstrates the alteration of this purely quantum-mechanical component of the electron-electron interaction for the first time. In a second experiment, an SWIR pulse induces coherent molecular vibrations with amplitudes of ten times the diameter of the nucleus. Subsequently, a time-delayed SXR pulse probes the bond-length changes via core-level transitions. This enables an unprecedented 14 femtometer precision which paves the way for site-specific vibrational metrology in gas-phase molecules. Overall, these results enable ultrafast chemical control on a quantum level.

List of publications

Parts of this work have been published or prepared in the following articles:

- P. Rupprecht, L. Aufleger, S. Heinze, A. Magunia, T. Ding, M. Rebholz, S. Amberg, N. Mollov, F. Henrich, M. W. Haverkort, C. Ott, and T. Pfeifer.
  Laser Control of Electronic Exchange Interaction within a Molecule.
  Physical Review Letters, 128(15):153001, 2022.
  For more information see [1].

- P. Rupprecht, L. Aufleger, S. Heinze, A. Magunia, T. Ding, M. Rebholz, S. Amberg, N. Mollov, F. Henrich, M. W. Haverkort, C. Ott, and T. Pfeifer.
  Resolving Vibrations in a Polyatomic Molecule with Femtometer Precision.
  Physical Review Letters (manuscript under peer review), 2022.
  For more information see [2].

- P. Rupprecht, L. Aufleger, A. Magunia, S. Amberg, N. Mollov, F. Henrich, C. Ott, and T. Pfeifer.
  Wavelength-tunable, few-cycle millijoule-level pulses in the short-wavelength infrared.
  Manuscript in preparation.

Additional publications with own contributions:

- L. Aufleger, P. Friebel, P. Rupprecht, A. Magunia, T. Ding, M. Rebholz, M. Hartmann, C. Ott, and T. Pfeifer.
  Line-shape broadening of an autoionizing state in helium at high XUV intensity.
  New Journal of Physics, 24(1):013014, 2022. For more information see [3].

- M. Rebholz, T. Ding, L. Aufleger, M. Hartmann, K. Meyer, V. Stooß, A. Magunia, D. Wachs, P. Birk, Y. Mi, G. D. Borisova, C. da Costa Castanheira, P. Rupprecht, M. Magrakvelidze, U. Thumm, S. Roling, M. Butz, H. Zacharias, S. Düsterer, R. Treusch, G. Brenner, C. Ott, and T. Pfeifer.
  UV-Initiated Dissociation Dynamics of Molecular Oxygen (O_2).
  The Journal of Physical Chemistry A, 125(47):10138–10143, 2021. For more information see [4].

- M. Ilchen, P. Schmidt, N. M. Novikovskiy, G. Hartmann, P. Rupprecht, R. N. Coffee, A. Ehresmann, A. Galler, N. Hartmann, W. Helml, Z. Huang, L. Inhester, A. A. Lutman, J. P.MacArthur, T. Maxwell, M. Meyer, V. Music, H.-D. Nuhn, T. Osipov, D. Ray, T. J. A. Wolf, S. Bari, P. Walter, Z. Li, S. Moeller, A. Knie, and Ph. V. Demekhin.
  Site-specific interrogation of an ionic chiral fragment during photolysis using an x-ray free-electron laser.
  Communications Chemistry, 4(1):119, 2021. For more information see [5].

- M. Rebholz, T. Ding, V. Despré, L. Aufleger, M. Hartmann, K. Meyer, V. Stooß, A. Magunia, D. Wachs, P. Birk, Y. Mi, G. D. Borisova, C. da Costa, P. Rupprecht, G. Schmid, K. Schnorr, C. D. Schröter, R. Moshammer, Z.-H. Loh, A. R. Attar, S. R. Leone, T. Gaumnitz, H. J. Wörner, S. Roling, M. Butz, H. Zacharias, S. Düsterer, R. Treusch, G. Brenner, J. Vester, A. I. Kuleff, C. Ott, and T. Pfeifer.
  All-XUV Pump-Probe Transient Absorption Spectroscopy of the Structural Molecular Dynamics of Di-iodomethane.
  Physical Review X, 11(3):031001, 2021. For more information see [6].

- T. Ding, M. Rebholz, L. Aufleger, M. Hartmann, V. Stooß, A. Magunia, P. Birk, G. D. Borisova, D. Wachs, C. da Costa Castanheira, P. Rupprecht, Y. Mi, A. R. Attar, T. Gaumnitz, Z.-H. Loh, S. Roling, M. Butz, H. Zacharias, S. Düsterer, R. Treusch, A. Eislage, S. M. Cavaletto, C. Ott, and T. Pfeifer.
  Measuring the frequency chirp of extreme-ultraviolet free-electron laser pulses by transient absorption spectroscopy.
  Nature Communications, 12(1):643, 2021. For more information see [7].

- L. Aufleger, P. Friebel, P. Rupprecht, A. Magunia, T. Ding, M. Rebholz, M. Hartmann, V. Stooß, C. Ott, and T. Pfeifer.
  Pulse length effects on autoionizing states under the influence of intense SASE XUV fields.

Journal of Physics B: Atomic, Molecular and Optical Physics, 53(23):234002, 2020. For more information see [8].

- T. Ding, M. Rebholz, L. Aufleger, M. Hartmann, V. Stooß, A. Magunia, P. Birk, G. D. Borisova, C. da Costa Castanheira, P. Rupprecht, Y. Mi, T. Gaumnitz, Z.-H. Loh, S. Roling, M. Butz, H. Zacharias, S. Düsterer, R. Treusch, C. Ott, and T. Pfeifer.
  XUV pump–XUV probe transient absorption spectroscopy at FELs.
  Faraday Discussions, 228:519–536, 2021. For more information see [9].

- A. Magunia, L. Aufleger, T. Ding, P. Rupprecht, M. Rebholz, C. Ott, and T. Pfeifer.
  Bound-State Electron Dynamics Driven by Near-Resonantly Detuned Intense and Ultrashort Pulsed XUV Fields.
  Applied Sciences, 10(18):6153, 2020. doi:10.3390/app10186153. For more information see [10].

- C. Ott, L. Aufleger, T. Ding, M. Rebholz, A. Magunia, M. Hartmann, V. Stooß, D. Wachs, P. Birk, G. D. Borisova, K. Meyer, P. Rupprecht, C. da Costa Castanheira, R. Moshammer, A. R. Attar, T. Gaumnitz, Z.-H. Loh, S. Düsterer, R. Treusch, J. Ullrich, Y. Jiang, M. Meyer, P. Lambropoulos, and T. Pfeifer.
  Strong-field extreme-ultraviolet dressing of atomic double excitation.
  Physical Review Letters, 123(16):163201, 2019. For more information see [11].

- T. Ding, M. Rebholz, L. Aufleger, M. Hartmann, K. Meyer, V. Stooß, A. Magunia, D. Wachs, P. Birk, Y. Mi, G. D. Borisova, C. da Costa Castanheira, P. Rupprecht, Z.-H. Loh, A. R. Attar, T. Gaumnitz, S. Roling, M. Butz, H. Zacharias, S. Düsterer, R. Treusch, S. M. Cavaletto, C. Ott, and T. Pfeifer.
  Nonlinear Coherence Effects in Transient-Absorption Ion Spectroscopy with Stochastic Extreme-Ultraviolet Free-Electron Laser Pulses.
  Physical Review Letters, 123(10):103001, 2019. For more information see [12].

- M. Ilchen, G. Hartmann, P. Rupprecht, A. N. Artemyev, R. N. Coffee, Z. Li, H. Ohldag, H. Ogasawara, T. Osipov, D. Ray, Ph. Schmidt, T. J. A. Wolf, A. Ehresmann, S. Moeller, A. Knie, and Ph. V. Demekhin.
  Emitter-site-selective photoelectron circular dichroism of trifluoromethyloxirane.
  Physical Review A, 95(5):053423, 2017. For more information see [13].

Contents

Abstract vii

List of publications ix

1. Introduction 1

2. Theory basics 5

2.1. Optics . . . 5
2.1.1. The electromagnetic spectrum . . . 5
2.1.2. Beam propagation . . . 7
2.1.2.1. Gaussian optics . . . 7
2.1.2.2. Refractive index . . . 9
2.1.2.3. Dispersion . . . 10
2.1.3. Ultrashort laser pulses . . . 11
2.1.4. Nonlinear optics . . . 13
2.1.5. High-order harmonic generation . . . 14
2.2. Quantum mechanics . . . 16
2.2.1. Quantum-mechanical harmonic oscillator . . . 17
2.2.2. Single-body versus many-body state . . . 18
2.2.3. Coulomb interaction . . . 19
2.3. Atomic physics . . . 20
2.3.1. Quantum numbers . . . 20
2.3.2. Spin-orbit splitting . . . 21
2.4. Light-matter interaction . . . 22
2.4.1. X-ray interaction with matter . . . 22
2.4.2. Laser-dressed states . . . 23
2.4.3. Dipole selection rules . . . 25
2.4.4. Strong-field ionization . . . 25

2.4.5. Absorbance . . . 26
2.4.5.1. Transient absorption spectroscopy . . . 26
2.4.5.2. Linking the optical density to the transition strength 27
2.5. Molecular dynamics . . . 28
2.5.1. Born-Oppenheimer approximation . . . 29
2.5.2. Vibrations in a potential energy curve . . . 30
2.5.3. Vibrational excitation . . . 31
2.5.3.1. Thermal excitation . . . 31
2.5.3.2. IR- and Raman-active modes . . . 32
2.6. The sulfur hexafluoride molecule . . . 33
2.6.1. Electronic structure . . . 34
2.6.2. Vibrational modes . . . 35

3. Experimental setup for transient absorption spectroscopy 37
3.1. Overview: Laser Laboratory 2 at MPIK . . . 38
3.2. Tunable SWIR few-cycle laser source . . . 39
3.2.1. Optical setup overview . . . 43
3.2.2. Laser front end . . . 44
3.2.2.1. Femtosecond oscillator . . . 45
3.2.2.2. Amplification chain . . . 46
3.2.3. Optical parametric amplifier . . . 48
3.2.4. Stretched flexible hollow-core fiber . . . 51
3.2.4.1. Hollow dielectric waveguides . . . 51
3.2.4.2. SF-HCF implementation . . . 53
3.2.5. Few-cycle pulse compression . . . 57
3.2.5.1. Theory of frequency-resolved optical gating . . . 58
3.2.5.2. LL2 FROG apparatus . . . 60
3.2.5.3. Compression via negative GVD . . . 64
3.2.5.4. Pre-beamline optical setup . . . 65
3.2.5.5. Long-term stability . . . 66
3.3. Transient-absorption beamline . . . 67
3.3.1. Beamline overview . . . 67
3.3.2. High-order harmonic generation . . . 70
3.3.3. SWIR-intensity scan – XAS beamline configuration . . . 72
3.3.4. Time-delay scan – TR-XAS beamline configuration . . . 74

3.3.5. Commissioning – measurements on neon and helium 76
3.3.5.1. Static absorbance of neon 77
3.3.5.2. Time-resolved measurement of laser-dressed states in helium 78
3.4. SWIR few-cycle pulse source and (TR-)XAS beamline – future directions 80

4. Tuning the effective electronic exchange energy with laser pulses 83
4.1. Laser control of chemistry 84
4.1.1. A short history of covalent bonds 84
4.1.2. Manipulating molecules on the electronic level 85
4.1.3. Toy model for exchange energy control 86
4.1.3.1. Branching ratios in XAS 86
4.1.3.2. Physical toy model 88
4.2. Experimental investigation of exchange energy in SF_6 with XAS . . . 92
4.2.1. SF_6 as molecular candidate for exchange-energy control 92
4.2.2. XAS of SF_6 – the experiment 93
4.2.2.1. Parameters of the optical setup and beamline 93
4.2.2.2. SWIR intensity calibration 94
4.2.2.3. XAS measurement parameters 96
4.2.3. XAS data analysis 97
4.2.3.1. XAS raw data analysis 98
4.2.3.2. Fit procedure 98
4.2.3.3. Applying the toy model 101
4.2.4. Effective exchange-energy control in SF_6 106
4.2.4.1. Extraction of the effective exchange energy 106
4.2.4.2. Comparison with an *ab-initio* quantum-mechanical simulation 109
4.3. Controlling chemistry on the fundamental electronic quantum level – an outlook 111

5. Resolving and controlling femtometer-scale vibrational dynamics 113
5.1. Exciting and measuring molecular vibrations – an overview 114
5.1.1. Vibrational excitation 114
5.1.2. Measuring structural dynamics 115
5.1.2.1. Diffraction techniques 115
5.1.2.2. Spectroscopic approaches 118

5.2. Vibrational metrology scheme based on TR-XAS 121
5.3. TR-XAS measurement in SF_6 122
5.3.1. TR-XAS of SF_6 – the experiment 122
5.3.1.1. Temporal overlap determination 124
5.3.1.2. SWIR intensity calibration of TR-XAS 125
5.3.2. TR-XAS data and evaluation 126
5.3.2.1. TR-XAS raw data processing 126
5.3.2.2. Denoising using singular value decomposition 128
5.3.2.3. Resonance fit procedure for TR-XAS data 129
5.3.2.4. $6a_{1g}$ resonance shifts in SWIR-perturbed SF_6 131
5.3.3. Discussion and comparison with theory 132
5.3.3.1. Combined many-body quantum-mechanical and classical simulation 134
5.3.3.2. Perturbative vibrational excitation 138
5.3.3.3. Femtometer-scale vibrations 140
5.3.3.4. Comparison with classical differential equation 142
5.4. Vibrational precision metrology with TR-XAS – an outlook 143

6. Summary and future directions **147**

A. Abbreviations **151**

B. Appendix **153**
B.1. Photos – Laser Laboratory 2 154
B.2. Experimental setup – details 161
B.2.1. Optical setup – details 161
B.2.2. Spectrometer calibration 164
B.3. SF_6 (TR-)XAS experiments – details 166
B.3.1. SF_6 bond-elongation to photon-energy mapping 166

Bibliography **167**

Danksagung **213**

1. Introduction

Our world is based on molecules. Actually, we as humans, are made of and surrounded by molecules. The air that we breathe consists overwhelmingly of small molecules like nitrogen (N_2) and oxygen (O_2). The existence of water (H_2O) is a general precondition for life on earth and potentially on other planets. More complex, carbon-containing molecules form the living matter and are thus called organic molecules. The entire genetic information of our body is encoded in a set of large DNA[1] molecules. Understanding, predicting and controlling how substances react with each other to form certain product molecules is one of the main achievements, but also continued challenges of chemistry. The chemical characteristics of molecules, so to say the *chemistry inside a molecule*, is based on the laws of physics, e.g., quantum mechanics. Looking at the very basics of a molecule's existence one can identify electrons as the chemical glue that holds atoms together in a molecule. Since all neutral molecules comprise more than one electron, the interaction of multiple electrons with each other needs to be considered. This electron–electron interaction does not only include the classical repulsion due to the negative charge of the electrons, but also a purely quantum-mechanical aspect: As electrons are fermions, their multi-particle wave function has to be antisymmetric with respect to the exchange of any two individual electrons. Two electrons which are bound in an atom or molecules are not allowed to share exactly the same quantum numbers. This is the famous Pauli exclusion rule [14]. Hence, also the spin of the electron plays a role in whether the electrons can be viewed as indistinguishable particles (parallel spins) or not (opposing spins). The respective energy difference is called *exchange interaction*. In most molecules, however, tens to hundreds of electrons are involved. Describing the respective multi-electronic interactions is very challenging and in most cases only possible with sophisticated assumptions and approximations – many of them Nobel-prize awarded [15–21].
Controlling the electronic properties of molecules is key when it comes to manipulating chemistry. While catalysts help to speed up chemical reactions or even to enable

[1] deoxyribonucleic acid

them, light as a quasi-catalyst promises a larger tunability and overall flexibility with sensitive control capabilities. In addition, ultrashort pulses of light match the natural timescale of bound electrons in atoms and molecules which is the femto- to attosecond regime (10^{-15} s to 10^{-18} s). To understand the microscopic working principle of chemical-control schemes, the behavior of the molecule's constituents, the electrons and atomic nuclei, has to be measured. One approach addresses electrons which are located near the atomic nuclei. These (core) electrons interact with the other, molecular-bond forming electrons, but are strongly bound to their respective nucleus at the same time. Hence, core electrons provide access to both: the global electronic structure within the molecule as well as the local one of their reporter atom. Besides the electrons, the nuclei in a molecule are quantum particles, too. As a consequence, only probabilities can be given in respect to their exact location. This thesis targets both: investigating and manipulating the electrons and the nuclei in a molecule on a quantum level with shortest flashes of light. The respective molecular quantum-control approach alters the *chemistry within a molecule* with highest precision and probes it from an element-specific point of view with x-ray pulses.

The first goal of this thesis is the transient manipulation of the electronic structure and thus chemical characteristics of a molecule. This is achieved without relying on ionization or considerable electronic population transfer within the molecule. Also, the atomic structure of the molecule should remain unaffected during the measurement. It turns out that the quantum properties of electronic interactions, manifesting themselves in the electronic exchange interaction, are the key to a very general, successful approach (for results, see chapter 4).

The second objective of this work is the precision-control of the atomic structure of molecules. Vibrations are often present in our everyday lives, e.g., when the vibrating string of a violin produces a sound. From a classical perspective, vibrations in molecules are oscillating bond-length changes. While quantized vibrational modes describe a (static) spatial distribution of the probability density, a small vibrational excitation leads to a temporal evolution comparable to a classical oscillation. This work explores the low-excitation, so-called *perturbative*, case and its limits. The distances between atoms within a molecule are usually on the order of Ångstrom (10^{-10} m) while the diameters of the atomic nuclei are on the femtometer (10^{-15} m) scale. With these five orders of magnitude difference in lengthscales, the question is, whether molecular bond-length changes can be initiated and characterized which are on the natural lengthscale of the femtometer nuclear diameter. Laser pulses are the

key to sensitively induce such tiny vibrations and subsequently measure them in real time, on a femtosecond timescale (results in chapter 5).
These two scientific showcases—the electron–electron-interaction control and the femtometer bond-length alteration and measurement—illustrate the importance of a suitable laser-pulse source to access molecular quantum phenomena. Thus, a major part of this work is devoted to implementing a suitable pulsed coherent light source. Such a laser source has become an integral part of the new *Quantum Dynamics and Control* laboratories at the *Max Planck Institute for Nuclear Physics*. Here, laser pulses with a duration of only a few optical cycles are tailored to the respective experiment. The pulses exhibit a peak power around 50 GW which equals dozens of large-scale power plants. With such tunable electromagnetic fields, the laser source can provide insights into the microscopic world of quantum phenomena within molecules. Focusing these pulses results in electric field strengths comparable or even larger than the intrinsic ones in an atom or molecule. Hence, this "ultrafast quantum microscope" not only probes but also controls quantum-dynamical processes in molecules. To extend the variety within the ultrashort-pulse portfolio, nonlinear optics are employed to generate shortest pulses with different spectral regimes ranging from the x-ray region to the infrared. Working with such extremely short flashes of light imposes special challenges on their temporal characterization. A thorough characterization of the laser source is possible, though, by utilizing nonlinear optical techniques. Hence, signatures of the quantum system are clearly disentangled from the ones of the measurement tool, the optical pulses.
The experiments on molecules are performed in a vacuum apparatus, the *beamline*, as the involved x-ray radiation is strongly absorbed by the molecules in air. This beamline provides access to different scan parameters. In particular, pulses can be delayed with respect to each other with sub-femtosecond precision and the intensities of the involved pulses can be tuned. The long-term stability of both, the laser source and the beamline, enables measurements with high statistics and thus a precise determination of smallest changes in the experimental observable. Here, the observable is the characteristic (soft-) x-ray spectrum of gaseous target molecules. Finally, the transmitted light—or rather the lack of it due to absorption—reveals the quantum secrets of the molecules with highest sensitivity and in real time.
Similar to molecules, this thesis is governed by structure: First, the theoretical basics that are used over the course of this work are introduced in chapter 2. Important concepts from the fields of optics, quantum mechanics, atomic physics, light-matter

interaction and molecular dynamics as required for the following experiments and results are shortly summarized. Furthermore, details on the characteristics of the target molecule of choice, sulfur hexafluoride (SF_6), are given.
Chapter 3 introduces the experimental setup. After presenting a general overview of the newly established laboratory, the optical setup is described. The laser front end, which is based on Titanium:Sapphire technology, is outlined along with the optical parametric amplifier that enables wavelength-tunability in the 1 µm to 2 µm region. Subsequently, the successive pulse compression to the few-optical-cycle regime and pulse characterization are introduced. In addition, the experimental setup consists of the beamline in which the experiments are conducted. The vacuum beamline is described with its two measurement configurations: In the *intensity scan* mode, only the infrared intensity in the target is altered. The *time-delay scan* configuration additionally allows for a tunable interferometric delay between the infrared and x-ray pulse. Finally, the experimental setup is commissioned on two atomic targets—neon and helium—to gain a first quantification of its technical capabilities.
In chapter 4, the intensity-scan scheme is employed with the aim to control the electronic-exchange energy inside SF_6 molecules. First, a general theoretical toy model for exchange-energy control is developed which is subsequently applied to SF_6. As experimental implementation, x-ray absorption spectroscopy on SF_6 is conducted with the infrared-pulse intensity as the scan variable. A controllable effective exchange energy is extracted by further reducing the complexity of the toy model. Finally, these results are compared to a full quantum-mechanical *ab-initio* calculation and future directions for exchange-energy-control studies are envisioned.
A second experiment, addressing directly the time-resolved molecular dynamics, is described in chapter 5: By employing the time-delay configuration of the beamline, vibrational precision-metrology is demonstrated from a core-electron perspective. After reviewing different experimental techniques for molecular structure determination, the time-resolved spectroscopic measurement on SF_6 molecules is presented. Further details are provided on extracting smallest vibrational signatures from the measurement traces. In combination with a quantum-classical simulation, the signal is disentangled into electronic and vibrational signatures and the respective electron-vibrational coupling dynamics are investigated. This chapter closes with remarks on realistically achievable bond-length precision in measurements on vibrating molecules.
An outlook completes this thesis with ideas about future directions of investigating molecular dynamics on the quantum level with x-ray absorption spectroscopy.

2. Theory basics

In the following chapter, the essential physical concepts that form the basis of this thesis are presented. As ultrafast transient absorption spectroscopy is at the heart of this thesis, the first section 2.1 discusses different aspects of optics including beam propagation, ultrashort laser pulses and nonlinear optics. The subsequent section 2.2 on quantum mechanics describes the quantum behavior of an electron in a harmonic potential as well as the Coulomb interaction of two electrons with each other. In the atomic physics section 2.3, the role of quantum numbers in the description of the electronic structure of atoms and spin-orbit splitting are discussed. The concepts of the above-mentioned fields are applied in section 2.4 which describes light-matter interactions. Here, the interactions of (weak) x-ray light and of strong electric fields with quantum systems are discussed. In addition, the concept of absorbance is introduced. As light-matter interactions trigger quantum-dynamical processes in the experiments in this thesis, aspects of molecular dynamics are presented in section 2.5, namely the Born-Oppenheimer approximation and vibrational dynamics. This chapter closes with a short review of the molecule SF_6 in section 2.6 since SF_6 is the investigated quantum system in the experimental chapters 4 and 5.

2.1. Optics

2.1.1. The electromagnetic spectrum

Light is essential in our everyday life. Our visual perception is based on visible light. In a physical sense, light is an electromagnetic wave, which is quantized in photons. The wave-particle dualism links photons, which are fundamental particles without rest mass, with a respective wavelength or frequency of the electromagnetic wave. The relation between the photon energy E_γ, the wavelength λ and the frequency f is given by

$$E_\gamma = h\,f = \frac{h\,c}{\lambda} \tag{2.1}$$

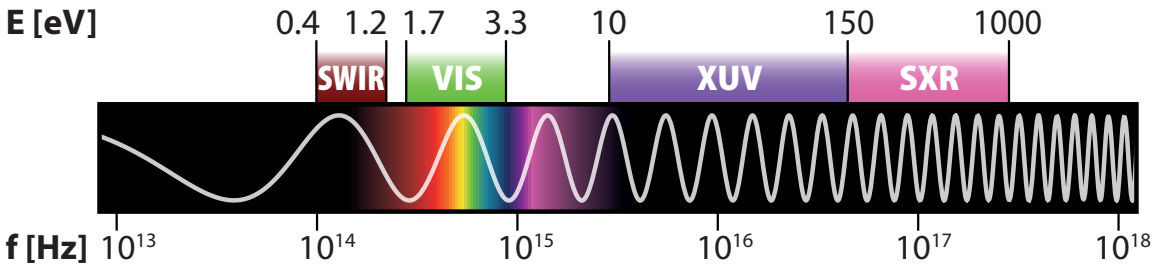

Figure 2.1.: Schematic overview of the electromagnetic spectrum on a logarithmic frequency scale. Here, the short-wavelength infrared (*SWIR*), the visible (*VIS*), the extreme ultraviolet (*XUV*) and the soft x-ray (*SXR*) spectral regions are indicated. Furthermore, the approximate photon-energy boundaries of the respective regions are given.

with the Planck constant $h = 6.62607015 \times 10^{-34}\,\mathrm{J/Hz}$ and the vacuum speed of light $c = 2.99792458 \times 10^{8}\,\mathrm{m/s}$. Furthermore, the frequency can be be converted into an angular frequency $\omega = 2\pi f$. Now, to link ω with E_γ the reduced Planck constant $\hbar = h/2\pi$ can be used:

$$E_\gamma = \hbar\omega \ . \tag{2.2}$$

Some examples for different frequency/photon energy regimes are shown in figure 2.1. Photon energies are typically given in units of electronvolts with $1\,\mathrm{eV} \approx 1.6022 \times 10^{-19}\,\mathrm{J}$. The most important spectral regions[1] within the electromagnetic spectrum in the context of this thesis are

- the **soft x-ray** (SXR) regime: Soft x-ray photons typically have energies between 150 eV and 1 keV (8 nm to 1 nm). These energies coincide with the binding energy of inner-shell electrons close to the core. Thus, SXR light is absorbed in air.

- the **extreme ultraviolet** (XUV) regime: Photons in the XUV regime possess energies between 10 eV and 150 eV (120 nm to 8 nm). XUV light is strongly absorbed by most atoms and molecules, as ionization energies are typically in this energy region. This makes the SXR and XUV regions highly interesting for spectroscopic investigations [22]. Technologically, modern semiconductor-lithography systems operate in the XUV regime [23].

- the **visible** (VIS) regime: This includes wavelengths of around 380 nm to 750 nm (3.3 eV to 1.7 eV). The human eye is sensitive to radiation typically in this red to blue/violet region.

[1] As spectral regions are in general not normed, the exact boundaries and nomenclature might differ considerably in the literature, especially for the infrared and x-ray regions.

- the **infrared** (IR) regime: The IR region is neighboring the VIS regime on the red-side. Thus, it starts around 750 nm and extents to about 1000 µm in wavelength (1.7 eV to 1.2 meV). Due to its energy dissipation, IR radiation is percepted as heat by the human skin, especially for $\lambda > 3\,\mu m$.

  - the **near-infrared** (NIR) regime: This directly neighbors (750 nm to 1000 nm – 1.7 eV to 1.2 eV) the visible range. The NIR region plays an important role in ultrafast laser-pulse technology [24, 25].

  - the **short-wavelength infrared** (SWIR) regime: This spectral region covers wavelength from 1 µm to 3 µm (1.2 eV to 0.4 eV).The SWIR region has a major technological impact in the telecommunication sector [26], among others. In addition, some major absorption bands of water are located in this regime [27].

2.1.2. Beam propagation

The first step towards controlling light is to understand how it propagates through a medium. Basic manipulations of the light beam comprise spatial focusing. Different propagation speeds of various wavelengths in a substrate are another aspect of beam propagation. The wavelength-dependent refractive index leads to dispersion, which is important for predicting the effects on the temporal structure of an ultrashort laser pulse.

2.1.2.1. Gaussian optics

An analytical approach to describe the focusing characteristics of a monochromatic light beam is Gaussian optics. When focusing light, the focus will have a certain spatial extent due to the uncertainty principle [28, 29]. Here, the spatial intensity profile when looking into the beam, the so-called beam mode, is given by a two-dimensional Gaussian function in cylindrical coordinates as

$$I(r,z) = I_0 \left(\frac{w_0}{w(z)} \right)^2 e^{\frac{-2r^2}{w(z)^2}} \tag{2.3}$$

with the peak intensity I_0 and the $1/e^2$ beam waist w_0 in the focus, as well as the on-axis position z and the radial off-axis position r. The parameters are visualized in figure 2.2(a). Here, the focal beam waist is linked to the wavelength λ and the

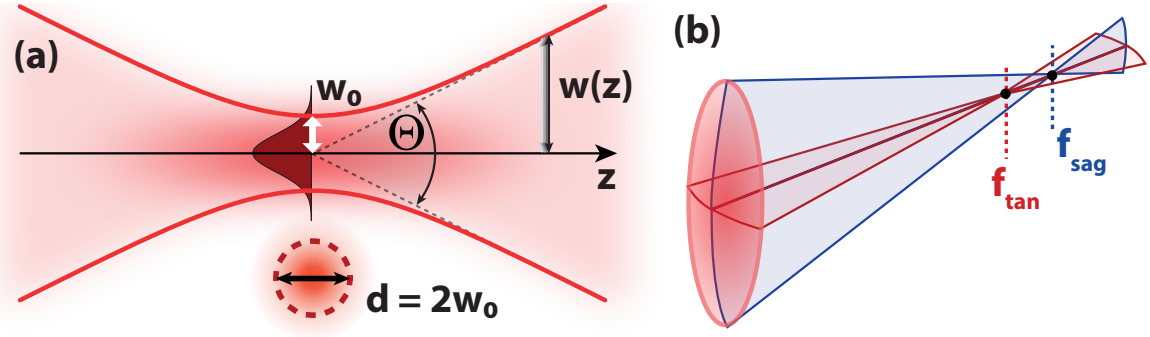

Figure 2.2.: Focusing a Gaussian beam. **(a)** Schematic view on the focus of a Gaussian beam with $1/e^2$ beam waist w_0 (and respective diameter $d = 2w_0$) in the focus and $w(z)$ in general. In addition, the divergence angle Θ is indicated. The Gaussian profile is shown in dark red and the beam mode with diameter indication is presented as inset. **(b)** Focal situation of an astigmatic beam with the tangential (f_{tan}) and saggital (f_{sag}) focus positions.

divergence angle Θ by

$$\Theta = \frac{\lambda}{\pi w_0} \,. \tag{2.4}$$

In case of a non-tight focus[2] geometrical considerations[3] lead to

$$w_0 = \frac{\lambda}{2\pi \tan\left(\frac{w(l_f)}{l_f}\right)} \approx \frac{\lambda\, l_f}{2\pi\, w(l_f)} \tag{2.5}$$

for a known beam waist $w(l_f)$ at a distance to the focus l_f. In reality, optical beams are rarely perfectly Gaussian. This is taken into account by introducing the beam-quality factor M^2 with $w_0^{real} = M^2 w_0$. In case that two orthogonal axes of the beam mode have different focal positions f_{sag} and f_{tan} as in figure 2.2(b), e.g., due to a misaligned lens, the focus becomes *astigmatic*.

A more complicated situation, however, arises if the Gaussian beam is cut by an aperture during focusing as shown in figure 2.3. In this case, diffraction effects have to be taken into account as well (compare figure 2.3(b)). Gillen *et al.* [31] derived an analytic formula that approximates this apertured-beam focusing if the aperture position is far away from the focus:

$$I_{peak}(\gamma) = I_{peak}^0 \left(1 + e^{-2\gamma^2} - 2e^{-\gamma^2}\right) \qquad \text{with} \qquad \gamma = \frac{r_{ap}}{w_{beam}} \,. \tag{2.6}$$

[2] This condition is met in the application scenarios of this thesis.
[3] For a derivation the reader is referred to any optics textbook, e.g., [30].

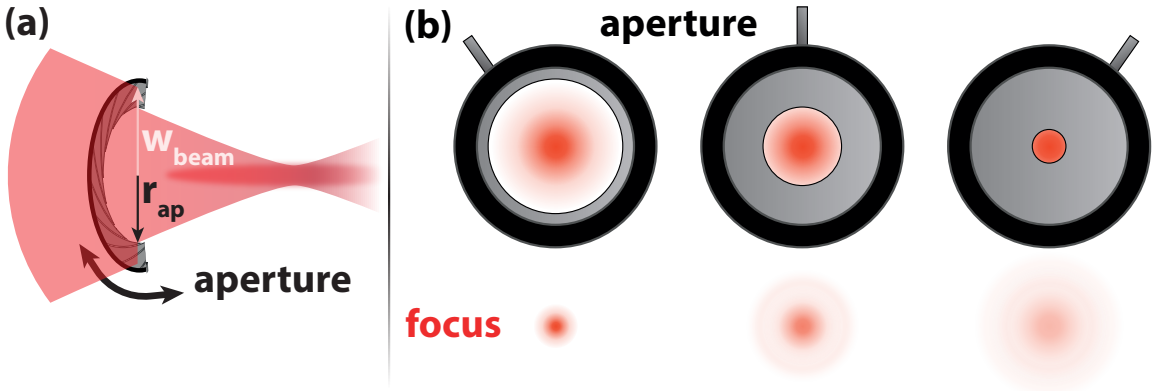

Figure 2.3.: Focusing of an apertured Gaussian beam. **(a)** Modified Gaussian beam focusing scenario in comparison to figure 2.2 with an aperture of radius r_{ap} and the Gaussian beam waist at the aperture position w_{beam}. **(b)** Impact of different aperture positions on the beam focus. Here, diffraction has to be accounted for in order to calculate the correct peak intensity (see equation (2.6)).

Here, I^0_{peak} is the focus peak intensity of the unconstrained beam, r_{ap} the aperture-opening radius and w_{beam} the beam waist at the aperture position.

2.1.2.2. Refractive index

For any light propagation outside of vacuum, the refractive index has to be taken into account. In general, the refractive index n is the ratio between the phase velocity in the medium v_p and the vacuum speed of light c:

$$n = \frac{c}{v_p} \qquad \text{with} \qquad v_p = \frac{\omega}{k} \ . \tag{2.7}$$

For calculating the phase velocity, the dispersion relation $\omega(k)$ (dependence of the angular frequency on the wave number) is required. Normally, materials (e.g., glass) have absorption features in the infrared spectral region due to vibrations (and in case of gaseous/liquid molecules rotation), in the ultraviolet range caused by valence-electron excitation and in the x-ray regime due to core-level electronic excitations. The refractive index can be formulated as complex number $\tilde{n}$ to account for absorption processes (related to α) as well,

$$\tilde{n} = n + i\alpha \qquad \text{with} \qquad \{n, \alpha\} \in \mathbb{R} \ . \tag{2.8}$$

Thus, the refractive index n experiences a jump around resonances as shown in figure 2.4(b). This results in the typical $n(\omega)$ dependence from the IR to the x-ray regime (see figure 2.4(a)). For many materials, the refractive index n can be modeled

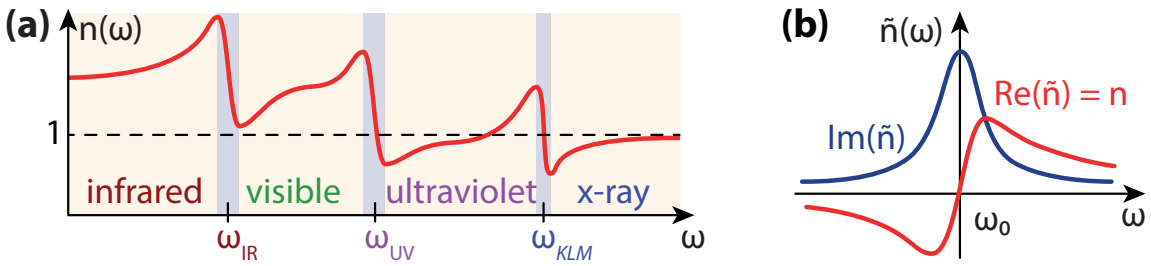

Figure 2.4.: General trend of $n(\omega)$ from the infrared to the x-ray region. **(a)** Multiple absorption bands exist, typically in the infrared (ω_{IR}), the visible/ultraviolet (ω_{UV}) and the x-ray (ω_{KLM}) spectral regions. Close to these resonances, the refractive index declines with ω. These regions (blue shaded) hence show *anomalous* dispersion. **(b)** Real and imaginary part of the complex refractive index $\tilde{n}(\omega)$ around a resonance. The peak in $\Im(\tilde{n})$ represents the absorption, while the real part $n = \Re(\tilde{n})$ exhibits a jump by π.

by the Sellmeier equation [32]:

$$n^2(\lambda) - 1 = \frac{B_1\,\lambda^2}{\lambda^2 - C_1} + \frac{B_2\,\lambda^2}{\lambda^2 - C_2} + \frac{B_3\,\lambda^2}{\lambda^2 - C_3}\ . \tag{2.9}$$

Here, the coefficients $B_{1/2/3}$ and $C_{1/2/3}$ are usually determined via a fit to measured refractive index data. The Sellmeier equation (2.9) is based on the assumption of three main absorption bands. This approximation works well in the infrared to ultraviolet spectral range and is thus often used for calculating $n(\lambda)$ for arbitrary λ [33, 34].

2.1.2.3. Dispersion

The wavelength/frequency dependence of the refractive index leads to *chromatic dispersion*. Chromatic dispersion is the reason for, e.g., rainbows, the spectral separation after transmitting a prism or complex photo-lens designs. For the qualitative description of dispersion, the change of the refractive index with frequency $^{\mathrm{d}n}/_{\mathrm{d}\omega}$ is decisive. Here, two different regimes of dispersion can be differentiated in figure 2.4(a): The wide frequency regions with *normal dispersion*, $^{\mathrm{d}n}/_{\mathrm{d}\omega} > 0$ (marked in light orange) and smaller frequency bands at the resonance showing *anomalous dispersion* $^{\mathrm{d}n}/_{\mathrm{d}\omega} < 0$ (marked in light blue). Looking at the effect of chromatic dispersion on ultrashort, polychromatic pulses of light, the propagation of the pulse envelope is governed by the group velocity

$$v_g = \frac{\mathrm{d}\omega}{\mathrm{d}k} = v_p\left(1 + \frac{\omega}{n}\frac{\mathrm{d}n}{\mathrm{d}\omega}\right)^{-1}\ . \tag{2.10}$$

Here, equation (2.7) is used for the transformation of $^{\mathrm{d}\omega}/_{\mathrm{d}k}$. Hence, the effect of a dispersive medium on the pulse is quantified by the change in the group velocity

at a certain frequency ω_0. A characteristic material property that accounts for the chromatic dispersion effect on pulses is the group velocity dispersion (GVD)

$$\mathrm{GVD}(\omega_0) = \frac{\partial}{\partial\omega}\frac{1}{v_g} = \left.\frac{\mathrm{d}^2 k}{\mathrm{d}\omega^2}\right|_{\omega_0} = \frac{\mathrm{d}}{\mathrm{d}\omega}\left(\frac{1}{v_g(\omega)}\right)\Bigg|_{\omega_0} = \frac{2}{c}\left.\frac{\partial n}{\partial\omega}\right|_{\omega_0} + \frac{\omega_0}{c}\left.\frac{\partial^2 n}{\partial\omega^2}\right|_{\omega_0} . \quad (2.11)$$

As the GVD is a measure for the dispersion per unit length, the overall dispersive effect of a material with thickness L is given by the group delay dispersion (GDD)

$$\mathrm{GDD}(\omega_0) = \mathrm{GVD}\ L\ . \quad (2.12)$$

2.1.3. Ultrashort laser pulses

These dispersion considerations come into play especially when considering ultrashort laser pulses with femtosecond duration. The respective time-dependent electric fields $E(t)$ can be mathematically described by disentangling the fast oscillatory part (with the center frequency ω_c) from the slowly-varying pulse envelope $\mathcal{E}(t)$

$$E(t) = \mathcal{E}(t)\cos\big(\phi(t)\big) \quad (2.13)$$

with the temporal phase $\phi(t)$. The corresponding intensity profile $I(t)$ of the pulse is given by

$$I(t) = \frac{1}{2}\varepsilon_0\, c\, n\, \mathcal{E}^2(t) \quad (2.14)$$

under the approximation of a slowly varying electric field envelope compared to ω_c. Here, the vacuum dielectric permittivity ε_0 is used. The τ_{FWHM} duration of the pulse refers to the full width at half maximum (FWHM) of the intensity profile

$$\tau_{FWHM} = 2\sqrt{2\ln 2}\,\sigma_I \quad (2.15)$$

for a Gaussian intensity envelope with standard deviation $\sigma_I = \sigma/\sqrt{2}$ (with σ being the standard deviation of the respective Gaussian $\mathcal{E}(t)$ function). Due to the limited technical accessibility to such pulse durations in the time domain, representing ultrashort pulses in the frequency domain is very useful. This is conducted by mathematically treating the electric field as a complex number

$$\tilde{E}(t) = \mathcal{E}(t)\, e^{i\phi(t)} \quad (2.16)$$

and employing the Fourier transformation

$$\tilde{S}(\omega) = \frac{1}{\sqrt{2\pi}} \int_{-\infty}^{\infty} \tilde{E}(t)\, e^{-i\omega t}\, \mathrm{d}t \quad \Longleftrightarrow \quad \tilde{E}(t) = \frac{1}{\sqrt{2\pi}} \int_{-\infty}^{\infty} \tilde{S}(\omega)\, e^{i\omega t}\, \mathrm{d}\omega \ . \tag{2.17}$$

Hence, equivalently to the time-domain representation of the electric field of the pulse in equation (2.16), its formulation in the spectral domain comprises the real-valued spectral envelope $\mathcal{S}(\omega)$ and the spectral phase $\varphi(\omega)$. While spectral intensities and thus $\mathcal{S}(\omega)$ are easily measurable with spectrometers, a full characterization of $\tilde{S}(\omega)$ and in consequence $E(t)$ requires knowledge of the respective phase. Starting with the Taylor expansion of the temporal phase

$$\phi(t) = \sum_{n=0}^{\infty} \frac{\phi_n}{n!} t^n = \phi_{CEO} + \omega_c\, t + \sum_{n=2}^{\infty} \frac{\phi_n}{n!} t^n = \phi_{CEO} + \omega_c\, t + \Phi(t) \ , \tag{2.18}$$

the constant *carrier-envelope offset*[4] ϕ_{CEO}, and the center frequency ω_c are separated from the higher-order phases $\Phi(t)$. Now, the instantaneous frequency $\omega(t)$ of the oscillating electric field is given by

$$\omega(t) = \frac{\mathrm{d}\phi(t)}{\mathrm{d}t} = \omega_c + \frac{\mathrm{d}\Phi(t)}{\mathrm{d}t} \ . \tag{2.19}$$

Here, higher-order phase terms ($\Phi(t) \neq 0$) lead to a shift of the instantaneous frequency over time. This is commonly referred to as *chirp* of an ultrashort pulse. The propagation through transparent media affects the chirp of the pulse according to the dispersion properties of the material. For further analysis the Taylor expansion of the spectral phase around the center frequency ω_c is employed:

$$\begin{aligned} \varphi(\omega) &= \sum_{n=0}^{\infty} \frac{\varphi_n}{n!} (\omega - \omega_c)^n = \\ &= \varphi_{CEO} + \mathrm{GD}\,(\omega - \omega_c) + \frac{\mathrm{GDD}}{2} (\omega - \omega_c)^2 + \frac{\mathrm{TOD}}{6} (\omega - \omega_c)^3 + \mathcal{O}\left[(\omega - \omega_c)^4\right] \ . \end{aligned} \tag{2.20}$$

Here, the group delay (GD) equals a constant time shift due to $n \neq 1$ of the material and the GDD results in a linear chirp. For very short pulses, e.g., of only a few optical cycles in duration, higher order spectral phases cannot be neglected. An example is the third-order dispersion (TOD) which leads to multi-pulse structures. Any spectral

[4] ϕ_{CEO} is also called carrier-envelope phase (CEP).

phase terms of second order or higher inevitably lead to a temporal elongation of the pulse. Hence, the shortest—so-called *Fourier-limited*—pulses are achieved by a "flat" spectral phase without polynomial contributions beyond the linear regime. More information on ultrashort pulses is provided in [24].

2.1.4. Nonlinear optics

While the effect of material properties on light has been discussed in the section 2.1.2.3 on the example of dispersion, intense electromagnetic fields can also transiently alter material properties including the refractive index. Such effects are discussed in the field of *nonlinear optics*. Since the demonstration of *light amplification by stimulated emission of radiation* (laser) by Maiman in 1960 [35], and especially with the development of pulsed laser sources [36–38], the required light intensities are readily available. For a mathematical description of nonlinear optics, the influence of the electric field $E(t)$ on the polarization[5] of the medium $P(t)$ is investigated by a power series in $E(t)$:

$$P(t) = \varepsilon_0 \left[\chi^{(1)} E(t) + \chi^{(2)} E^2(t) + \chi^{(3)} E^3(t) + \mathcal{O}\left(E^4(t)\right) \right] . \tag{2.21}$$

Here, χ are the susceptibilities. While the refractive index (defined in equation (2.7)) is linked to the linear susceptibility via $n = \sqrt{1 + \chi^{(1)}}$, nonlinear processes are described by $\chi^{(n \geq 2)}$. Here, an example is second-harmonic generation which is the frequency doubling of the fundamental frequency, $\omega_{out} = 2\,\omega_{in}$. Difference-frequency generation can be described equivalently by $\omega_{out,1} = \omega_{in} - \omega_{out,2}$ with $\omega_{in} > \omega_{out,2}$. In this case, the energy $\hbar\omega_{in}$ of a photon is effectively split into two lower energy photons $\hbar\omega_{out,1}$ and $\hbar\omega_{out,2}$. The $\omega_{out,1}/\omega_{out,2}$-ratio can be controlled by stimulating the emission with another photon and thus effectively copying this photon, hence the name *optical parametric amplification*. Note, that $\chi^{(2)}$ processes can only take place in non-centrosymmetric materials, e.g., certain birefringent media. In the next-higher nonlinear order, $\chi^{(3)}$, four photons have to be considered. With a monochromatic input field $E\cos(\omega t)$ and using the cosine-identity

$$E^3 \cos^3(\omega t) = {}^1\!/_4\, E^3 \cos(3\omega t) + {}^3\!/_4\, E^3 \cos(\omega t) , \tag{2.22}$$

[5] The polarization is the dipole moment per unit volume of the material.

two different resulting effects can be differentiated: First, similar to frequency doubling, *third-harmonic generation* (THG) occurs with $\omega_{out} = 3\,\omega_{in}$. Second, the $^3/_4 \cos(\omega t)$ represents the nonlinear, intensity-dependent refractive index n_2:

$$n' = n + n_2\, I \quad \text{with} \quad n_2 = \frac{3}{2n^2\varepsilon_0}\chi^{(3)} \ . \tag{2.23}$$

Here, the overall resulting refractive index is n'. As the electric field of the laser pulse is in general time and space-dependent, intense ultrashort pulses can induce an $n_2(\vec{r}, t)$. The spatial effect of n_2 which is induced by a Gaussian beam mode leads to a radially refractive-index alteration which is comparable to a lens. Hence, this spatial nonlinear effect is referred to as *self focussing* or *Kerr lensing*. Another spatial $\chi^{(3)}$ effect is the generation of a *transient grating* (TG) refractive-index modulation induced by two noncollinear beams which overlap in a medium. Another pulse can then diffract from this transient grating. Secondly, the temporal pulse structure can induce a time-dependent $n_2(t)$. The transmission of a (dispersion-free) medium of length L leads to a time-varying phase of the pulse by

$$\phi_{SPM}(t) = -\frac{n_2\omega_c}{c}\, I(t) \ . \tag{2.24}$$

Thus, this effect is called *self-phase modulation* (SPM). As a consequence of the phase modulation, new frequency components are generated as shown by applying (2.24) to the instantaneous frequency equation (2.19):

$$\omega(t) = \omega_c + \frac{\mathrm{d}\phi_{SPM}}{\mathrm{d}t} = \omega_c - \frac{n_2\omega_c}{c}\frac{\mathrm{d}}{\mathrm{d}t} I(t) \ . \tag{2.25}$$

Hence, SPM is an efficient mechanism to spectrally broaden ultrashort pulses. A thorough discussion of nonlinear optics is found in [39].

2.1.5. High-order harmonic generation

While second- and third-harmonic generation can be well described via the polarization series in equation (2.21), peak intensities in the $10^{13}\,\mathrm{W/cm^2}$ to $10^{15}\,\mathrm{W/cm^2}$ regime can lead to photon energy up-conversions of a factor >100. This phenomenon is known as *high-order harmonic generation* (HHG) and requires a different explanatory approach: At these intensities, only accessible with focused, ultrashort laser pulses, the laser-field strength ($10^8\,\mathrm{V/cm}$ to $10^9\,\mathrm{V/cm}$ regime) is comparable to the intra-atomic

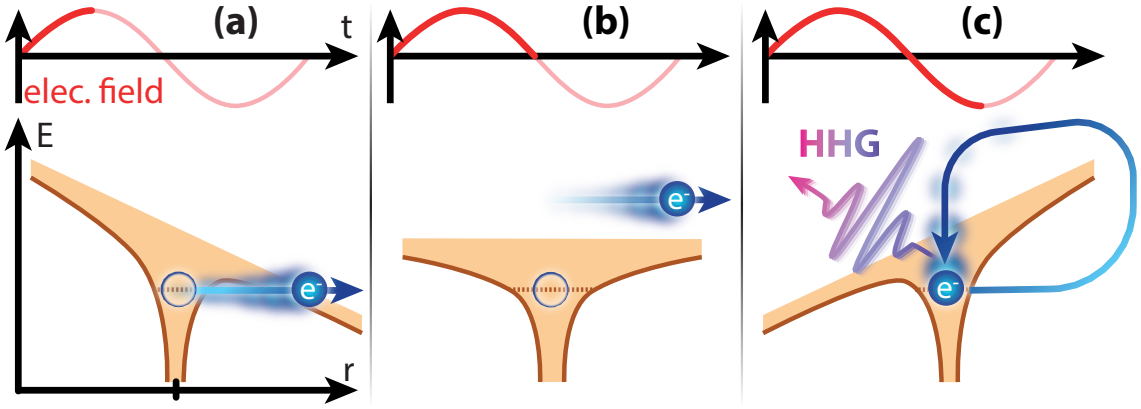

Figure 2.5.: Three-step model of high-order harmonic generation. **(a)** The peak electric field bends the binding potential of the electron such that it can tunnel through the barrier. **(b)** The quasi-free electron gains kinetic energy as it is further accelerated by the electric field of the pulse. **(c)** Due to the oscillatory behavior of the electric field, the electron is accelerated back towards the parent ion. Upon recombination, the electron emits its kinetic energy in form of an HHG photon.

fields ($\sim 5 \times 10^9$ V/cm in a hydrogen atom). The light–electron interaction that results in the emission of high harmonics can be explained with the semi-classical three-step model [40, 41] as illustrated in figure 2.5: Here, the laser field distorts the Coulomb potential which binds the atom to the atomic core. Now, in the first step, the electron can tunnel through the remaining potential barrier. Subsequently, the quasi-free electron is further accelerated by the electric field of the pulse in the second step. Due to the sign change in the oscillating electric driver field, the electron is accelerated back to the atomic core it originated from. In the final step, the electron recombines with a certain probability with the parent ion. When recombining, the kinetic energy that the electron gained in combination with the binding energy is emitted in form of a high-energy photon in the XUV or x-ray spectral region. The HHG process takes place every half cycle which results in a train of attosecond high-harmonic pulses for a multi-cycle driving pulse. This pulse-train structure translates to the spectral regime and leads to defined harmonic intensity peaks. In centrosymmetric media such as noble gases, the resulting spectrum consists of discrete harmonics at $(2n+1)\,\omega_d$ with $n \in \mathbb{N}$ of the driver laser frequency ω_d. The highest reachable photon energy (the so-called *cutoff*) is approximately

$$E_{cutoff}[eV] = I_P + 3 \times 10^{-13}\, I_0\, \lambda^2 \,, \tag{2.26}$$

with the ionization potential I_P of the HHG medium in eV, the driver-field intensity I_0 in W/cm^2 and the driver wavelength λ_d in µm [42]. As the I_P of noble gases is

in the 10 eV to 25 eV range and the peak intensity I_0 is limited due to ionization and phase-matching constraints, *wavelength scaling* is the method of choice to reach highest photon energies [43]. This increase in photon energy, however, comes at the cost of a dramatically reduced efficiency by $\sim \lambda^{-6}$ [44] which can be explained with full quantum-mechanical models [45]. Hence, the low conversion efficiency of around 10^{-6} for common $\lambda_d = 0.8\,\mu\text{m}$ driver pulses is further reduced by shifting towards the 1 µm to 2 µm region for wavelength-scaling purposes and makes corresponding counter measures, e.g., loose focusing of a high-energy pulse, necessary.
For reviews on HHG and its applications, the reader is referred to [42, 46, 47].

2.2. Quantum mechanics

While some aspects of the generation and manipulation of light—the *tool* for the experiments in this thesis—were presented in the previous section 2.1, the principle physical laws for *target* systems like molecules are discussed in the following: quantum mechanics.
To determine the stationary states of a quantum system, the time-independent Schrödiger equation is employed:

$$\hat{H} \left|\Phi\right\rangle = E \left|\Phi\right\rangle \ . \tag{2.27}$$

The Hamilton operator $\hat{H}$ describes the quantum system and the wave function Φ the system's eigenstate with a corresponding eigenenergy E. In addition, the non-relativistic motion within quantum-mechanical systems are calculated via the time-dependent Schrödinger equation (TDSE)

$$i\hbar\frac{\partial}{\partial t}\left|\Psi(t)\right\rangle = \hat{H}\left|\Psi(t)\right\rangle \ . \tag{2.28}$$

Here, $\Psi(t)$ is the quantum state in which the system is at time t. The wave function can be represented as a superposition of the eigenstates $|\Phi_k\rangle$ which form an orthogonal basis:

$$\left|\Psi(t)\right\rangle = \sum_k c_k(t) \left|\Phi_k\right\rangle \tag{2.29}$$

with the state coefficients $c_k(t)$. Now, the dynamical propagation of the system's state is given by the time-evolution operator $\hat{U}$ applied to the system's state at an

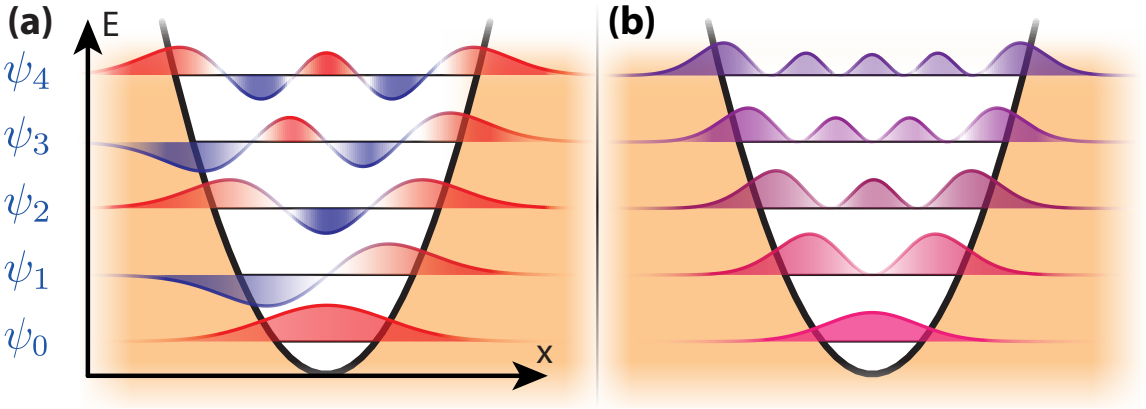

Figure 2.6.: Schematic view of the quantum-mechanical harmonic oscillator. **(a)** First five wave functions ψ_n with $n \in \{0, 1, 2, 3, 4\}$. **(b)** Corresponding probability densities $|\psi_n|^2$.

initial time $t = 0$,

$$\left|\Psi(t)\right\rangle = \hat{U} \left|\Psi(0)\right\rangle \ . \tag{2.30}$$

For a time-independent Hamiltonian, the time propagation is described by

$$\left|\Psi(t)\right\rangle = e^{-\frac{i\hat{H}t}{\hbar}} \left|\Psi(0)\right\rangle \ . \tag{2.31}$$

2.2.1. Quantum-mechanical harmonic oscillator

One of the most basic but highly relevant scenarios is a quantum particle (e.g., an electron) in a parabolic potential – the quantum harmonic oscillator. Here, the Hamiltonian is

$$\hat{H} = \underbrace{\frac{1}{2} m \hat{p}^2}_{\substack{E_{kin} \\ particle}} + \underbrace{\frac{1}{2} m \omega^2 \hat{x}^2}_{\substack{harmonic \\ potential}} \tag{2.32}$$

with the particle's mass m, the momentum operator $\hat{p} = -i\hbar\frac{\partial}{\partial x}$, the position operator $\hat{x}$ and the oscillator frequency ω. The oscillator frequency is defined by the potential and the force constant k by $\omega = \sqrt{k/m}$. By employing the time-independent Schrödinger equation, the wave function of the n-th ($n \in \mathbb{N}_0$) state is determined to

$$\psi_n(x) \propto \frac{1}{\sqrt{2^n\, n!}} e^{-\frac{m\omega x^2}{2\hbar}} H_n\left(\sqrt{\frac{m\omega}{\hbar}} x\right) \quad \text{with} \quad H_n(x) = (-1)^n e^{x^2} \frac{\mathrm{d}^n}{\mathrm{d}x^n} e^{-x^2} \ . \tag{2.33}$$

The eigenenergies of $|\psi_n\rangle$ are

$$E_n = (2n + 1)\frac{\hbar\omega}{2} \ . \tag{2.34}$$

These results are illustrated in figure 2.6 together with the probability density $\left|\psi_n(x)\right|^2$ of a populated state n. Notably, the eigenenergies E_n in equation (2.34) distinctly differ from the classical-harmonic-oscillator case:

- Only quantized energy levels exist with an equidistant level spacing of $\hbar\omega$.
- The ground-state energy level is not zero, but $\frac{\hbar\omega}{2}$.
- The probability density is non-zero outside the potential.

These quantum characteristics are the basis for corresponding effects without classical correspondence such as tunneling. As the time-evolution of the wave functions $\psi_n(x)$ is given by (compare equation 2.30)

$$\psi_n(x,t) = e^{-\frac{i E_n t}{\hbar}} \psi_n(x,0) \ , \tag{2.35}$$

the probability density $\left|\psi_n(x,t)\right|^2$ of an excited state $n \geq 1$ shows no time dependence while the classical analogue exhibits oscillatory dynamics. Only the mixing of multiple states (e.g., ground and excited state) leads to an overall $\left|\psi(x,t)\right|^2$ that varies in time. The probability density $\left|\psi(x,t)\right|^2$ of such a mixed state ψ is called *wave packet*.

2.2.2. Single-body versus many-body state

As we have discussed one particle in a potential in the previous section 2.2.1, this situation is expanded to two quantum particles (electrons in the following). Here, the question is how the total wave function Ψ of these two electrons, the so-called many-body state, can be derived from the states of each single electron ψ_1 and ψ_2. The ansatz for two electrons at the positions $\vec{r}_1$ and $\vec{r}_2$, respectively, is

$$\Psi(\vec{r}_1, \vec{r}_2) = \psi_1(\vec{r}_1)\ \psi_2(\vec{r}_2) \tag{2.36}$$

which is called the Hartree product [48] of the single-particle wave functions. As electrons are fermions, Pauli's exclusion principle applies and the many-body wave function has to fulfill the antisymmetrization condition $\Psi(\vec{r}_1, \vec{r}_2) = -\Psi(\vec{r}_2, \vec{r}_1)$. This

is guaranteed by the linear combination of Hartree products

$$\Psi(\vec{r}_1,\vec{r}_2) = \frac{1}{\sqrt{2}}\left[\psi_1(\vec{r}_1)\ \psi_2(\vec{r}_2) - \psi_1(\vec{r}_2)\ \psi_2(\vec{r}_1)\right] = \frac{1}{\sqrt{2}}\begin{vmatrix}\psi_1(\vec{r}_1) & \psi_2(\vec{r}_1)\\ \psi_1(\vec{r}_2) & \psi_2(\vec{r}_2)\end{vmatrix} = |\psi_1\psi_2\rangle\ . \tag{2.37}$$

This construction of $\Psi(\vec{r}_1,\vec{r}_2)$ via a matrix is called Slater determinant [49] and can be formulated for an N-particle problem as the corresponding determinant of an $N \times N$ matrix with a $1/\sqrt{N!}$ normalization prefactor.

2.2.3. Coulomb interaction

Now, the contribution of the electron–electron interaction to the total energy of the system can be derived. The interaction energy E_C between two electrons at distance $r = \left|\vec{r}_1 - \vec{r}_2\right|$ is given by the Coulomb operator $\hat{Q} = \frac{e^2}{4\pi\varepsilon_0\,\hat{r}}$ which is applied to the two-electron wave function (equation 2.37):

$$\begin{aligned} E_C &= \left\langle \Psi(\vec{r}_1,\vec{r}_2)\right| \hat{Q} \left|\Psi(\vec{r}_1,\vec{r}_2)\right\rangle = \\ &= \frac{e^2}{8\pi\varepsilon_0}\Bigg[\iint \psi_1^\dagger(\vec{r}_1)\ \psi_2^\dagger(\vec{r}_2)\ \frac{1}{r}\ \psi_1(\vec{r}_1)\ \psi_2(\vec{r}_2)\ \mathrm{d}\vec{r}_1\,\mathrm{d}\vec{r}_2 \\ &\qquad - \iint \psi_1^\dagger(\vec{r}_1)\ \psi_2^\dagger(\vec{r}_2)\ \frac{1}{r}\ \psi_1(\vec{r}_2)\ \psi_2(\vec{r}_1)\ \mathrm{d}\vec{r}_1\,\mathrm{d}\vec{r}_2 \\ &\qquad - \iint \psi_1^\dagger(\vec{r}_2)\ \psi_2^\dagger(\vec{r}_1)\ \frac{1}{r}\ \psi_1(\vec{r}_1)\ \psi_2(\vec{r}_2)\ \mathrm{d}\vec{r}_1\,\mathrm{d}\vec{r}_2 \\ &\qquad + \iint \psi_1^\dagger(\vec{r}_2)\ \psi_2^\dagger(\vec{r}_1)\ \frac{1}{r}\ \psi_1(\vec{r}_2)\ \psi_2(\vec{r}_1)\ \mathrm{d}\vec{r}_1\,\mathrm{d}\vec{r}_2 \Bigg]\ . \end{aligned} \tag{2.38}$$

By exchanging $\vec{r}_1 \leftrightarrow \vec{r}_2$ in the last two integrals, this results in

$$\begin{aligned} E_C = &\underbrace{\frac{e^2}{4\pi\varepsilon_0}\iint \psi_1^\dagger(\vec{r}_1)\ \psi_2^\dagger(\vec{r}_2)\ \frac{1}{r}\ \psi_1(\vec{r}_1)\ \psi_2(\vec{r}_2)\ \mathrm{d}\vec{r}_1\,\mathrm{d}\vec{r}_2}_{\text{direct integral } E_d} \\ &\underbrace{-\frac{e^2}{4\pi\varepsilon_0}\iint \psi_1^\dagger(\vec{r}_1)\ \psi_2^\dagger(\vec{r}_2)\ \frac{1}{r}\ \psi_1(\vec{r}_2)\ \psi_2(\vec{r}_1)\ \mathrm{d}\vec{r}_1\,\mathrm{d}\vec{r}_2}_{\text{exchange integral } E_x} = E_d + E_x\ . \end{aligned} \tag{2.39}$$

Equation (2.39) demonstrates that the electron–electron interaction can be split into two parts – the so-called *direct* Coulomb interaction E_d and the exchange interaction E_x. Here, the direct Coulomb interaction is the classical repulsion ($E_d > 0$) of the two

negatively charged electrons. The exchange interaction has no classical analogue and is a purely quantum-mechanical contribution as a consequence of the Pauli principle.

2.3. Atomic physics

The previous section 2.2 discussed the general quantum-mechanical principles of electrons in a potential and the interaction of electrons with each other. In the following, this is applied to electrons which are bound in an atomic potential and the resulting electronic structure of atomic systems is discussed.

2.3.1. Quantum numbers

For one-electron atomic systems, e.g., atomic hydrogen, the Schrödinger equation (2.27) can be solved analytically. The resulting wave function Ψ turns out to be separable into two functions if Ψ is expressed in the polar coordinates with radius r and the polar angles Θ and ϕ:

$$\Psi_{n,l,m_l}(r,\Theta,\phi) = R_{n,l}(r)\, Y_{l,m_l}(\Theta,\phi) \ . \tag{2.40}$$

Here, $R_{n,l}(r)$ is called the *radial wave function*, whereas $Y_{l,m_l}(\Theta,\phi)$ is a spherical harmonic. The derivation of equation (2.40) is given in [50], for example. Now, the state and hence the overall wave function Ψ of a bound electron is determined by a set of four quantum numbers:

- *principal* quantum number $\boldsymbol{n}$ with $n \in \mathbb{N}$: n is linked to the eigenenergy E_n of the n-th state Ψ_n. Here, $n = \{0,1,2,3,4,...\}$ are referred to as $K, L, M, N, O...$ shell [51].

- *angular momentum* quantum number $\boldsymbol{l}$ with $0 \leq l \leq n-1$: l is the *degree* of the spherical harmonic Y_{l,m_l}. The quantum number l determines the orbital angular momentum and hence the shape of the respective atomic orbital. The values $l = \{0,1,2,3,...\}$ are represented by $\{s,p,d,f,...\}$.

- *magnetic* quantum number $\boldsymbol{m_l}$ with $-l \leq m_l \leq l$: m_l is the *order* of the spherical harmonic Y_{l,m_l}. The quantum number m_l is the projection of the angular momentum (e.g., to the z-axis) and thus orientation of the orbital.

- *spin* quantum number $\boldsymbol{m_s}$ with $-s \leq m_s \leq s$: as an electron is a fermion ($s = 1/2$), the quantum number m_s fulfills $m_s \in \{-1/2, 1/2\}$. These two values of m_s are also referred to as *spin-down* and *spin-up*, respectively.

The orbital symmetry is linked to the orbital shape and hence l. Here, the behavior of the electronic state under point reflection is described by the *parity* quantum number $P = (-1)^l$ with even ("gerade") symmetry $P = 1$ or odd ("ungerade") symmetry $P = -1$. From the quantum-number perspective, Pauli's exclusion rule states that two electrons are not allowed to share all four quantum numbers $\{n, l, m_l, m_s\}$ within the same quantum system.

2.3.2. Spin-orbit splitting

While the Schrödinger equation 2.27 does not include relativistic effects, they have to be accounted for in order to explain precision spectroscopy measurements. In respective experiments, a so-called *fine-structure* splitting of the energy levels is observed. Hence, $\{n, l, m_l, m_s\}$ are not considered *good quantum numbers*[6] any longer. To solve this problem, the *total angular momentum* quantum number j is introduced which takes the interaction between the spin and the angular-momentum quantum number into consideration. Two extreme cases can be differentiated concerning how l and s couple to j:
When the electron–electron interaction is much smaller than the spin-orbit interaction, the total angular momentum of a system with i electrons is

$$\vec{J} = \sum_i \vec{j}_i = \sum_i \left(\vec{l}_i + \vec{s}_i\right) \ . \tag{2.41}$$

Thus, $j \in \{|j_1 - j_2|, |j_1 - j_2| + 1, ..., j_1 + j_2\}$ for two electrons with j_1 and j_2, respectively. Here, the spin and the orbit of a single electron couple first before all electrons couple their respective j_i. This *jj-coupling* scheme is typically found in large atoms where the high positive charge of the nucleus results in relativistic kinetic energies of inner-shell electrons. Hence, relativistic effects dominate over the electron–electron correlations.

[6] If an operator commutes with the Hamiltonian, the corresponding eigenvalue is a *good quantum number*. For a mathematical treatment, see e.g., [52].

In the contrary case, $\vec{J}$ calculates to

$$\vec{J} = \vec{L} + \vec{S} = \sum_i \vec{l}_i + \sum_i \vec{s}_i \ . \tag{2.42}$$

In the *LS-coupling* case j is hence given by $j \in \{|L-S|, |L-S|+1, ..., L+S\}$. Due to the strong interaction among the electrons they couple their respective angular momenta and spins first, before the combined angular momentum couples with the total spin. This is also referred to as Russel-Saunders coupling and is a good description for light atoms and systems with strong electronic correlations.
Now, the quantum number m_j is given by $m_j \in \{-j, -j+1, ..., j-1, j\}$. A thorough discussion of quantum numbers and spin-orbit splitting is given in [50].

2.4. Light-matter interaction

As some aspects of the electronic structure of the constituents of matter—atoms—have been discussed in section 2.3, the next step is to manipulate matter by targeting its electrons using light. Here, different wavelength- as well as intensity-regimes of light have different effects on atoms.

2.4.1. X-ray interaction with matter

First, the interaction of x-ray radiation with matter is discussed. The photon energy of x-rays can reach the binding energies of inner-shell electrons as illustrated in figure 2.7(a). Here, a core-level electron with binding energy $E_{binding}$ is ejected upon interaction with the photon and moves in the continuum with an energy according to the photoelectric effect [53], $E_{kin}^{e^-} = E_{x-ray} - E_{binding}$. Subsequently, two different mechanisms can occur to fill the core-level electron vacancy (compare figure 2.7(b) and 2.7(c)): In a fluorescence process, an electron from a higher shell takes the vacant inner-shell place of the ejected photo-electron. The excess in binding energy is emitted in form of another x-ray photon. Alternatively, the surplus of energy is transferred to another electron and can respectively lead to further ionization in a process called Auger-Meitner decay [54, 55]. While the Auger-Meitner decay is dominant for light atoms, fluorescence becomes the major relaxation mechanism for heavier elements [56]. More details on x-ray light-matter interaction are presented in [57].

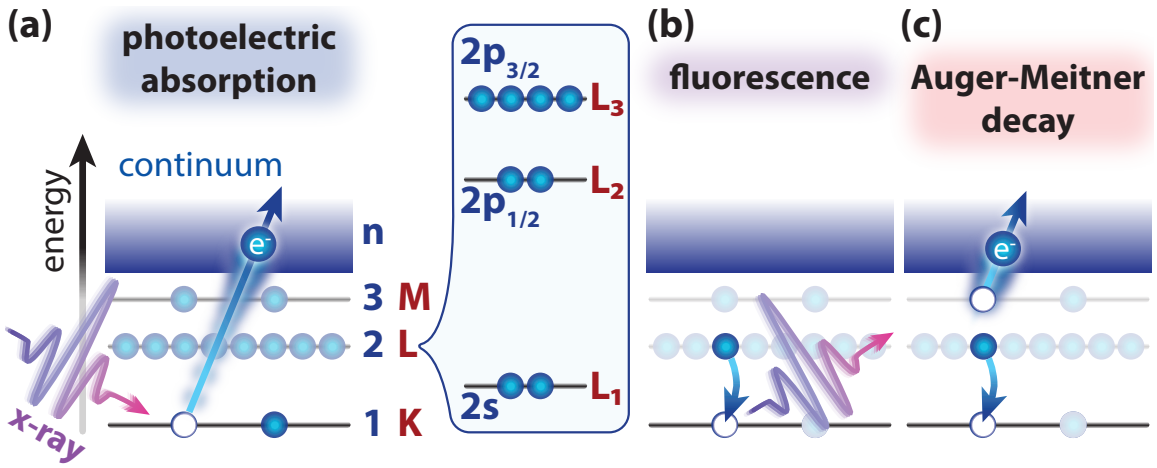

Figure 2.7.: Interaction between an x-ray photon and an atom. **(a)** The photoelectric effect through the absorption of an x-ray photon (*photoelectric absorption*) can eject an inner-shell electron into the continuum. The inset shows an exemplary spin-orbit splitting of the energy levels with the respective nomenclature. **(b)** The remaining core hole is filled by an electron from a more weakly bound shell. The difference in binding energies is emitted as a *fluorescence* photon. **(c)** Alternatively, the excess energy is transferred to another electron to overcome its binding energy in a process called *Auger-Meitner decay*.

2.4.2. Laser-dressed states

While the x-ray electric fields that are produced in the experimental setup which is described later in this thesis (compare section 3.3.2) are comparably weak, this assumption cannot be made for the utilized intense pulses in the IR regime. Hence, the interaction of such intense pulses with a prototypical two-level system is investigated in the following. Here, $|\phi_a\rangle$ and $|\phi_b\rangle$ are two eigenstates of the unperturbed system. A strong electric field $E(t)$ couples these two states via the dipole operator $\hat{d}$. Thus, the total wave function Ψ is described as a superposition of these two states:

$$|\Psi(t)\rangle = c_a(t)\ |\phi_a\rangle\ +\ c_b(t)\ |\phi_b\rangle\,. \tag{2.43}$$

Here, $c_a(t)$ and $c_b(t)$ are the corresponding time-dependent state coefficients. The TDSE (equation (2.28)) for this system in its matrix/vector representation is

$$i\hbar\frac{\partial}{\partial t}\begin{bmatrix} c_a(t) \\ c_b(t) \end{bmatrix} = \hat{H}(t)\begin{bmatrix} c_a(t) \\ c_b(t) \end{bmatrix} \qquad \text{with} \qquad \hat{H}(t) = \begin{pmatrix} E_a & d^*_{ab}\,E(t) \\ d_{ab}\,E(t) & E_b \end{pmatrix}. \tag{2.44}$$

The dipole matrix element d_{ab} is used in equation (2.44) in combination with the eigenenergies E_a and E_b of ϕ_a and ϕ_b. Employing the rotating-wave approximation

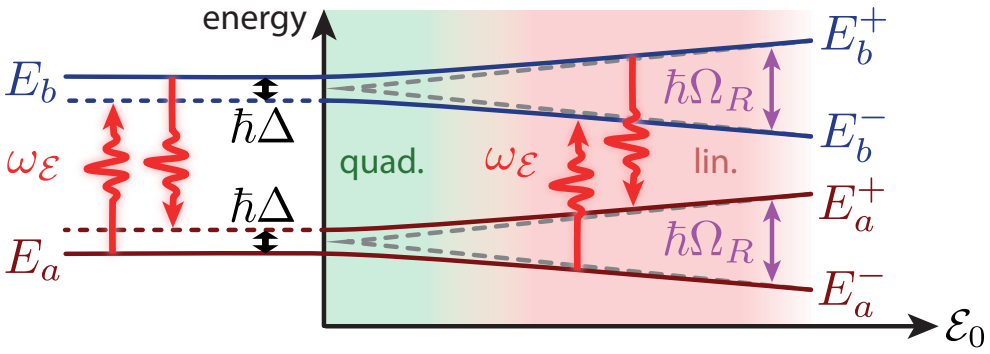

Figure 2.8.: AC Stark effect. Two states with energies E_a and E_b are coupled by an off-resonant field $E(t) = \mathcal{E}_0 \cos(\omega_\mathcal{E} t)$ which is detuned by $\hbar\Delta$. With rising field strength $\mathcal{E}_0$ the levels split into $E_a^\pm$ and $E_b^\pm$. For large $\mathcal{E}_0$, the splitting is proportional to the generalized Rabi frequency Ω_R. The level shifts are quadratic in field strength (green-shaded) for moderate and linear (red-shaded) for high field strengths.

results in

$$\hat{H}_{rot} = \hbar \begin{pmatrix} \Delta/2 & \Omega \\ \Omega^* & -\Delta/2 \end{pmatrix} \tag{2.45}$$

with $\Omega = d_{ab}\,{}^{\mathcal{E}_0}/\hbar$ being the Rabi frequency of the system and $\mathcal{E}_0$ the slowly-varying envelope of the electric field. Furthermore, the detuning $\Delta = \left({}^{E_b}/\hbar - {}^{E_a}/\hbar\right) - \omega_\mathcal{E}$ of the electric field with carrier frequency $\omega_\mathcal{E}$ is used. Now, this Hamiltonian is solved by diagonalizing the matrix and determining the eigenstates and -vectors. The corresponding energies of the laser-dressed eigenstates are

$$\begin{aligned} E_a^\pm &= E_a + \frac{\hbar}{2}\Delta \pm \frac{\hbar}{2}\,\Omega_R \qquad \text{and} \\ E_b^\pm &= E_b - \frac{\hbar}{2}\Delta \pm \frac{\hbar}{2}\,\Omega_R \end{aligned} \tag{2.46}$$

with the generalized Rabi frequency $\Omega_R = \sqrt{\Delta^2 + |\Omega|^2}$. The level energies $E_a^\pm$ and $E_b^\pm$ as a function of the field strength $\mathcal{E}$ are illustrated in figure 2.8. Here, a quadratic shift in the level energies is observed for comparably weak fields strengths with $\Omega \ll \Delta$ which is referred to as quadratic AC Stark shift [58, 59]. For higher intensities $\Omega \gg \Delta$ this evolves into the linear AC Stark regime. A complete derivation of the AC Stark effect is given in [60] for example.

To summarize, by interaction with intense light fields, a general two-level system shows a level splitting and shifting.

2.4.3. Dipole selection rules

Not all quantum states can be coupled with each other via a photon, though. If an electronic state is excited by a laser field in the electric dipole approximation—which is valid for most experiments including the ones discussed in this thesis—certain selection rules apply:

1. $\Delta m_j \in \{0, \pm 1\}$
2. $\Delta J \in \{0, \pm 1\}$ with $0 \nleftrightarrow 0$
3. $P_{out} = -P_{in}$

If electronic-interactions dominate over the spin-orbit coupling (LS-coupling – compare section 2.3.2) further selection rules can be deducted:

- $\Delta m_L \in \{0, \pm 1\}$; for linearly polarized light: $\Delta m_l = 0$
- $\Delta L \in \{0, \pm 1\}$ with $0 \nleftrightarrow 0$;
  for a one-electron transition: $\Delta l_i = \pm 1$ due to required parity change
- $\Delta S = 0$

A derivation of the dipole selection rules can be found in [50] or other text books on atomic physics.

2.4.4. Strong-field ionization

Intense laser fields do not only lead to laser-dressed states as shown in section 2.4.2, but can also result in an ionization of the atomic/molecular target. Photon energies in the infrared spectral region might not be sufficient to overcome the binding energy of a valence electron as demanded by the linear photoelectric absorption (compare section 2.4.1). In intense laser fields, however, *strong-field ionization* can take place. Different regimes of this phenomenon can be distinguished: While multiple photons can contribute together to overcome the ionization potential in a nonlinear process, namely *multiphoton ionization*, the perspective of the atomic-potential distortion by the laser field leading to *tunneling* or even *over-the-barrier ionization* is favorable in different scenarios. The multiphoton and the tunneling regime can be differentiated by the Keldysh parameter [61]:

$$\gamma = \sqrt{\frac{I_P}{2U_P}} = \frac{\omega}{e}\sqrt{\frac{\varepsilon_0 c\, m_e I_P}{I_0}} \propto \frac{1}{\sqrt{I_0}\lambda} \,. \tag{2.47}$$

Here, the ionization potential of the target medium is denoted as I_P and the ponderomotive potential $U_P = {e^2 E_0^2}/{4 m_e \omega_0^2}$ comprises the electron mass m_e, the laser frequency ω (wavelength λ, respectively), the electron charge e and the peak intensity $I_0 = {\varepsilon_0 c E_0^2}/{2}$. Pure multiphoton absorption is found for $\gamma \gg 1$, whereas the tunneling regime is indicated by $\gamma \ll 1$. Examples for the multiphoton regime comprise resonance-enhanced multiphoton ionization [62] or above-threshold ionization [63]. The tunneling description, on the other side, is used in high-order harmonic generation (compare section 2.1.5). A thorough discussion of strong-field ionization and the respective ionization rates is given in [64–67].

2.4.5. Absorbance

2.4.5.1. Transient absorption spectroscopy

Light-matter interaction is at the heart of the experimental technique that is employed in this thesis—transient absorption spectroscopy. Spectroscopy characterizes a physical system by the energy spectrum of particles after they interacted with the system. Here, these particles are photons and they interact with the system's charged constituents[7] via electromagnetism. Furthermore, absorption spectroscopy implies that light with a known spectrum propagates through a target medium and its transmitted spectrum is compared with the incident one. In the case of x-ray photons, the light-matter interactions as illustrated in figure 2.7 are crucial.
While Fraunhofer first discovered dark lines in the visible spectrum of the sun [69] in the early 19th century, Kirchhoff and Bunsen [70] linked the missing spectral components to chemical elements. Since then, photon spectroscopy has developed into a powerful tool for analytical chemistry. The classical absorption spectroscopy scheme in the visible and UV spectral region relies on excitations of valence electrons in atoms and molecules. Targeting the strongly-bound electrons via x-ray core-level spectroscopy can provide the opportunity to investigate the influence of the nucleus on energy splittings or offer a localized view on a certain atom or element within a complex system like molecules [71] or solids [72] amongst others. While the development of electron spectroscopy of core-level electrons was awarded with the Nobel prize in physics in 1981 [71], the all-optical alternative, x-ray absorption spectroscopy (XAS), is readily used nowadays to study the electronic structure of matter [73, 74].

[7] As the nucleus is much heavier than the electrons, the electric field can be assumed to only couple with the electrons [68].

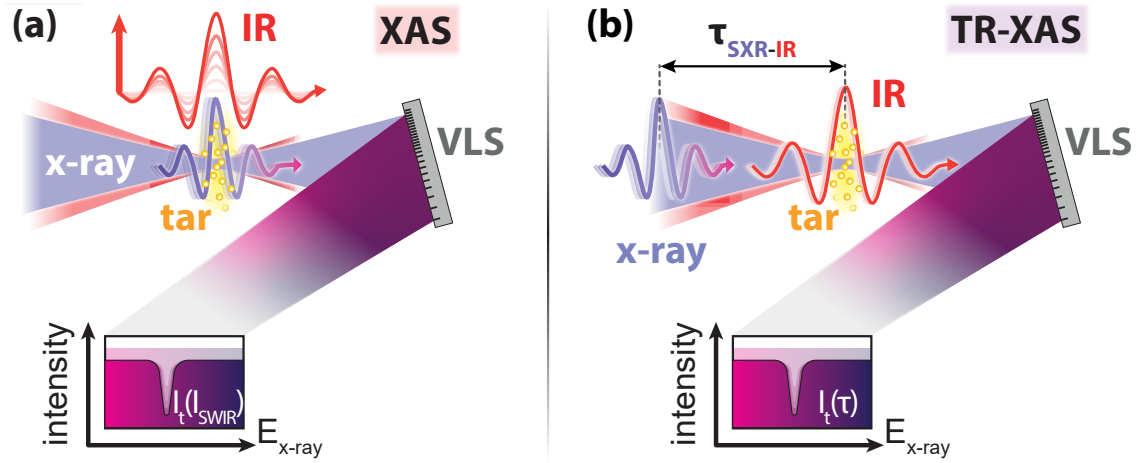

Figure 2.9.: XAS with perturbing IR pulse versus TR-XAS scheme. **(a)** XAS scheme, where an x-ray pulse is focused into the target (*tar*) in temporal and spatial overlap with an intense IR pulse. The IR pulse can be tuned in intensity. After transmission through the target, the x-ray spectrum is dispersed by a grating (*VLS*). The spectral intensity of the x-ray I_t is measured for different IR intensities I_{IR}. **(b)** In the TR-XAS scheme, the scan variable is the time delay $\tau_{SXR\text{-}IR}$ between x-ray and IR pulse.

As an expansion of the classical XAS scheme, an x-ray pulse can be combined with another optical pulse. In a first variation of XAS, the additional optical pulse with variable intensity and the x-ray pulse interact with the target at the same time (see figure 2.9(a)). Alternatively, the perturbing pulse can be delayed in time with respect to the x-ray pulse and reveal the system's dynamics which is encoded in the x-ray absorption spectrum (see figure 2.9(b)). This approach is referred to as time-resolved x-ray absorption spectroscopy (TR-XAS). Without the restriction to the x-ray spectral region, this concept is known as transient absorption spectroscopy (TAS).

2.4.5.2. Linking the optical density to the transition strength

In absorption spectroscopy, the data are usually represented in form of the absorbance or optical density (OD). The OD is calculated via the spectral intensity without the target $I_0(\omega)$ and the spectral intensity after transmitting the target $I_t(\omega)$:

$$OD(\omega) = -\log_{10}\left(\frac{I(\omega)_t}{I(\omega_0)}\right) \tag{2.48}$$

For weak fields and hence in the case of linear absorption, the absorbance in equation (2.48) can be linked to Beer-Lambert's law and hence to the absorption cross

section σ:

$$OD(\omega) = \frac{\rho_N \, d}{\ln(10)} \, \sigma(\omega) \ . \tag{2.49}$$

Here, the transmitted sample thickness d and the particle density in the target ρ_N are utilized. A derivation of equation (2.49) is given in [75, 76]. Now, the connection to other fundamental measures for light-matter-interaction processes are investigated. One example is the Einstein coefficient B_{ik} related to the probability of absorption of a photon with energy $\hbar\omega$ that leads to a transition from state $|i\rangle$ to state $|k\rangle$:

$$B_{ik} = \frac{c}{\hbar\omega} \underbrace{\int \sigma_{ik}(\tilde{\omega}) \, \mathrm{d}\tilde{\omega}}_{\text{line strength } S_{ik}} \ . \tag{2.50}$$

Furthermore, the Einstein coefficient is proportional to the oscillator-strength parameter of the transition, $B_{ik} \propto f$. In addition, B_{ik} can be expressed employing the dipole operator $\hat{d}$,

$$B_{ik} = \frac{e^2}{6\varepsilon_0\hbar^2} \left| \langle k | \, \hat{d} \, | i \rangle \right|^2 = \frac{e^2}{6\varepsilon_0\hbar^2} |d|^2 \ , \tag{2.51}$$

with the transition dipole moment d. Overall, this can be summarized to

$$B_{ik} \propto f \propto |d|^2 \propto \int \sigma_{ik}(\omega) \ \mathrm{d}\omega \propto \int OD(\omega) \ \mathrm{d}\omega \ . \tag{2.52}$$

Hence, the strength of a dipole transition is proportional to the absorbance area under the respective resonance. For the derivations of the Einstein-coefficient relations, the reader is referred to [77].

2.5. Molecular dynamics

The experiments in this thesis employ light-matter interactions to investigate and control molecular systems on the quantum level. Here, the main concepts of molecular dynamics are discussed on an exemplary diatomic molecule consisting of the hypothetical atoms A and B. Here, the molecule AB is bound together by a covalent bond consisting of valence electrons from A and B. This molecule exhibits possible excitations on different scales: While the strongly-bound core-level electrons have approximately the same energy as in the atomic case and are addressed in the x-ray regime, excitation energies of the bond-contributing valence electrons are expected to

be in the visible to ultraviolet spectral region, $E_e \approx$ few eV. Furthermore, vibrational quanta with energies in the infrared region, approximately one hundred times smaller than for valence-electronic excitations are expected ($E_{vib} \approx$10 meV to 100 meV). Finally, the vibrational level structure is further split by rotational excitations on the few-meV level and thus in the far-infrared regime.

2.5.1. Born-Oppenheimer approximation

Now, the system's dynamics are described by a Hamiltonian operator of the form

$$\hat{H} = \hat{T}_N + \hat{T}_e + \hat{V} \tag{2.53}$$

with the kinetic energy operator of the nuclei $\hat{T}_N$ and of the n electrons in the molecule $\hat{T}_e$ as well as the total potential energy of the system $\hat{V}$. The potential energy comprises the Coulomb interactions between the electrons and the nuclei, between the n electrons and between the two nuclei with charges $Z_A\,e$ and $Z_B\,e$

$$\hat{V}(\vec{R}_A,\vec{R}_B;\vec{r}_1,...,\vec{r}_n) = \frac{e^2}{4\pi\varepsilon_0}\left\{\underbrace{\sum_{i=1}^{n}\left[-\frac{Z_A}{\left|\vec{r}_i-\vec{R}_A\right|}-\frac{Z_B}{\left|\vec{r}_i-\vec{R}_B\right|}\right]}_{electronic-nuclear}+\underbrace{\sum_{i<j}^{n}\frac{1}{\left|\vec{r}_i-\vec{r}_j\right|}}_{electronic}+\underbrace{\frac{Z_A Z_B}{\left|\vec{R}_A-\vec{R}_B\right|}}_{nuclear}\right\} \tag{2.54}$$

with the coordinate of the k-th electron $\vec{r}_k$ and the nuclear coordinates $\vec{R}_A$ and $\vec{R}_B$. The complete molecular wave function Ψ can be written as[8]

$$\Psi(\vec{R}_A,\vec{R}_B;\vec{r}_1,...,\vec{r}_n) = \sum_q \eta_q(\vec{R}_A,\vec{R}_B)\phi_q(\vec{R}_A,\vec{R}_B;\vec{r}_1,...,\vec{r}_n)\ . \tag{2.55}$$

Here, $\eta_k(\vec{R}_A,\vec{R}_B)$ is the nuclear wave function which describes vibrations and rotations for the electronic state q. The set of electronic wave functions ϕ_q describes the electron movements in the potential of the fixed nuclei. Due to the high dimensionality of the problem, the molecular Schrödinger equation is only solvable under certain assumptions and approximations.

The most common approximation is based on the fact that the mass of the nucleus is more than 2000 times the electron mass. Thus, the movement of the nuclei is much slower than the electronic dynamics. As a consequence, the approximation is

[8] In general, combined space and spin coordinates have to be used instead of spatial coordinates only. For simplicity, though, the space-only-coordinates notation is utilized throughout this section.

made that the electrons follow the movement of the nuclei instantaneously (hence the *adiabatic* nature of the approximation) while the nuclei are unaffected by the instantaneous movement of the electrons. Instead, the nuclei move within the effective potential of the electronic state. Hence, the system's wave function reduces to

$$\Psi_s(\vec{R}_A, \vec{R}_B; \vec{r}_1, ..., \vec{r}_n) = \eta_s(\vec{R}_A, \vec{R}_B)\phi_s(\vec{R}_A, \vec{R}_B; \vec{r}_1, ..., \vec{r}_n) \tag{2.56}$$

for an electronic state s. This adiabatic approximation which leads to the decoupling of electronic and nuclear wave functions is referred to as *Born-Oppenheimer approximation* (BOA) and is the basis of most quantum-dynamical calculations of molecular dynamics nowadays.

2.5.2. Vibrations in a potential energy curve

The disentangling of nuclear and electronic dynamics in the BOA is used to establish a procedure to solve molecular dynamics' problems: First, the purely electronic Schrödinger equation is solved for different internuclear distances $\left|\vec{R}_A - \vec{R}_B\right| = d$. This results in the d-dependent energy of the electronic state s, $E_s(d)$. Secondly, $E_s(d)$ acts as a potential in which the nuclear wave equation is solved. Hence, $E_s(d)$ is called *potential energy curve* (PEC). Analogous to the electronic state-structure for a bound electron in the Coulomb-potential of the nucleus, the PEC governs the vibrational/rotational wave functions and energy levels. For a diatomic molecule, an empirical approximation of the PEC is given in form of the Morse potential [78]

$$V_M(d) = D_e\left(e^{-2\alpha(d-d_0)} - 2e^{-\alpha(d-d_0)}\right) \tag{2.57}$$

with the well depth D_e, the equilibrium bond length d_0 and the constant α. Figure 2.10 shows a comparison of a Morse and a harmonic potential. For large internuclear separations d, the Morse potential levels off which gives rise to a bond breakage or dissociation of the molecule. While the harmonic potential shows a constant level spacing (compare section 2.2.1), the energy-level spacing of the anharmonic Morse potential is decreasing according to the energy of the n-th vibrational level

$$E_n = \hbar\omega_0\left(n + 1/2\right) - \frac{\left[\hbar\omega_0\left(n + 1/2\right)\right]^2}{4\,D_e} \tag{2.58}$$

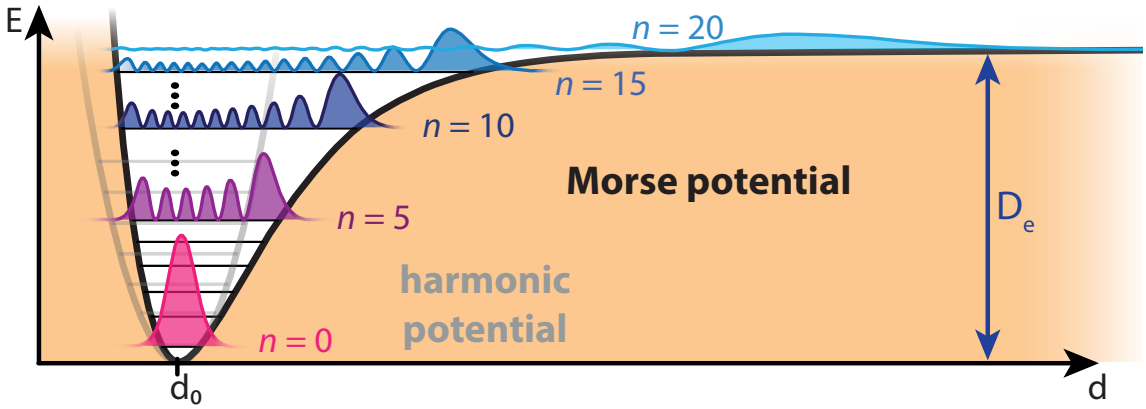

Figure 2.10.: Morse versus harmonic potential. A Morse potential (black solid line) with potential depth D_e is illustrated together with the probability density (here normalized to constant probability for each state) for six states. The equilibrium internuclear distance is denoted by d_0. For comparison, a harmonic potential is overlayed in shaded grey.

with the fundamental vibrational frequency ω_0. For small n, the harmonic and the Morse potential match reasonably well. A frequently used alternative to the Morse potential is the Lennard-Jones potential [79–81].
For molecules with more than two atoms, the PEC becomes a potential energy *surface* with the different molecular-structure related axis, e.g., bond angle in addition to bond length. Situations occur, where the potential energy surfaces of two different electronic states become degenerate. These so-called *conical intersections* are prone to non-adiabatic couplings and hence a breakdown of the BOA. The experimental and theoretical description of non-Born-Oppenheimer dynamics is a thriving field in chemical dynamics [82–84].

2.5.3. Vibrational excitation

2.5.3.1. Thermal excitation

Even without any actively induced excitation, the excited vibrational levels within a PEC have a certain population. The statistical probability of a population of the i-th excited vibrational state at a temperature T is given by the Boltzmann statistics:

$$p_i = \frac{1}{Q} e^{\frac{-E_i}{k_B T}} \tag{2.59}$$

with the Boltzmann constant $k_B = 1.380649 \times 10^{-23}\,\mathrm{J/K} \approx 8.617333 \times 10^{-5}\,\mathrm{eV/K}$ and the normalization factor, the canonical partition function

$$Q = \sum_{i=0}^{\infty} e^{\frac{-E_i}{k_B T}} \ . \tag{2.60}$$

For calculating vibrational-state occupations, degeneracies of the vibrational states have to be taken into account. With $k_B T \approx 25\,\mathrm{meV}$ at room temperature, some molecules show a significant population of excited vibrational states (see table 2.1).

Table 2.1.: Thermal populations of excited vibrational states at room temperature. A vibrational normal mode with fundamental frequency ν of an exemplary molecule is denoted. Furthermore, the information about the mode's Raman- and IR-activeness (*Raman?/IR?*) is given in combination with its degeneracy (*deg.*). Moreover, the respective energy of the vibrational excitation is noted by E_ν and the resulting relative population (in comparison to the vibrational ground state) at room temperature, *p(300 K)*. The vibrational data originate from [85].

molecule	ν [$\mathrm{cm^{-1}}$]	Raman?	IR?	deg.	E_ν [meV]	p(300 K) [%]
H_2	4342	y	n	1	538	1×10^{-7}
O_2	2061	y	n	1	256	2×10^{-4}
H_2O	1885	y	y	1	234	1×10^{-2}
CH_4	1380	y	y	3	171	0.4
CO_2	526	n	y	2	65	14

2.5.3.2. IR- and Raman-active modes

To target and control a specific transition to a certain vibrationally excited state, light can be employed. Direct dipole excitation with infrared light prerequisits that the respective vibration induces a change of the molecular dipole. Hence, homo-nuclear molecules such as H_2 or O_2 cannot be vibrationally excited by linear IR absorption. In contrast to that, polar covalent bonds like in the molecule HF show very strong infrared absorption at their vibrational resonance.

Another mechanism for vibrational excitation is the Raman effect [86]. In a non-resonant Raman excitation, a far off-resonant infrared photon[9] ($\omega_{IR} \gg \omega_{vib}$) can couple to a virtual state and induce a transition to the excited vibrational state under

[9] While Raman excitation is a general process and can in principle originate from vibrationally excited states, the coupling from the vibrational ground state is discussed in the following, as this is the relevant case in the experiment in chapter 5.

emission of a correspondingly lower-energy (so-called *Stokes*) photon. The photon energies are given by the energy conservation $\omega_{IR} = \omega_{Stokes} + \omega_{vib}$. In stimulated Raman scattering, the concept of this spontaneous Raman approach is modified by using both, pump and Stokes beam, as an input. Hence, the vibration is excited more efficiently. Stimulated Raman scattering is a $\chi^{(3)}$ nonlinear process and thus can only target vibrational modes that show a change in polarizability (compare section 2.1.4). A stimulated Raman excitation can be conducted with an ultrashort laser pulse that has a spectral bandwidth larger than the vibrational frequency. If the pulse is Fourier-limited, the spectral consideration translates to a pulse duration similar to or shorter than the vibrational period. The nuclear coordinate Q in a Raman-induced vibration is described classically in form of a damped, driven oscillator [87, 88]

$$\ddot{Q} + 2\gamma\,\dot{Q} + \omega_{vib}^2\,Q = \frac{1}{2}N\left(\frac{\mathrm{d}\alpha}{\mathrm{d}Q}\right)_0 E^2 \tag{2.61}$$

with the damping constant γ, the frequency of the vibrational mode ω_{vib}, the number of oscillators N, the change in polarizability per internuclear-distance variation $\left(\frac{\mathrm{d}\alpha}{\mathrm{d}Q}\right)_0$ and the electric field of the driver laser E. Two regimes with respect to the laser-pulse duration τ can be differentiated in equation 2.61:

- $\tau \gg {}^{2\pi}/_{\omega_{vib}}$: If the laser pulse is significantly longer than the vibrational period, the molecular coordinate follows the intensity envelope adiabatically. Hence, the resulting dynamics are significantly longer than the Raman-mode period.
- $\tau \ll {}^{2\pi}/_{\omega_{vib}}$: If the laser pulse is much shorter than the vibrational period, the molecule shows the impulsive response of a damped harmonic oscillator. This is called *impulsive stimulated Raman excitation* (ISRE).

Symmetry considerations are a viable tool to predict whether a vibrational mode is IR- and/or Raman active. Hence, vibrational spectroscopy is a major application of *group theory* in chemistry [89].

2.6. The sulfur hexafluoride molecule

The sulfur-hexafluoride molecule (SF_6) is the target of choice for the quantum-dynamical experiments in this thesis. SF_6 comprises seven atoms of two elements, sulfur and fluorine, as well as 70 electrons overall. With a mass of 146 u, SF_6 is significantly heavier than the main components of air, nitrogen (N_2, 28 u) and oxygen

(O_2, 32 u). As the most electronegative element, fluorine, is involved in the chemical bonding, SF_6 is chemically inert under normal conditions. At the same time, SF_6 exhibits a high ionization potential[10] of $I_P = 15.3\,\text{eV}$ [90] and a large electron-capture cross-section [91, 92]. Hence, SF_6 is widely used as arc-interrupting buffer gas in electrical insulation applications [93, 94]. Moreover, industrial applications such as silicon plasma etching [95] and magnesium casting [96] employ SF_6 gas. The pressure to find alternatives to SF_6 in the industrial context has risen, though, due to its potential role in climate warming: SF_6 is 24 000 times more potent than CO_2 as a greenhouse gas due to its strong absorption in the IR in combination with its long lifetime in the atmosphere [94, 97]. From an experimental point-of-view, SF_6 is a non-poisonous, sulfur-containing molecule which is gaseous under normal conditions. This results in an easy handling and sample delivery in the experiment.

2.6.1. Electronic structure

Taking a closer look at the electron configuration of the involved elements, sulfur and fluorine, [Ne] $3s^2\,3p^4$ and [He] $2s^2 2p^5$, respectively, illustrates the sp^3d^2 hybridization of sulfur in SF_6: Here, one s, three p and two d mix to six orbitals orthogonally oriented to each other. In the case of sulfur in SF_6, all the mentioned orbitals belong to $n = 3$. These six hybrid orbitals overlap with the $2p$ orbitals of the fluorine atoms resulting in covalent molecular bonds. As a consequence, the sp^3d^2 hybridization leads to the octahedral molecular geometry as shown in Fig. 2.11. Thus, SF_6 is a representative of the O_h point group [98], which will be important for the vibrational modes discussed in the next section 2.6.2. In its vibrational ground state, the S–F equilibrium bond length is $d_0 = 1.561\,\text{Å}$[99]. The molecular-orbital structure of SF_6 around the lowest unoccupied molecular orbital (LUMO) is shown in figure 2.11 including the atomic orbital contributions. Overall, SF_6 exhibits ten occupied valence orbitals with in total 48 electrons [91]. In the following, x-ray excitations from the core-level $2t_{1u}$ spin-orbit-split molecular orbital with *ungerade* symmetry to the $6a_{1g}$ LUMO with *gerade* symmetry are of interest. This represents an excitation close to the sulfur $L_{2,3}$-absorption edges (compare figure 2.7(a) in the light-matter interaction section). A measured x-ray absorption spectrum that comprises the $6a_{1g}$ doublet is shown in figure 2.11(a). With 172.27 eV and 173.44 eV, the $2t_{1u}^{-1}(j = {}^3/_2, {}^1/_2)\,6a_{1g}^1$ resonances are located slightly below the L_3 (180.27 eV) and L_2 (181.48 eV) edges [101].

[10] The ionization potential of SF_6 is comparable to the one of the noble gas argon, $I_P(\text{Ar}) = 15.8\,\text{eV}$.

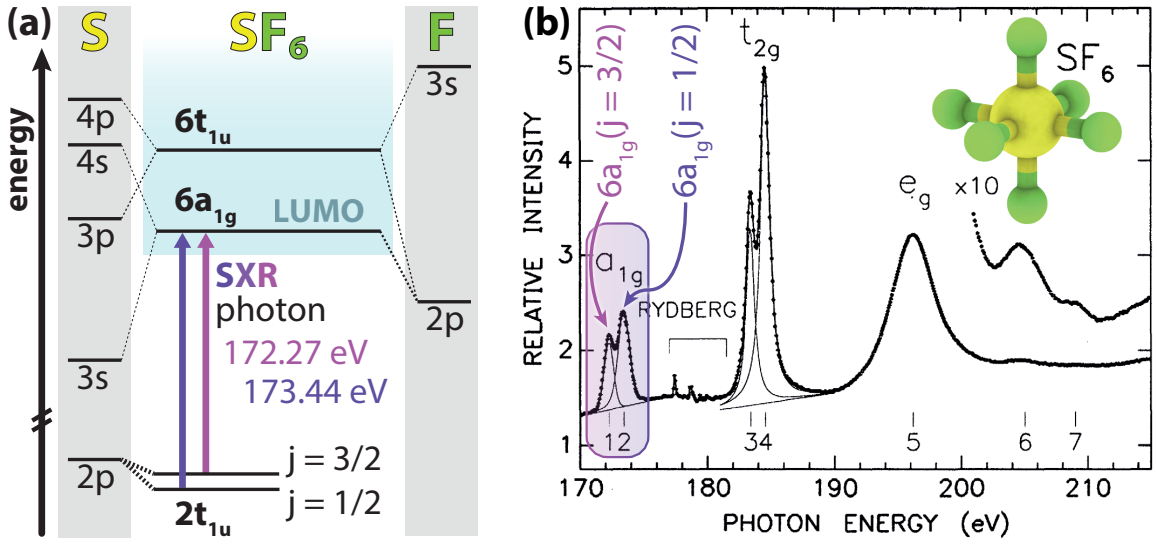

Figure 2.11.: Electronic structure and absorbance of SF_6 around the $L_{2,3}$-edges. **(a)** Schematic molecular orbital structure including the core-level spin-orbit-split $2t_{1u}$ orbital (sulfur $2p$), the LUMO ($6a_{1g}$) and an example for above-LUMO orbitals with *ungerade* symmetry ($6t_{1u}$). The contributions of the atomic orbitals are indicated with dashed lines. The line strength is equivalent to the relative contribution (for more details see [100]). **(b)** Measured absorption spectrum of SF_6 around the sulfur $L_{2,3}$-edges, reprinted from [101]. The respective core-to-LUMO transitions indicated by the violet arrows in (a) result in the marked $6a_{1g}$ doublet resonance. The inset illustrates the molecular structure of SF_6.

2.6.2. Vibrational modes

The vibrational characteristics of SF_6 are given by its O_h symmetry which results in the normal modes that are illustrated in figure 2.12. Besides the schematic vibrational geometry changes of the six normal modes, figure 2.12 indicates their wave number, vibrational period, Raman/IR character, degeneracy and relative strength of the resonance. Here, the very strong IR-active mode ν_3 at a wavelength of $\lambda_3 = 10.5\,\mu m$ is a major reason for the effectiveness of SF_6 as a greenhouse gas as it is located in the atmospheric transparency window around $\lambda = 10\,\mu m$ [94]. The Raman-active, fundamental symmetric breathing mode A_g (ν_1 in figure 2.12) at a wave number of $775\,cm^{-1}$ ($\lambda = 12.9\,\mu m$) is of specific interest for this thesis and is targeted in the experiments in chapter 5.

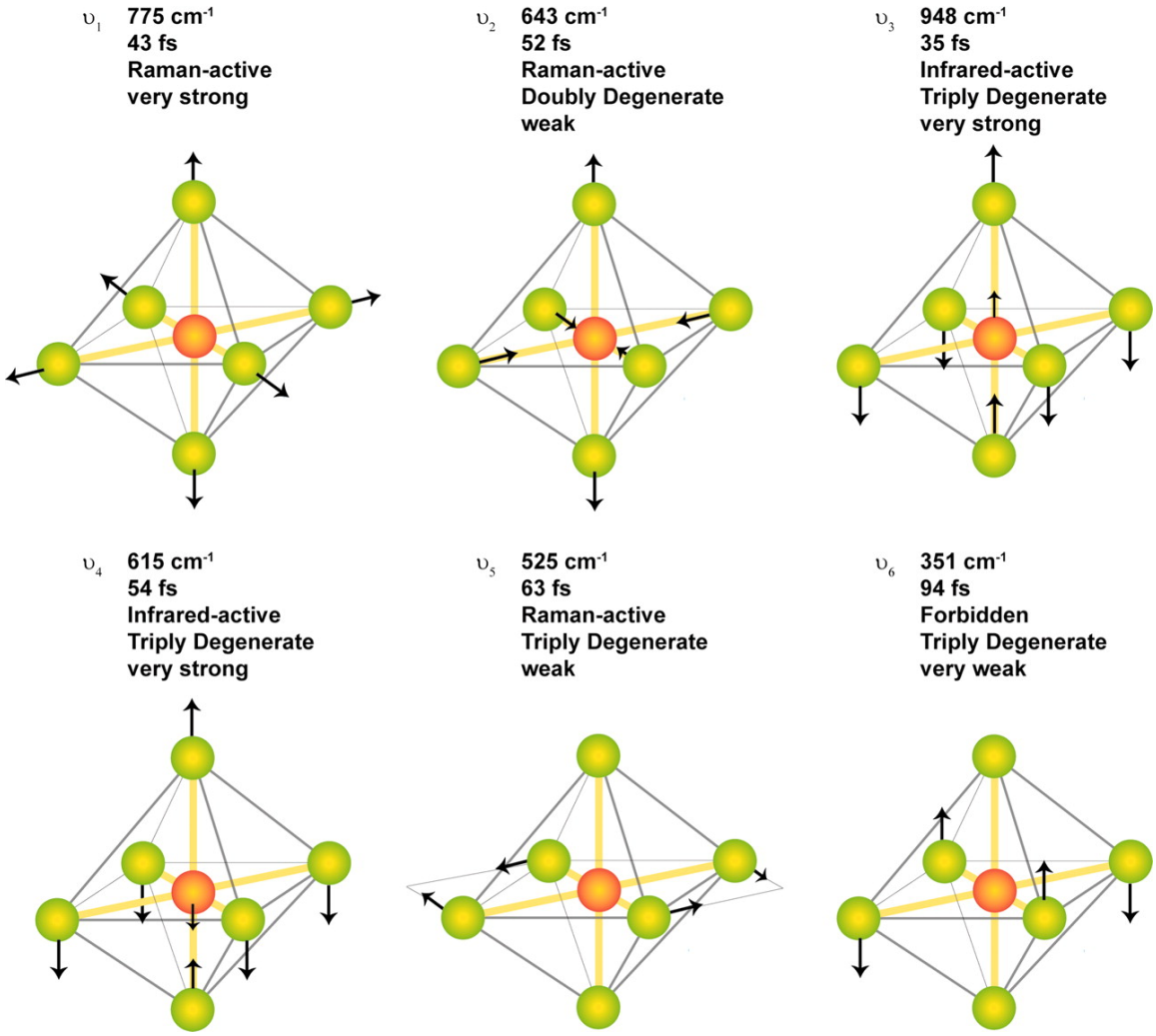

Figure 2.12.: Vibrational normal modes of SF_6. Here, the respective wave number, vibrational period, Raman/IR character, degeneracy and relative strength of the respective resonance are indicated. The Raman-active vibrational mode ν_1 is the symmetric breathing mode A_g and will be of special interest in chapter 5 of this thesis. Reprinted from [102].

3. Experimental setup for transient absorption spectroscopy

Two main experimental ingredients are required to successfully perform core-level transient absorption spectroscopy: A source for ultrashort and intense laser pulses and a vacuum beamline in which the extreme ultraviolet/soft x-ray pulses are generated and the TAS experiment is conducted.
Firstly, ultrashort laser pulses with peak intensities typically between $10^{13}\,\mathrm{W/cm^2}$ to $10^{15}\,\mathrm{W/cm^2}$ are required to drive the highly nonlinear HHG process [42, 47, 103, 104]. Secondly, the aim is to investigate the quantum dynamical processes of atoms and molecules under the influence of strong fields with intensities around $10^{12}\,\mathrm{W/cm^2}$ to $10^{15}\,\mathrm{W/cm^2}$. To resolve fastest dynamics and reach these high peak intensities, laser pulses with a duration of only a few optical cycles are crucial. In addition, a tunability of the pulses' center wavelength is highly desirable as this grants flexibility in addressing the electronic structure and atomic coordination of the specific quantum system that is investigated. A center wavelength in the short-wavelength infrared region and thus longer than the conventional 800 nm is ideal to avoid multiphoton ionization and operate in the quasi-adiabatic regime [105]. If the optical period of the pulses is longer than the lifetime of an excited state in atoms and molecules, the laser pulses can be treated as a comparably strong, quasi-static field which perturbs the system without ionization or dissociation on the timescale of the measurement. Furthermore, due to the ponderomotive scaling of the HHG process this enables the generation of higher photon energies in the SXR region [43, 106–108]. Nevertheless, an emphasis is put on the long-term stability of the laser system to enable long and complex measurement campaigns under stable conditions to extract smallest signals in the data. The key to reach this goal of constantly monitoring the system are thorough characterization capabilities.
Besides an innovative laser source, a flexible and stable experimental vacuum beamline enables to further push the frontiers of TAS. As XUV and SXR photons are absorbed

in air, their generation as well as the TAS experiment itself has to be carried out in a vacuum environment. Flexibility is maximized by choosing an all-reflective, Fraunhofer-like TAS approach. Thus, a spectrally broadband use of the beamline due to its grazing-incidence, metal-coated optics is possible. Furthermore, the design is optimized such that one can switch between different measurement schemes (e.g., varying only the SWIR intensity or also changing the SXR-SWIR time delay) within minutes. Here, closed-loop motorized in-vacuum actuators are extensively used. In addition, this grants the possibility to conduct fast, precise and repeatable optimizations, e.g., concerning HHG flux. The long-term stability is further accomplished by abstaining from long-legged, external interferometers for time-dependent measurements and instead re-using the SWIR beam after HHG and employing a split-and-delay assembly. In the following, an overview is given of the experimental capabilities in the newly established *Laser Laboratory 2* (*LL2*) of the *Quantum Dynamics and Control* division at MPIK. Afterwards, more details are presented on the flexible SWIR few-cycle pulse source setup and its characterization. This is accompanied by a description of the vacuum beamline. Finally, two TAS measurement examples in neon and helium are given to illustrate the technical capabilities of the overall setup. A section that summarizes the key features of the experimental setup and provides perspectives for further technical developments closes the chapter.

3.1. Overview: Laser Laboratory 2 at MPIK

The first goal of this PhD project was to build a new laser laboratory at *MPIK* from scratch. Here, the general idea was to enable stable high-energy laser operation by having a dedicated temperature- and humidity-controlled clean room[1]. To furthermore enhance the stability of the environmental conditions, another large-scale laser housing covers the region of the optical table assembly that contains the laser system and optical setup. This effectively shields the setup from heat sources like power supplies, controllers and computers. Flow boxes on top of the laser housing guarantee an even better temperature stability and the laminar airflow prevents dust particles from settling. Smaller-scale covers and boxes finally shield the different parts of the laser and optical setup and guarantee a stable thermal equilibrium. Furthermore,

[1]The temperature stability in the laser laboratory is specified to $\pm 0.5^{\circ}$C and under the flow boxes $\pm 0.1^{\circ}$C at a constant relative humidity $+10\%/-5\%$. As no continuous particle monitoring takes place, the laboratory is considered a *grey room* but approximately matches a clean room class ISO 4-5 under the flow boxes [109].

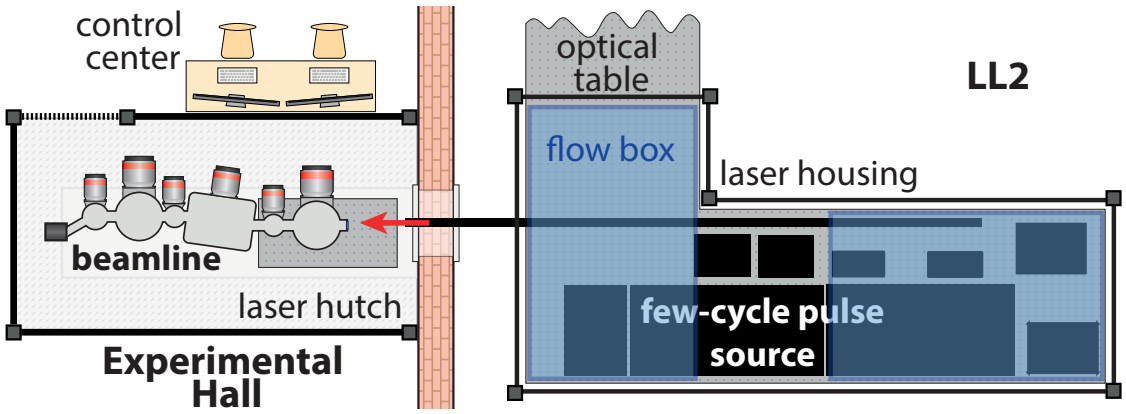

Figure 3.1.: Overview of the experimental setup at MPIK. The optical setup for few-cycle pulse generation is located in the *LL2* clean room and shielded by another large-scale laser housing. The few-cycle laser pulses are sent outside to the *Experimental Hall* where the vacuum beamline is situated. It is surrounded by an interlocked large-scale shielding (*laser hutch*). The beamline and data acquisition can be controlled and monitored from outside the hutch (*control center*).

the vacuum beamline is located outside this room in the *Experimental Hall* with less strictly controlled environmental conditions. Hence, the respective beamline operation is isolated from laser operation and no entrance to the laser laboratory is needed during a measurement campaign. In addition, the beamline can be more easily disconnected and transported to large-scale facilities like free-electron lasers for experiments which employ intense XUV pulses. One further measure to enhance the stability is to outsource big, vibration-producing pre-vacuum pumps to the basement below the laboratory. An overview of the large-scale setup is given in figure 3.1. Photographs of the *LL2* in different stages of its construction can be found in the appendix.

3.2. Tunable SWIR few-cycle laser source

Quantum dynamics in atoms and molecules takes place on the inherent timescale of the motion of nuclei and electrons and thus on the femto- to attosecond regime. Thus, the presented experiments rely on sources capable of producing such short flashes of light. Femtosecond laser technology is nowadays widely used in science and industry: In biology, multiphoton microscopy [110–112] relies on nonlinear absorption and thus ultrashort laser pulses in the infrared to be able to locate a fluorescent tracer in a certain depth of a comparably thick biological sample. On the other side of the application spectrum, femtosecond pulses are commonly used to micro-machine [113] detailed structures making use of the fact that material is not melted, but rather just

vaporized in a process called ablation [114].
For the application discussed in this thesis—the investigation and control of the quantum dynamical behavior of atoms and molecules in strong laser fields—we make use of the same underlying technology but with specific requirements:

- Peak intensities up to $10^{15}\,\mathrm{W/cm^2}$ even under loose focusing conditions are anticipated.
- The laser-pulse duration is short enough to resolve vibrational dynamics in molecules, which are typically on the order of $> 10\,\mathrm{fs}$. In the SWIR spectral region, this translates to a pulse duration of only a few optical cycles.
- The demanded peak-intensity in combination with the targeted pulse duration results in a pulse energy of around 1 mJ in the vacuum beamline.
- Finally, the repetition rate of the laser system is high enough to enable complex measurement campaigns with multi-parameter scans in a reasonable time. This is typically the case for kilohertz repetition rates.

There are two commercially available classes of solid-state active laser media that can meet these criteria. The titanium-doped sapphire (Ti^{3+}:Al_2O_3; Ti:Sa) technology [115, 116] is well established, commercially available from multiple manufacturers and the workhorse of most ultrafast laboratories these days. Ti:Sa lasers operate around a center wavelength of 800 nm and can typically deliver amplified pulses with 20-40 fs duration in commercial systems. They can provide multi-millijoule pulse energies and respective peak powers (GW to TW) at moderate average powers (few tens of watts) and thus repetition rates. The limitations of Ti:Sa technology are heat-related and restrict their multi-millijoule operation to repetition rates $\leq 10\,\mathrm{kHz}$ for cryogenically-cooled active media [117, 118]. In recent years, ytterbium-based gain media have shown new perspectives on increasing the repetition rate without sacrificing pulse energy. While ytterbium-doped crystals (e.g., Yb:YAG) as active laser media allow for a broader variety of geometries (thin discs, slabs, fibers) in comparison to bulk Ti:Sa crystals, the supported spectral gain bandwidth centered around 1030 nm restricts pulse durations to the 100 fs to 1 ps regime. The outstanding power scalability of the Yb-technology, though, leads to ultrafast laser systems in the kilowatt average-power regime [119–121]. Combining Yb-technology with optical parametric chirped-pulse amplification (OPCPA) has already led to commercial products that can deliver high-average power pulses that are shorter than the respective output of Ti:Sa systems

[122–124]. Furthermore, these OPCPA systems are not technically fixed to a specific wavelength and thus represent an important source for SWIR pulses. More technical details on the OPCPA technology can be found in [125].

To generate pulses with few-cycle duration, the spectrum of the laser output is broadened and subsequently its chirp is corrected in order to get as close as possible to the Fourier-transform duration limit (compare section 2.1.3 in the theory chapter). These so-called post-compression techniques are needed for both, Ti:Sa and Yb-based systems[2]. The different post-compression approaches utilize the nonlinear self-phase-modulation process (see section 2.1.4 in the theory chapter) in solids or gases. In solid-state substrates, laser-induced damages due to dielectric breakthrough limit the laser pulses' peak intensity. This, in return, restricts the amount of SPM and thus spectral broadening that is achievable. To circumvent this limitation, one can split a bulk solid-state medium into multiple thinner plates [128, 129]. Gaseous media have the advantage of more control parameters (e.g., pressure) and no permanent damage. Nonlinear refractive indices, however, are much smaller in gases compared to solid-state materials. One possible solution is to use special micro-structured, gas-filled nonlinear fibers, so-called photonic crystal fibers [130, 131]. These nonlinear fibers, however, are typically constrained to pulse energies in the microjoule regime. Another approach for gas-based SPM is to propagate the focused laser beam over a long distance to gain enough spectral broadening. Here, again, multiple solutions exist. One idea is based on achieving a long effective focal length by focusing the beam multiple times inside a gas-filled optical cavity, which is referred to as multi-pass cell [132, 133]. This represents a promising approach to compress highest average- and peak-power pulses [135] to the few-cycle regime in the future. Moreover, one can make use of ionization in the gas medium, leading to plasma defocusing which acts against the Kerr lensing and thus can lead to an elongated self-channeled focus. This process is called filamentation [136]. Filamentation-based approaches can be realized in a relatively simple manner [137]. A disadvantage, though, is the possible degeneration of the beam-mode quality due to multi-filamentation and the absorption caused by plasma generation. Besides channeling the focus via filamentation, one can alternatively couple the focused beam into a gas-filled, hollow waveguide. This technique, often realized in form of hollow-core fibers (HCFs) [134, 138–145], has many advantages. First, in principle, there is no length limitation. Secondly, as long

[2]Some OPCPA systems can deliver few-cycle pulses without separate post-compression [126, 127]. These systems, however, have lacked other characteristics like high pulse energy or average power up to now.

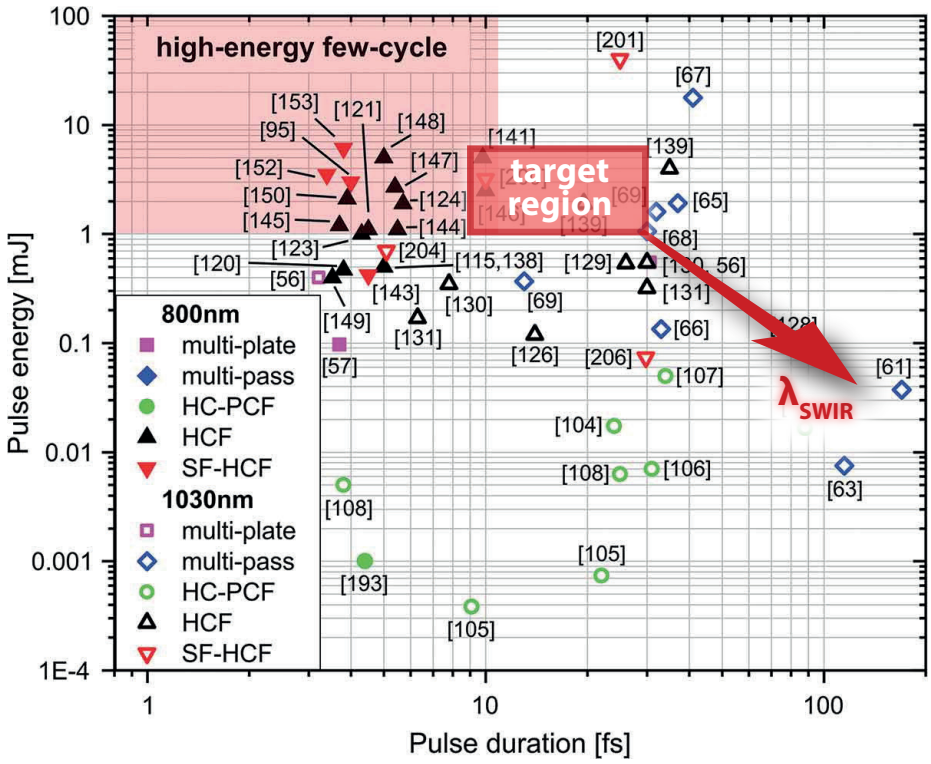

Figure 3.2.: Overview of high-energy few-cycle sources with center wavelengths around 800 nm and 1030 nm (the overview plot is reprinted from [134]). Here, the pulse energy over the pulse duration is shown. Furthermore, the targeted region concerning pulse-energy and pulse durations for a tunable few-cycle source at *MPIK* is indicated. The wavelength-tunability of the source is visualized by expanding the plot in the third dimension by an additional λ_{SWIR} axis.

as the focus diameter is fixed, the same setup can be applied to different wavelengths. This leads to HCFs being used with very high pulse energies up to tens of millijoules [142, 146, 147]. In addition, as the HCF acts as a stationary waveguide, the beam pointing after the HCF is fixed. Any pointing variation in front of the HCF translates into a power fluctuation after the HCF. As a disadvantage, the beam has to be carefully characterized (e.g., concerning focus diameter) to guarantee an efficient coupling into the HCF. Also, being a dielectric, multimode waveguide, even with perfect incoupling into the HCF losses occur: besides inevitable losses during the electromagnetic mode-coupling to the hollow waveguide, a length-dependent dampening is unavoidable. Reviews of the current state of post-compression techniques are given in [133, 134]. To decide for the best-suited laser-system and compression approach for the envisioned experimental investigations of molecules under the influence of strong fields, these target parameters have to be fulfilled: The laser source of choice should produce pulses with millijoule-level output and few-cycle character. A comparison of the targeted

parameters with the ones of existing systems is presented in figure 3.2. This enables peak intensities up to $10^{15}\,\mathrm{W/cm^2}$ even under loose focusing conditions which is a prerequisite for testing the behavior of small quantum systems in extreme conditions. In addition, the source should deliver output pulses with center wavelengths readily tunable in the SWIR spectral region between 1 µm and 2 µm. The SWIR regime enables photon energies of high-order harmonics reaching 200 eV and above (see section 2.1.5 in theory chapter). Moreover, experiments employing intense SWIR pulses can access the quasi-adiabatic regime, which is manifested by a Keldysh parameter $\gamma \ll 1$ (see section 2.4.4 in the theory chapter). Besides that, the field is quasi-static compared to fast transitions like Auger-Meitner decays due to the long optical-cycle period of SWIR pulses. This fact can facilitate the description of the experiments by theoretical models while avoiding complications arising from explicit time dependence. As the envisioned multi-parameter-scan experiments necessitate a large amount of measurement "shots", the repetition rate and the long-term stability of the laser-pulse source have to meet certain requirements: To keep measurement-campaign durations in an acceptable range, a repetition rate of at least 1 kHz is required. Furthermore, the system should be without significant laser-parameter drifts over multiple days enabling uninterrupted experiments for more than 100 hours.

3.2.1. Optical setup overview

To best meet these goals, a combination of the well-established Ti:Sa technology with parametric amplification for SWIR tunability and a subsequent HCF-based post-compression scheme is employed.
Figure 3.3 presents an overview of the optical setup. First a Ti:Sa front end produces high-energy pulses (up to 23 mJ) at a center wavelength of $\lambda_c^{Ti:Sa} = 800\,\mathrm{nm}$ with a duration of 27 fs FWHM at a repetition rate of 1 kHz. The laser front end is equipped with a thorough in-situ characterization (pointing, average power, pulse energy, spectrum) to monitor the condition of the system and potential drifts in its parameters. Due to the long beam path in the amplification chain of the Ti:Sa system, small variations in the beam direction translate to measurable pointing drifts at the output. These pointing-drifts are corrected by a 4D[3] beam stabilization system (*TEM Aligna 60 MoPiA* [148]). A Ti:Sa output pulse energy of 20 mJ is used to pump a three-stage optical parametric amplifier (OPA). Here, the 800 nm pump pulses are shifted

[3]Beam position (x and y) and direction (φ_x and φ_y) are measured and corrected.

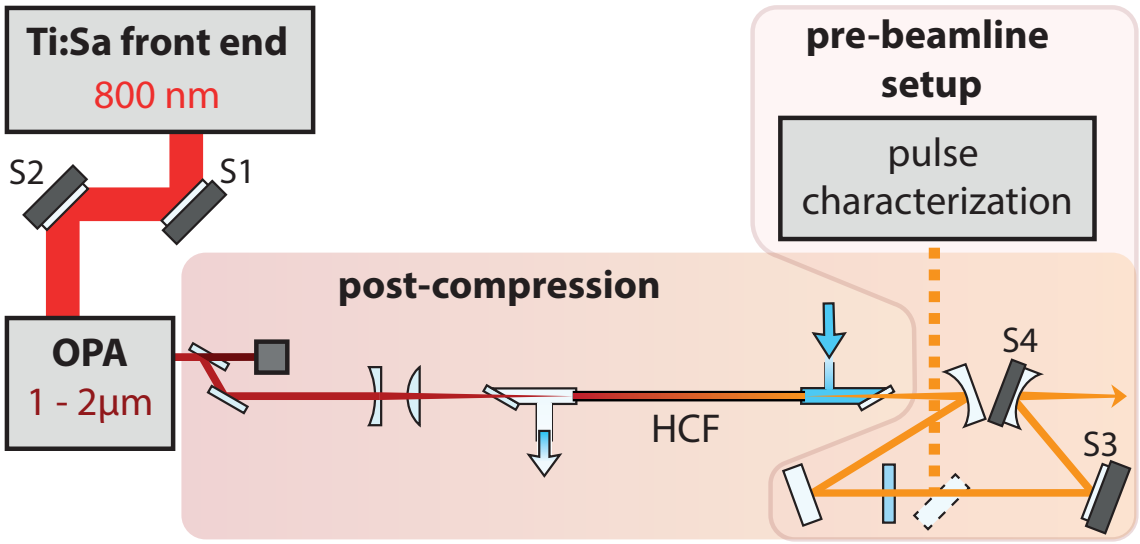

Figure 3.3.: Schematic overview of the optical setup for high-energy, wavelength-tunable few-cycle pulse generation in the SWIR spectral region. The optical setup consists of the *Ti:Sa front end*, which pumps an *OPA*. The OPA output in the SWIR spectral region is spectrally broadened in an HCF and subsequently temporally compressed in the *post-compression* optical setup. A thorough *pulse characterization* is conducted in the *pre-beamline setup* part. Afterwards, the compressed SWIR few-cycle pulse is focused into the vacuum beamline. Two beam-pointing stabilization systems are employed in the setup: between front end and OPA (mirrors *S1* and *S2*) and in front of the beamline (mirrors *S3* and *S4*). Further details on the setup are given in sections 3.2.2 to 3.2.5.

towards the SWIR spectral region by employing nonlinear optics. The OPA output is coupled into a gas-filled, stretched-flexible hollow-core fiber (SF-HCF) for spectral broadening. Finally, the SF-HCF output is temporally compressed, characterized and further prepared for the required experimental conditions in a pre-beamline optical setup and focused into the vacuum beamline.

3.2.2. Laser front end

In the following, the Ti:Sa laser system that acts as front end for the overall optical setup is described. The *Coherent Legend Elite Cryo CEPS*[4] system was specifically acquired for the new *LL2* and has the specialty of combining a high pulse energy with a short pulse duration at a 1 kHz repetition rate. The Ti:Sa system is schematically depicted in figure 3.4. In short, the initial pulses are generated in a femtosecond oscillator before they are temporally stretched and further amplified in a three-stage amplification chain and finally re-compressed via a grating-based compressor.

[4]The sales of this system were discontinued. Hence, no public official information on the overall system is available/can be referenced.

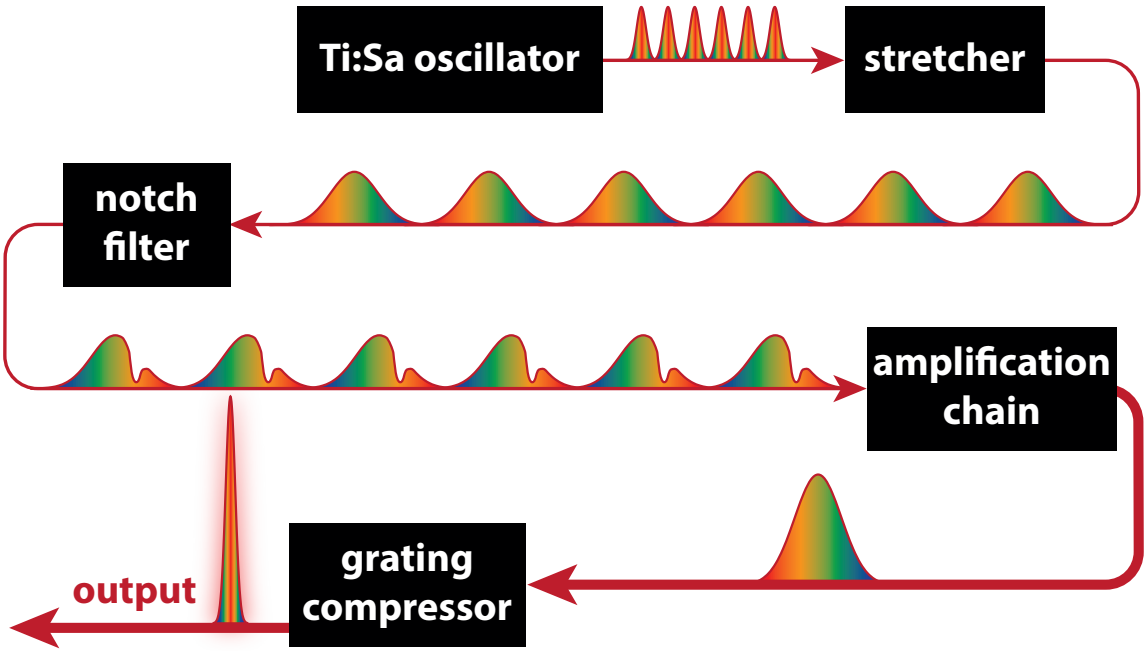

Figure 3.4.: Schematic overview of the Ti:Sa front end. The femtosecond pulses from an oscillator are stretched approximately by a factor of 10^4. A spectral notch filter (for illustrative purposes shown here after the stretcher) modifies the spectrum to compensate the red-shift in the subsequent amplification. In the amplification chain, one out of every 80 000 pulses is amplified and subsequently compressed in time by a grating compressor.

3.2.2.1. Femtosecond oscillator

The femtosecond pulses originate from a Kerr-lens mode-locked femtosecond oscillator. Here, a green laser in continuous-wave (cw) operation optically pumps a Ti:Sa crystal which is placed inside a resonator. The cavity- and pump-beam geometry is designed such that intense pulses can propagate in the cavity with reduced losses mediated by Kerr lensing in the Ti:Sa crystal. Thus, the Kerr lensing serves as an artificial saturable absorber and results in broadband, femtosecond pulses. The broadband lasing properties of Ti:Sa, the Kerr-lens mode-locking scheme and the dispersion-corrected cavity lead to very short (~ 15 fs) pulses at MHz repetition rates.
In the Ti:Sa front end of the described optical system, a *Coherent Vitara-T* [149] oscillator is used which is hermetically sealed and optimized for short pulses and high stability. It is pumped by a *Coherent Verdi-G* [150] cw laser at 532 nm. The oscillator outputs an average power of 560 mW at 80 Mhz repetition rate which results in a pulse energy of 7 nJ at a center wavelength of 800 nm. Thus, the required pulse energies are six orders of magnitude too low which makes a subsequent high optical amplification of the laser pulses necessary.

3.2.2.2. Amplification chain

A direct amplification of the oscillator's pulses in subsequent optically-pumped Ti:Sa crystals is limited by the Ti:Sa crystal damage threshold. The electric-field strengths of the near-Fourier-limited pulses would lead to a dielectric breakdown and thus permanent damage inside the gain material. An approach to overcome this limitation was demonstrated by Strickland and Moureau in 1985 [151] and Nobel-prize awarded in 2018 [152, 153]: the chirped pulse amplification (CPA). In CPA, the pulses originating from the oscillator are first temporally stretched by modifying the spectral phase which results in chirped pulses. Hence, the peak intensity of the pulses is reduced accordingly. Afterwards, the pulse energies are amplified by multiple orders of magnitude in an amplification chain. Finally, the amplified pulses are temporally compressed again to achieve high-energy, Fourier-limited pulses. The CPA technique is employed in the Ti:Sa front end as illustrated in the overview figure 3.4.
In the *LL2* laser system, the spectrum of the oscillator pulses is altered by a spectral notch-filter to counter-act the spectral red shift[5] in the amplification chain. Afterwards, the initially 15 fs pulses from the oscillator are chirped to approximately 200 ps in a grating-based stretcher. Now, the pulses are amplified in the first amplification stage which is a regenerative amplifier [154, 155] as shown in figure 3.5. A regenerative amplifier has the advantage of an electronical adjustablity of the amount of passes through the gain medium. The optical switching is conducted with Pockels cells in combination with wave plates and polarizers. Here, one pulse of every 80 000 oscillator pulses is injected in the regenerative amplifier cavity, conducts eleven round trips until the population inversion in the gain medium is depleted and finally is ejected with another Pockels cell. The regenerative amplification stage is pumped with 24 W optical power from a nanosecond-pulsed laser at 527 nm (*Coherent Revolution 65* [156]). Furthermore, the Ti:Sa crystal is located inside a dry-air-purged housing and cooled to -10 °C via thermoelectric cooling. After the regenerative amplifier, the energy of the stretched pulses is E_{Regen} = 6.2 mJ.
The second amplification stage is a single-pass amplifier pumped by 43.9 W from a *Coherent Revolution 80* pump laser. Equivalently to the regenerative amplification stage, this single-pass amplifier crystal is thermoelectrically cooled. The pulse energy achieved after the second stage is E_{SPA} = 14.4 mJ.

[5] As the pulses are positively chirped in the CPA process here, the longer-wavelength spectral components experience a higher degree of population inversion in the gain medium and are thus more amplified than the shorter-wavelength spectral components in the amplification chain.

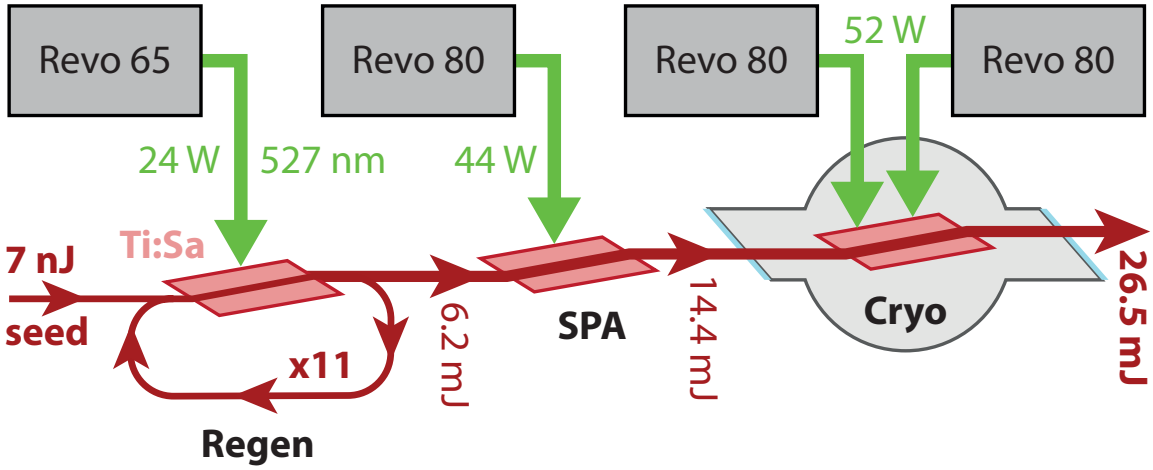

Figure 3.5.: Schematic view of the Ti:Sa front-end amplification chain. There are three amplification stages: The thermoelectrically-cooled regenerative amplifier (*Regen*) with eleven cavity roundtrips, the thermoelectrically-cooled single-pass amplifier (*SPA*) and the cryogenically-cooled single-pass amplifier (*Cryo*). The three stages are pumped by overall four nanosecond-pulsed pump lasers (*Revo 65/80*).

For further amplification, a conventional cooling scheme like the one used in the first two stages cannot counteract the thermal load in the Ti:Sa amplifier crystal that is induced by the required optical pumping powers. Thus, the Ti:Sa gain medium is located inside an ultrahigh-vacuum (10^{-9} mbar) chamber and cooled to cryogenic temperatures around 100 K by a cryo-cooler [157]. Two counter-propagating *Coherent Revolution 80* laser beams pump the final amplification stage with overall 52 W of green light. This stage nearly doubles the energy of the uncompressed pulses to E_{Cryo} = 26.5 mJ. After amplification, the output beam can be variably split into two different beams using a half-wave plate in combination with a polarizer. One beam with a maximum pulse energy (low-energy beam; *LE*) of 10 mJ is compressed in a grating compressor within the laser system housing. The other beam's diameter is extended and its temporal length shortened in a larger, external grating compressor. Hence, this beam can comprise the full amplified pulse energy of 26.5 mJ and is accordingly called the high-energy (*HE*) output. With the 87 % overall transmission of the reflective-grating compressor, a maximum compressed pulse energy of 23 mJ is achieved with this laser system. Throughout this work, the *HE* beam is adjusted to the optimal pulse energy for driving the subsequent OPA (20 mJ) whereas the *LE* beam is blocked.

An extensive characterization of the Ti:Sa front end is conducted: The different spectra along the amplification chain are presented in figure B.8 in the appendix. Furthermore,

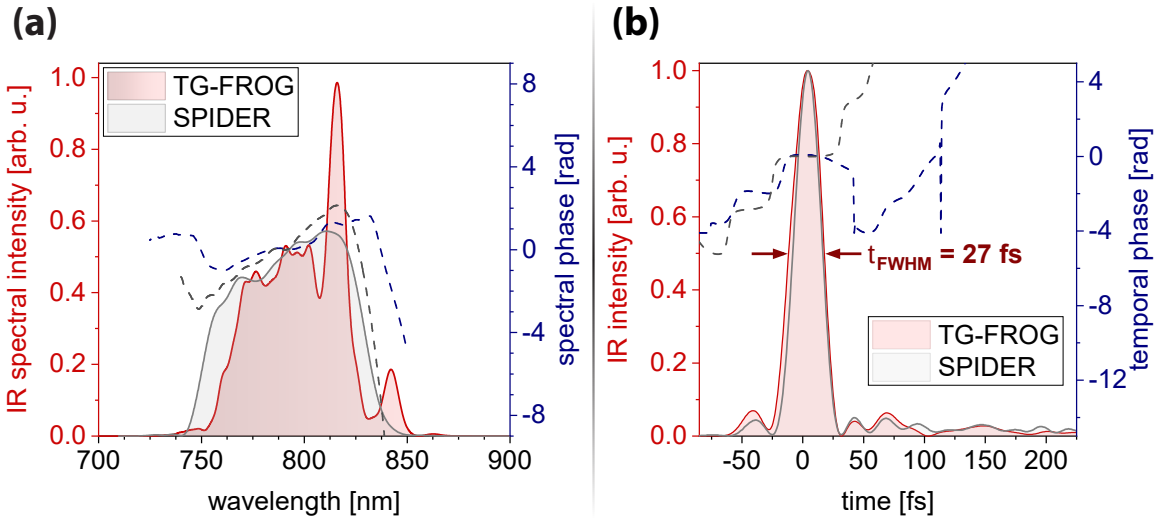

Figure 3.6.: Measurement of the temporal intensity structure of the Ti:Sa *HE* output pulses using a home-built FROG apparatus (details see section 3.2.5.2) and a commercial SPIDER device. **(a)** Spectral intensities (SPIDER in grey) and phases. **(a)** Intensities (SPIDER in grey) and phases in the time domain.

the temporal intensity structure of the *HE* pulses is measured by means of nonlinear optics. Figure 3.6 shows two independent measurements employing a home-built FROG setup (more details concerning this setup and the underlying physical principle are given in section 3.2.5.2) and a commercial SPIDER [158] apparatus. A FWHM duration of $\tau_{FWHM}^{HE} = 27\,\text{fs}$ is determined. The beam quality factor (see equation (2.4) in section 2.1.2.1) is determined to $M^2 < 1.2$. Furthermore, a shot-to-shot pulse-energy fluctuation of $\sigma/\varnothing = 0.2\%$ over 100k shots is measured[6]. Long-term-stability power data are presented and discussed in chapter 3.2.5.5. Besides these measurements, an *in-situ* characterization is available to monitor the laser parameters' stability during a measurement campaign. Here, the *HE*-beam pointing, the average power, the shot-to-shot fluctuations and the spectrum can be monitored and logged. Figure B.9 in the appendix presents the respective optical logging setup located between the *HE* output and the external grating compressor.

3.2.3. Optical parametric amplifier

The part of the setup that enables wavelength-tunability in the SWIR is an optical parametric amplifier. In general, the parametric amplification process is a second-order

[6]Due to pulse-energy sensor-head restrictions, this measurement is conducted at the *LE* output. Since the *LE* and the *HE* beams are separated after the last amplification stage, however, the measured shot-to-shot stability is expected to be the same at both outputs.

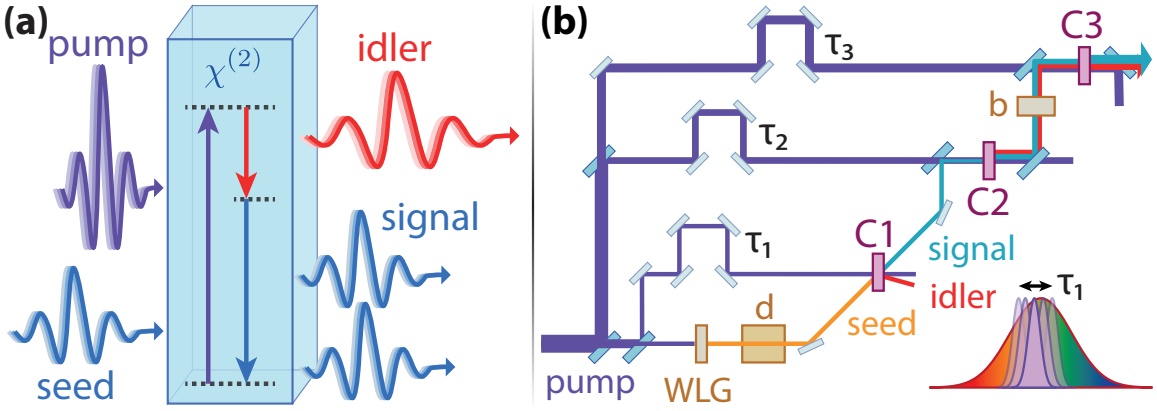

Figure 3.7.: Optical parametric amplification. **(a)** General scheme of optical parametric amplification. A pump photon (violet) is split into two photons in a $\chi^{(2)}$ nonlinear process. Under the influence of a seed photon (blue; photon energy more than half of the pump photon), a signal photon and a lower-energy idler photon (red) are generated. **(b)** Schematic view of the three-stage OPA used in the *LL2*. A small part of the pump beam is used to generate white light in a sapphire plate (*WLG*). The broadband pulses are temporally chirped by propagation through a dispersive substrate (*d*). The chirped pulses act as seed for the first OPA stage (*C1*). Hence, the respective seed spectrum can be adjusted via the time delay τ_1 (see inset lower right). Here, the first stage has a slightly noncollinear geometry. Afterwards, the signal beam is overlapped with another portion of the pump beam in the second stage (*C2*). The resulting signal and idler pulses are time-delayed by a birefringent substrate (*b*) and via the setting of τ_3 either beam can be used as seed for the final amplification stage (*C3*).

$\chi^{(2)}$ nonlinear effect (compare section 2.1.4 in the theory chapter). In a parametric scheme, a pump photon (in our case of an energy of $E_{Ti:Sa}$ = 1.55 eV) is converted into two lower-energy photons. The resulting higher-energy photon is called *signal* photon, whereas the lower-energy one is the *idler* photon. Together, the *signal* and *idler* photons obey the energy conservation, $E_{signal} + E_{idler} = E_{pump}$. One of the parametric output photons has the same energy as the seed photon which is sent into the nonlinear crystal simultaneously with a pump photon. Due to phase-matching conditions, the signal and idler photon typically have orthogonal polarizations. Figure 3.7(a) illustrates this parametric amplification process. Notably, parametric amplification is conceptually different to a lasing process: During the optical parametric amplification, no excited state is populated or energy deposited in the gain medium. Rather, the nonlinear crystal is just mediating the parametric process. Thus, the heat load in the nonlinear crystals is dramatically reduced compared to a laser gain medium pumped by an equivalent amount of energy. This makes OPAs very suitable for both, high-energy and high-average-power applications.

Here, a commercial OPA consisting of three amplification stages (*Light Conversion TOPAS HE Prime+* [159]) is located behind the Ti:Sa front end. A beam stabilization

between the external *HE* compressor and the OPA guarantees the reproducible incoupling into the OPA. Figure 3.7(b) gives a schematic view of the OPA beampath. First, a small portion of the Ti:Sa *HE* beam is used to generate an optical more-than-octave-spanning spectrum, a supercontinuum, inside a sapphire plate. This weak pulse with an ultrabroad spectral bandwidth also comprises the SWIR regime. Now, the supercontinuum is heavily chirped by propagation through a dispersive substrate and much longer in duration than the Ti:Sa pump pulse. By introducing a suitable time delay between another part of the Ti:Sa pump beam and the spectral region of interest of the supercontinuum, one can effectively choose which spectral components of the supercontinuum act as seed pulse for the first OPA stage. Here, beta barium borate (BBO) crystals [160] are used as nonlinear media for the parametric process [161] as they exhibit suitable phase-matching conditions for 800 nm-driven OPAs. The first OPA stage is realized in a slightly noncollinear manner. Thus, the pump, signal and the idler beams are spatially separated and only the signal beam can be used as seed for the next amplification stage. After the second, collinear amplification stage, the signal and the idler beam are temporally separated from each other in a birefringent crystal as signal and idler have orthogonal polarizations. This enables the choice of either one, signal or idler, as seed for the last amplification stage by adjusting the final pump-seed time delay. While in theory it should not make any difference which of the beams is chosen as seed, the choice of signal/idler seed does have an influence on shot-to-shot stability, divergence and beam mode in practice. One reason is the use of transmitted, dispersive refractive optical elements like lenses in the OPA. Thus, the idler is chosen as seed of the last stage for overall idler output and the signal seed for a respective signal output. The last, so-called *power amplification stage* consists of a large-aperture BBO which is pumped collinearly by more than 90% of the overall Ti:Sa input pulse energy. After the power amplification stage, the pump beam is spatially separated from the signal and idler beams by a dichroic mirror. Furthermore, the signal beam is separated from the idler by using an additional pair of dichroic beamsplitters (DBSs) at Brewster's angle. Here, two different pairs of DBSs are used: Due to the dispersive properties of the 5 mm-thick beamsplitter substrates, only the reflected beam is used for experiments. Overall, a DBS specifically for using the signal beam in experiments exists and another one for idler use[7].

[7] The specifications of the signal reflecting DBS are high-reflective for s-polarization (HRs) 1120 nm - 1600 nm, while the idler-reflecting one is specified with HRs 1600 nm - 2100 nm. Due to the orthogonal polarizations of signal and idler, the idler DBS has to be mounted orthogonally rotated to the signal DBS orientation.

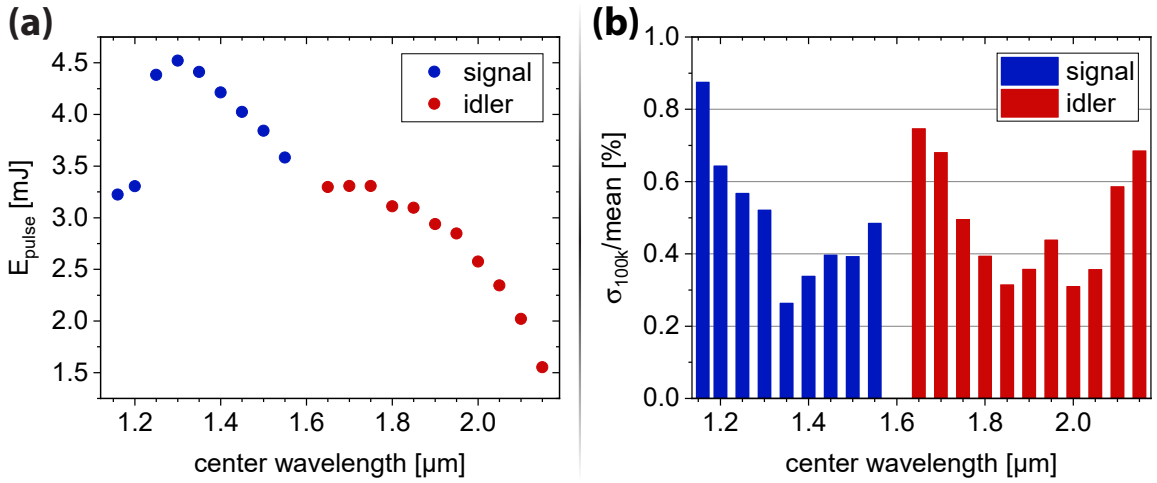

Figure 3.8.: OPA signal/idler output powers and fluctuations. **(a)** OPA output power over center wavelength (*tuning curve*). **(b)** Relative shot-to-shot stability (in $\sigma/\varnothing$) over 100 k shots.

With this setup, an overall pump to combined signal/idler optical efficiency of up to 37 % is achieved. The tuning curve, which is the resulting signal/idler pulse energy over the respective OPA wavelength, is shown in figure 3.8 in combination with the corresponding shot-to-shot fluctuations over 100 k shots. Figure 3.8 shows that multi-millijoule pulses over a tuning region from 1.1 µm to 2.2 µm are generated with a relative shot-to-shot fluctuations of less than 1%. The respective OPA spectra are presented in figure 3.9.

3.2.4. Stretched flexible hollow-core fiber

While the pulse durations directly at the OPA output are already relatively short with around six optical cycles [163], a further reduction of the pulse duration to the few-cycle regime is targeted. Hence, the spectral bandwidth of the pulses has to increase. Furthermore, the spectral phase needs to be flattened in order to generate unchirped pulses with highest intensities for the experiments.

3.2.4.1. Hollow dielectric waveguides

In this section, the first part of the compression scheme—the spectral broadening inside a HCF—is discussed. First, the optical basics for an efficient HCF-based compression scheme are given. Here, the OPA output can be assumed as a Gaussian beam which is coupled into the hollow dielectric waveguide. The free-space Gaussian TEM_{00} beam mode couples to different modes of the waveguide [164]. By adjusting

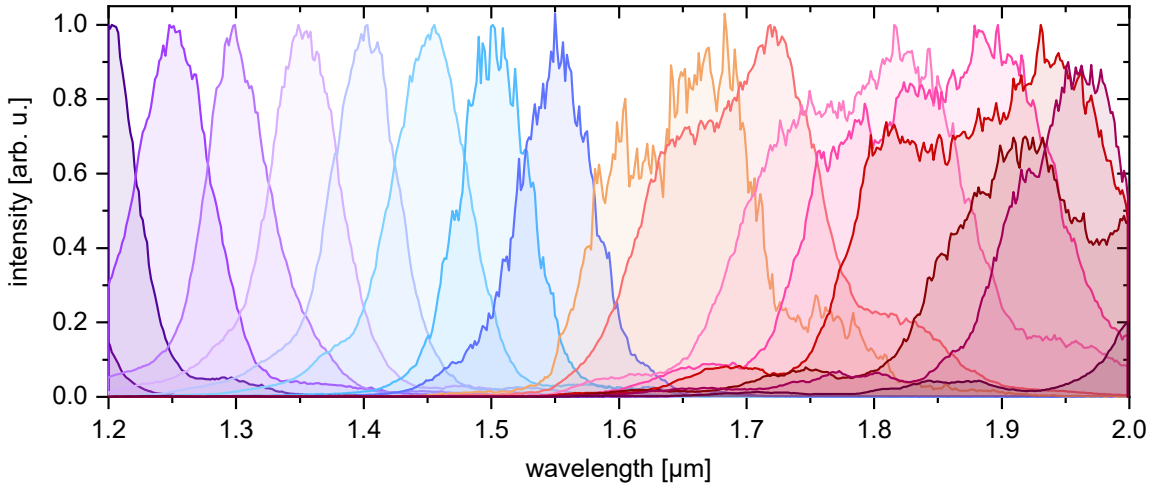

Figure 3.9.: Output spectra of the OPA measured with the InGaAs spectrometer (*Ocean Optics NIRQuest 512* [162]; whole measurement range is depicted). The wavelength of the pulses was tuned from 1160 nm to 2150 nm. Here, the signal (purple - blue) and the idler (yellow - red) range are color coded.

the Gaussian beam waist size w_{focus} at the capillary entrance to $w_{focus}/r_{core}^{HCF} \approx 64\%$ [165, 166] of the hollow-core radius r_{core}^{HCF}, a maximum coupling of about 98 % of the free-spaced TEM_{00} mode to the EH_{11} mode in the waveguide is achieved. The hybrid EH_{11} mode has the lowest propagation loss of all the modes in the waveguide. This propagation loss α consists of two parts, the inevitable attenuation of the beam mode inside the waveguide α_0 and an additional loss α_R due to a potential curvature of a long waveguide: $\alpha = \alpha_0 + \alpha_R$. The propagation losses of the EH_{11} mode in a fused silica hollow waveguide solely depend on the incoupled wavelength λ and the core radius r_{core}^{HCF} of the waveguide:

$$\alpha_0 = B \frac{\lambda^2}{\left(r_{core}^{HCF}\right)^3}, \tag{3.1}$$

with the prefactor $B = 1.85\,{}^{db}/_{m}$ [164]. The attenuation due to waveguide bending with radius R obeys the proportionality [164]

$$\alpha_R \propto \frac{1}{R^2} \frac{\left(r_{core}^{HCF}\right)^3}{\lambda^2}. \tag{3.2}$$

Thus, a challenge for long hollow waveguides is to make sure that the waveguide is perfectly straight in order to avoid substantial losses in its overall transmittance. Besides the general transmission of a hollow waveguide, the question concerning the

ideal core-diameter for an effective spectral broadening remains. While a small core diameter helps with the amount of spectral broadening via SPM, too high intensities can lead to a catastrophic Kerr lensing and even multi-filamentation inside the gas-filled core. Also, extreme intensities can lead to a substantial amount of ionization and thus a reduced transmission. Furthermore, according to equation (3.1), a smaller core diameter leads to a lower transmission if the waveguide length is kept the same. Taking ionization rates into account, Vozzi *et al.* [167] come to the conclusion that the core radius should not be smaller than

$$r_{core,min}^{HCF} = A\,\tau_{pulse}^{-0.45}\,E_{pulse}^{0.51}\,, \tag{3.3}$$

with the gas-dependent prefactor A, the input pulse duration τ_{pulse} and pulse energy E_{pulse}. This shows that especially for high pulse energies, larger core diameters have to be used, which in turn leads to longer waveguides for substantial spectral broadening [133, 134].

3.2.4.2. SF-HCF implementation

To implement a suitable HCF for the wavelength-tunable SWIR source, the first step is to determine the HCF core diameter with equation (3.3) for the respective experimental conditions. As the HCF setup should be applicable to the whole 1.1 µm to 2.2 µm center-wavelength tuning range, average pulse parameters of $E_{pulse} = 3\,\mathrm{mJ}$ and $\tau_{pulse} = 40\,\mathrm{fs}$ [163] are assumed as input. Furthermore, argon (Ar) will be used as the nonlinear medium inside the HCF for this evaluation. The respective prefactor for Ar in equation (3.3) is $A_{Ar} = 4.7 \times 10^{-9} m\,s^{0.45}\,J^{0.51}$ [167]. Thus, the minimal HCF core radius is calculated to be $r_{core,min}^{HCF} = 518\,\mu\mathrm{m}$. With this rather large core diameter, the required HCF length is expected to be multiple meters. Therefore, the HCF curvature-associated attenuation α_R becomes eminent.
Historically, glass rods with a center bore have been used as hollow-core waveguides and structurally supported by an aluminium or steel guide [138]. Above an HCF length of 1 m, it becomes ever more challenging to maintain the straightness of the HCF with this approach. While complicated mechanical support structures [168] can minimize the curvature introduced by gravitational deformation under the mass of the HCF/the support structure itself, the scalability of these approaches is limited.
An alternative to solid rods are flexible, thin-walled glass capillaries. Such capillaries are often used in microfluidics and chromatography [169, 170]. They are readily

available in different diameters, large quantities, high qualities and are relatively cheap (~ 10 € per meter). Nagy *et al.* showed that by stretching a flexible glass capillary on both ends, a very straight ($R \sim$ km) waveguide can be realized [171]. As the radius of curvature is proportional to $^{F}/_{M}$, the stretching force F over the weight of the capillary per unit length M, the required force for a certain straightness of the stretched flexible hollow-core fiber (SF-HCF) is independent of its length. Due to the low weight of the thin-walled capillaries, a stretching force F on the order of 10 N is enough to achieve near-perfect straightness for arbitrary waveguide lengths. This technique enabled spectral broadening of multi-millijoule pulses with waveguides up to 6 m in length [144, 146, 172]. In combination with water cooling, the SF-HCF approach is also scalable to high average powers of hundreds of watts [172].
With the calculated minimal $r_{core,min}^{HCF} = 518\,\mu m$ for the case of the *LL2* laser system, a commercial flexible glass capillary with 530 µm inner and 700 µm outer diameter was used (*Polymicro TSP530700* [173]). The optical table as well as the laser system placement during installation ensured a maximum HCF length for the given laboratory dimensions. This resulted in an overall 7.2 m-long HCF assembly including a 3.2 m-long SF-HCF and long vacuum tubes on either end to ensure that the beam is large enough to avoid parasitic nonlinear processes in the 2 mm-thick input and output windows. As a first step, the fiber was glued, cleaved and stretched at a test space. To extend the lifetime of the SF-HCF, the capillary walls of the input-facet are protected with a 550 µm ceramic aperture (*Lenox Laser HP-3/8-DISC-CER-550* [174]). At the test space, the SF-HCF was visually inspected and its transmission characterized using a $\lambda = 785\,nm$ continuous-wave diode laser. In this case, equation (3.1) results in an attenuation of $\alpha(785\,nm) = 61.3 \times 10^{-3}\,{}^{dB}/_{m}$. For the overall 3.2 m-long SF-HCF, this leads to a theoretical transmission (including the incoupling losses) of 93.8 %. Experimentally, a transmission of 89% was achieved, meaning that this HCF comes within 5% of the theoretical maximum transmission. In order to use the SF-HCF efficiently for pulse compression of tunable-wavelength SWIR pulses, a good incoupling into the waveguide over the whole tuning range has to be ensured. While an all-reflective and thus achromatic focusing setup in front of the HCF would theoretically be the optimal solution, in practice, using refractive optics proved to provide the best results and flexibility. The reason is manifested in the OPA itself: As the pulses propagate through lenses and other dispersive materials, the resulting divergence of the OPA output changes for different wavelengths. In fact, the whole OPA output beam mode looks different as shown later in figure 3.11. Figure 3.10 provides an

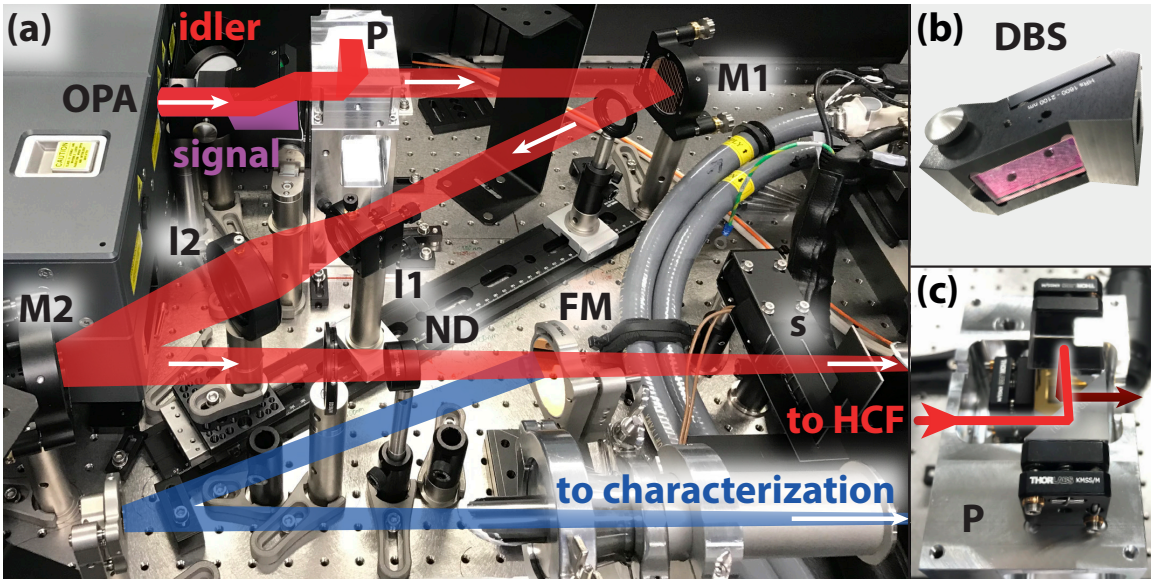

Figure 3.10.: Optical setup between OPA and SF-HCF. **(a)** The OPA output beams (*signal* and *idler*) are separated. In the shown example, the signal beam is blocked and the idler beam is propagating to the SF-HCF. A three-mirror polarization rotating periscope assembly (*P*) is only needed for the idler beam and couples the idler into the beampath that is set up for the signal beam. The flat, gold-coated mirrors *M1* and *M2* redirect the beam. The movable telescope lenses *l1* and *l2* are adjusted for the appropriate HCF-incoupling focus size. To measure the focus size, the beam can be sent to a beam profiler via the flip mirror *FM* after transmitting neutral density filters (*ND*). A shutter *s* is connected to the laser interlock system. **(b)** A photograph of the dichroic beamsplitter (*DBS*) pair used for the idler beam. **(c)** Detailed view on the beampath in the three-mirror periscope.

overview of the optical setup between OPA and SF-HCF.

The SWIR spectral region puts further challenges on a spatial characterization of the beam mode: Due to its bandgap, the sensitivity of silicon-based CCD chips cuts off at 1100 nm [175]. While there are cameras with chips made of indium gallium arsenide (InGaAs), they typically do not provide the performance of Si-based chips. In addition, InGaAs cameras are more difficult to handle due to the required cooling and are cost intensive ($>10\,$k€). The SWIR pulses in the *LL2*, however, are very intense and can induce a nonlinear two-photon absorption (TPA) signal in conventional Si-based image sensors [176–178]. This has the further benefit of providing a spatio-temporal characterization which is crucial here as the pulses are used for (highly) nonlinear optical processes in the SF-HCF and later in the experiment. Thus, only the portions of the pulse that are well focusable and temporally compressible at the same time are of interest. Using a lens instead of a mirror telescope has furthermore the advantage of the ability to compensate for existing astigmatism. In the SWIR case, chromatic aberrations of the involved lenses can be minimized by using appropriate lens

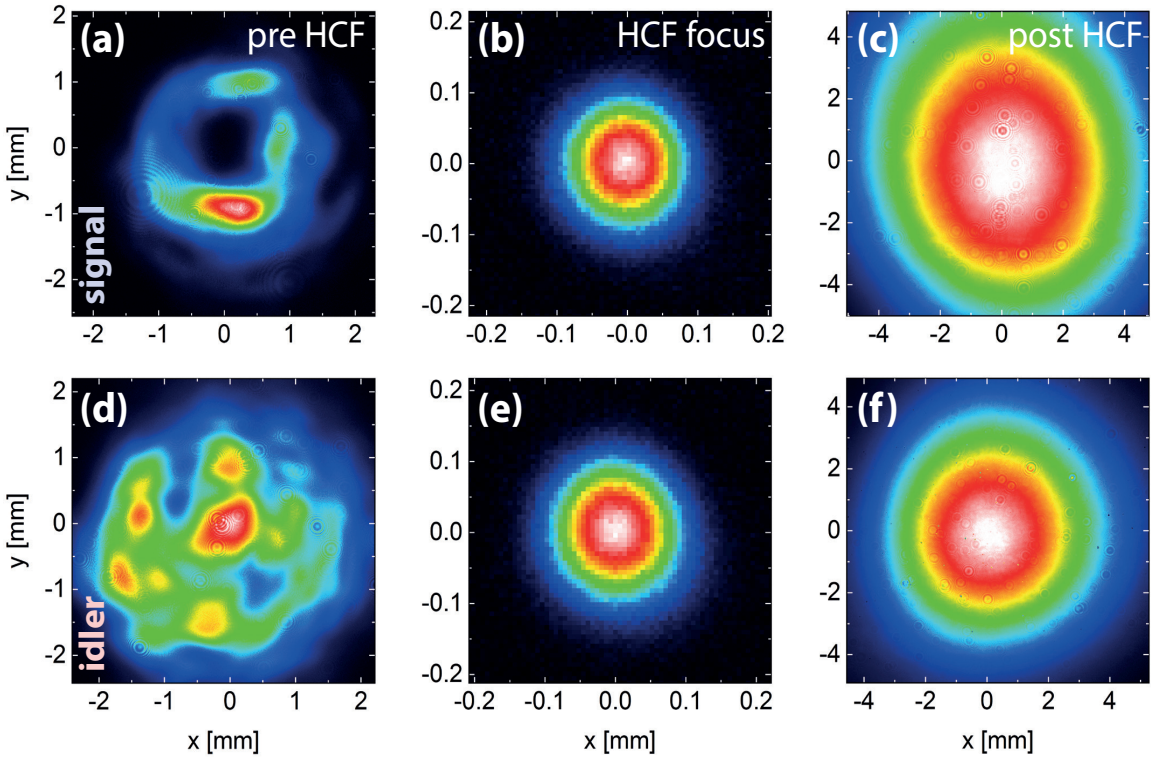

Figure 3.11.: Two-photon-absorption beam modes of representative signal and idler beams before and after the SF-HCF as well as in the focus. **(a)** Far-field TPA beam mode of a signal wavelength of λ = 1400 nm before the SF-HCF, **(b)** in the focus and **(c)** after the SF-HCF. **(d)** Far-field TPA beam mode of an idler wavelength of λ = 1900 nm before the SF-HCF, in the focus and after the SF-HCF. Similar to a focus-size reduction of the fluorescence signal in multi-photon microscopy [112], the real diameter of the Gaussian SWIR beam mode is factor of $\sqrt{2}$ larger than the measured TPA one.

materials that have low second-order dispersion (GVD) at the respective wavelength. The minimal impact of chromatic aberration of the lens telescope on the incoupling was ensured by comparing the transmitted spectrum with the input spectrum as shown in figure B.10 in the appendix. With these characterization capabilities, the most suitable lens materials and focal lengths in combination with optimized lens positions within the telescope are determined to ensure the best possible SF-HCF performance over the whole available wavelength range (see table B.1 in the appendix). The thorough characterization of the HCF setup includes measuring beam modes, spectra, powers and shot-to-shot fluctuations before and after the evacuated SF-HCF. Two examples (signal/idler) of the TPA beam modes in the far field in front of the HCF, in the focus and in the far field after the HCF are shown in figure 3.11. These examples show that the SF-HCF acts as a spatial Fourier filter and efficiently cleans the SWIR beam mode. By adjusting the focus diameter on the beam profile measured via TPA,

only the parts of the beam that can contribute to the highly nonlinear processes like HHG are propagated through the SF-HCF. Furthermore, the SF-HCF acts as a beam transport that provides a fixed source point for the optical assembly in front of the beamline (see section 3.2.5.4). Due to the spatial filtering, the SWIR transmission of the SF-HCF remained around 45-50 % (see appendix figure B.11(a)), while the shot-to-shot fluctuations only showed a small increase (see appendix figure B.11(b)). As a next step, the SF-HCF is filled with noble gas to spectrally broaden the SWIR pulses. Here, a pressure gradient along the SF-HCF is applied [179]: In order to avoid Kerr lensing and plasma generation in the gas volume in front of the SF-HCF that would lead to a lower incoupling efficiency, a vacuum is preserved at the beam input side of the HCF, whereas the gas is supplied at the beam output side. This differential-pumping scheme results in a pressure gradient along the HCF. While this technique leads to a smaller overall amount of SPM inside the waveguide and thus a necessity for longer HCFs [180], it is a key approach to enable the broadening of multi-millijoule pulse energies with hollow waveguides [181] and provides the option to freely tune the gas pressure without any need for incoupling adjustments. Two different noble gasses as nonlinear media are chosen: argon (Ar) and neon (Ne). While Ne shows a higher ionization potential than Ar, it has a lower nonlinear refractive index [182]. Depending on input wavelength and pulse energy, the noble gas itself (Ar or Ne) and the respective pressure is adjusted in order to generate a close-to-supercontinuum spectral broadening at moderate (< 2 bar) pressures and low losses due to ionization and only a slight increase of shot-to-shot fluctuations. A summary of the gas parameters for the different wavelengths can be found in table B.2 in the appendix. Figure 3.12 presents the resulting broadened spectra which support pulse durations of a few optical cycles. The residual chirp of these pulses, however, still has to be analyzed and compensated in order to temporally compress them.

3.2.5. Few-cycle pulse compression

A characterization of the spectral phase of the few-cycle pulses and thus of their intensity structure in the time domain is not straightforward: While the available electronics today are orders of magnitude too slow to measure femtosecond pulses in the time domain, manipulating distances on the respective lengthscale (1 fs $\hat{=}$ 300 nm) is easily possible.

The overall goal is to have one device at hand that can temporally characterize different wavelengths from the VIS to the SWIR as well as pulse durations—from

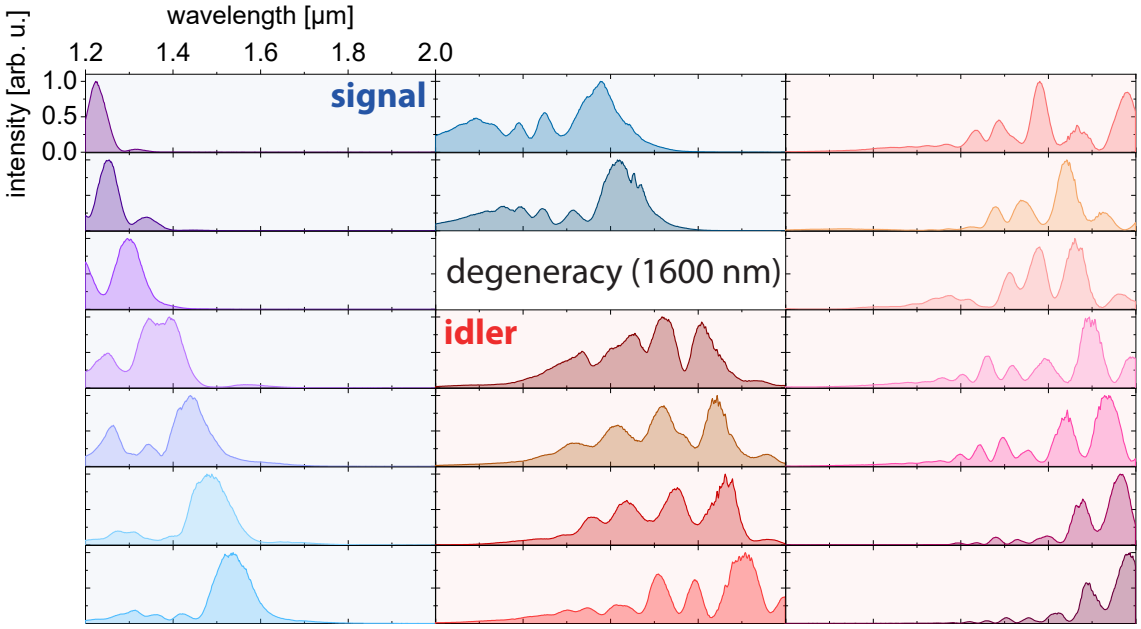

Figure 3.12.: Broadened spectra after the gas-filled SF-HCF for input-pulse center wavelengths from 1160 nm to 2150 nm (compare figure 3.9). Pulses originating from the OPA signal output have a light blue background, while the idler pulses share a light red background. The OPA degeneracy at 1600 nm is indicated as well. Due to the limited spectral range of the InGaAs SWIR spectrometer (1200 nm to 2000 nm), the spectral tails are partly cut.

uncompressed Ti:Sa pulses with picosecond duration to few-cycle pulses of few-femtosecond duration—that are available in the *LL2*. While there are many different nonlinear pulse characterization techniques [183, 184] available today (e.g., SPIDER [185], 2DSI [186], MIIPS [187], dispersion scan [188] and time-domain ptychography [189]), the required flexibility favors one technique especially: frequency-resolved optical gating (FROG) [190, 191].

3.2.5.1. Theory of frequency-resolved optical gating

In the following, the basic principle of FROG is introduced. Measuring the nonlinear signal intensity of an autocorrelation—a convolution of the pulse with itself—can already give hints about the pulse duration [192] if certain assumptions on the pulse structure are made. Spectrally resolving this signal, however, grants access to a full, assumption-free pulse characterization. This spectrally-resolved autocorrelation technique is called frequency-resolved optical gating or FROG. The different FROG implementations [191] differ by the used optical nonlinearity, geometry and their single-shot- [193] or multi-shot-measurement character. In the following, only multi-shot FROG is discussed as it offers more flexibility in respect to the pulse-duration range.

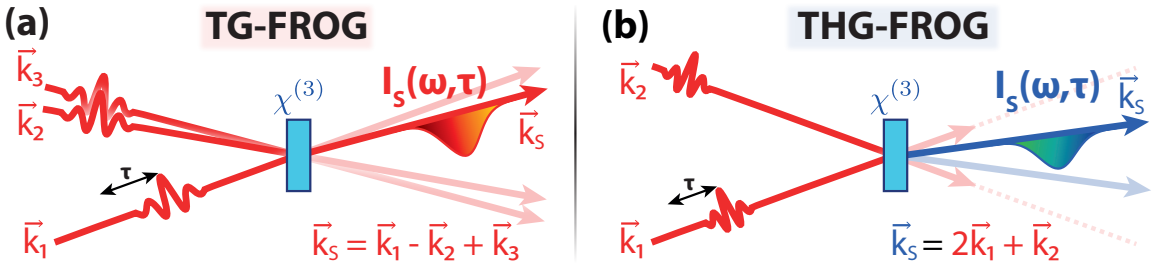

Figure 3.13.: Schematic view of a THG- and TG-FROG. **(a)** Three input beams with respective wave vectors $\vec{k}_1$, $\vec{k}_2$ and $\vec{k}_3$ are focused into a target medium. Here, the first pulse is time-delayed to the others by τ. The third-order nonlinear transient-grating process results in a degenerate signal with wave vector $\vec{k}_S$. The spectral intensity of the signal $I_S(\omega,\tau)$ is subsequently measured with a spectrometer. **(b)** In the THG configuration, only two pulses are noncollinearly focused into the target. Here, the third-harmonic is generated by two photons from one beam and one photon from the other.

The data resulting from a FROG measurement is a two-dimensional spectrogram $I_{FROG}(\omega,\tau)$ in which the spectra are shown over the time-delay τ of two pulse copies

$$I_{FROG}(\omega,\tau) = \left| \int_{-\infty}^{\infty} E(t)\, g(t-\tau)\, e^{-i\omega t}\, dt \right|^2 , \tag{3.4}$$

with the frequency ω, the electric field of the pulse $E(t)$ and nonlinearity-specific gate function $g(t-\tau)$. There are different implementations of FROG making use of second and third-order nonlinearities, $\chi^{(2)}$ and $\chi^{(3)}$, respectively. In the following, two $\chi^{(3)}$ implementations, transient-grating (TG) [194] and third-harmonic-generation (THG) FROG [195], are discussed. The working principles of TG- and THG-FROG are shown in figure 3.13. The TG- and THG FROG variations have the advantage of no phase-matching constraints: While in the TG version two noncollinearly focused beams generate a transient refractive-index grating from which the third beam diffracts, a THG-FROG relies on third harmonic generation at the surface of a medium as the broken symmetry at the material/air boundary enables odd-harmonic generation. The measurement signals of TG- and THG-FROG differ in their spectral output: As TG is a degenerate four-wave-mixing process, the spectral range of the measurement signal matches the one of the input pulse. In contrast to that, the signal of the THG process is in the spectral range of the original frequency cubed. Thus, the TG and THG spectrograms are given by

$$I^{TG}_{FROG}(\omega,\tau) = \left| \int_{-\infty}^{\infty} E(t-\tau)\, |E(t)|^2\, e^{-i\omega t}\, dt \right|^2 \tag{3.5}$$

for the TG case and

$$I_{FROG}^{THG}(\omega,\tau) = \left| \int_{-\infty}^{\infty} E(t)^2 \, E(t-\tau) \, e^{-i\omega t} \, dt \right|^2 \tag{3.6}$$

for the THG implementation. While the TG scheme has the advantage of very intuitive measurement traces that can be qualitatively interpreted in most cases even without a full pulse retrieval, the THG scheme has advantages in the SWIR as the measured signal is upconverted to the more accessible visible spectral regime.
As the aim is to determine the input field $E(t)$ from the measured spectrogram $I_{FROG}(\omega,\tau)$ the question arises how the electric field can be extracted from the equations (3.5) and (3.6). This, however, is not analytically possible. Especially, due to measuring spectral intensities, one does not have direct access to the spectral phase of the pulse. Such phase-retrieval problems [196] are common also in different fields of physics, e.g., in scattering measurements [197]. Hence, iterative algorithms are used to reconstruct the amplitude and phase of the pulse. Notably, FROG measurements do not contain any information about the zeroth order of the spectral phase, the CEP. The respective phase-retrieval approaches range from the generalized projections algorithm [198] to ptychographic approaches [199] or even machine learning-based reconstructions [200]. In this work, the recently developed *common pulse retrieval algorithm* (COPRA) [201] is employed. COPRA can be applied to a broad class of different nonlinear pulse-measurement techniques and provides accurate and robust retrieval results.

3.2.5.2. LL2 FROG apparatus

Besides the required flexibility in wavelength and pulse durations, the pulse characterization setup for the *LL2* laboratory has to fulfill further demands:

- *portability* and *stability*: it should be small enough to be carried around the lab and robust enough to not require re-alignment after moving it around.
- *efficiency*: the FROG setup should be easy to align and debug to enable an efficient workflow. In addition, the control software should be optimized for everyday lab usage.
- *flexibility*: a fast switching between operational modes (TG ↔ THG) should be possible without major hardware changes.

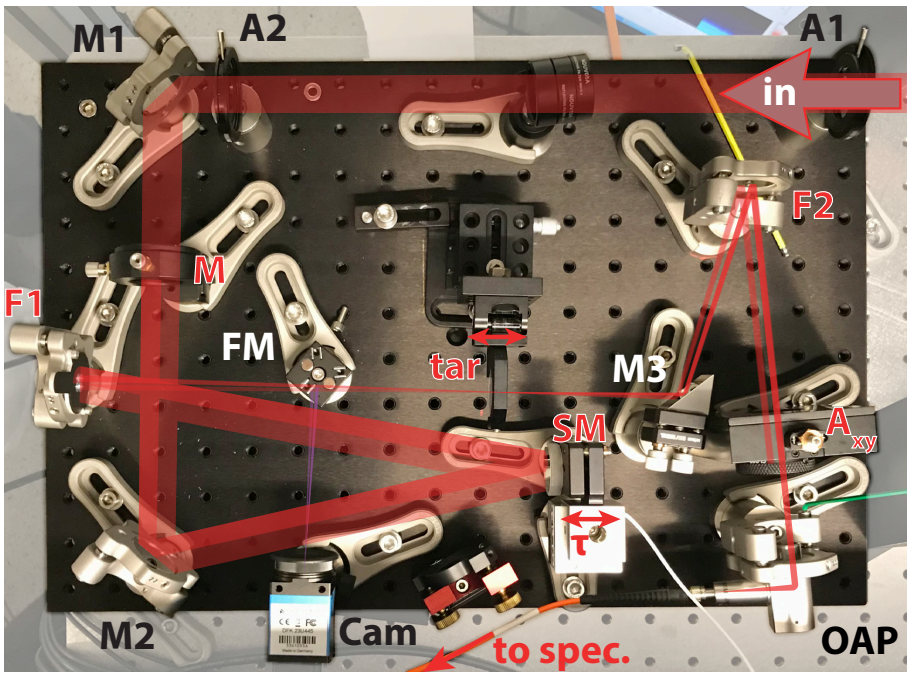

Figure 3.14.: Photography with overlaid beampath of the TG/THG-FROG (here in THG mode). First, the incoming beam is aligned by external mirrors on the two apertures *A1* and *A2*. The flat mirrors *M1* and *M2* can be used to center the beam on the split-mirror *SM* and the focusing mirror *F1*, respectively. The focusing mirror is covered by an exchangeable four-hole mask. During a TG-FROG measurement, the fourth, alignment-specific hole is covered by a flip-in partial beam stop *M*. The resulting three beamlets are focused into a target *tar* (typically a thin fused silica plate) which can be moved along the beam propagation axis with a linear stage to optimize the signal strength. Afterwards, all beamlets including the measurement signal are rerouted by mirror *M3* and recollimated by mirror *F2*. Finally, the adjustable aperture A_{xy} spatially isolates the signal which is then focused into a multimode fiber by the off-axis parabolic mirror *OAP*. The fiber is connected to the respective spectrometer.

- *free of dispersion*: the device should be able to accurately characterize the shortest few-cycle pulses. Hence, the setup itself should not contain dispersive optical elements up to the point of measurement.

As an ideal solution to meet these requirements, a compact, all-reflective TG/THG-FROG apparatus has been built. The setup including its beampath is presented in figure 3.14. The all-reflective design in combination with the spatial beam separation enables a virtually dispersion-free measurement [202]. Instead of using (dispersive) beamsplitters, a mask divides the beam mode into beamlets as shown in figure 3.15. This enables an easy implementation of a BOXCARS [203] geometry in the TG case and a noncollinear focusing geometry in the THG case. Thus, the wavelength compatibility is only restricted by the reflectivity of the broadband metallic mirrors, the transparency of the target medium and the connected spectrometer including

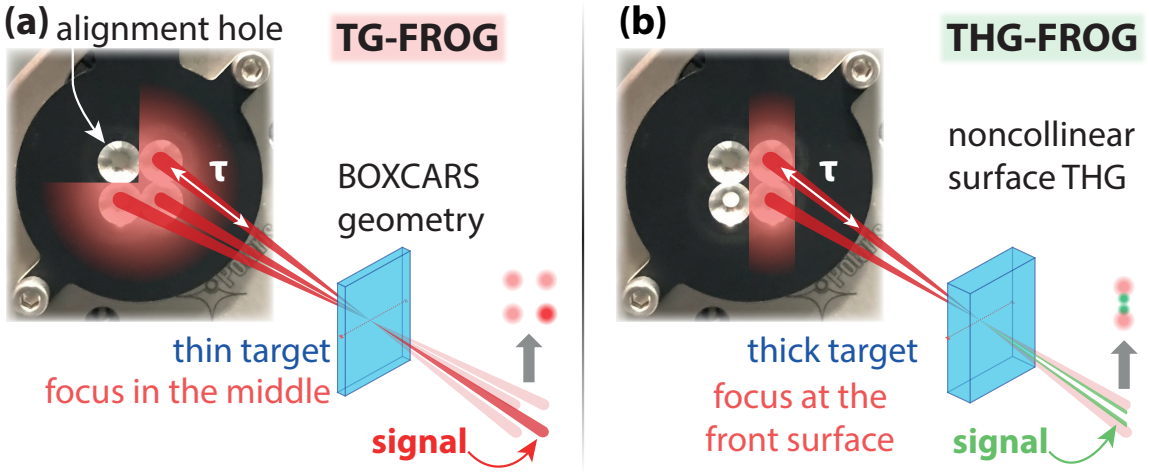

Figure 3.15.: Four-hole mask in TG and THG operation mode of the FROG device. **(a)** In TG mode, the beam is centered on the mask, illuminating all holes (quadrant of alignment hole is blocked) equally. A thin target is placed in the common beam focus of the BOXCARS beam geometry. The signal appears at the position of the covered fourth hole. **(b)** In THG mode, the beam is slightly realigned to be centered on two vertical holes. The beam mode is truncated in a way that the other two mask holes are not illuminated. A thick target is used and positioned such, that the foci are at the incident target surface in order to maximize the THG signal originating from only one surface.

the multimode fiber. While the available SWIR spectrometer, which is used for the TG-FROG measurements, is restricted in range (compare figure 3.12), the THG scheme allows for the upconversion of SWIR wavelengths to the UV/VIS regime and thus the use of conventional silicon-based spectrometers (here *OceanInsight Ocean-FX-XR1* [204]) in order to characterize the respective pulse over its entire bandwidth. Therefore, the TG-mode is used for pulses with spectra that fit within the InGaAs-spectrometer range, while the THG-FROG measurements are used for wavelengths above and below that range, enabling a temporal characterization over the whole wavelength-tunability dimension of the SWIR few-cycle source. As this is a multi-shot, scanning FROG apparatus, it relies on time-delaying at least two beamlets with respect to each other. This is enabled by a slip-stick piezoelectric actuator (*SmarAct CLS-3232* [205]) enabling motion over multiple millimeters with nanometer precision. This enables a sub-femtosecond temporal resolution at a range up to the picosecond regime. As the whole setup is built on a 30 cm × 45 cm breadboard, it can be easily carried around together with a miniature, fiber-connected spectrometer of choice. Still, it offers enough space and access to optical elements as well as alignment features to efficiently use the FROG device in everyday laboratory operation and adapt it to different sources. This capability is further enhanced by the software (developed in-house) that can be used for alignment as well as the measurement itself.

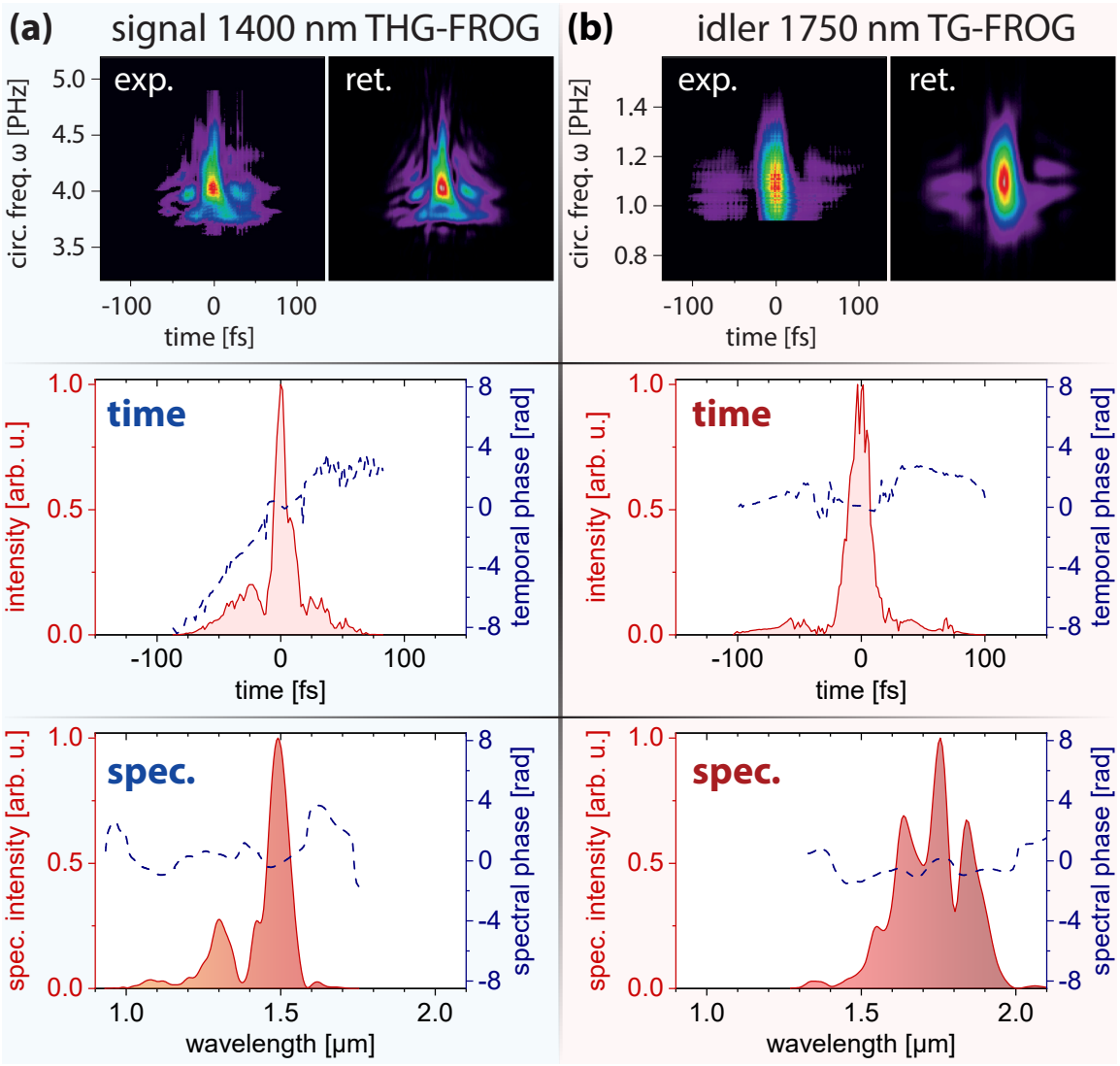

Figure 3.16.: FROG measurements and retrievals of exemplary few-cycle SWIR pulses. Traces (experimentally measured and retrieved), temporal and spectral retrievals of **(a)** signal pulses at λ_c = 1400 nm using THG-FROG and **(b)** idler pulses at λ_c = 1750 nm using TG-FROG.

While this FROG setup has characterized multiple different laser sources, including the Ti:Sa front end (and there benchmarked against a commercial temporal characterization product – see figure 3.6), it is the main tool to systematically compress the spectrally broadened SWIR pulses in an iterative approach. More details on the pulse compression itself are given in the following section 3.2.5.2. Figure 3.16 shows two examples of compressed signal and idler pulses. While the signal pulse is characterized via THG-FROG in figure 3.16(a), the idler pulse is measured in TG-configuration in figure 3.16(b). With the spectrally broadened SWIR pulses and the availability of a

tool to characterize their temporal structure, all prerequisites are met to temporally compress the pulses. While complicated and expensive compression schemes like compressors based on prisms or gratings [206–208] or chirped mirrors [209] have to be used in the visible and NIR spectral regime, the SWIR region offers the advantage of the availability of transparent materials with negative GVD/chirp as shown in table 3.1.

Table 3.1.: Dispersion of multiple transparent materials in the SWIR region. The zero-GVD wavelength $\lambda_{GVD=0}$ is given as well as GVD values (in $^{fs^2}/_{mm}$) for four different IR wavelengths. For birefringent materials ("*"), the dispersion for the ordinary axis is given. GVD values are only given for the transparency region of the respective material. The data are calculated using [210].

material	$\lambda_{GVD=0}$ [nm]	GVD [$^{fs^2}/_{mm}$] @ 800 nm	1150 nm	1550 nm	2150 nm
ADP*	971	29	-36		
KDP*	978	27	-29	-132	
FS	1273	36	10	-28	-136
CaF_2*	1546	28	14	0	-30
NaCl	2760	85	56	38	19

3.2.5.3. Compression via negative GVD

The SWIR region is typical for vibrational resonances, especially of OH-stretching modes in the respective materials [211]. Hence, optical substrates often exhibit anomalous dispersion (see theory section 2.1.2.2) in the SWIR spectral regime. By a suitable choice of the dispersive material and its thickness, compressed pulses can be achieved over the whole tunability range of the SWIR source. This bulk-compression approach [143, 212, 213] results in the pulse durations which are depicted in figure 3.17 together with the pulse energy after compression, at the entrance of the vacuum beamline. While the second-order dispersion, the GVD, can be negative in the anomalous-dispersion regime, the third-order dispersion is positive for non-artificial materials [145, 214–216]. Thus, by using thick dispersive materials for compression near their 0-GVD wavelength $\lambda_{GVD=0}$ leads to a tendency for a double-pulse structure due to third-order dispersion. In consequence, relatively exotic materials with $\lambda_{GVD=0} < 1000$ nm such as ADP or KDP are necessary to compress the short-wavelength end of the tuning range. In the presented case, the overall

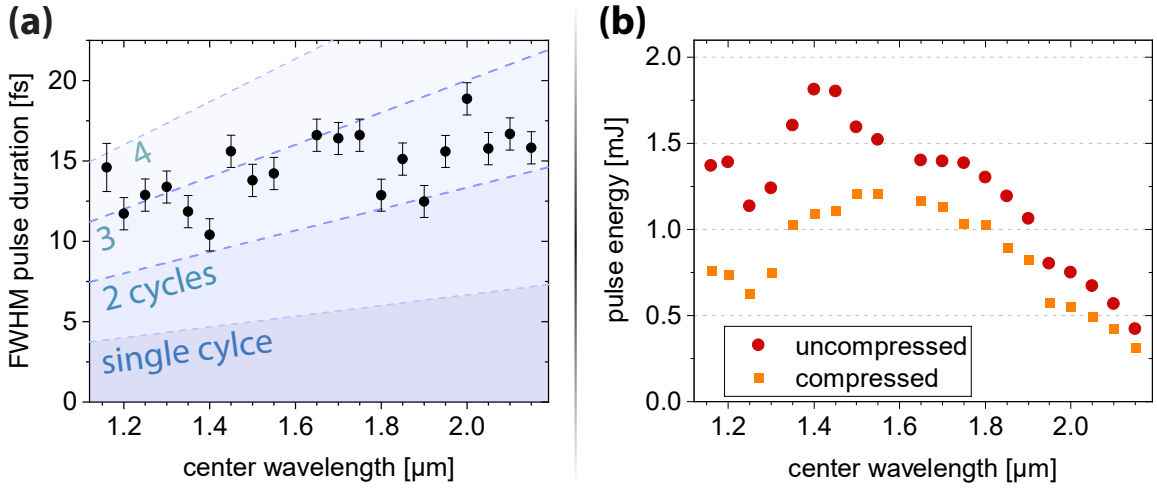

Figure 3.17.: Intense few-cycle SWIR pulses. **(a)** FWHM duration of the compressed, wavelength-tunable SWIR pulses extracted from the FROG retrievals. **(b)** Pulse energies of the pulses after the SF-HCF (*uncompressed*) and in front of the vacuum beamline (*compressed*).

spectral phase consists of contributions from dispersive media in the OPA, other dispersive media in the setup (entrance/exit windows of the SF-HCF assembly and of the beamline) and from SPM and other nonlinear processes, as well as propagation in the gas-filled SF-HCF. A table with the SF-HCF parameters and the additional inserted material for optimal compression is presented in table B.2 in the appendix.

3.2.5.4. Pre-beamline optical setup

The pulses are compressed directly in front of the beamline (compare figures 3.1 and 3.3). This pre-beamline optical setup is sketched in figure 3.18. There, a thorough pulse characterization is possible: The far-field beam mode (via TPA in a Si-CMOS chip – see figure 3.11 for an example), the spectrum and the temporal intensity structure (via FROG), as well as the pulse energy/power are measured at the pre-beamline optical assembly. Furthermore, this setup includes a beam-pointing stabilization (*TEM Aligna 60 MoPiA* [148]) in order to ensure a reliable and stable beam incoupling into the vacuum beamline. By solely relying on reflective, gold-coated optics[8], the pre-beamline setup guarantees achromatic focusing of the broadband few-cycle pulses as well as its usability over the whole SWIR wavelength-tunability range.

[8] Only the beamline/HCF windows and the bulk-compression substrate are transmitted.

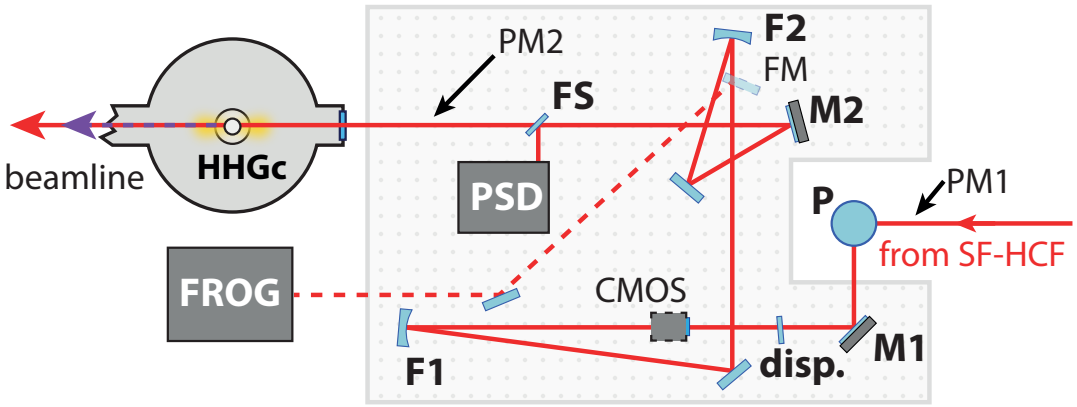

Figure 3.18.: Schematic view of the pre-beamline optical setup. After the exit window of the SF-HCF, the beam is elevated in height and its polarization rotated by a periscope (*P*). The first and the last re-routing mirror, *M1* and *M2*, respectively, are motorized and connected to a beam-pointing stabilization system. Afterwards, some space is reserved for the dispersive material (*disp.*) to compress the pulse. For characterization purposes, the far-field beam mode can be measured with an insertable *CMOS* camera. The concave mirror *F1* with a focal length of 3 m collimates the beam. Just before the focusing mirror *F2* (f = 1 m), the flip mirror *FM* can send the collimated beam into the FROG device for temporal characterization. A 1 mm-thin fused silica plate (*FS*) reflects a small part into the beam stabilization sensor unit (*PSD*) just in front of the beamline's entrance window. In the vacuum beamline (see figure 3.21), the beam generates XUV/SXR in an HHG cell (*HHGc*). Two designated locations, where the power/pulse energy is typically measured (*PM1* and *PM2*) are indicated.

3.2.5.5. Long-term stability

One major goal of the whole optical setup is to provide few-cycle pulses for uninterrupted multi-day measurement campaigns. A basis for the required long-term stability is set in the temperature- and humidity-controlled *LL2* and the multiple levels of housing which shield the optical setup from environmental influences and enable a stable thermal equilibrium. Furthermore, pointing drifts of the laser system are taken care of by the beam stabilization system in front of the OPA (see figure 3.7). Therefore, power drifts of the SF-HCF output are minimized. Moreover, the gas input pressure of the SF-HCF is chosen rather conservatively to avoid plasma-induced fluctuations even at the cost of a maximized achieved broadening. Figure 3.19 shows a benchmark stability measurement of broadened pulses at λ_c = 1750 nm over the course of a week of continuous operation. In parallel, the SWIR spectrum is measured and further laboratory parameters are logged. The standard deviation of pulse energy over the duration of this long-term measurement is 1.2%. Here, the long-term power drifts (solid red line in figure 3.19(a)) show a standard deviation of 0.8%. Also, the spectrum did not significantly shift during this multi-day measurement (see figure 3.19(b) and (c)). The residual long-term fluctuations are partially correlated with the *LL2*

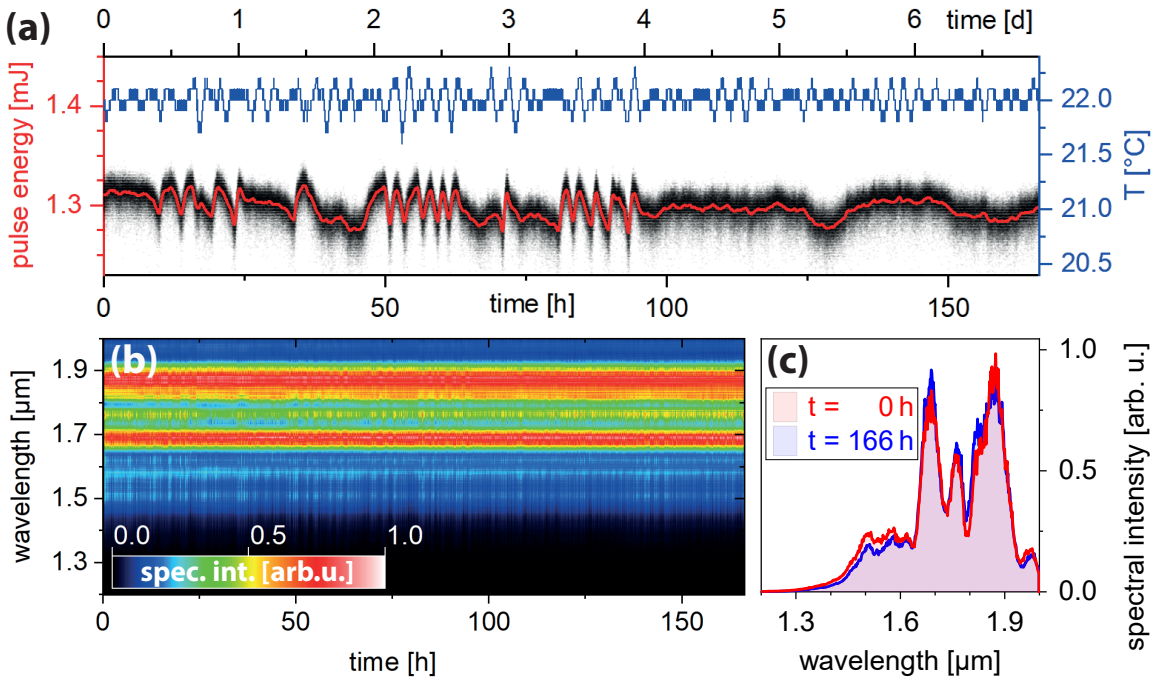

Figure 3.19.: Stability of the SWIR few-cycle laser source at λ_c = 1750 nm over the course of 166 h. **(a)** Pulse-energy stability (every tenth pulse is measured) as black dots and smoothed (σ = 500 data points) as red line. The measured air temperature near the OPA in the *LL2* is shown as blue line. **(b)** SF-HCF output spectra measured over 166 h. **(c)** Spectral lineouts at the beginning (red) and the end (blue) of the long-term measurement.

temperature shown in figure 3.19(a) as solid blue line. Overall, the stability of this optical setup enables measurement campaigns with an unprecedented duration of more than 160 h.

3.3. Transient-absorption beamline

A powerful, stable and flexible few-cycle laser source is only one prerequisite for experiments which reveal ultrafast phenomena in atoms and molecules. The measurement apparatus itself, in our case a vacuum transient-absorption-spectroscopy beamline, is the other crucial component. There, the measurement takes place and the data are acquired.

3.3.1. Beamline overview

The general scheme of TAS has been discussed in section 2.4.5.2 in the theory chapter. Now, the aim is to realize both strong-field perturbation approaches—the IR-intensity

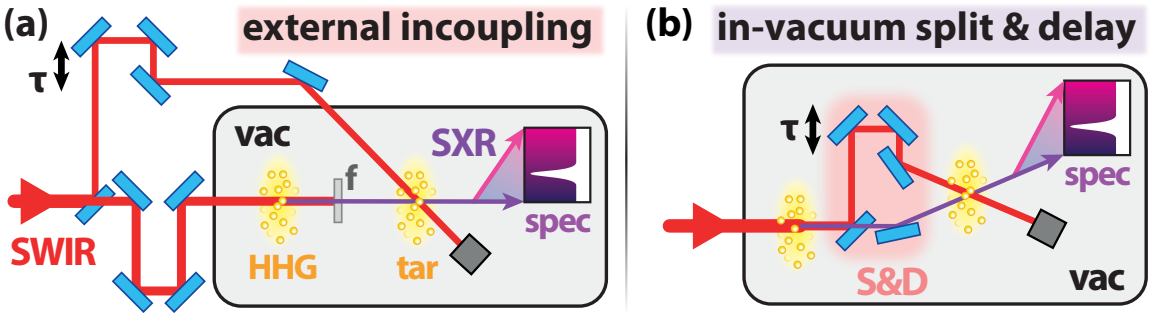

Figure 3.20.: External-incoupling versus in-vacuum split-and-delay TAS scheme. **(a)** External incoupling scheme, in which an SWIR beam is split in front of the vacuum beamline in two parts. One is exclusively used for HHG and then filtered out with a metal filter (f). The other SWIR beam is externally time-delayed by τ and then focused into the target in spatial overlap with the SXR. Afterwards, the SWIR beam is dumped, while the spectrum of the transmitted SXR beam is measured. **(b)** In-vacuum split-and-delay scheme, where the SWIR beam after HHG is reused and the interferometric split-and-delay (*S&D*) assembly is located inside the vacuum chamber.

scan scheme and the time-delay technique as shown in figure 2.9 in the theory chapter—in the x-ray spectral region and in a single beamline. To get an idea of possible implementations, an overview of existing x-ray absorption-spectroscopy beamlines can be helpful: XAS endstations are often found at synchrotron large-scale facilities [217–220] and enable high-resolution absorbance studies of atoms, molecules and solids. Synchrotron facilities, however, lack the required time resolution[9] for TR-XAS experiments that target electron dynamics. Other large-scale facilities, so-called free-electron lasers (FELs) [221], can offer femtosecond time resolution. In this case, however, an exact timing with optical pulses is challenging as well as the stochastic SXR pulse structure. Furthermore, building, maintaining and operating FELs is very cost intensive and thus the access to beamtimes is restricted and highly competitive. Hence, a more suitable inspiration in the context of this thesis are experimental table-top (TR-)XAS beamlines. In the most straightforward implementation, relatively compact beamline-laser-combinations that fit inside an average laboratory represent an SXR source for static XAS measurements [106, 222–226]. Such setups are often built with the perspective of a future update to a full time-resolved measurement scheme employing a perturbing IR pulse in the target. For table-top TR-XAS, two different experimental schemes can be distinguished as schematically shown in figure 3.20: In both approaches, the SXR radiation is produced via high-order harmonic generation (see section 2.1.5 in the theory chapter) driven by intense IR laser pulses. Since a

[9] Special techniques to enable femtosecond pulse durations at synchrotrons are discussed in section 5.1.1. In general, however, synchrotron sources provide pulses in the picosecond regime.

portion of the initial IR pulse is used as perturbing pulse in the target, the experimental setup represents a Mach-Zehnder interferometer [227, 228] in which a distance change in one leg results in an SXR-IR time delay. Now, the two approaches in figure 3.20 differ in where the beam is split for the interferometric measurement. In most cases [229–233], the beam-splitting is conducted in front of the beamline and one part of the IR pulse is exclusively used for HHG as shown in figure 3.20(a). The other part of the IR beam is then time-delayed and used as perturbing pulse in the target. Hence, in this *external-incoupling* approach, the legs of the interferometer are comparatively long. As a (sub-)femtosecond time-delay resolution is aspired this results in the challenge of actively stabilizing delay drifts in long-legged interferometers. In principle, this can be overcome by tracing these changes in the interferometer with the help of an overlayed cw laser and using these *in-situ* measurements as feedback for an active stabilization of the interferometer [232, 234, 235] at the cost of a significant increase in complexity. An advantage of this long-legged interferometer scheme, though, is the flexibility in modifying the perturbing IR pulse independently from the HHG pulse. This can include polarization alteration, wavelength conversion or additional pulse compression. An alternative approach is to reuse the IR pulse after the HHG process and add an in-vacuum pulse-delay via a split-and-delay assembly [234, 236–238]. This is illustrated in figure 3.20(b). Here, the phase-locked nature of the driving IR and the HHG pulse is used to provide a few-attosecond delay precision between the pulses and an intrinsic inter-pulse pointing stability. This technique, however, is limited concerning the available time-delay range and restricted with respect to perturbation-pulse manipulation due to intrinsic space limitations inside the vacuum beamline.

To choose the most suitable approach, a look at the aims for the respective beamline at *MPIK* is helpful. The (TR-)XAS beamline should provide:

- *XAS and TR-XAS* – a fast switching between a XAS scheme with an intensity-controlled IR perturbation pulse and an TR-XAS scheme with time-delay control between the two pulses should be possible. A combined (TR-)XAS measurement scheme is optional.

- *Sub-femtosecond accuracy* – a time-delay accuracy below 1 fs in TR-XAS mode is the aim to be able to resolve fastest electron dynamics on the scale of less than one IR cycle.

- *Wavelength tunability* – generating and measuring XUV/SXR photon energies

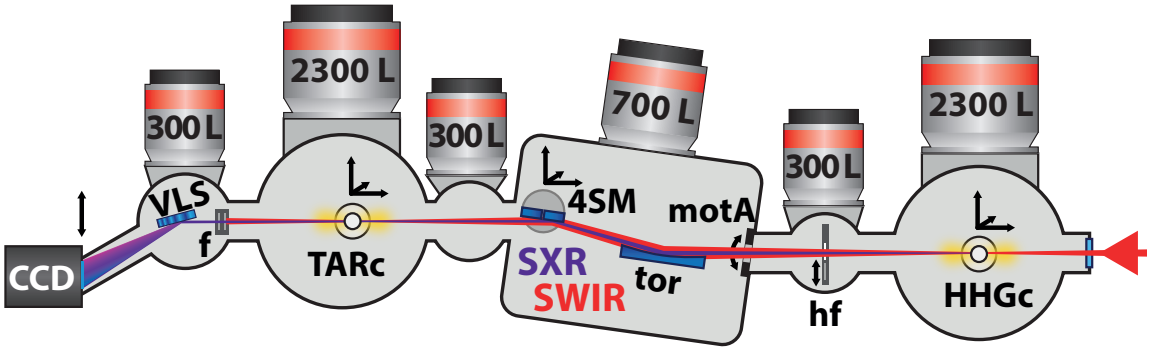

Figure 3.21.: Overview of the vacuum (TR-)XAS beamline. The SWIR beam enters the beamline from the right and is focused into a motorized HHG cell (*HHGc*). Afterwards, metal (half) filters (*hf*) can be inserted for TR-XAS or full filters for a static absorption spectrum. The co-propagating SXR/SWIR beams enter the cuboid mirror chamber through a motorized aperture (*motA*). The SXR/SWIR beams reflect off a toroidal mirror (*tor*) under grazing incidence and are rerouted by the movable four-split-mirror assembly (*4SM*). Both beams are refocused into the target cell (*TARc*). The transmitted SXR beam is cleaned from the remaining SWIR by two stacks of metal filters (*f*). A variable-line-spacing grating (*VLS*) disperses the SXR spectrum which is finally measured with a *CCD* camera. The position of the CCD camera can be adjusted in order to flexibly acquire spectra in different photon energy regions. The turbo-molecular vacuum pumps with their respective pumping volume per second are illustrated as well.

from $< 40\,\mathrm{eV}$ to $> 200\,\mathrm{eV}$ and using them in experiments enables measuring at electronic resonances of simple atoms as well as element-specific absorption edges of complicated molecules.

- *Multi-usability* – the beamline should be usable for both, experiments at FELs and HHG-based table-top measurements.

The *multi-usability* requirement is based on the research group's involvement in FEL-based absorption spectroscopy experiments [3, 4, 6–9, 11, 12, 239–241]. In order to fulfill these goals, the in-vacuum split-and-delay approach with IR-driver pulse recycling (figure 3.20(b)) is chosen. Furthermore, the main optical elements inside the beamline are mirrors operating under grazing incidence which means a reflection under a shallow angle. This ensures high beamline transmission over a large wavelength regime from the IR to the SXR. An overview over the beamline is depicted in figure 3.21. In the following, the separate segments of the beamline are discussed.

3.3.2. High-order harmonic generation

First of all, the focused SWIR beam enters the beamline through a thin fused silica window and is focused into a gas target. This gas target consist of an effusive cell

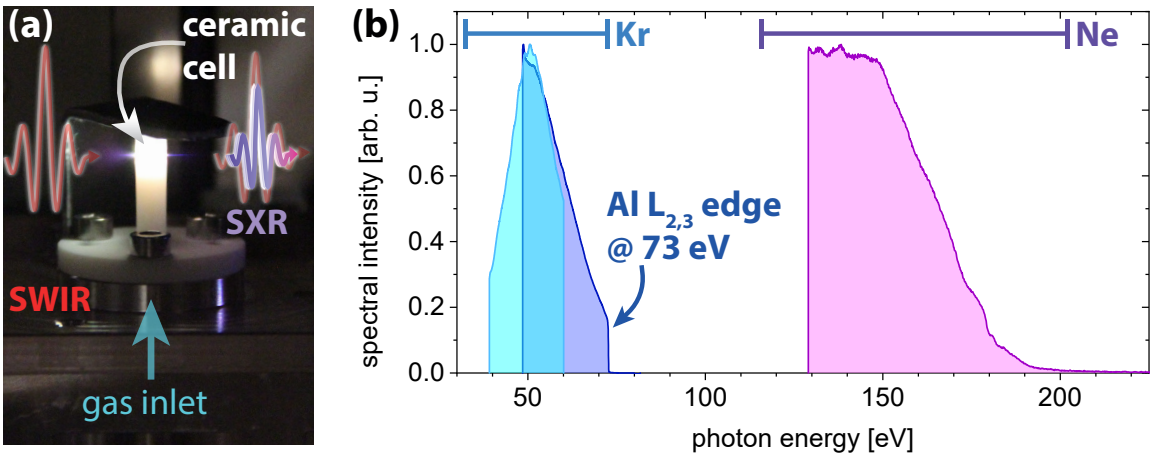

Figure 3.22.: SWIR-driven HHG. **(a)** Image of the ceramic cell during HHG. A krypton plasma-plume in front and behind the cell is clearly visible. **(b)** HHG spectra achieved with a ≥ 1 mJ few-cycle SWIR pulse at λ_c = 1550 nm. Different colors represent different HHG parameters and CCD-spectrometer positions. The photon-energy regions of the used HHG gas are indicated as well.

made from a ceramic (*Macor*® [242]) tube of 4 mm outer and 2 mm inner diameter. Holes with a diameter of 200 µm are drilled on either side of the cell (see figure 3.22(a)). The HHG cell is fully xyz-motorized. Thus, in combination with a suitable choice of target gas and pressure, phase-matching conditions are found to generate photons from below 40 eV up to above 200 eV in photon energy. Examples of obtained HHG spectra with a λ_c =1550 nm SWIR few-cycle driver pulse are shown in figure 3.22. Backing pressures of up to 1 bar (depending on HHG gas) can be maintained over a long period. The maximum pressure is just restricted by the available pumping speed of the attached turbomolecular pumps (see figure 3.21). Table 3.2 summarizes the respective parameter regimes.

Table 3.2.: Parameters for HHG in different photon energy regimes reaching from < 40 eV to > 200 eV. The used HHG gas, its backing pressure as well as suitable metal filter materials to clean the HHG beam from residual SWIR are given. The resulting HHG spectra are shown in figure 3.22.

photon energy region [eV]	HHG gas	gas pressure [mbar]	filter material
< 40 - 73	Kr	200 - 300	Al
120 - 200	Ne	550 - 600	Zr/In

Notably, the obtained XUV/SXR spectra are relatively smooth. Due to no carrier-envelope-phase stabilization of the laser source, this source is not expected to provide isolated attosecond pulses [243]. The expected $2\omega_{SWIR}$ spectral high-harmonic structure that is characteristic for HHG pulse trains [244, 245], however, is not strongly

pronounced. The measured flat, stable and gap-free spectra are very beneficial for XAS, especially if the intention is to measure closely-stacked resonances like Rydberg series converging to an absorption edge. While the free-running CEP of the few-cycle pulses and thus averaging over different XUV/SXR[10] pulse trains might play a role in this unexpected behavior, the plasma effects during HHG with high peak intensities around $10^{15}\,\mathrm{W/cm^2}$ [246, 247] comparable to the intensities used here in the setup at *MPIK* are probably the main contributor.

3.3.3. SWIR-intensity scan – XAS beamline configuration

After the HHG process, the residual SWIR and the SXR are co-propagating. Their divergence differs due to phase-matching. While the general spatio-temporal properties of high-harmonic pulses are highly nontrivial and linked to the quantum-nature of the process [248, 249], the SXR divergence is much smaller than the SWIR divergence under the employed condition of placing the HHG cell slightly behind the focus [250]. By using this approach throughout the experiments discussed in this thesis, the significantly smaller SXR beam size is exploited in order to control the SWIR intensity without affecting the SXR pulses. This is the aim of the XAS measurement scheme: To perturb the system with the SWIR pulse of tunable intensity while measuring the respective signatures of this perturbation via the SXR absorption spectrum at the same time. Figure 3.23 shows the beamline schematically in its XAS configuration. Here, the SWIR intensity control is realized by cutting the beam mode of the SWIR with a motorized, in-vacuum aperture (*motA* in figure 3.23; *SmarAct SID-5714-ID22-S-HV* [251]) while leaving the much smaller SXR beam mode unaffected. This corresponds to the scenario of focusing an apertured beam as discussed in section 2.1.2 and illustrated in figure 2.3 in the theory chapter. Thus, the SWIR intensity can be controlled while both beams remain co-propagating and reflect off the same optical elements. Therefore, their intrinsic temporal and spatial overlap from the HHG is preserved in the target and no interferometric assembly is needed. A toroidal mirror (provided by *optiX fab* [252]; $r_{tan} = -7185\,\mathrm{mm}$, $r_{sag} = -139.17\,\mathrm{mm}$) is used to image the HHG focus into a target cell in a 1:1 manner (with a 1 m distance of the HHG/target focus to the toroidal mirror). Another flat mirror corrects the introduced beam-deflection angle after the toroidal mirror. For alignment purposes[11], the flat mirror can be moved out of the beampath, such that the target focus of the toroid can be imaged and analyzed

[10] For simplicity and readability, the HHG pulse will be referred to as SXR in the following.
[11] An alignment procedure for the toroidal focusing mirror is outlined in [253].

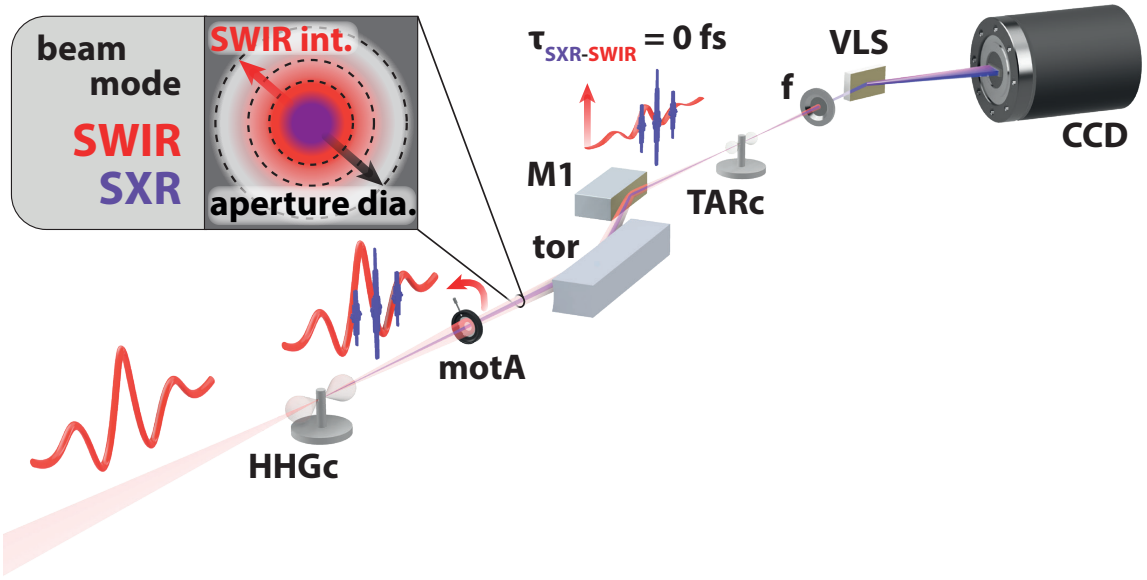

Figure 3.23.: Schematic view of the vacuum beamline in XAS configuration. The SWIR driver pulse is focused into the HHG cell (*HHGc*) from the left-hand side. The XUV/SXR (for simplicity *SXR* in the following) is generated in the gas-filled HHG cell (*HHGc*) and co-propagates with the residual SWIR. A motorized aperture (*motA*) can variably cut the SWIR beam mode and thus vary the SWIR intensity accordingly without affecting the SXR (see inset). Both beams, the diverging SXR and SWIR are re-focused by a toroidal mirror (*tor*) and rerouted by a flat mirror (*M1*) into the target cell (*TARc*). Afterwards, the transmitted SXR beam is cleaned from the remaining SWIR by a thin metal filter (*f*). The SXR spectrum is dispersed with a variable-line-spacing grating (*VLS*) and measured with an SXR-sensitive *CCD* camera.

outside the vacuum beamline. Both mirrors are gold-coated and reflect the beam under a grazing angle of $\Theta_g = 8^\circ$. The target-cell design is identical to the HHG-cell design besides the slightly larger hole diameters of the target cell of 300 µm. Thin (typically 100 - 200 nm) metallic filters remove any residual SWIR light to prevent stray light in the SXR spectrometer. Up to 2×8 different filter combinations can be chosen to enable full flexibility concerning the XUV/SXR region of interest (see table 3.2) and redundancy, thus maximizing measuring time. A double-filter design is chosen to prevent SWIR leakage [254] through microholes in the respective metal filters (see figure B.12 in the appendix). Finally, a variable-line-spacing (VLS) grating with a 1200 $^1/_{\text{mm}}$ groove density (*Hitachi 001-0640* [255]) disperses the spectra on a flat field in which a thermoelectrically-cooled, back-illuminated CCD camera (*Princeton Instruments PIXIS-XO 400B* [256]) is placed. VLS gratings [257] are advantageous in comparison to a constant-line-spacing concave grating as the spectral focus plane matches the flat CCD chip and not the conventional Rowland circle [258]. Here, the SXR focus in the target cell acts as an effective entrance slit to the spectrometer. The

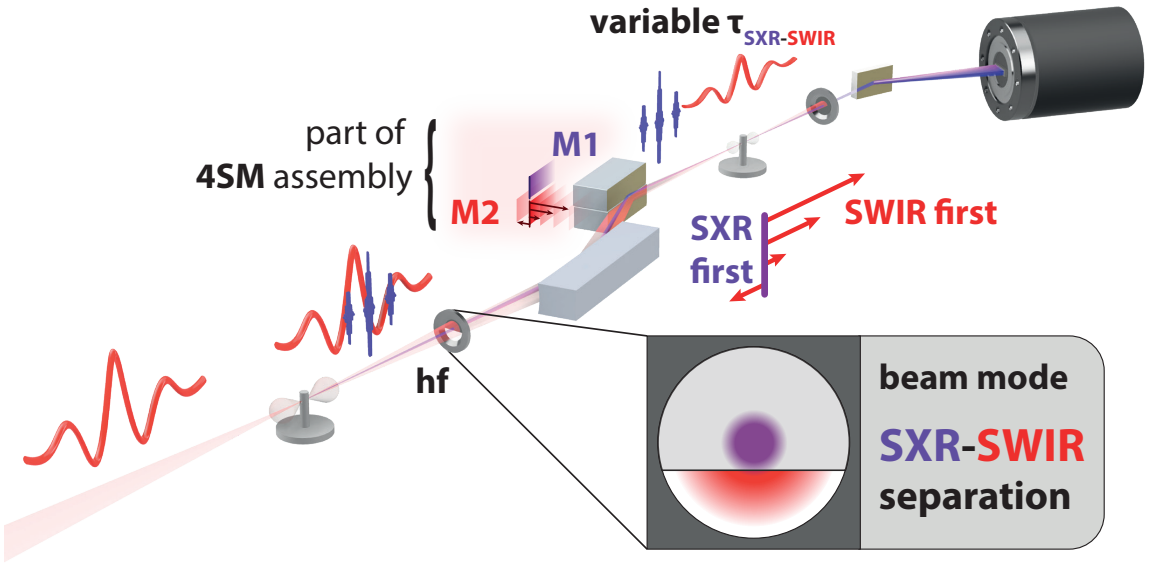

Figure 3.24.: Schematic view of the beamline in TR-XAS configuration. The major differences to the XAS mode (see figure 3.23), in which only the SWIR intensity is tunable, are the insertion of a thin metallic half filter (*hf*) after the HHG cell for spatial SXR-SWIR separation (see inset) and the changed setting of the 4SM assembly from just a re-routing configuration (*M1* only) to a split-and-delay configuration (details are given in figure 3.25). Here, the mirror *M1* reflects the SXR and stays fixed, whereas *M2* reflects the SWIR and is moved to induce a time delay.

CCD can be positioned manually along the spectral plane, enabling access to different spectral regions within the SXR continuum. Furthermore, the CCD's distance to the grating can be varied and thus the resolution optimized. The spectrometer is calibrated to well-known resonances in the static, SWIR-unperturbed absorbance of the target by a fit of the grating equation (see appendix section B.2.2). More information on the SXR spectrometer design is given in [60, 237, 239, 240].

3.3.4. Time-delay scan – TR-XAS beamline configuration

A major feature of the beamline is the capability to easily change to another operation mode – to the *SXR-SWIR time-delay-scan* configuration. This TR-XAS scheme of the beamline is illustrated in figure 3.24. All necessary changes to switch from a XAS to a time-resolved measurement are solely conducted in the beamline and hence in vacuum. As the time-delay is introduced geometrically by changing the optical path lengths of the SXR beam relative to the SWIR (compare figure 3.20(b)), two requirements are imposed: First, the SXR and the SWIR beams have to be spatially isolated and secondly, a path-length difference has to be introduced. For the spatial separation of the two beams, a thin metallic half filter (*hf* in figure 3.24) is inserted

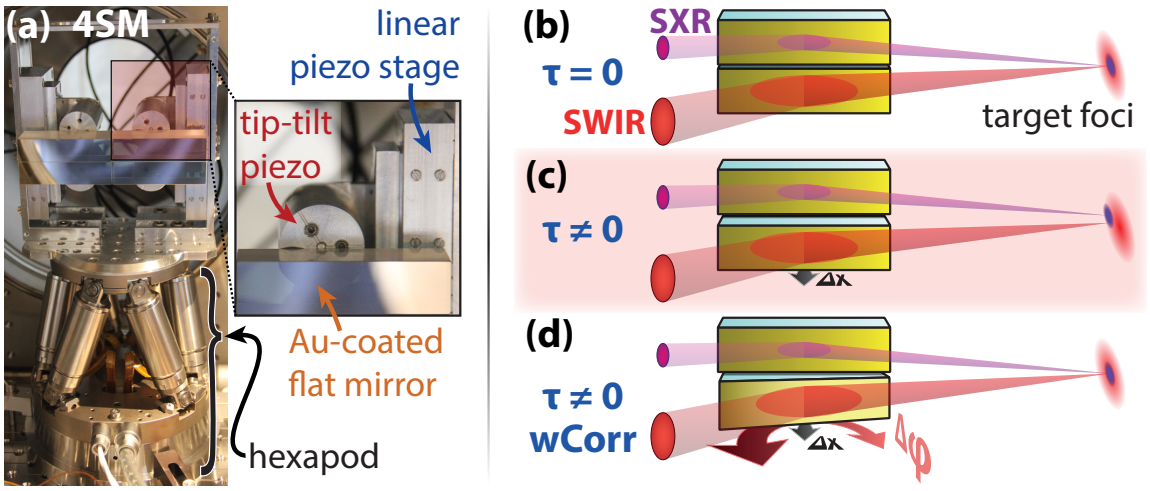

Figure 3.25.: Four-split-mirror (4SM) assembly. **(a)** Annotated picture of the 4SM assembly with detailed view on a motorized mirror segment. **(b)** Sketch of a two-mirror split-and-delay scheme, where the SXR and SWIR foci are in spatial and temporal overlap. **(c)** When inducing a large time delay τ with the linear piezo stage of the SWIR mirror, the two foci move out of spatial overlap in the target cell. **(d)** To correct for this spatial walk-off, the SWIR mirror is rotated which is conducted via the tip-tilt piezo actuators.

into the divergent SXR/SWIR beams after the HHG cell. Similar to the intensity control in the XAS scheme (compare figure 3.23), the different SXR/SWIR divergence is exploited. Here, the half filter is inserted just enough to cover the complete SXR beam mode (see inset in figure 3.24). The metallic filter enables a cleaning of the SXR beam mode from residual SWIR as only the SXR can partly penetrate through the filter. While more than half of the SWIR beam mode is blocked this way, there is still a part of the SWIR beam that is not affected by the half filter. This residue of the SWIR beam mode is spatially located below the SXR beam and thus isolated. With the spatially separated SXR/SWIR beams, the interferometric scheme is implemented via the split-and-delay unit, here in form of the four-split-mirror (4SM) assembly. As illustrated in figure 3.25, the 4SM consists of four identical flat mirrors. Three of these mirrors are equipped with piezo actuators. First, a linear piezo stage (*Physik Instrumente PIHera P-622Kyyy* [259]) can move the mirror orthogonally to the mirror plane over a range of 250 µm. This acts as the optical path-length control of the interferometer. The relation between mechanical movement Δx and time delay Δt is given by

$$\Delta t = \frac{2\Delta x \cos(\Theta_{AOI})}{c} , \tag{3.7}$$

with the angle of incidence $\Theta_{AOI} = 90^\circ - \Theta_g$ and the speed of light c. Considering the grazing angle $\Theta_g = 8^\circ$, the time delay calculates to

$$\Delta t = 0.9825\, {}^{fs}/_{\mu m}\, \Delta x \ . \tag{3.8}$$

Due the large angle-of-incidence, extensive Δx movements result in a spatial displacement of the SWIR target focus as depicted in figure 3.25(c). To compensate for this walk-off effect, the mirror angles can be slightly adjusted with piezo tip-tilt actuators (*Physik Instrumente S-325K030* [260]) as shown in figure 3.25(d). Hence, the whole time-delay range of the interferometer can be utilized despite the shallow grazing-angle that is necessary for high SXR reflectance over a broad spectral range. The correct settings of the tip-tilt mirrors have to be calibrated and experimentally verified, though. This is conducted using an in-vacuum CMOS camera that is mounted next to the target cell (see figure B.13 in the appendix). With the target-cell xyz-motorization, the camera chip can be placed at the exact position of the target cell. Thus, the focus at the target position can be imaged and the spatial overlap of multiple beams verified. In this way, a time-delay-scan tip/tilt calibration curve is recorded. Making use of nonlinear two-photon absorption in the silicon-based CMOS chip, even a z-scan can be conducted along the beam propagation axis to determine the exact SWIR focus position and ensure highest SWIR peak intensity in the target. The key component that enables the fast switching between the two beamline configurations is an in-vacuum heaxpod (*Physik Instrumente H-811.DV2* [261]) on which the four-mirror assembly is mounted. A variable spatial splitting of the SXR/SWIR beam is adjusted with the hexapod height position. In XAS configuration, the hexpod moves a single mirror into the common SXR/SWIR beampath, while in TR-XAS mode, two separate mirrors reflect the spatially separated SWIR and SXR beams.
In the TR-XAS configuration mode, the aperture-based SWIR-intensity adjustment can be employed, too, enabling combined scans of the time delay and the intensity. Due to the obligatory post-HHG half-filter, though, the maximum achievable SWIR peak intensity is significantly lower in TR-XAS mode than in the XAS scheme.

3.3.5. Commissioning – measurements on neon and helium

The capabilities of this unique laser-source and beamline combination are tested with measurements on the atomic targets neon (Ne) and helium (He). These studies give first hints concerning spectral resolution and dynamic range as well as temporal

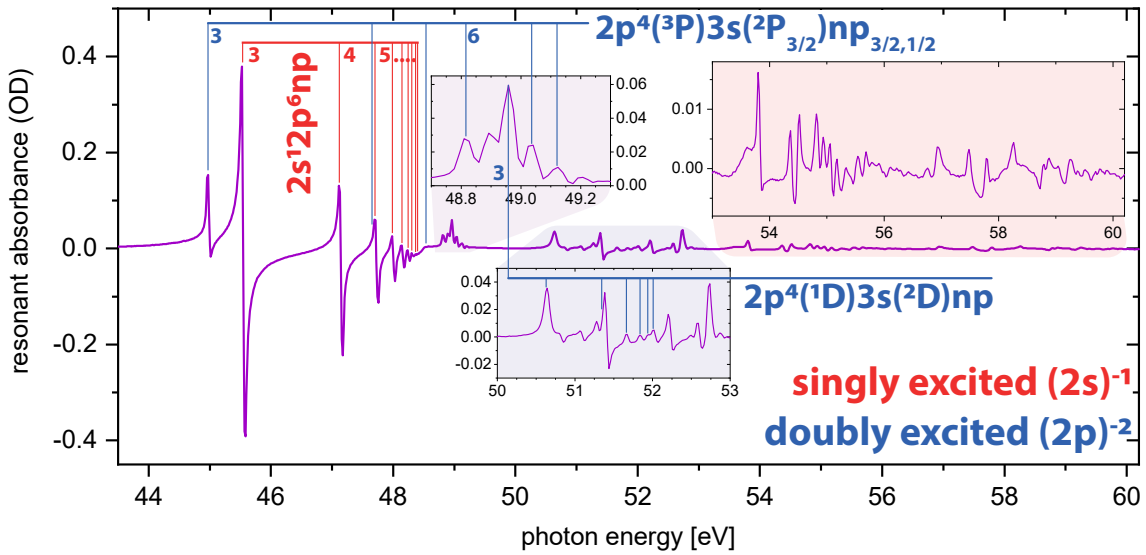

Figure 3.26.: Measured static absorbance of Ne in the 44 eV to 60 eV spectral region. Here, the HHG is conducted with a 1550 nm SWIR pulse and the SWIR blocked by a full filter directly after the HHG. Exemplary Rydberg-series resonances are indicated (compare [262]). In this spectral region, singly excited states (red) are interleaved with doubly excited ones (blue). In this measurement, the noise-floor is < 1 mOD. Thus, a complex manifold of resonances in the 53 eV to 60 eV region (red shaded inset) is measured. Only few reported measurements [263, 264] exist in this region close to the double-ionization threshold at 62.6 eV. Thus, the presented XAS capabilities might enable advances in electronic-structure determination of Ne in this interesting spectral region between two ionization thresholds.

resolution and of new scientific opportunities by employing SWIR few-cycle pulses in (TR-)XAS experiments.

3.3.5.1. Static absorbance of neon

First, to test the spectral resolution and sensitivity of measured absorbances with the overall setup, neon is chosen as target. Neon has the advantage that while it is readily available and a noble gas that has been thoroughly spectrally characterized with synchrotrons [262–264], it offers a very dynamic and complex absorbance structure above its first ionization threshold. Here, short-lived autoionizing states are observed. Interestingly, in the 20 eV to 60 eV region between the first ($I_P(Ne_I)$ = 21.6 eV [265]) and the second ionization potential ($I_P(Ne_{II})$ = 41.0 eV [266]), states in which two electrons are simultaneously excited by one photon (so-called doubly-excited states) and singly-excited states coexist [262]. This is of great interest, as the behavior of electron-interaction-enabled states (the doubly-excited ones) can be studied in direct spectral neighborhood to excited states, in which electronic correlations are not crucial. Figure 3.26 depicts a measured static Ne absorbance spectrum using the table-top

XAS setup described above. Here, the electronic character of exemplary Rydberg series is noted according to [262]. Based on this measurement, a resolving power of $\lambda/\Delta\lambda \approx 1300$ in this XUV region around $\lambda = 25\,\text{nm}$ (50 eV) is determined. One advantage that HHG-based static XAS has over synchrotron-based measurements is the very broad spectral region that can be measured by every single shot. Furthermore, the demonstrated absorbance sensitivity/dynamic range is in a similar order of magnitude to the published synchrotron data. Especially the 53 eV to 60 eV region (zoomed-in view in the red-shaded inset in figure 3.26) has the potential for a significant progress in the understanding of the electronic structure of neon due to its convergence to the double-ionization threshold. Furthermore, SWIR-perturbed (TR-)XAS measurements can help to further clarify the electronic structure by looking at the resonances' behaviors under the influence of strong laser fields. This illustrates the power of the few-cycle laser source and beamline even for static, broadband XAS investigations into the electronic structure of atoms and molecules that have been a stronghold of large-scale-facility-based measurements so far. Further measurements that have been conducted on neon with the presented beamline are discussed in [267].

3.3.5.2. Time-resolved measurement of laser-dressed states in helium

While some basic characteristics of the experimental setup for static XAS, e.g., resolution and sensitivity have been investigated in the preceding section 3.3.5.1, the capabilities concerning time-resolved measurements of the TR-XAS beamline configuration are tested on the atomic target helium. Helium is the simplest atomic two-electron system. Similar to the described Ne case, electronic transitions exist that require an interaction of two electrons. One example is the dipole transition from the electronic ground state $1s^2$ to the doubly-excited, autoionizing state $2s2p$ at 60.15 eV [268]. The behavior of the $2s2p$ resonance in strong laser fields has been extensively investigated in resonant [3, 8, 11] and non-resonant [269–271] intense fields. While some TAS experimental results on singly-excited states in He with SWIR perturbation pulses have been reported [272, 273], the tunable-wavelength few-cycle source described in section 3.2 provides unprecedented possibilities for electronic precision control in this prototypical system: One idea is to systematically investigate the excited states that are not accessible from the ground state via a dipole transition (so-called *dark states*). Such states can be measured with all-optical methods by laser-dressing these states in the presence of a nearby state that can be dipole-excited from the ground state (so-called *bright state*). While this mechanism of transient, light-induced states (LISs)

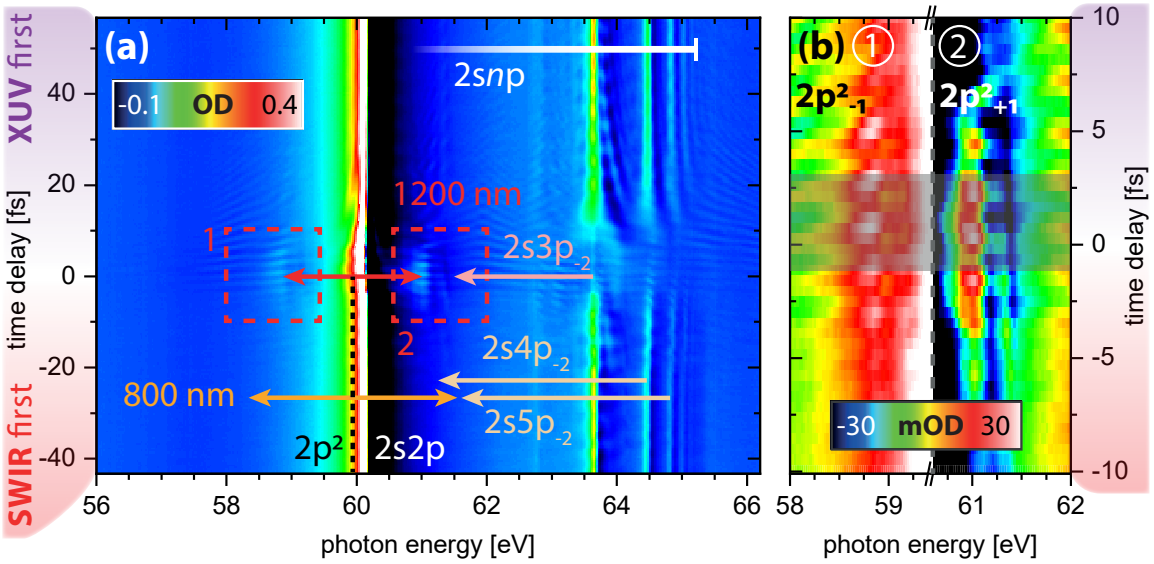

Figure 3.27.: Time-resolved measurement of doubly-excited states in He. **(a)** Overview of the dynamics of the $2snp$-Rydberg series ($n \geq 2$) under the influence of a strong SWIR pulse ($\lambda = 1200\,\text{nm}$). Here, the $2p^2$ dark state in direct neighborhood to the $2s2p$ bright state is indicated. In time overlap, signatures of the light-induced $2p^2_{\pm1}$ states are visible (red marked regions). The SWIR photon energy is indicated with red arrows. For comparison, the position of the LISs driven by 800 nm photons are indicated (orange arrows). Note, for 1200 nm, the $2p^2_{+1}$ state is not influenced by the $2s3p_{-2}$ or any other LIS. For 800 nm, however, the LIS of the dark state is overlapped by signatures of the LISs of the Rydberg series (light orange arrows). **(b)** Detailed view of the $2p^2$ region from (a). A clear 2ω structure is visible (for comparison: grey-shaded box marks the duration of one optical cycle). This illustrates sub-femtosecond resolution.

has been applied to singly-excited states in helium [274–278], a measurement of both (higher- and lower-energy) LISs originating from a doubly-excited state has not been published so far. To measure and analyze the respective coupling dynamics in all detail, both, a high spectral resolution and time-delay precision much better than one optical SWIR-cycle are crucial, as oscillations with a frequency of $2\omega_{SWIR}$ are expected [279]. Thus, taking the Nyquist-Shannon sampling theorem [280] into consideration, the temporal resolution thus has to be better than $1/4$ of a single laser cycle (e.g., $1/4 \times 5\,\text{fs}$ for $\lambda_{SWIR} = 1500\,\text{nm}$) for resolving these 2ω features. Hence, a sub-femtosecond temporal resolution is the aim. Figure 3.27 shows the results of a exemplary TAS measurement on the $2s2p$ resonance in He using a few-cycle SWIR driver pulse of 15 fs duration. Here, the SWIR laser pulse makes the dark state $2p^2$ transiently "visible" via its LISs by all-optical means. The $2p^2$ dark state ($E(2p^2\,{}^1D^e) = 59.95\,\text{eV}$ [281]) is spectrally located close to the $2s2p$ bright state ($E(2s2p\,{}^1P^0) = 60.15\,\text{eV}$). Due to dipole-selection rules (see section 2.4.3 in the theory chapter), LISs that originate from the dipole-accessible $2s2p$ state require an even number of additional SWIR

photons and thus have energies of $E(2s2p) \pm (2n\,\hbar\omega_{SWIR})$ with $n \in \mathbb{N}$. In contrast to this, laser-dressed states that are based on the dipole-forbidden $2p^2$ state can couple to the electronic ground state if an odd number of additional SWIR photons is involved and result in transition energies of $E(2s2p) \pm \left[(2n+1)\,\hbar\omega_{SWIR}\right]$, respectively. Studies targeting a comparison of the higher and the lower-energy LIS with each other utilizing 800 nm Ti:Sa-based pulses result in data which are difficult to interpret: the right-hand-side LIS signature overlaps with other resonances (e.g., the $2snp$ Rydberg series). Thus, having a tunable SWIR source at hand offers the possibility to adjust the photon energy accordingly to be able to shift the LISs to spectral regions where they are isolated. As figure 3.27 shows, the left and right SWIR-induced LIS signatures of the $2p^2$ state can indeed be well separated even by eye. Here, a moderate 0.5 µm step-size ($\hat{=}$ 0.5 fs) clearly unveils 2ω signatures as shown in the zoomed-in regions in figure 3.27. This sub-femtosecond resolution[12] without any special stabilization highlights the ability to resolve electronic processes on the attosecond timescale.

3.4. SWIR few-cycle pulse source and (TR-)XAS beamline – future directions

In summary, the optical setup and vacuum beamline apparatus for (TR-)XAS experiments in the newly established *Laser Laboratory 2* at *MPIK* has been presented in this chapter. The SWIR laser source that has been built over the course of the PhD project exhibits the unique characteristic of combining wavelength-tunability with millijoule pulse energies, a few-cycle pulse duration and stable laser parameters over a full week. This flexibility and versatility approach is continued in the vacuum beamline for (TR-)XAS experiments: The beamline is not only used for both, table-top and large-scale-facility experiment, but also offers to switch between SWIR intensity and SXR-SWIR delay time as scan parameters within minutes. A commissioning of the pulse-source–beamline combination has been conducted in the atomic systems helium and neon. The respective (TR-)XAS measurements illustrate the spectral and temporal resolution and sensitivity but also reveal the scientific relevance of the SWIR-tunable source.

This experimental setup provides a rich toolbox for investigating atomic and molecular dynamics on shortest timescales and with highest resolution in the *LL2* at *MPIK*. Un-

[12] The minimum achievable time-delay precision is expected to be on the 20 as level as a characterization of an earlier version of this beamline suggests [282].

interrupted (TR-)XAS measurements of multi-day duration and with correspondingly high statistics are readily available and have enabled the insights of this work into the quantum-character of electronic interactions (see chapter 4) as well as vibrational dynamics in molecules with highest spatial precision (see chapter 5). Furthermore, a significant scientific potential lies in combined time-delay/intensity-dependent measurement campaigns with durations up to several weeks. Here, an important future development is a further improvement of the long-term stability of the system by minimizing the fluctuations of the laboratory environment. An additional beam-pointing stabilization system right in front of the SF-HCF will counteract any long-term drifts concerning the incoupling into the HCF. Moreover, digitizing the gas-supply control system (of the SF-HCF input gas and the HHG/target gas supply) will cancel another source of long-term drifts. With these measures, a multi-week continuous operation with pulse-energy fluctuations limited to the intrinsic shot-to-shot level and hence without significant long-term drifts is possible.

Another direction that will enhance the impact of the laser system's wavelength-tunability is a motorization and automation of the focusing optical assembly in front of the SF-HCF. Up to now, the movement of the lenses, the respective alignment and characterization has to be conducted by hand. Using motorized stages in combination with the aforementioned beam stabilization will not only enable a significant reduction of the time needed to switch between few-cycle pulses of different center wavelength but also improve the reproducibility of the output pulse parameters. With such a (semi-)automated wavelength-switching, systematic wavelength-dependent studies can be conducted with less experimental uncertainties and more time efficiently. Thus, this will add the SWIR wavelength to the standard parameter-space of continuous measurement campaigns.

Another step that will considerably broaden the range of potential target systems is a further extension of the accessible HHG photon energies. Using xenon as HHG gas will open the $< 40\,\mathrm{eV}$ spectral window to investigate singly-excited low-lying resonances, e.g., 10 eV to 20 eV in H_2 [283, 284] or 10 eV to 25 eV in O_2 [285, 286]. On the other hand, employing idler wavelengths as HHG-driver might significantly expand the spectrum towards higher photon energies in the 300 eV region with the existing optics. Also, employing extra-thin metal filters (e.g., $2\times100\,\mathrm{nm}$ instead of $2\times200\,\mathrm{nm}$) or replacing the current optics with differently coated optics (e.g., Cr instead of Au; see figure B.15 in the appendix) might result in a beamline-transmission enhancement high enough to conduct TR-XAS measurements in the so-called *water*

window [107, 213, 229, 231, 287–290], the regime between the carbon and oxygen K-edges (284 eV and 543 eV). This water-window region is of fundamental interest for the investigation of ultrafast dynamics in biologically-relevant, organic molecules [231, 233, 291]. Besides that, the vacuum setup was designed with the thought of flexibility, allowing for optical assemblies of shallower grazing angle which also results in a significantly higher reflectivity in the SXR.
Overall, there are many different realistic options to further enhance the efficiency and flexibility of this setup. Even at its current state, the setup is ready to be employed in systematic, complex measurement campaigns which will grant many new insights into the dynamics of small quantum systems.

4. Tuning the effective electronic exchange energy with laser pulses

The experimental capabilities described in the previous chapter 3 have the potential to provide new insights into atomic and molecular dynamics. In a first research application, the focus is set on the mediators of fundamental chemistry: The electrons that are the structural glue for atoms within molecules. The interactions between electrons play a crucial role in the paired electrons of a covalent bond. An electron–electron interaction can be split into a classical charge-based repulsion part (also called *direct* Coulomb interaction) and a purely quantum-mechanical one. The latter is named *exchange* interaction and is at the heart of Pauli's principle. A theoretical approach to exchange interaction is presented in the theory section 2.2.3.

In this chapter, a theoretical model for the manipulation of the effective electronic exchange energy within a molecule is developed and experimentally demonstrated. First, section 4.1 will shortly review theoretical approaches to describe electron-mediated chemical bonding and give an overview of established experimental techniques for controlling chemistry with lasers. Furthermore, a theoretical model system is developed to target the exchange energy. Afterwards, section 4.2 covers the experimental realization of exchange-energy control in the molecule sulfur hexafluoride. The data analysis is outlined after describing the experimental parameters and the measurement itself. This comprises the raw data analysis, the subsequent fit procedure of the data and the comparison of the experimental observations with the theoretical toy model. In addition, the effective electronic exchange energy is extracted from the data by utilizing a reduced theoretical model. Finally, the findings are verified by a full quantum-mechanical *ab-initio* simulation. Section 4.3 highlights the opportunities of this approach for laser-based precision control of chemistry on the quantum level as an outlook.

The main results of this chapter are published in *Physical Review Letters* [1].

4.1. Laser control of chemistry

In the following, a short overview of approaches to control chemistry with laser radiation is given. First, a historical perspective on the theoretical description of the covalent bond and its electronic character is presented in section 4.1.1. Such a theoretical description and understanding is the basis for experimental techniques that target the control of chemical dynamics via electronic properties. The state-of-the-art of corresponding experimental schemes for laser control is discussed in the subsequent section 4.1.2. This is followed by the development of a theoretical toy model that enables exchange-energy control in section 4.1.3.

4.1.1. A short history of covalent bonds

Electronic interactions represent the foundation of chemistry and biology. These interactions are not only involved when forming electron pairs within a covalent bond, but also on a larger scale. For example, the folding mechanism of proteins is impacted by complex multi-electron-mediated interactions [292, 293]. The description of covalent bonds was pioneered among others by the Nobel-prize-winning works of Pauling [294] and Mulliken [295], culminating in the description of molecular orbitals as a linear combination of atomic orbitals. In a multi-electron system, the Coulomb-based electron–electron interaction is given by the direct repulsion and the exchange interaction as shown in section 2.2.3 in the theory chapter. For two charged particles that are far apart, the product $|\psi_1(\vec{r})\,\psi_2(\vec{r})|$ of their respective wave functions is much smaller than the absolute square $|\psi_{1/2}(\vec{r})|^2$. Hence, the direct Coulomb repulsion is much larger compared to the exchange interaction, allowing for a classical description. On the atomic scale, however, the exchange and direct Coulomb interactions are on the same order of magnitude. This necessitates to include quantum effects for an accurate description of the problem.
Very successful approaches for describing the electronic properties of multi-electron systems such as molecules are Hartree-Fock-based (HF) methods [296–298] or density functional theory (DFT) [299, 300]. Within the HF approximation, the Coulomb interaction between all electrons is replaced by an effective (mean-field) potential in which each electron propagates. As a result, one can express the multi-electron state as a single anti-symmetric product of one-particle states. Although in many cases highly successful, this picture of strictly filled highest occupied and completely empty lowest unoccupied molecular orbitals (HOMO/LUMO) is not sufficient to

describe every many-electron quantum state correctly. Due to Coulomb interactions, electrons from two occupied orbitals can scatter into two unoccupied ones, resulting in a different electronic configuration. To take this into consideration, many-body quantum eigenstates are expressed as linear superpositions of different electron configurations which interact via the Coulomb forces between the electrons. Configuration interaction (CI) approaches [301–304] tackle this problem by using the linear combination $\sum_i^N c_i \, \phi_i$ of N configurations ϕ_i with variational parameters c_i. Alternatively, one can keep the restriction to a single configuration and modify the effective interaction strength such that the correct dynamics and expectation values of the full system are predicted. This is an analogueto renormalization group theory [305], in which effective interactions between a set of relevant states provide a full description of the system's dynamics.

4.1.2. Manipulating molecules on the electronic level

These theoretical approaches are put to a test by advances in experimental techniques. In experiments, the coherent light emitted from lasers represents an ideal tool to measure and control chemical properties and dynamics on the electronic level: The development of techniques to resolve the dynamics of chemical reactions with femtosecond temporal resolution by using laser pulses founded the field of *femtochemistry* [306] and was recognized with the Nobel prize in chemistry in 1999 [307]. Besides the mere observation, a targeted control of reaction pathways by manipulating the collisions of the reagents is possible [308]. In general, the laser fields interact with charged particles via the electromagnetic interaction. Due to the respective masses and energies, the direct interaction of a photon with the nuclei in an atom or molecule can be mostly neglected and the influence of the electrons is dominant [68]. This enables to observe and manipulate molecular dynamics by targeting the electronic structure. First steps in this direction were conducted by investigating diatomic molecules [309–311]. Soon afterwards, studies on molecules that involve three or more atoms were initiated [312–314]. This culminated in time-resolved techniques that unravel the dynamics in large and complex biologically relevant molecules involved in the photosynthesis process [315, 316]. A further scaling of complexity is achieved in solid-state materials, where macroscopic phenomena can be manipulated with laser pulses. Examples of the alteration of strongly-correlated effects comprise the ultrafast control of magnetism [317, 318] and transient laser-induced superconductivity [319]. The available laser-based control schemes rely on a considerable population/charge transfer [320] or on ionization [321]. Alternatively, laser-control techniques are medi-

ated by dynamics that comprise the nuclei, such as vibrations [310], rotations [314] or couplings of different sites within a lattice of a solid-state material [317–319, 322]. Without these mediators, altering directly the fundamental electronic structure of neutral molecules has remained elusive so far.

4.1.3. Toy model for exchange energy control

In the following, the experimental observable that grants access to electronic exchange—the absorbance area branching ratio—is discussed. Subsequently, an ideal physical system is developed on a theoretical basis to achieve the goal of electronic structure manipulation on the fundamental quantum level.

4.1.3.1. Branching ratios in XAS

A key to the direct electronic control is the purely quantum-mechanical part of the Coulomb interaction: the exchange energy which is introduced in the theory section 2.2.3.
A first inspiration for accessing the electronic exchange is drawn from literature about spectroscopic experiments on correlated solid-state systems: In photoelectron spectroscopy (PES), the relative photoelectron yield from spin-orbit-split core levels coincides with the multiplicity factor which is deducted from Pauli's exclusion principle [323]. According to this statistical ratio, the relative signal strengths $S(j_\pm)$ of the single peaks within a spin-orbit-split resonance doublet is given by the square of the multiplicity factor $\mu_\pm$, with

$$\mu_\pm = \sqrt{2j_\pm + 1}\ . \tag{4.1}$$

The multiplicity factor is linked to the degeneracies of the spin-orbit-split wavefunctions $\psi_{c_\pm}$. As an example, one can look at a p-orbital ($l = 1$) with

$$j_\pm = |l \pm s| = |1 \pm 1/2| = \{3/2, 1/2\} \tag{4.2}$$

and in consequence with $\mu_\pm \in \{2, \sqrt{2}\}$. Therefore, the signal strength S of the j_+ level is expected to be twice as strong as the one from j_-. This can be intuitively understood by comparing the number of degeneracy of j_+ with $m_{j_+} \in \{-3/2, -1/2, 1/2, 3/2\}$ to the one of j_- with $m_{j_-} \in \{-1/2, 1/2\}$.
The multiplicity-induced statistical ratio, however, is violated in x-ray absorption spectroscopy measurements of certain solid-state materials [324, 325]. In XAS, the

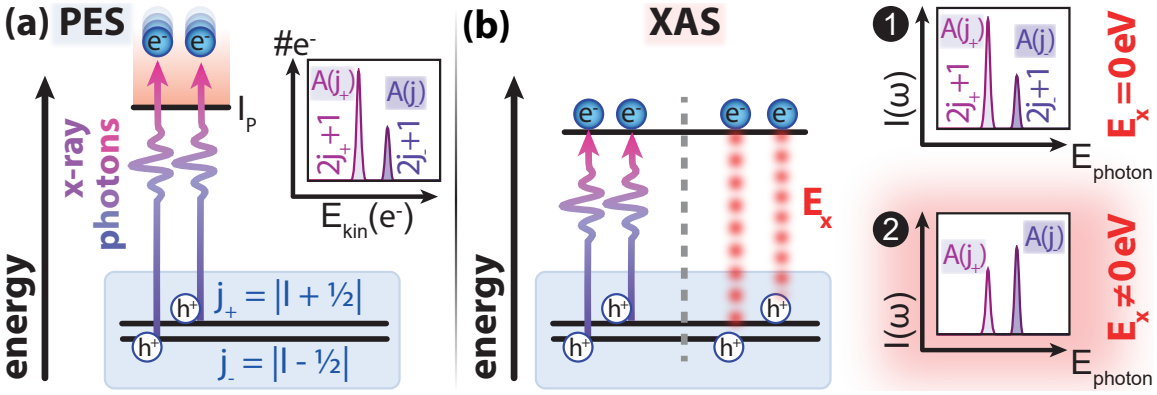

Figure 4.1.: Illustration of branching ratios in photoelectron and x-ray absorption spectroscopy (PES/XAS). **(a)** In PES, electrons (e^-) are ejected from a spin-orbit-split orbital ($j_\pm$) into the continuum above the ionization potential I_P by x-ray photons. Subsequently, the photoelectron yield over kinetic energy of the photoelectrons is measured as shown in the inset. In PES, the area ratio is equal to the statistical one. **(b)** In XAS, no photoelectrons are required for the measurement. Thus, bound excited states can be populated, leaving electron vacancies (holes, h^+) in the spin-orbit-split orbital. Now, these excited electrons can experience exchange interaction with the remaining electrons in the core orbital [326]. If no such exchange energy E_x is present, the measured absorption signal $I(\omega)$ equals the statistical ratio (inset 1) as in PES, otherwise, it differs considerably (inset 2).

experimental observable and thus "signal" is the oscillator strength of a transition (compare section 2.4.5 in the theory chapter). The relative ratio of the two signals within a spin-orbit-split doublet structure is called *branching ratio* R in the following. A comparison of the branching ratio in PES and XAS is illustrated in figure 4.1. Deviations of the experimentally determined branching ratio from the statistical value triggered theoretical works, e.g., of Onodera and Toyozawa [327]: By modeling the resulting core-hole–excited-electron exciton of $p^6 \rightarrow p^5 s^1$ transitions in alkali halides with an effective mass approach, they were able to find an analytical expression for the oscillator strength ratio and the measured peak splitting (distance of the fitted peak maxima). Figure 4.2 summarizes the results of their work. Here, the branching ratio is highly dependent on the relative strength of the electronic exchange in comparison to the spin-orbit coupling. The peak splitting, however, remains rather constant for $0 \leq E_x \leq E_{so}$. Three cases are distinguished: In the first case, for electronically uncorrelated systems ($E_x = 0$), the spin and the orbit of each electron couples first. This is the regime of jj-coupling as described in section 2.3.2. Here, the branching ratio is equal to the statistical value (compare figure 4.1(b) case 2). In the second case, the electron–electron interaction becomes comparable in magnitude to the spin-orbit-splitting ($E_x \approx E_{so}$). Hence, the jj-coupling breaks down and a transition to the LS-coupling regime is observed, in which the spins and orbits of all electrons couple

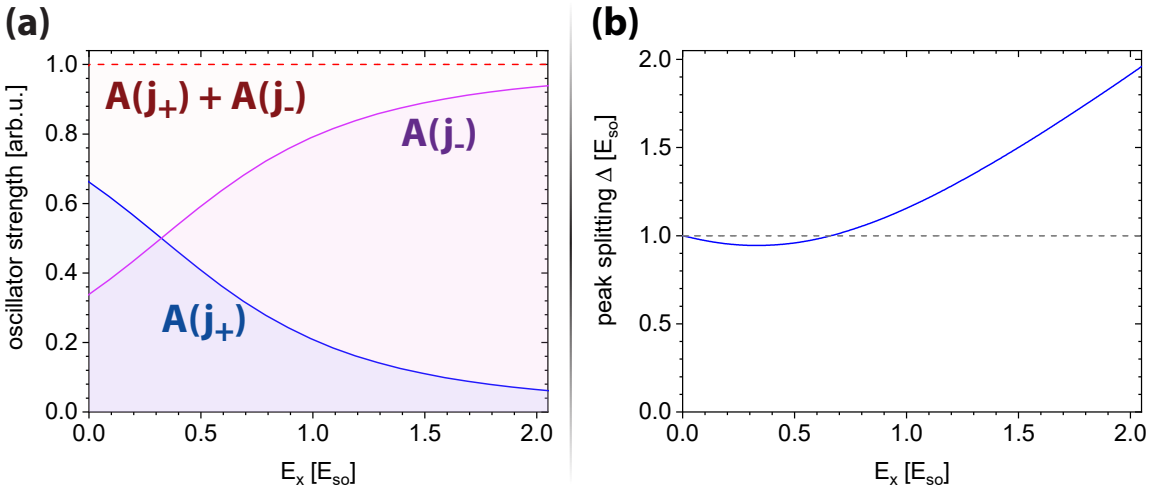

Figure 4.2.: Theoretical approach to spin-orbit-split absorbance doublet resonances in alkali halides by Onodera and Toyozawa [327]. The observables in XAS, oscillator strength and peak splitting, are shown in respect to the electronic exchange energy E_x in units of the spin-orbit splitting E_{so}. **(a)** Oscillator strengths of the j_+ ($A(j_+)$ in blue) and the j_- ($A(j_-)$ in purple) absorbance peak, and the overall doublet ($A(j_+) + A(j_-)$ in red). **(b)** Peak splitting within the absorbance doublet. A constant value of $\Delta = E_{so}$ is indicated as a dashed line.

to a total spin and orbit. For $L_{2,3}$-edge transitions, the oscillator strength of the j_+ peak decreases, whereas the one of the j_- peak increases. Finally, for the extreme case of fully dominating inter-electronic interaction ($E_x \gg E_{so}$, pure LS-coupling), the j_+ peak is fully suppressed, while the j_- peak now contains the whole absorbance area of the doublet resonance, $A(j_-) = A_{doublet}$. Notably, the overall oscillator strength of the spin-orbit split doublet is not affected by the jj- to LS-coupling transition.
This sensitivity of XAS to electron–electron interactions has led to its extensive use in research on solid-state materials by analyzing branching ratios in the static x-ray absorbance spectra [72]. Such investigations are usually conducted at synchrotron facilities with high-resolution spectrometers [73, 217].

4.1.3.2. Physical toy model

While the branching-ratio-analysis approaches have led to fundamental insights into strongly correlated condensed matter so far, the question has remained unaddressed whether and how one can transiently manipulate the electronic exchange interaction. A general exchange-control scheme should not be limited to complex solid-state systems, though, but should be realizable in comparably simple atoms or molecules as well. As a starting point to address this research question, a theoretical toy model is constructed in the following. The aim is the most basic model that describes the

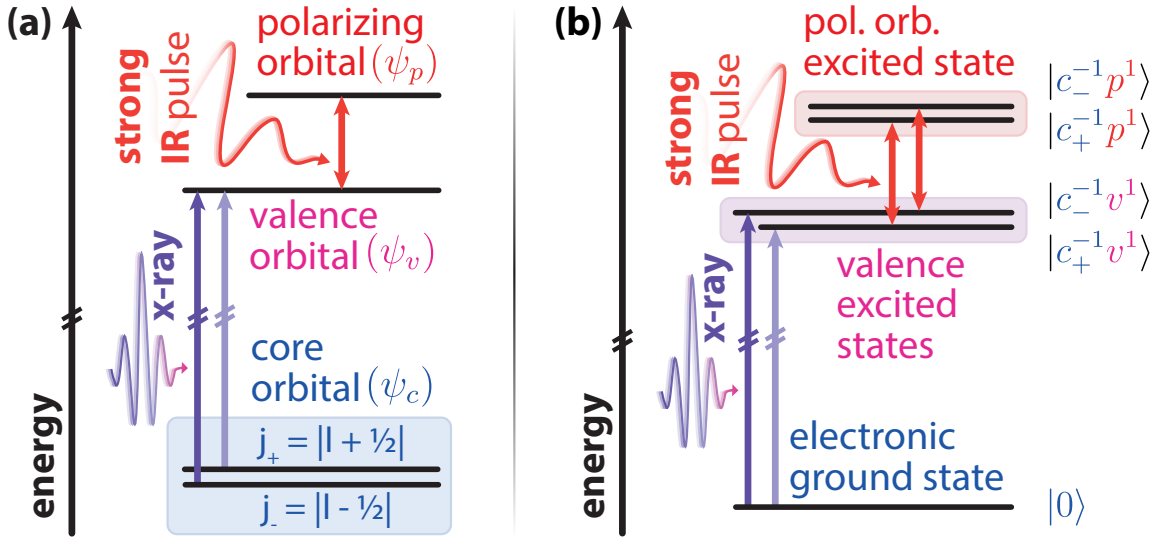

Figure 4.3.: Electronic level scheme and control/probing approach for exchange-energy alteration. **(a)** Level scheme in the single-active electron picture with the spin-orbit-split core orbtial ψ_c, the valence orbital ψ_v and the polarizing orbital ψ_p. By design, the core and valence orbital can be dipole-coupled as well as the valence and the polarizing orbital. **(b)** Level scheme in the many-body electronic state picture. Here, the electronic many-body ground state is denoted by $|0\rangle$ and the spin-orbit-split character transfers to the valence- and polarizing-orbital-excited states, $\left|c_\pm^{-1}v^1\right\rangle$ and $\left|c_\pm^{-1}p^1\right\rangle$, respectively.

manipulation and quantification of the electronic exchange interaction.

The resulting theoretical description of such a system to control the effective exchange energy is shown in figure 4.3. To clearly distinguish the single-electron picture in figure 4.3(a) from the many-body representation in figure 4.3(b) in the following, the terminology *orbital* is only used in the single-body description, whereas *electronic state* is reserved for the many-electron picture. As shown in the orbital scheme 4.3(a), the minimal system consists of four orbitals: A pair of spin-orbit-split core orbitals $\psi_c(j_\pm)$, a valence orbital ψ_v and a polarizing orbital ψ_p. The orbital symmetries and quantum numbers are chosen such, that a dipole transition from the core orbitals to the valence orbital is possible. The respective transition energies are typically in the x-ray regime. Furthermore, the valence and polarizing orbital can be dipole-coupled with each other. Here, the photon energy will be typically in the visible to infrared spectral region. The multi-electron states in 4.3(b) are deducted from the single-electron orbitals. In the following, without restriction of generality, a molecular system is chosen for clarity. If the system is in the electronic ground state $|0\rangle$, all orbitals are filled to the molecular Fermi edge, or in other words up to the HOMO. Of course, the single-electron scheme 4.3(a) does not include all molecular orbitals, but only the relevant ones for the

considered exchange-interaction control. The valence orbital ψ_v corresponds to the LUMO. Beside the ground state, four excited states are crucial: The first two excited states are created by promoting an electron from the spin-orbit-split core orbital to the valence orbital resulting in a populated ψ_v^1. Hence, these many-body states are denoted as $\left|c_{\pm}^{-1}v^1\right\rangle$. Secondly, an IR pulse can promote the already excited valence electron to the polarizing orbital $\left(\psi_p^1\right)$, resulting in $\left|c_{\pm}^{-1}p^1\right\rangle$. Notably, all these excited states exhibit an electron vacancy in the core orbital $\left(\psi_{c_{\pm}}^{-1}\right)$, commonly referred to as a *core hole*. These many-body states form the basis of a Hamiltonian matrix H that describes this physical system,

$$H = \begin{array}{c} \begin{array}{ccccc} |0\rangle & |c_+^{-1}v^1\rangle & |c_-^{-1}v^1\rangle & |c_+^{-1}p^1\rangle & |c_-^{-1}p^1\rangle \end{array} \\ \begin{pmatrix} 0 & \mu_+ d\mathcal{E} & \mu_- d\mathcal{E} & 0 & 0 \\ \mu_+ d\mathcal{E} & E_+ & \boldsymbol{E_x} & d'\mathcal{E}' & 0 \\ \mu_- d\mathcal{E} & \boldsymbol{E_x} & E_- & 0 & d'\mathcal{E}' \\ 0 & d'\mathcal{E}' & 0 & E'_+ & \boldsymbol{E'_x} \\ 0 & 0 & d'\mathcal{E}' & \boldsymbol{E'_x} & E'_- \end{pmatrix} \end{array}. \tag{4.3}$$

The header row above H shows the many-body states that form the basis set. The blue 3×3 submatrix describes the model in absence of the polarizing orbital and is thus equivalent to the unperturbed (*static*) case which is typically subject of investigations in synchrotron measurements (see section 4.1.3.1). The $\mu_{\pm}$ is the multiplicity factor as given in equation (4.1). The energy expectation values of the respective valence-populated many-body states $\left|c_{\pm}^{-1}v^1\right\rangle$ are given by $E_{\pm}$. A transition to these states from the ground state is realized by the product of the dipole moment d with the x-ray electric field $\mathcal{E}$ and weighted by $\mu_{\pm}$. The exchange interaction between the two excited electronic configurations $\left|c_{\pm}^{-1}v^1\right\rangle$ is given by E_x. By adding the two excited states $\left|c_{\pm}^{-1}p^1\right\rangle$, additional energy expectation values $E'_{\pm}$ need to be included in H (in the violet 2×2 submatrix). Moreover, the populated-polarized-orbital states $\left|c_{\pm}^{-1}p^1\right\rangle$ can interact with each other via E'_x. To couple the static-case system (blue 3×3 submatrix in equation (4.3)) with the polarizing orbital extension (violet 2×2 submatrix), the off-diagonal matrix elements $d'\mathcal{E}'$ are introduced. By design, these matrix elements can only couple $\left|c_+^{-1}v^1\right\rangle \leftrightarrow \left|c_+^{-1}p^1\right\rangle$ and $\left|c_-^{-1}v^1\right\rangle \leftrightarrow \left|c_-^{-1}p^1\right\rangle$ due to dipole selection rules. The electric field $\mathcal{E}'$ represents the strong IR pulse in figure 4.3(b).

If the lifetime of the core-hole-excited states is much shorter than the duration of the strong IR pulse $\mathcal{E}'$, no time-dependence is required in H. Due to the absence of an explicit time-dependency in the matrix elements of H, the peak center positions and

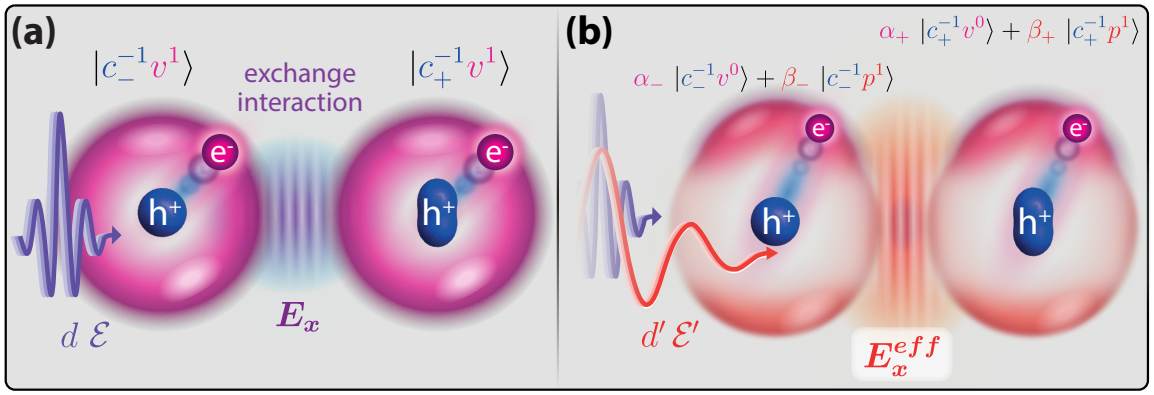

Figure 4.4.: General mechanism of exchange-energy control utilizing the toy-model described by the Hamiltonian matrix in equation (4.3). **(a)** The two final electronic configurations $\left|c_\pm^{-1}v^1\right\rangle$ induced by the x-ray field $\mathcal{E}$. **(b)** The two final mixed electronic states induced by an additional IR field $\mathcal{E}'$ in temporal overlap with the x-ray field $\mathcal{E}$. This results in an effective exchange energy E_x^{eff} of the mixed states. The mixed states and their notation are described in section 4.2.4 in more detail.

oscillator strengths can be extracted via an adiabatic approach and without solving the time-dependent Schrödinger equation. Instead, one determines the eigenvalues of the Hamiltonian matrix at a vanishing probe field $H|_{\mathcal{E}=0}$. Now, by expressing the full matrix $H|_{\mathcal{E}\neq 0}$ in the basis of the respective eigenvectors, the off-diagonal elements are determined [328]. The square of the largest two off-diagonal values corresponds to the oscillator strengths of the resonance's doublet peaks. The two eigenvalues that belong to these two off-diagonal elements are the resonance energies of the doublet lines. Thus, their difference is the measure of the peak splitting Δ. This mathematical extraction mechanism for the oscillator strengths $A(j_\pm)$ and the peak splitting Δ is also graphically illustrated in figure 4.13 in the data analysis section.

In absence of electronic exchange, $E_x = E_x' = 0\,\text{eV}$, the oscillator strength ratio is given by $R = \mu_+^2/\mu_-^2$. For non-vanishing exchange coupling $E_x \neq 0\,\text{eV}$, however, R will differ from the statistical ratio of the static case. In addition, a strong IR field $\mathcal{E}'$ will lead to a further alteration of R. This is due to the dipole coupling to the polarizing orbital. Consequently, in the case of $E_x \neq 0\,\text{eV}$ and $\left|\mathcal{E}'\right| \gg 0$, the core hole (and thus the remaining core-orbital electrons) partially overlaps with the initially (absent IR) dipole-inaccessible polarizing orbital. In general, the valence and the polarizing orbital have different exchange energies $E_x \neq E_x'$. This orbital-mixing approach is illustrated in figure 4.4. Therefore, the overall exchange energy of the remaining electrons in the core orbital ψ_c with the excited electron will be different as well for $\left|\mathcal{E}'\right| \gg 0$.

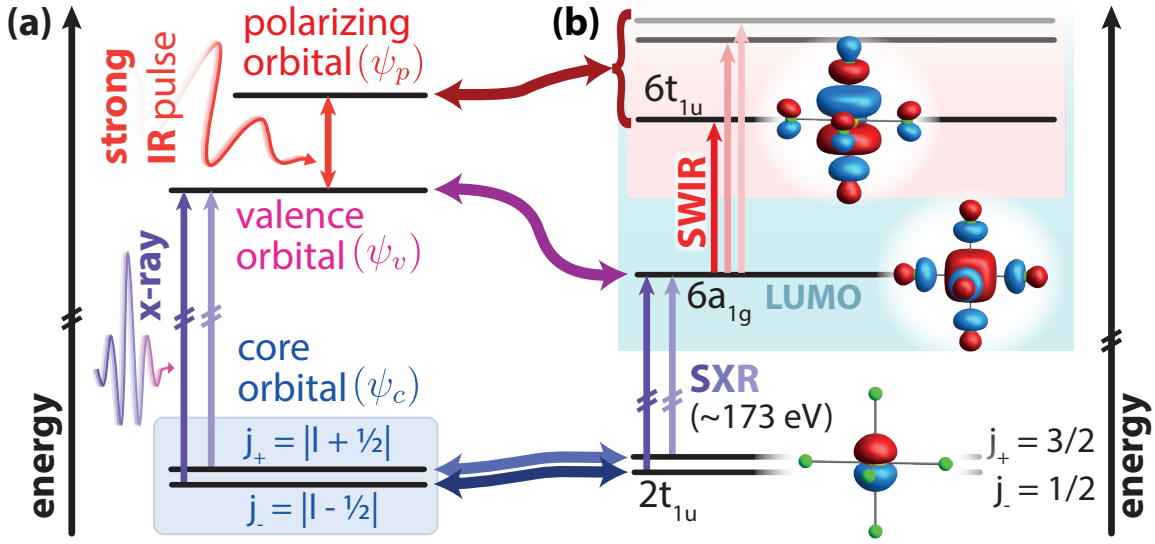

Figure 4.5.: Comparison of **(a)** the single-electron level schemes of the toy model for exchange control (compare figure 4.3) with **(b)** the respective molecular orbitals of SF_6 (compare figure 2.11). Here, the $2t_{1u}$ is identified with the core orbital, the LUMO $6a_{1g}$ acts as the valence orbital and a manifold of *ungerade* unoccupied states represents the polarizing orbital. The isosurfaces of the respective MOs in SF_6 are given as well.

4.2. Experimental investigation of exchange energy in SF_6 with XAS

The basic model sketched in figure 4.3 defines the requirements of a physical system to exhibit electronic-exchange controllability. As shown in the following section, these electronic-structure conditions are fulfilled by the sulfur-hexafluoride molecule. Consequently, the toy model is put to a test in a XAS experiment on SF_6 molecules.

4.2.1. SF_6 as molecular candidate for exchange-energy control

Within the electronic structure of the SF_6 molecule, orbitals can be identified that match the demands of the toy model of section 4.1.3. Figure 4.5 links suitable orbitals in SF_6 with the orbitals of the toy model: Here, the $2t_{1u}$ MO with sulfur $2p$ core-level character resembles the spin-orbit-split $\psi_{c_\pm}$ orbital. The valence orbital ψ_v is realized by the LUMO $6a_{1g}$. Due to the $6a_{1g}$ being an inner-well MO [101, 329, 330] within the double-well potential of SF_6, it is spatially relatively compact and thus has a significant Coulomb overlap with the core-level $2t_{1u}$ orbital. A manifold of unoccupied states LUMO+n with ungerade symmetry (e.g., mt_{1u} with $m \geq 6$) form the effective polarizing orbital ψ_p. The static $6a_{1g}$ spin-orbit-split absorbance peaks have each

a width of around 1 eV [101]. Thus, their approximate lifetime [77] can be derived from the resonance's spectral width via the time-frequency Fourier relation to be roughly 1 fs. This calculated value, however, underestimates the lifetime due to spectral-broadening factors like unresolved vibrational structures [101, 331] that are specific to the molecule. Nevertheless, realistic lifetimes of core-level excited states are on the same order of magnitude—on the few-femtosecond level [332, 333]—due to Auger-Meitner decay. The influence of electronic exchange within SF_6 is already obvious from the static absorbance: the relative oscillator-strength ratio within the $6a_{1g}$ doublet, $R = {}^{A_{j+}}/_{A_{j-}} \approx {}^{1}/_{2}$, significantly deviates from the statistical ratio $R = {}^{2}/_{1}$ (compare figure 2.11(b) in the theory chapter.
Overall, the SF_6 molecule with its electronic structure and short core-hole lifetime represents an ideal candidate for investigations into exchange-interaction control.

4.2.2. XAS of SF_6 – the experiment

Now, the approach of exchange energy control described in chapter 4.1 is realized experimentally by employing XAS of SF_6. Here, the relatively weak probing field $\mathcal{E}$ in the x-ray region is generated via HHG, whereas the strong, orbital-mixing field $\mathcal{E}'$ originates from the residual SWIR pulses after the HHG process. Both phase-locked pulses are focused into a gaseous SF_6 target inside the vacuum beamline with a tunable SWIR pulse intensity. The experimental parameters are presented in the following section 4.2.2.1.

4.2.2.1. Parameters of the optical setup and beamline

The SWIR pulses which are used for the experiment originate from the laser system that is described in chapter 3.2. Here, the OPA output is spectrally broadened in the SF-HCF with an inlet pressure of 200 mbar of Ar. The resulting pulses with a center wavelength of $\lambda_{SWIR} = 1535$ nm are compressed by propagating through 1 mm of additional fused silica. This results in a measured pulse FWHM duration of $\tau_{FWHM} = 15$ fs, equal to sub-three optical cycles. The retrieved pulse intensity envelope from the TG-FROG measurement is presented in figure 4.6. Pulses with an energy of $E_{SWIR} = 1$ mJ are focused into the HHG cell of the vacuum beamline. As the SWIR-pulse intensity in the SF_6 target volume acts as the control knob for exchange-energy manipulation, the experiment is performed in the intensity-scan XAS configuration of the beamline as described in section 3.3.3.

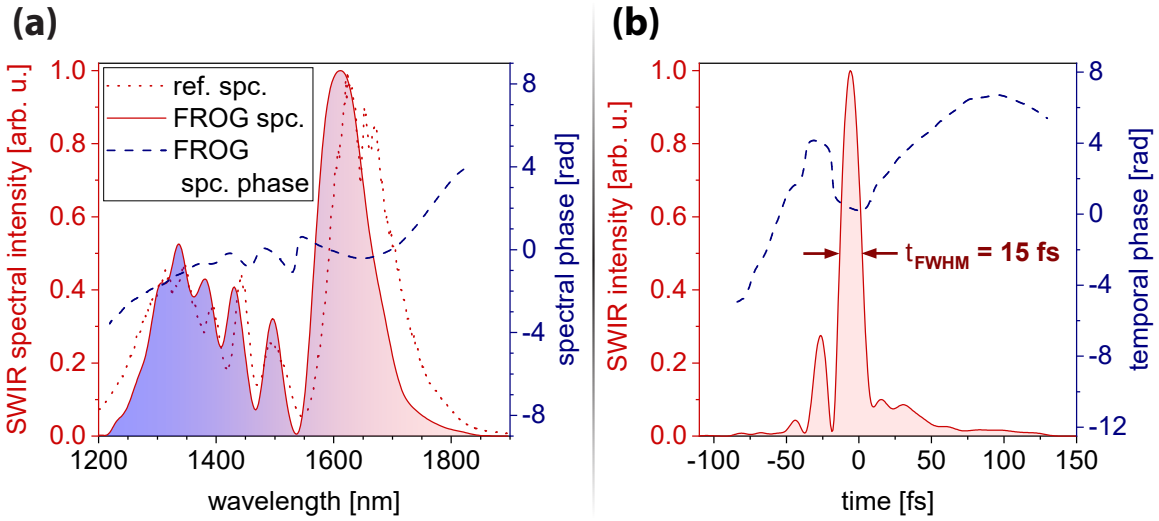

Figure 4.6.: SWIR pulse characterization. **(a)** Measured (red dotted line) and FROG-retrieved (solid red line) SWIR spectrum, as well as FROG-retrieved spectral phase (blue dashed line). The broadened spectrum is centered around λ_c = 1535 nm. **(b)** Retrieved time-domain SWIR intensity (red solid line) and phase (blue dashed line) from the TG-FROG measurement.

4.2.2.2. SWIR intensity calibration

The SWIR-intensity scan scheme of the beamline is realized by cutting the SWIR beam mode while making use of the different divergences of the SXR and SWIR beams. As the SWIR-intensity manipulation is conducted in-vacuum by constraining the beam mode with a motorized aperture, the aperture opening has to be linked to an SWIR peak intensity in the target. Section 2.1.2.1 in the theory chapter approaches this issue by utilizing Gaussian beam propagation in combination with aperture-induced diffraction. These considerations result in equation (2.6) for calculating the peak-intensity value. One of the main input parameters in this formula is the $1/e^2$-diameter of the SWIR beam before focusing. This parameter is indirectly determined via nonlinear two-photon absorption [177] of the collimated beam on a silicon CMOS chip. The measured beam mode is shown in figure 4.7 in combination with the corresponding axes' projections and the calculated linear absorption beam mode. Based on these measurements, a collimated, round Gaussian beam with a $1/e^2$-diameter of d = 15.8 mm is approximated in the following. Using the input parameters[1] of the SWIR beam and Gaussian beam propagation, a focus diameter of 124 µm is calculated. The assumption of a perfect Gaussian beam, however, does not take any astigmatism into account that is introduced by the non-collinear mirror-based focusing and other beam-quality

[1] These parameters are: SWIR center wavelength λ_c = 1535 nm, $1/e^2$-diameter of d = 15.8 mm and d = 1 m focal distance.

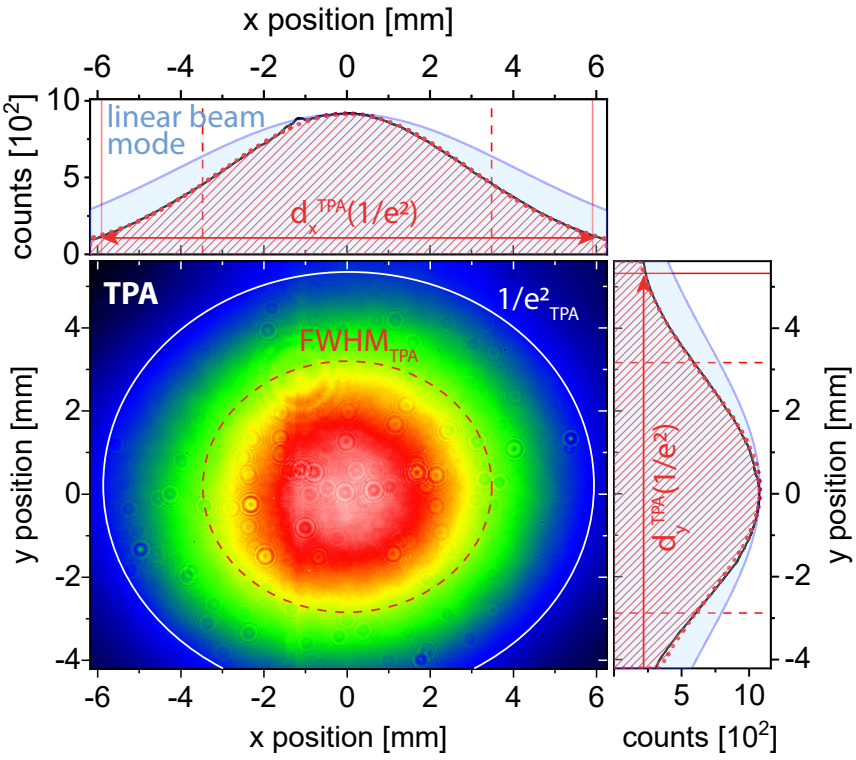

Figure 4.7.: Nonlinear measurement of the collimated SWIR beam mode before focusing into the vacuum beamline. The measurement is conducted via TPA in a silicon CMOS chip. The projections on the x- and y-axis are given (black solid lines) in combination with a Gaussian fit (red dotted line) and the respectively reconstructed linear beam mode projection (blue solid line). The beam diameters in FWHM and $^1/_{e^2}$ metric are given. An averaged linear $^1/_{e^2}$ beam diameter of d = 15.8 mm is reconstructed from the TPA diameters d_x^{TPA} = 11.8 mm and d_x^{TPA} = 10.5 mm.

reducing aspects. Thus, an additional approach to determine the SWIR focus diameter is conducted for calculating the correct maximum peak intensity in the target. This measurement is realized by a z-scan of an in-vacuum silicon-based CMOS chip as beam profiler at the target position (see figure B.13 in the appendix). This results in focus diameters of d_x^{foc} = 196 µm and d_y^{foc} = 161 µm, averaging to d^{foc} = 179 µm. As a result, the measured focus is a factor of ≈ 1.4 larger compared to calculation based on a perfect Gaussian beam. The temporal pulse structure of the SWIR intensity envelope is considered in the final step of the peak-intensity calculation. From the temporal retrieval of the few-cycle pulse (see figure 4.6), a peak power of around 58 GW is extracted. This results in a peak intensity of 4.6×10^{14} W/cm^2 in the HHG cell by taking d^{foc} into account. Considering the losses between beamline input and the target cell focus by a transmission of 60% for the SWIR pulses, this results in a maximum peak intensity in the target cell of I_{max} = 2.7×10^{14} W/cm^2. With

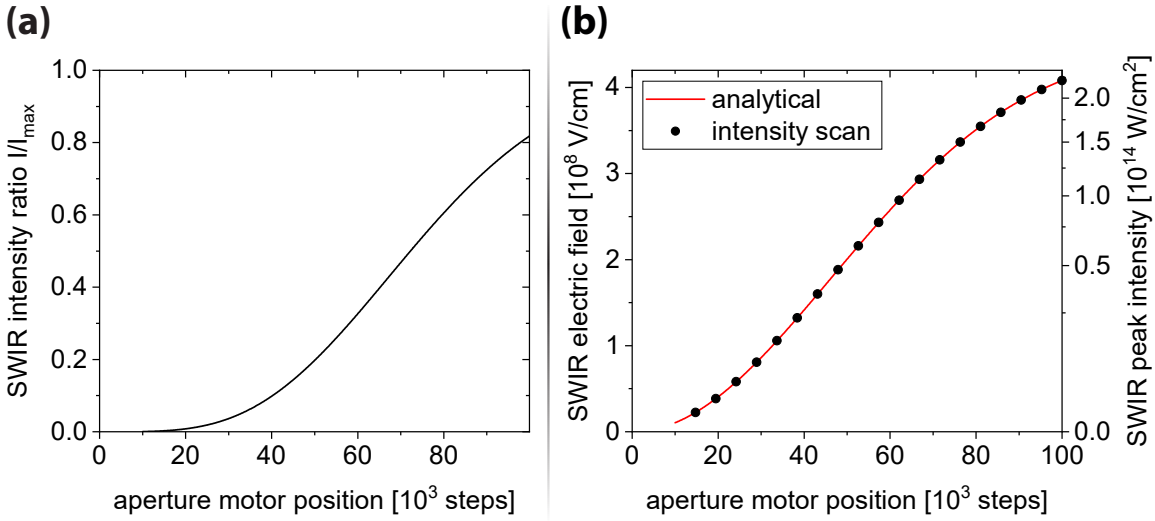

Figure 4.8.: Mapping of the aperture motor position to the corresponding SWIR electric field/peak intensity in the target cell. **(a)** Intensity ratio in respect to unconstrained maximum peak intensity I_{max} in the target cell according to equation (2.6) in the theory chapter. **(b)** Mapping of aperture position to electric field (left y-axis)/intensity (right y-axis). The analytically derived mapping is shown (red line) in combination with the aperture motor positions employed during the intensity scan (black dots).

equation (2.6), the peak-intensity dependence on the aperture opening[2] is calculated as visualized in figure 4.8(a). Figure 4.8(b) shows the resulting aperture-to-intensity mapping.

4.2.2.3. XAS measurement parameters

In the intensity-scan configuration of the experimental setup, the SXR and SWIR beams remain intrinsically phase-locked and see identical optical elements during copropagation in the beamline, guaranteeing spatial and temporal overlap in the target cell. Thus, no further pulse-overlap verification is required. The scan variable in the experiment and thus only physically moving component is the motorized aperture. Neon is used as HHG gas with a backing pressure of 590 mbar to generate SXR pulses. Multiple experimental parameters like laser-power and -pointing as well as HHG/target-gas backing pressures are logged to ensure a stable operation over the entire duration of the measurement. The experimental observable is the SXR spectrum which is recorded in form of binned lines on the spectrometer CCD.

[2]The aperture is located 90 cm away from the HHG source point. Therefore, the SWIR beam diameter is 14.2 mm at this position. The aperture diameter is scanned from a minimum of 2.2 mm up to 21.8 mm. Here, the aperture diameter depends in a linear manner on the aperture motor position [334].

Here, the intrinsic hardware-binning feature of the CCD drastically improves the signal-to-noise ration (SNR) in comparison to a software-based spectral binning of the full-chip images during the data analysis. As the CCD read-out speed is much slower than the 1 kHz repetition rate of the laser and the required integration times for HHG spectra are >1s, the CCD acquisition is free-running and integrates over many laser shots. The measurement procedure consists of multiple parts: First, the SWIR pulse is thoroughly characterized in front of the beamline, followed by an SXR-only reference measurement without target gas. An integration time of 30 s proved to be optimal in this case. This reference acquisition is conducted with the same intensity-scan routine as the main measurement to take a potential impact of the closing aperture on the SXR beam into consideration. Secondly, the intensity scan in SF_6 itself is conducted. Therefore, the target cell is supplied with a backing pressure of 16 mbar of SF_6 gas. This is a compromise between clearest resonance signature (and thus highest target density and absorption) and still useful number of detected photons within the integration time. The 19 equally-spaced aperture positions are cycled nine times to account for systematic drifts which might occur over the measurement duration of 13 hours. At each aperture position, 50 spectra with an integration time of 50 s each are acquired[3]. Afterwards, another SXR reference is measured to ensure that the SXR spectrum itself did not change considerably. In addition, dark images with a shuttered SWIR beam are taken for both integration times of the HHG reference and the intensity scan, 30 s and 50 s, respectively. Moreover, an SF_6 absorption spectrum with fully-blocked SWIR beam after the HHG cell (*static* spectrum) is recorded for comparison with synchrotron-based measurements (see figure 2.11(b) in the theory chapter). Finally, the same SWIR beam characterization as in the first procedure step is repeated to confirm drift-free laser properties over the duration of the XAS measurement.

4.2.3. XAS data analysis

To obtain the SXR spectra which comprise insights about the exchange-energy tuning in SF_6 molecules, several analysis steps are necessary and explained in the following.

[3]The off-resonant absorption of SF_6 around 200 eV caused the significantly longer integration time compared to the HHG reference. Hence, the integration time of the HHG reference had to be reduced to avoid saturation of the CCD.

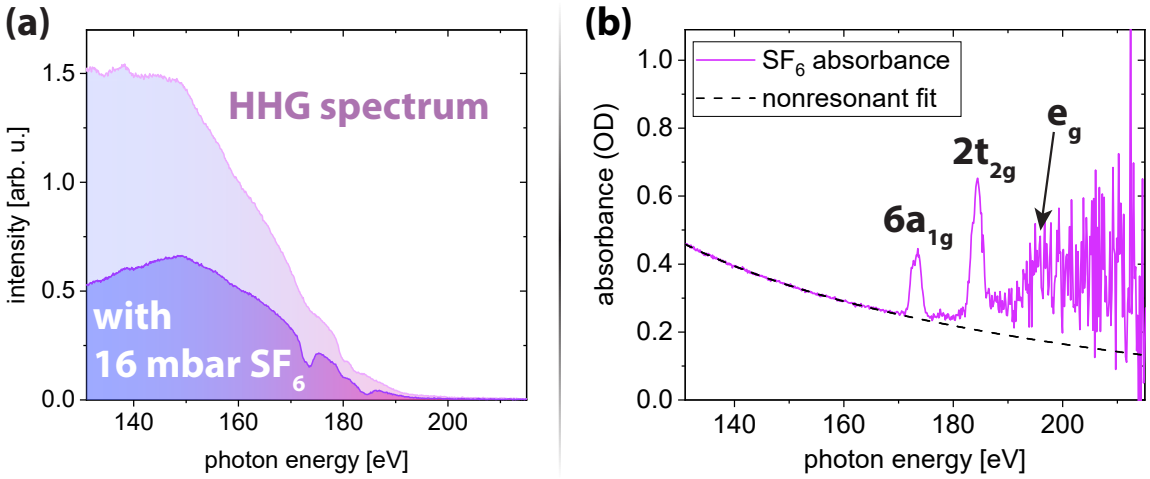

Figure 4.9.: Exemplary HHG spectrum around 200 eV and SF_6 absorbance. **(a)** HHG spectrum driven by 1535 nm SWIR pulses in neon with and without SF_6 gas in the target cell. **(b)** Corresponding static SF_6 absorbance. The off-resonant background (dashed line) is indicated. The corresponding $L_{2,3}$-edge absorbances are indicated as shown in the synchrotron-based measurement in figure 2.11(b) in the theory chapter.

4.2.3.1. XAS raw data analysis

First, the reference and intensity-scan spectra are dark-image corrected. Afterwards, the spectra are normalized to the off-resonant absorption in the < 170 eV photon-energy region for each aperture position. Then, the intensity-scan spectra and the HHG-reference spectra are each averaged per aperture position and used to calculate the absorbance according to equation (2.48) in the theory chapter. Figure 4.9 shows an exemplary HHG and static spectrum as well as the resulting absorbance of SF_6. Comparing the measured static SF_6 absorbance around the $L_{2,3}$-edge with spectra from the literature (see figure 2.11(b) in the theory chapter), the $6a_{1g}$ and $2t_{2g}$ doublet resonances are identified. Their known energies [101] are used for the spectrometer calibration (compare section B.2.2 in the appendix). The e_g resonance around 196 eV is barely visible due to the low SXR-photon statistics in this spectral region.

4.2.3.2. Fit procedure

The data analysis focuses on the S $2p \rightarrow$LUMO transition and thus the $6a_{1g}$ absorption doublet as depicted in figure 4.10 for demonstrating exchange-interaction control. The global off-resonant background of the absorbance is fitted for each intensity step with a third-order polynomial. Here, the off-resonant background shows no significant dependence on the SWIR intensity. Hence, the background is subtracted and only

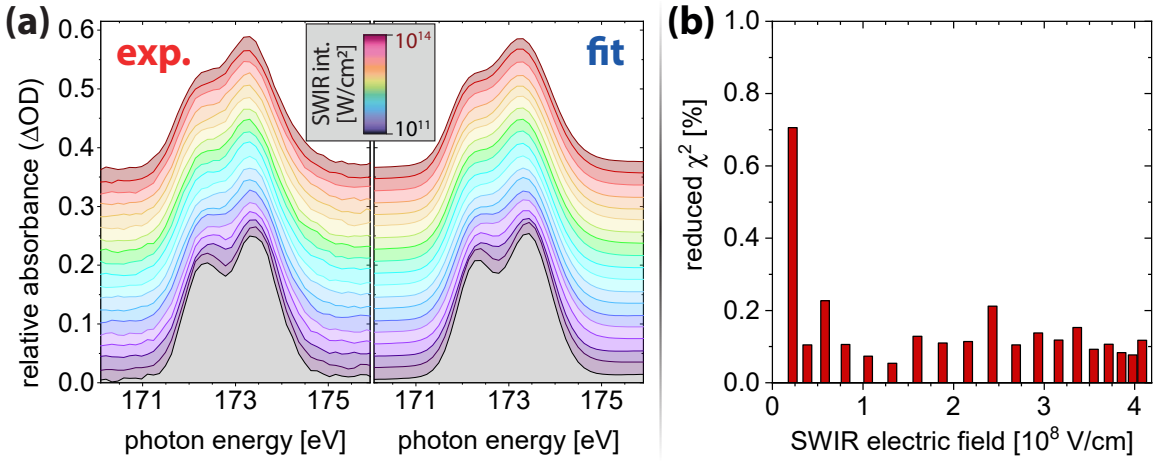

Figure 4.10.: Resonant $6a_{1g}$ doublet absorbance under the influence of different SWIR intensities. **(a)** Experimentally determined (left) and fitted (right; here shown on the same grid as the experimental data) $6a_{1g}$ absorbance. The spectra are vertically shifted by 20 mOD for each intensity step for better visibility. **(b)** Reduced χ^2 value over the SWIR electric-field-strength range as a goodness-of-fit parameter. The fit of the spectra with the lowest SWIR intensity shows a slightly worse fit quality due to the influence of the aperture on the SXR and thus the SNR.

the resonant absorbance data which are presented in figure 4.10 are discussed in the following. Notably, the intensity-independence of the off-resonant background is an indication that ionization can be neglected in the data interpretation [231]. Furthermore, the overall doublet structure is preserved without large photon energy shifts. The visible changes comprise a decrease of the area under the j_+ peak and an increase of the j_- peak area with rising SWIR intensity. In order to quantify the absorbance alterations, a fit based on Voigt profiles is conducted. This approach is common in spectroscopy since a Voigt profile is the convolution of a Gaussian with a Lorentzian function. The combination of both functions accounts for different contributions to the resonance linewidth: While the natural linewidth is of Lorentzian character, other inhomogeneous broadening mechanisms, e.g., vibrational substructures, impact/thermal broadening or the spectrometer resolution lead to a Gaussian contribution. Due to the absence of a fully analytical formulation of a Voigt function [335, 336] $V(x;\sigma,\gamma)$, its implementation via the Faddeeva-function $w(z)$ is used:

$$V(x;\sigma,\gamma) = A\frac{\Re[w(z)]}{\sigma\sqrt{2\pi}}, \text{ with } z = \frac{(x - x_c + i\gamma)}{\sigma\sqrt{2}}. \tag{4.4}$$

Here, γ is the Lorentzian half-width-at-half-maximum value, σ the Gaussian standard deviation, A the area scaling factor, x_c the peak center position, and $\Re$ denotes the

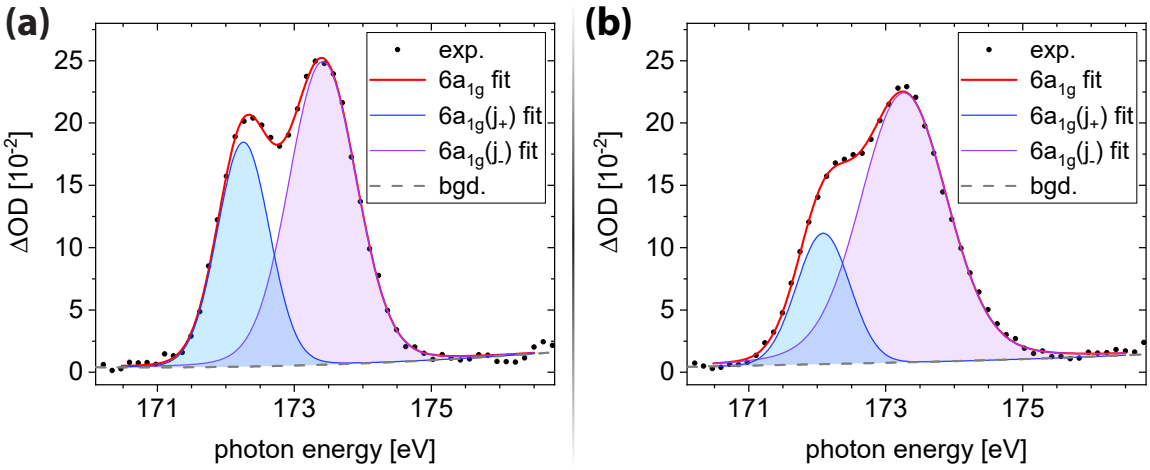

Figure 4.11.: $6a_{1g}$ absorbance doublet fit consisting of a sum of two Voigt functions and a polynomial local background. **(a)** Data and fit for the lowest SWIR intensity of $6.7 \times 10^{11}\,\mathrm{W/cm^2}$. **(b)** Data and fit for the highest SWIR intensity of $2.2 \times 10^{14}\,\mathrm{W/cm^2}$.

real part. The complex-valued Faddeeva function [337] is defined as

$$w(z) = e^{-z^2}\left(1 + \frac{2i}{\sqrt{\pi}}\int_0^z e^{t^2}\,\mathrm{d}t\right). \tag{4.5}$$

Here, the overall fit function consists of a sum of two independent Voigt profiles representing both resonance peaks and a third-order polynomial which accounts for the local off-resonant background that remained after the global background subtraction. Figure 4.11 shows the spectra and respective fits[4] for the highest and the lowest SWIR intensity during the scan. The fits are conducted with unconstrained parameters, namely the peak centers $E_c(j_\pm)$, the areas $A(j_\pm)$ and the Gaussian and Lorentzian widths, that can be combined to a total FWHM width [339]. A comparison of the measured absorbance data with their respective fits as well as the reduced χ^2 fit-quality parameter are depicted in figure 4.12. The reduced χ^2 value as defined in [340] is used:

$$r\chi^2 = \frac{\chi^2}{DOF}\,, \text{ with } \chi^2 = \sum_{k=1}^{n}\frac{(O_k - E_k)^2}{E_k}\,. \tag{4.6}$$

The input parameters in equation (5.3) are the degrees-of-freedom (DOF), the number of pixels n, the measured spectral intensity at the k-th pixel O_k and the respective fit value E_k. The DOF parameter is given by the number of pixels in the fit range

[4] The fits are conducted using the `scipy.optimize.curve_fit` function [338] in PYTHON with the Levenberg-Marquardt least-squares algorithm.

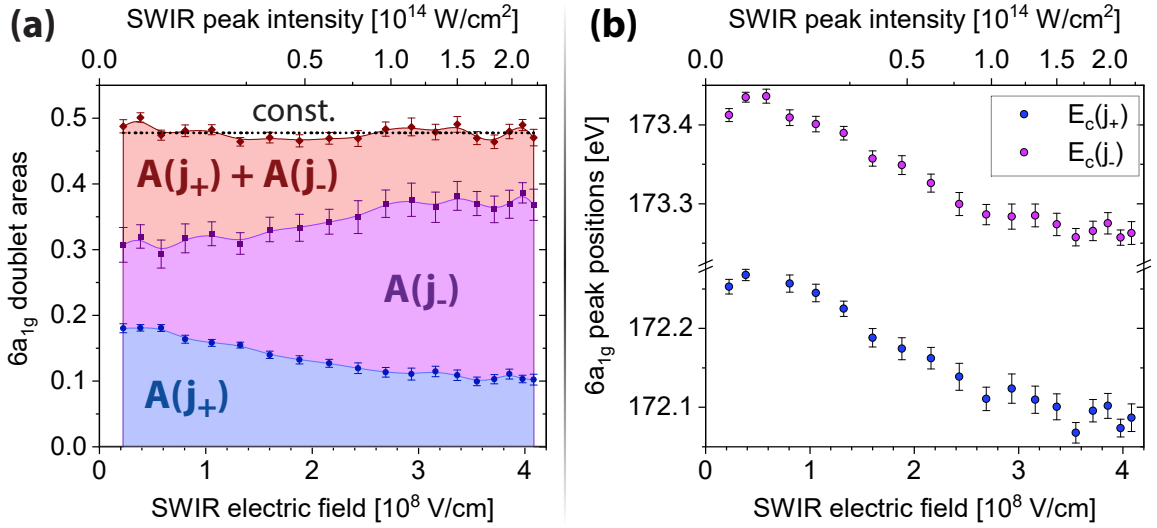

Figure 4.12.: Absorbance areas and positions extracted from the $6a_{1g}$ doublet fits. **(a)** Peak areas of the $j_+ = 3/2$ (blue) and the $j_- = 1/2$ (purple) peak over SWIR field strength. The sum of the areas is shown as well (red) in combination with a constant guide to the eye (black dotted). **(b)** Peak positions of the $j_+ = 3/2$ (blue) and the $j_- = 1/2$ (purple) peak over SWIR field strength.

($n = 47$ pixels) subtracted by the number of fit parameters. As figure 4.10(b) shows, $r\chi^2$ is well below 1 % for the entire intensity scan range. This is a solid indication for the validity of the fit model. For the lowest intensity bin, the fit is less accurate due to the reduced SNR at the most-closed aperture setting.

4.2.3.3. Applying the toy model

For further evaluation of the experiment concerning the control of the exchange energy, the toy model that has been developed in section 4.1.3.2 is applied to the data. The physical observables for this exchange control in the experiment are the branching ratio R and the doublet-peak splitting Δ. These parameters can be extracted from the Voigt fits. As outlined in section 2.4.5 in the theory chapter, the absorbance peak area which is needed to calculate R is a measure for the oscillator strength of the respective transition in absorption spectroscopy. To test whether the toy model can emulate the measured data, a numerical fit of the matrix elements of the 5×5 Hamiltonian (equation (4.3)) to the experimental data is conducted: The necessary steps for the fit procedure are schematically shown in figure 4.13. Here, the Hamiltonian matrix can be compared to the experimental results as the oscillator-strength ratio and the peak splitting are directly accessible after the rotation of H to the basis of its excited-state eigenvectors. The excited states form the lower-right 4×4 submatrix in H. As a 4×4 matrix is in general not analytically diagonalizable, a differential

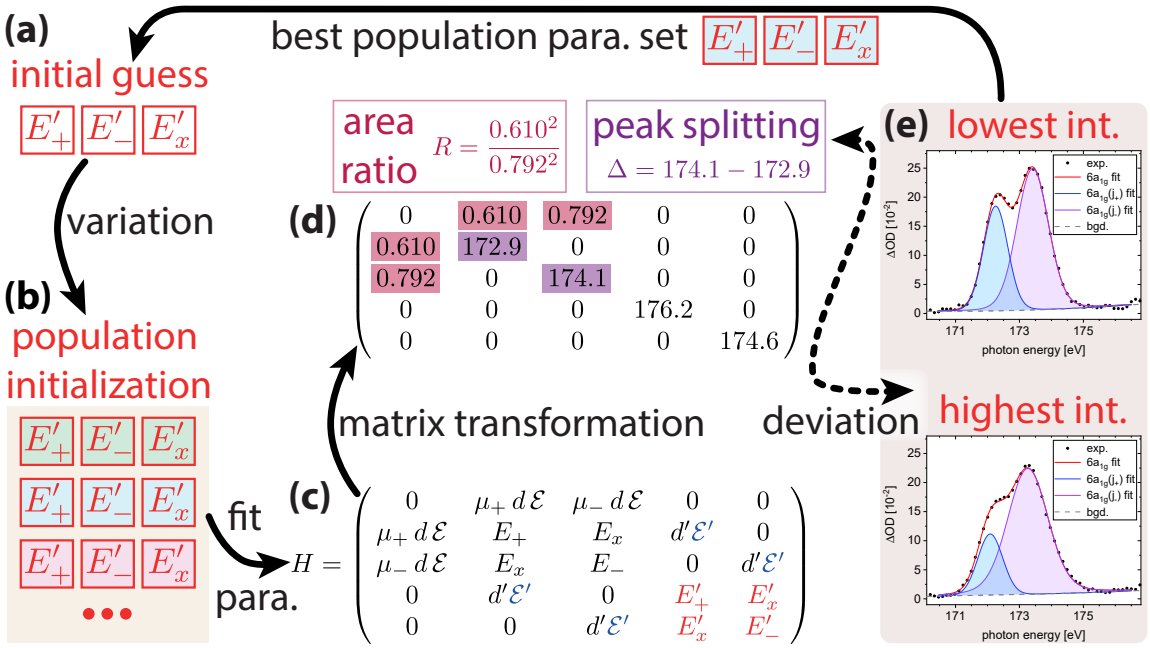

Figure 4.13.: Differential evolution fit algorithm for applying the toy model to the experimental data. **(a)** An initial guess for fit parameters acts as seed for a fit parameter population of the evolution algorithm. **(b)** The fit parameter population is initialized by arbitrarily varying the initial parameters. **(c)** Each set of fit parameters within the population is applied to the 5×5 Hamiltonian matrix of the toy model (equation (4.3)) for the high-SWIR- and the low-SWIR-intensity case of the fit variable $\mathcal{E}'$. **(d)** A matrix transformation (including a numerical diagonalization) provides access to the area ratio R and the peak splitting Δ [328]. **(e)** The extracted R and Δ values from (d) are compared to the area ratio and peak splitting of the experimentally measured $6a_{1g}$ absorbances under influence of the lowest/highest SWIR intensity. The population's parameter set with the smallest deviation from the experimental values is chosen as initial guess for the next iteration of the algorithm. The differential evolution algorithm stops when a certain agreement with the experiment is achieved.

evolution algorithm is applied to find matrix-element values of H that reproduce the measured R and Δ. First, many parameters of H are calculated beforehand or remain fixed: The weak SXR field $\mathcal{E}$ is treated perturbatively and is thus set to $d\,\mathcal{E} \approx 0\,\text{eV}$. In addition, the valence-to-polarizing-orbital dipole element is calculated via DFT. The sulfur $L_{2,3}$-valence-edge expectation value is given as well, $E_+ = 173\,\text{eV}$. Furthermore, the exchange interaction of the valence-populated final states E_x and the spin orbit splitting $\Delta_{jj} \overset{\text{def}}{=} E_- - E_+$ are calculated from atomic parameters. These parameters are the spin-orbit coupling of sulfur ζ and the Hartree-Fock Coulomb exchange-integral value G_1. The respective relations are given by:

$$E_x = \frac{2\sqrt{2}}{9} G_1 \quad \text{and} \quad \Delta_{jj} = \frac{3}{2}\zeta - \frac{2}{9} G_1\,. \tag{4.7}$$

As ζ and G_1 are atomic parameters, a slight corrective scaling of $0.847\,G_1$ and $1.05\,\zeta$ is introduced to achieve agreement with the experimentally observed branching ratio and peak splitting in the static case. This is a common procedure when using atomic HF-derived parameters for XAS of complex systems [72].
As a result, the remaining fit parameters in the Hamiltonian matrix of equation (4.3) are the energy-expectation values of the polarizing-orbital-populated final states, $E'_{\pm}$, and their respective exchange energy E'_x. The SWIR field strength $\mathcal{E}'$ acts as the variable of the fit process. Due to the multi-fit-parameter character of the problem, a differential evolution algorithm is employed[5]. The main idea of an evolution algorithm is to use a set of arbitrarily varied starting parameters resulting in the so-called *population*. In the specific case here, each element of the population consists of values for the three fit parameters E'_+, E'_- and E'_x. After comparing the outcome for every element of the population, the element that matches the experimental observations the best "survives" and advances the evolution. The Hamiltonian matrix with the corresponding population element is evaluated at only two fit-variable values: the lowest and the highest SWIR field strength used in the experiment (see figure 4.11). The lower-right 4×4 submatrix of H is numerically diagonalized and H subsequently rotated into the basis of the determined eigenstates. Now, the $j_{\pm}$ peak centers and oscillator strengths are extracted and compared with the experimental spin-splitting and peak area ratio at these two SWIR intensities. The calculated deviation serves as error value in order to quantitatively evaluate the respective agreement with the experiment. Hence, the population element which leads to the smallest error value is used as the new starting-parameter set in the next iteration. Once a convergence below a certain threshold value of the error value is reached, the fit procedure is terminated and the corresponding fit parameter values in combination with their fit uncertainties are returned as outputs by the algorithm. While this fit method is slow in comparison to gradient-based approaches, it provides a higher probability of converging to the global minimum [342]. Notably, the fit comprises only the two extremes of the whole intensity-tunability range being the lowest and the highest SWIR field strength and thus the quasi-static and the most perturbed spectra. If the results of the fit procedure can correctly replicate R and Δ over the whole measurement range with only two variable values as input for the optimization, this is a robust confirmation that the fit model is indeed capable of describing the underlying physics. To summarize, the used

[5]The fit procedure is implemented in Python using the `scipy.optimize.differential_evolution` function [341].

constants, fit-variable and optimized-fit-parameter values are:

- Constant parameters:
  - $\mathcal{E} = 4.16 \cdot 10^5\,\mathrm{V/cm}$
  - $d\,\mathcal{E} \approx 0\,\mathrm{eV}$
  - $d' = 6.47 \cdot 10^{-9}\,\mathrm{e{\cdot}cm}$
  - $E_+ = 173\,\mathrm{eV}$
  - $\Delta_{jj} = E_- - E_+ = 0.9577\,\mathrm{eV}$
  - $E_x = 0.3265\,\mathrm{eV}$
- Fit variable (two values – SWIR extreme cases as depicted in figure 4.11):
  - $\mathcal{E}' = 2.25 \cdot 10^7\,\mathrm{V/cm}$ and $4.08 \cdot 10^8\,\mathrm{V/cm}$
- Resulting optimized fit parameters:
  - $E'_+ = E_+ + (2.33 \pm 0.04)\,\mathrm{eV}$
  - $E'_- - E'_+ = (0.15 \pm 0.05)\,\mathrm{eV}$
  - $E'_x = (0.80 \pm 0.01)\,\mathrm{eV}$

The results for R and Δ which are based on the fit of only two SWIR-intensity data points are compared to the experimental results over the whole intensity-scan range in figure 4.14. As one can see in subfigure 4.14(a), the fit exhibits a good agreement with the experimental area ratio behavior within the measurement uncertainties for different SWIR field strengths. Hence, the fit model is capable of correctly describing the complex, non-analytical area ratio decrease for the highest SWIR intensity by up to $(53 \pm 4)\%$. In accordance with the theoretical considerations of chapter 4.1.3.1, the experimentally measured peak splitting Δ remains rather constant over the complete SWIR field-strength range. Even though smaller deviations in the $1 \times 10^8\,\mathrm{V/cm}$ to $2 \times 10^8\,\mathrm{V/cm}$ region between the fit and the experiment are evident, the basic toy model still describes the relatively constant behavior of the peak splitting well. Notably, the basis set of this toy model is comparatively small with only five many-body states, which represents a drastic simplification of the electronic structure of SF_6. Thus, it is rather astonishing that a spectroscopic measurement of a molecule consisting of seven atoms can be emulated with such a basic toy model.
After this analysis of the validity of the toy model to describe the measured SWIR-intensity dependence of the area ratio and peak splitting, the optimized fit parameters

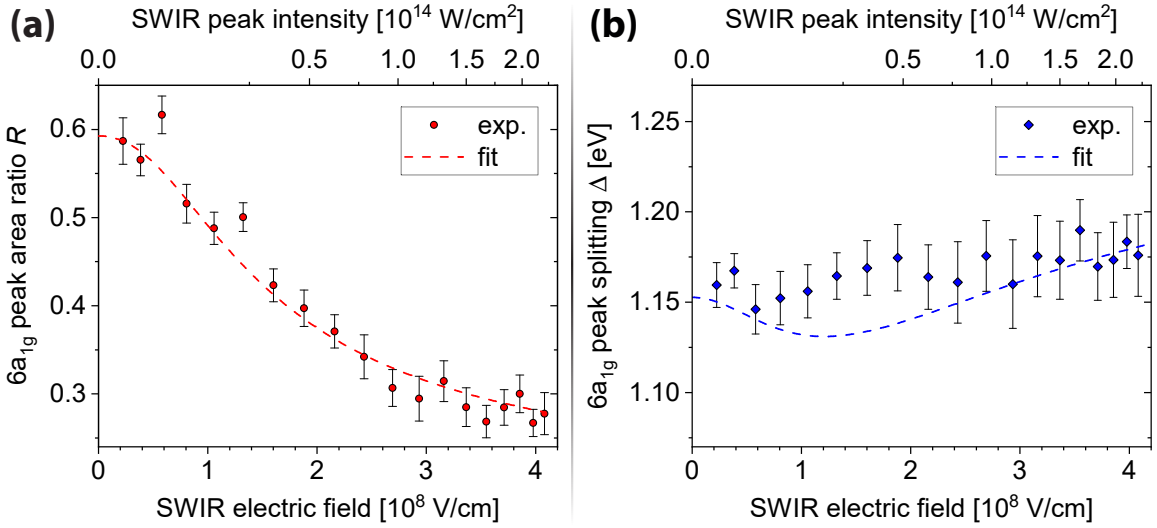

Figure 4.14.: Experimental and fitted $6a_{1g}$ area ratio and peak splitting dependence on the SWIR field strength. For the fit, the Hamiltonian H (equation (4.3)) is numerically optimized for the Δ and R of the lowest and highest SWIR field strength (respective absorbances shown in figure 4.11). **(a)** Area ratio R over SWIR field strength. **(b)** Peak Splitting Δ over SWIR field strength.

are discussed. Notably, the resulting exchange interaction E_x' of the polarizing-orbital-populated states $\left|c_{\pm}^{-1}p^1\right\rangle$ is much higher than the exchange energy E_x of the valence-occupied states $\left|c_{\pm}^{-1}v^1\right\rangle$: $E_x' \approx 2.5\,E_x$. While this might seem counter-intuitive at first glance, it can be well understood by looking at the parity of the involved orbitals (the respective MO isosurfaces are illustrated in figure 4.5): Upon each dipole excitation, the parity is changed. Thus, the excited electron in the valence orbital $6a_{1g}$ has an opposite parity to the orbital it originated from, the $2t_{1u}$. This is also the reason for the inaccessibility of the polarizing orbitals like the $6t_{1u}$ with a single dipole transition from the ground state. The additional SWIR photon, however, can dipole couple the valence and polarizing orbital and thus flip the parity again. Looking at the realizations of the general exchange integral as defined in the theory section 2.2.3 (equation (2.39)) for both cases,

$$E_x \propto \iint \psi_{c_-}^{\dagger}(\vec{r}_1)\ \psi_{v_\uparrow}^{\dagger}(\vec{r}_2)\frac{1}{|\vec{r}_1-\vec{r}_2|}\psi_{c_+}(\vec{r}_2)\ \psi_{v_\downarrow}(\vec{r}_1)\ \mathrm{d}\vec{r}_1\,\mathrm{d}\vec{r}_2\,, \tag{4.8}$$

and

$$E_x' \propto \iint \psi_{c_-}^{\dagger}(\vec{r}_1)\ \psi_{p_\uparrow}^{\dagger}(\vec{r}_2)\frac{1}{|\vec{r}_1-\vec{r}_2|}\psi_{c_+}(\vec{r}_2)\ \psi_{p_\downarrow}(\vec{r}_1)\ \mathrm{d}\vec{r}_1\,\mathrm{d}\vec{r}_2\,, \tag{4.9}$$

provides a systematic perspective on the exchange-value impacting terms. First of all, the inverse-distance term $\frac{1}{|\vec{r}_1-\vec{r}_2|}$ is positive. Here, the point reflection $\vec{r}_1 \to -\vec{r}_1$ is

conducted to investigate the parity of the orbital product terms: As $\psi_c(-\vec{r}_1) = -\psi_c(\vec{r}_1)$ is of odd parity and $\psi_{v_\downarrow}(-\vec{r}_1) = \psi_{v_\downarrow}(\vec{r}_1)$ is of even parity, the overall integrand in the E_x calculation changes its sign[6] for a point reflection. In contrast, the integrand in E_x^I does not show any sign change upon point reflection of either coordinate, $\vec{r}_1$ or $\vec{r}_2$, due to ψ_c and ψ_p both being odd parity orbitals. Thus, these symmetry considerations result in smaller exchange values for the valence ψ_v in comparison to the polarizing orbital ψ_p, $E_x < E_x^I$. This is based on the evaluation of the integral over a sign-changing integrand for ψ_v in comparison to ψ_p orbitals of similar spatial extent.

4.2.4. Effective exchange-energy control in SF_6

4.2.4.1. Extraction of the effective exchange energy

In the toy-model Hamiltonian (equation (4.3)), the exchange energies E_x and E_x^I are fixed. This is based on the fundamental physical character of the exchange interaction as part of the Coulomb interaction (compare section 2.2.3 in the theory chapter). Consequently, this quantum-mechanical interaction itself cannot be manipulated. What can be shown, however, is that a system acts as if the exchange interaction within an effective system is varied. This resembles normalization group theory [305]. To demonstrate such an effective exchange control, the 5×5 Hamiltonian is reduced to an effective Hamiltonian matrix. Here, the mathematically smallest possible scheme to describe a spin-orbit split system is given by a basis of three many-body states. Such a system is realized by introducing the laser-dressed, mixed valence orbitals $\psi_{m_\pm} \stackrel{\text{def}}{=} \alpha_\pm \psi_v + \beta_\pm \psi_p$. From a mathematical perspective, this is a basis transformation of H. Hence, the new basis of the reformulated 5×5 Hamiltonian of equation (4.3) is given by $|0\rangle$ as well as the excited states

$$\left|c_+^{-1} m_+^1\right\rangle = \alpha_+ \left|c_+^{-1} v^1\right\rangle + \beta_+ \left|c_+^{-1} p^1\right\rangle \ , \tag{4.10}$$

$$\left|c_-^{-1} m_-^1\right\rangle = \alpha_- \left|c_-^{-1} v^1\right\rangle + \beta_- \left|c_-^{-1} p^1\right\rangle \ , \tag{4.11}$$

$$\left|c_+^{-1} \tilde{m}_+^1\right\rangle = \tilde{\alpha}_+ \left|c_+^{-1} v^1\right\rangle + \tilde{\beta}_+ \left|c_+^{-1} p^1\right\rangle \ \text{and} \tag{4.12}$$

$$\left|c_-^{-1} \tilde{m}_-^1\right\rangle = \tilde{\alpha}_- \left|c_-^{-1} v^1\right\rangle + \tilde{\beta}_- \left|c_-^{-1} p^1\right\rangle \ . \tag{4.13}$$

The system reduction of H to H^{eff} is carried out by disentangling the upper-left 3×3 submatrix with $|0\rangle$ and $\left|c_\pm^{-1} v^1\right\rangle$ as basis set from the lower right 2×2 submatrix

[6] This can be shown equivalently for $\vec{r}_2 \to -\vec{r}_2$ as well.

which comprises the states $\left|c_{\pm}^{-1}p^{1}\right\rangle$. This is achieved by choosing the prefactors $\alpha_{\pm}$ and $\beta_{\pm}$ such, that the off-diagonal $d^{I}\mathcal{E}^{I}$ terms vanish. Only the states with the lowest transition energy from the ground state $|0\rangle$ are of interest during evaluation of H after the basis transformation, which are referred to as the two $\left|c_{\pm}^{-1}m_{\pm}^{1}\right\rangle$ states. With this choice of prefactors, no element in H explicitly depends on the SWIR field strength any more. Such a dependence, however, is implicitly included in the prefactors $\alpha_{\pm}$, $\beta_{\pm}$, $\tilde{\alpha}_{\pm}$ and $\tilde{\beta}_{\pm}$ and thus in the basis set, which has to be accordingly adapted for every SWIR intensity. Therefore, by eliminating the explicit SWIR dependence in H, the parameters of H have to be adjusted for every step of the intensity-scan data. This corresponds to a transition to a system with effective parameters. Now, the behavior of the physical system can be emulated by only considering the part of H that has to be varied for each intensity point: the effective Hamiltonian H^{eff} of size 3×3,

$$H^{eff} = \begin{array}{c} \begin{array}{ccc} |0\rangle & |c_{+}^{-1}m_{+}^{1}\rangle & |c_{-}^{-1}m_{-}^{1}\rangle \end{array} \\ \begin{pmatrix} 0 & d_{+}^{eff}\mathcal{E} & d_{-}^{eff}\mathcal{E} \\ d_{+}^{eff}\mathcal{E} & E_{+}^{eff} & \boldsymbol{E_{x}^{eff}} \\ d_{-}^{eff}\mathcal{E} & \boldsymbol{E_{x}^{eff}} & E_{-}^{eff} \end{pmatrix} \end{array}, \tag{4.14}$$

with the effective dipole moments $d_{\pm}^{eff}$ that also include the multiplicity factors. Furthermore, the energy expectation values of $\left|c_{+}^{-1}m_{+}^{1}\right\rangle$ and $\left|c_{-}^{-1}m_{-}^{1}\right\rangle$, $E_{\pm}^{eff}$, respectively, and the effective exchange energy E_{x}^{eff} are matrix elements of H^{eff}. In principle, all effective parameters depend on the SWIR field strength. In order to find the values of these effective parameters, the 5×5 Hamiltonian matrix H is numerically reduced for every SWIR intensity step with the parameters which are extracted from the numerical fit (compare section 4.2.3.3). While this provides access to E_{x}^{eff}, it also illustrates that the ratio of the effective dipole moments is still well approximated by the multiplicity ratio, $d_{+}^{eff}/d_{-}^{eff} \approx \mu_{+}/\mu_{-}$, over the entire SWIR intensity range. Even for the highest SWIR field strength in the measurement, these ratios match within 5 %. Taking advantage of $d_{+}^{eff}/d_{-}^{eff} \approx \mu_{+}/\mu_{-}$, the diagonalizability of the reduced Hamiltonian matrix (4.14) leads to an analytical relation[7] between the effective exchange E_{x}^{eff} and the experimental observables, namely the area ratio R and the peak splitting Δ:

$$R = \frac{-4\sqrt{2}E_{x}^{eff} + 3\Delta + \sqrt{\Delta^{2} - 4(E_{x}^{eff})^{2}}}{4\sqrt{2}E_{x}^{eff} + 3\Delta - \sqrt{\Delta^{2} - 4(E_{x}^{eff})^{2}}} \,. \tag{4.15}$$

[7] Further details on the derivation of this analytical formula are given in [100].

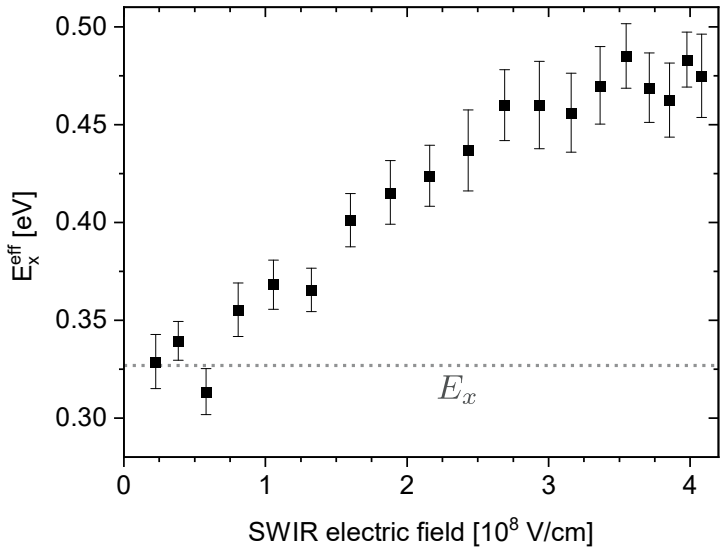

Figure 4.15.: Effective exchange energies E_x^{eff} extracted from the experimental area ratio R and peak splitting Δ (compare figure 4.14) via equation (4.16). For comparison, the exchange energy of the unperturbed system is E_x = 0.3265 eV as indicated by the grey dotted line.

Transforming $R(E_x^{eff}, \Delta)$ to an analytical expression for $E_x^{eff}(R, \Delta)$ does not result in any insights as this explicit expression has an overly complicated analytical form. In order to calculate the effective exchange energy, the implicit analytical form (4.16) is instead solved numerically for each (R, Δ)-pair (see figure 4.14) of the measured dataset. The corresponding results are shown in figure 4.15. The mathematically more rigorous, but physically less insightful alternative of the numerical 5×5 to 3×3 matrix reduction leads to effective exchange values well within the error bars, which further justifies the chosen analytical approach.

The extracted effective exchange energy increases drastically for higher SWIR field strengths as figure 4.15 illustrates. The effect of the SWIR on the mixed valence orbital ψ_m is represented by the respective isosurfaces shown in subfigure 4.16(a). A clear symmetry breaking of the effective valence orbital, caused by the polarizing orbital admixture, is evident. Based on these mixed valence MO shapes, the above mentioned symmetry analysis for the exchange integral can be visualized. The exchange integral for the mixed orbitals is

$$E_x^{eff} \propto \iint \psi_{c_}^{\dagger}(\vec{r}_1)\ \psi_{m_}^{\dagger}(\vec{r}_2) \frac{1}{|\vec{r}_1 - \vec{r}_2|} \psi_{c+}(\vec{r}_2)\ \psi_{m+}(\vec{r}_1)\, d\vec{r}_1 d\vec{r}_2\ . \tag{4.16}$$

Due to the mixed-orbital nature of ψ_m, a visualization of the $\psi_c\psi_m$ orbital product (see subfigure 4.16(b)) is necessary to draw conclusions for the trend of E_x^{eff}. Here, the

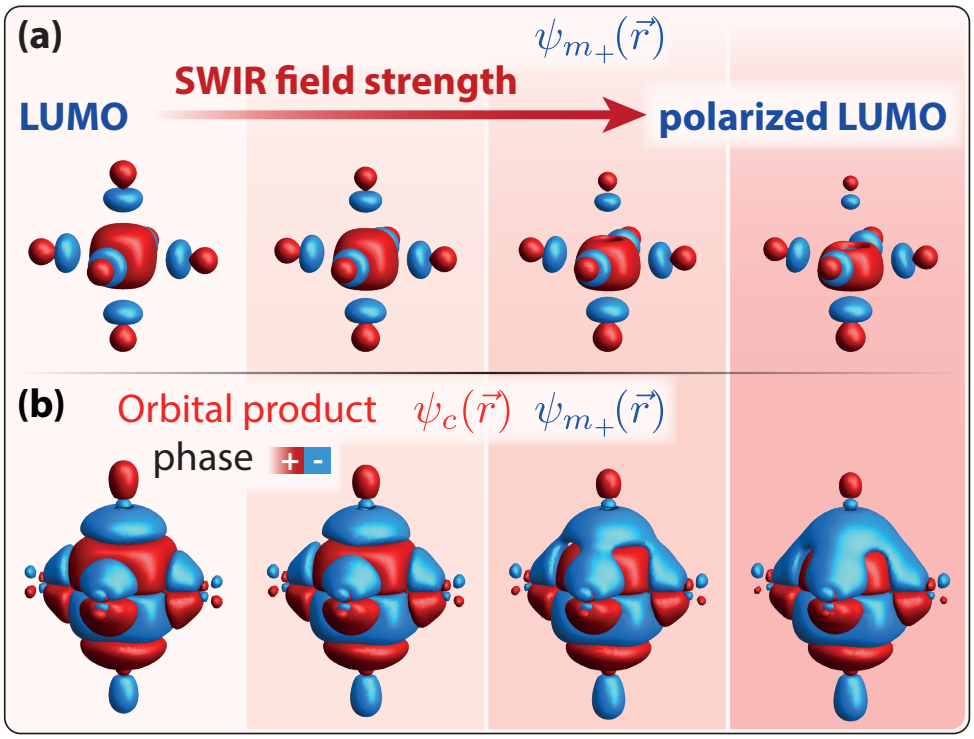

Figure 4.16.: Visualization of the mixed valence orbital and its product with the core-orbital for different SWIR field strengths. **(a)** Visualization of the laser-dressed valence orbital. While the valence orbital is of pure $6a_{1g}$ character (compare subfigure 4.5(b)) in the absence of the SWIR field, it evolves into a symmetry-broken, effective valence orbital by the polarizing-orbital admixture induced by the SWIR. **(b)** To draw conclusions from the effective MO alterations shown in (a) for the value of the effective electron–electron exchange energy, the product of the core with the mixed orbital is decisive (compare equation (4.16)). The reduction of sign-changes over the isosurface of the orbital product are an illustration for the increase in electronic exchange.

amount of sign changes within the orbital product is reduced for a high SWIR field due to breaking the odd $\psi_c\psi_v$ symmetry. Therefore, the isosurfaces in subfigure 4.16(b) are a visualization of the effective exchange increase itself.

4.2.4.2. Comparison with an *ab-initio* quantum-mechanical simulation

To cross-check our physical understanding of effective electronic exchange control, the results obtained in the previous section 4.2.4.1 by applying the toy model are benchmarked against the outcome of an *ab-initio* simulation performed by Dr. Simon Heinze and Prof. Dr. Maurits Haverkort from the Institute for Theoretical Physics at Heidelberg University. The aim is to simulate the electronic structure of SF_6 and the influence of the SWIR field and retrieve XAS spectra that can be analyzed in an equal manner as the experimental data in section 4.2.3.2. First, the molecular

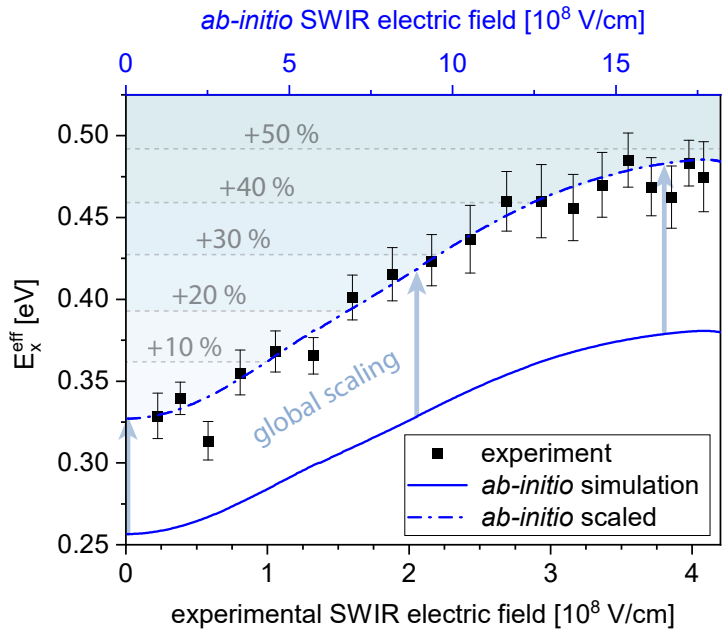

Figure 4.17.: Comparison of effective exchange energy E_x^{eff} extracted from experimental data (black data points) and *ab-initio* theory (solid blue line). A global scaling in the SWIR field strength (see blue axis at the top) as well as the y-axis is needed to match the simulation with the experiment. These scalings can be well understood (see main text) and lead to a scaled *ab-initio* graph (blue dashed line) that can emulate the complex field-dependence of the experimentally obtained effective exchange energy in a precise manner.

orbitals are calculated via the full-potential local-orbital (FPLO) minimum-basis DFT code [343, 344] within the local density approximation. Secondly, the resulting $2t_{1u}$, $6a_{1g}$, $6t_{1u}$ and $7a_{1g}$ MOs of SF_6 are used in a full many-body quantum simulation employing the QUANTY code [345, 346]. The light-matter interactions are calculated as dipole couplings. As a result, QUANTY calculates corresponding XAS spectra. Further information on the *ab-initio* simulation can be found in [100]. The simulated XAS absorbances for different SWIR field strengths are fitted and evaluated in the same manner as the experimental data. Figure 4.17 presents the direct comparison of the effective exchange interaction E_x^{eff} over SWIR field strength for the experiment (compare figure 4.15) and the *ab-initio* simulation. While the $E_x^{eff}(\mathcal{E})$ extracted from the simulation data (blue solid line in figure 4.15) shows a similar qualitative behavior as the experimental data suggest, a complete match is only achieved by globally scaling both, the x- and y-axis of the simulation results. The required scalings, though, are expected: DFT orbitals with their intrinsic limitation of DFT being a ground-state theory act as input for the quantum many-body simulation. Hence, the spatial extent of the excited states is overestimated due to the lack of considering the core hole.

As a consequence, the exchange integral values are systematically smaller and the exchange energy is accordingly underestimated ($E^{eff}_{x,\,abInit} \approx 0.79\,E^{eff}_{x}$). The x-axis scaling ($\mathcal{E}_{abInit} \approx 4.3\,\mathcal{E}_{exp}$) arises from the fact that only one polarizing orbital, the $6t_{1u}$, is considered[8], while a manifold of odd-parity unoccupied orbitals contributes to the effective polarizing orbital in reality. Thus, the polarization is underestimated by the *ab-initio* simulation.
Overall, the *ab-initio* theory can replicate the complex impact of the SWIR field on the effective exchange energy in an astonishingly precise manner (blue-dashed line in figure 4.17). The physical interpretations drawn from the basic toy model are backed by this independent simulation, indicating that the effective exchange interaction is indeed increased by up to 50% using intense SWIR laser pulses.

4.3. Controlling chemistry on the fundamental electronic quantum level – an outlook

To summarize, the control of the effective electronic exchange in a molecular system with intense SWIR pulses has been demonstrated in this chapter. The probing of this exchange control is conducted via XAS, which provides a high sensitivity for electronic-exchange-related phenomena. First, a simple toy model consisting of a 5×5 Hamiltonian matrix is developed that enables the description and control of electronic exchange via orbital mixing which is mediated by light. Secondly, the toy model is put to the experimental test in SF_6 which matches the required electronic structure including a very short-lived excited state and a spin-orbit-split core orbital. The control scheme is realized by conducting the XAS core-level probe scheme while the molecule is perturbed by an SWIR pulse of tunable intensity of up to $2.2\times10^{14}\,\mathrm{W/cm^2}$. A reduction of the toy model to an effective model of size 3×3 enables the extraction of an effective exchange energy E^{eff}_{x}. Here, the observed absorbance-area ratio R of the two peaks within the spin-orbit-split doublet resonance and the peak splitting Δ are utilized. Symmetry considerations of the involved molecular orbitals within the exchange integral lead to a physical interpretation of the increased electronic exchange to originate from a laser-induced orbital mixing. This orbital mixing results in a distorted, polarized LUMO. Furthermore, physical conclusions drawn from the toy model are verified with an *ab-initio* quantum many-body simulation. At the highest

[8] The reason for not considering more polarizing orbitals is linked to the limitations of DFT concerning higher-excited MOs as described above.

SWIR intensity, an increase of E_x^{eff} by 50% in comparison to non-perturbed SF_6 is determined.

These findings represent the first step in the field of controlling the electronic structure on a solely quantum-mechanical level by targeting exchange interaction. Thus, the results presented in this chapter pave the way for future studies within the newly-established exchange-control field, addressing questions like: How can geometrical effects, e.g., molecular alignment or a varied laser polarization, influence the exchange-energy control? Can this control be realized for transitions of two electrons excited by one photon, so-called doubly excited states? How large and complex can a molecule be before the toy-model approach breaks down? Or on the other extreme: Can an exchange-control scheme be applied to a small atomic system? In addition, the manipulation of electronic exchange could inspire the extension of the toolbox for ultrafast chemical control. For the application to chemistry, the core-to-LUMO excitation which enables observing the alteration of the electronic exchange energy will be replaced with a more relevant HOMO-to-LUMO excitation in the visible to ultraviolet spectral region. The presented scheme can help to selectively control chemistry and molecular properties on a fundamental electronic quantum level with the exchange interaction being crucial in chemical bonding, for potential energy surfaces in chemical dynamics and many more chemical parameters.

5. Resolving and controlling femtometer-scale vibrational dynamics

The previous chapter 4 has presented one method on how to expand the scientific toolbox for laser control of chemistry. There, the constituents of a covalent chemical bond, the electrons, have been targeted. While chemistry is mediated by electrons, it is ultimately realized by the atomic coordination within a molecule. With the idea of precision control in mind, one can think of the smallest possible alteration of a molecular structure: A minimal perturbation is achieved by slightly manipulating the distance between atoms within the molecule but leaving its atomic and electronic composition unchanged. This kind of an initial perturbation leads to successive oscillatory dynamics of the respective inter-atomic distances – a molecular vibration. Thus, a molecule represents an exemplary quantum-mechanical realization of a classical oscillator with the chemical bond acting as the spring between the atomic nuclei. The electrons and the atomic nuclei in a molecule are all charged quantum particles and interact with each other by the laws of quantum mechanics. Hence, it is crucial to understand the electronic-vibrational coupling dynamics to access an additional tuning knob for chemical precision control and elucidate its potential limits.
This chapter sheds light on the question, how small the tiniest measurable molecular vibrations are and how they can be controlled. Its results expand the frontiers of molecular-structure metrology and manipulation of gas-phase molecules using ultrashort laser pulses. First, section 5.1 gives an overview of the current techniques for initiating and measuring molecular vibrations. Afterwards, section 5.2 introduces TR-XAS as a suitable tool for initiating and tracking vibrations at the perturbative limit. Section 5.3 provides details on the experimental realization of TR-XAS of gas-phase SF_6 molecules and the corresponding data analysis. Subsequently, the results are discussed in the context of a combined quantum-mechanical/classical

simulation. Finally, section 5.4 summarizes the findings and gives perspectives on TR-XAS as a tool for precision molecular-structure metrology.
A manuscript based on the results of this chapter is currently under peer review at *Physical Review Letters* [2].

5.1. Exciting and measuring molecular vibrations – an overview

5.1.1. Vibrational excitation

In principle, there are multiple ways to excite a molecular vibration. All techniques rely on pumping energy into the molecular system which enables a transition from one vibrational level in an electronic PEC (see section 2.5.2 in the theory chapter) to another. Figure 5.1 illustrates the corresponding mechanism that is explained in the following. First, the vibrational excitation energy can be delivered by collisions. One form is the statistical collision of the molecule with another due to their intrinsic thermally-induced kinetic energy. This is known as thermal excitation and is described by the Boltzmann distribution (equation (2.59) in the theory chapter). Due to the statistical nature of this process, thermally excited vibrations in a molecular ensemble are not phase-locked and thus incoherent. Another mechanism is the collision with externally accelerated particles. These can be other atoms, molecules and also electrons or neutrons. The scattering of light on the other hand is a collision of the molecule with a light particle, a photon. Collisions that provide more energy than the first ionization/dissociation threshold may result in a vibrationally excited final state within a PEC of the ionized or dissociated species. Low-intensity light excitation, though, can still directly excite a vibration in a neutral molecule if the respective vibrational mode is accompanied by a change in the dipole moment of the molecule. A molecule-specific distribution of IR-active modes (see section 2.5.3.2 in the theory chapter) is typically located in the mid-infrared between 5 µm and 20 µm, the vibrational *fingerprint* region [347–349]. Vibrational modes that induce a varying polarizability can be excited in a two-photon process using Raman scattering (see section 2.5.3.2 in the theory chapter). Here, the exciting light pulse is significantly shorter than the vibrational period of the molecule in an impulsive Raman regime. As long as a Raman-active mode is targeted, such an impulsive stimulated Raman process is universally applicable as it does not rely on a specific electronic structure

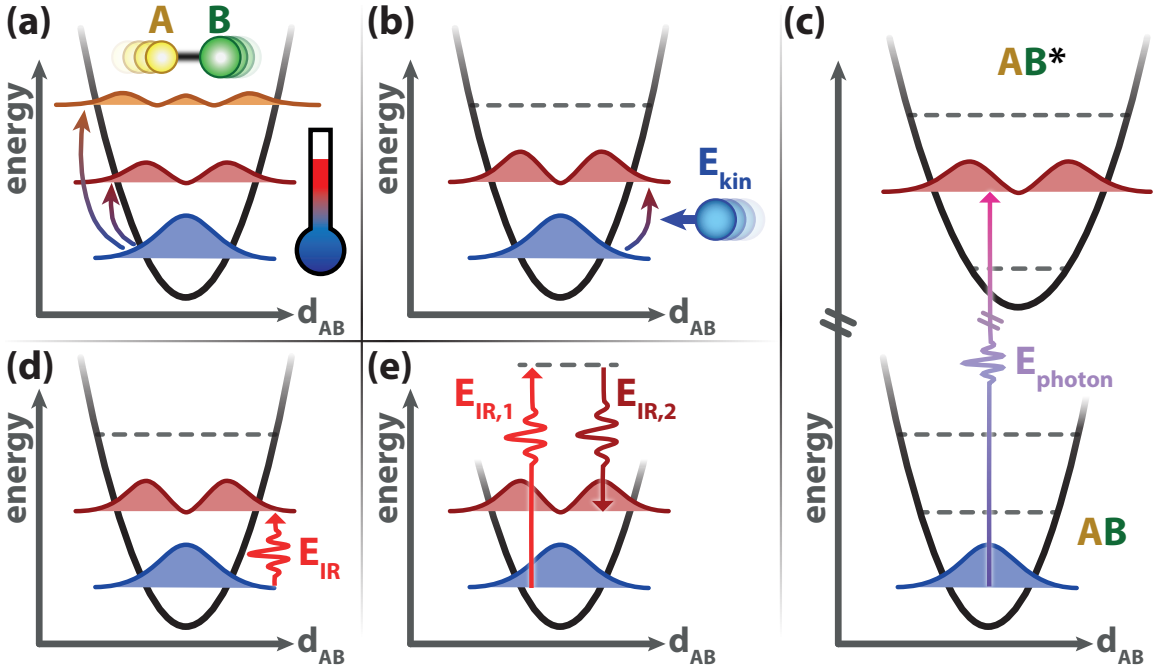

Figure 5.1.: Different vibrational excitation schemes for an exemplary molecule AB. **(a)** Thermal excitation according to the Boltzmann distribution (equation (2.59) in the theory section 2.5.3). **(b)** Collision with an externally accelerated particle (e.g., another molecule or electron). **(c)** Vibrational excitation after electronic excitation/ionization leading to AB*. **(d)** Dipole excitation of an IR-active mode with a resonant photon. **(e)** Nonlinear excitation of a Raman-active mode. More details on the cases (d) and (e) are given in the theory section 2.5.3.2.

(e.g., nearby electronic resonance as mediator) or photon energy.

5.1.2. Measuring structural dynamics

A full vibrational molecular-dynamics control scheme requires a time-resolved measurement technique of the molecular structural changes. The following section provides an overview of established experimental techniques for structure determination on the (sub-)atomic level.

5.1.2.1. Diffraction techniques

One approach which is dedicated to molecular structure determination is diffraction. In a diffraction experiment, particles that have or can be associated with a certain wavelength diffract off the target-molecule's constituents. After propagation through the target, the transmitted spatial distribution of the diffracted particles is measured. An overview of different diffraction techniques is given in figure 5.2.

Electrons can act as scattered particles, making use of their small de-Broglie wave-

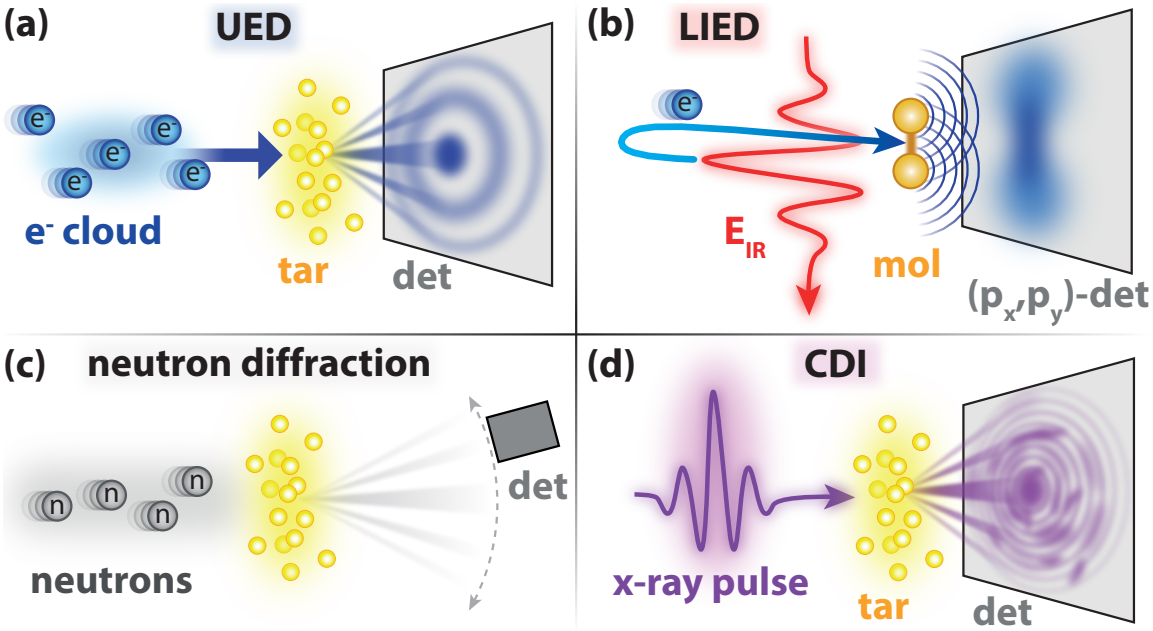

Figure 5.2.: Diffraction techniques for investigating molecular structural dynamics. **(a)** Ultrafast electron diffraction (UED). (b) Laser-induced electron diffraction (LIED). (c) Diffraction with neutrons. (d) Coherent diffractive imaging (CDI) with x-rays.

length when being accelerated. Using conventional linear accelerator techniques [350] or laser-based acceleration [351], one can generate ultra-relativistic electrons. If the accelerated electron cloud is sent into a sample, it interacts with both, negatively charged electrons and positively charged atomic nuclei. When the electron cloud is preceded by an ultrashort laser pulse which induced dynamics in the sample, the technique is referred to as ultrafast electron diffraction (UED) [352–354]. Often, the aim of UED experiments is a real-time view on molecular dynamics [355, 356], which is referred to as *molecular movie*. A disadvantage, however, is the charge-based repulsion of the electrons within the accelerated, pulsed electron cloud. This leads to a compromise concerning electron-pulse length and the overall number of charges in a single electron pulse. Several approaches to address this issue are currently under development [357–359]. The integration of the UED approach into a transmission electron microscope results in so-called 4D microscopy [360, 361].

Another technique that uses accelerated electrons to gain information about molecular structure is *laser-induced electron diffraction* (LIED) [362, 363]. In contrast to UED, LIED uses electrons that actually originate from the same molecule that they diffract off. Here, the methodology is very similar to the three-step model of the HHG process (see figure 2.5 in the theory chapter): In the classical picture, the

electric field of an infrared laser pulse accelerates a bound molecular electron. After the next field maximum, the direction of the field is reversed and the quasi-free electron is accelerated back towards the ionized molecule. In consequence, the electron can diffract off the molecular structure. Structural information is reconstructed by measuring the diffracted electron's momentum. The major advantage of LIED is the coherent nature of the target-molecule ensemble's signal. All molecules in the target see the same coherent laser field and thus the microscopic diffraction processes are perfectly in phase. Furthermore, LIED can be combined with a pump-probe approach, where a time-delayed pump pulse triggers, e.g., a molecular dissociation or an orientation/alignment of the molecules within the ensemble. In some cases, the intense laser pulse that leads to the diffraction process already triggers molecular dynamics before diffraction takes place [364]. Conceptually, LIED is unable to measure neutral, unperturbed molecules.

Besides charged particles like electrons, neutral particles with a rest mass can be used for diffraction [365, 366]. Neutron diffraction is especially useful for cases in which the targeted vibrational mode is neither IR- nor Raman-active and can otherwise not be addressed [367]. Furthermore, neutrons have a magnetic momentum and a rest mass about 2000 times higher than an electron. As neutrons do not have an electric charge, conventional acceleration schemes as discussed for electrons in the paragraphs above cannot be applied. In combination with the limited availability of neutron sources, this imposes major disadvantageous to this technique. Moreover, sources providing ultrashort neutron pulses are still under development [368, 369].

Besides the above mentioned examples, diffraction is also possible with particles without rest mass like photons. In this case not the acceleration imposes the technical challenge but the generation of light with a photon energy that corresponds to a wavelength small enough to resolve molecular bonds. This requires photons with energies in the hard x-ray regime [370, 371]. Up to now, sources that can provide such high photon energies in combination with a sufficient number of photons within a (partially) coherent ultrashort pulse have only been available at large-scale facilities. While femtosecond pulses with a low photon number can be achieved by the laser-slicing technique at synchrotrons [372], free-electron lasers (FELs) [221] are the workhorse nowadays for femtosecond hard x-ray diffraction experiments. With their high brilliance, FELs enable structural analysis of a single particle [373] with a technique called coherent diffractive imaging [374]. In combination with their intrinsic femtosecond-pulsed character, FELs offer ideal condition for diffraction-based

molecular movies [375]. On the other hand, due to the large-scale-facility character of such experiments, corresponding studies are extremely expensive and the demand exceeds the beamtime availability by far. The most striking physical disadvantage is the limited spatial resolution due to the technically achievable wavelengths. Even though in planning [376], gamma-ray FELs do not exist yet.
To conclude, diffraction-based methods are widely used for the measurement of the absolute molecular structure and its ultrafast dynamics. Besides specific dis-/advantages of the respective diffraction techniques, their spatial resolution is limited by the (de-Broglie) wavelength. Hence, the spatial resolution and precision of diffraction techniques is limited to the nano- to picometer regime at the moment.

5.1.2.2. Spectroscopic approaches

Another approach is detecting the energy/momentum of scattered or emitted particles. This is realized in spectroscopic measurements.
Radiation that is generated within the target system contains information about the molecular structure. Here, one example is to conduct high-order harmonic generation (see section 2.1.5 in the theory chapter) in the target molecule and analyze the emitted spectrum. This can be combined with a time-delayed pump pulse that initiates dynamics within the system. The data obtained by high-harmonic spectroscopy (HHS) carry electronic [321, 377] as well as structural [102, 378] information about the molecule. Similar to LIED, HHS requires strong fields in the probing step itself and relies on reconstruction algorithms during the data analysis. More information on HHS of molecules is summarized in [379].
An alternative spectroscopic approach involves measuring the momenta/energies of the molecular constituents after destruction of the molecules. Here, the original molecular structure before the ionization/dissociation is reconstructed. One implementation of this scheme is photoelectron spectroscopy [380, 381]. Using light with photon energies above the single-ionization threshold, an electron is ejected with a kinetic energy that equals the difference of the photon energy and the electron's binding energy in the potential of the molecule. An altered molecular structure leads to a change in binding energy, so-called *chemical shifts*, and thus can be reconstructed. Due to the different local chemical environments, the various atomic sites within the molecule can be distinguished if the orbital from which the photoelectron originates is close to the atomic core. This core-level probe intrinsically requires x-ray photon energies [71]. An overview of different core-level spectroscopic techniques is presented in figure 5.3.

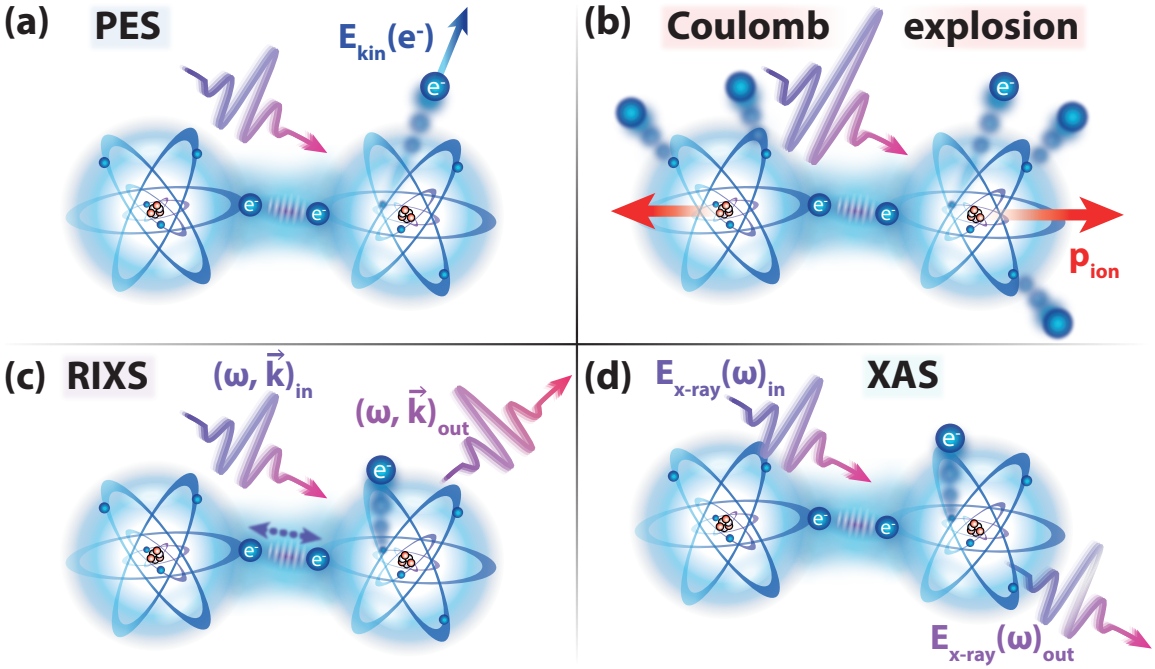

Figure 5.3.: Core-level spectroscopy methods for investigating molecular structural dynamics. **(a)** Photoelectron spectroscopy (PES). **(b)** Coulomb explosion spectroscopy. **(c)** Resonant inelastic x-ray scattering (RIXS). **(d)** X-ray absorption spectroscopy (XAS).

Another spectroscopic technique uses intense laser pulses to remove multiple electrons from the molecule at once [382, 383]. In the Born-Oppenheimer picture, the atomic nuclei remain quasi-static on the timescale of electron ejection. The highly positive charge state of the remaining molecular structure leads to an explosion of the whole molecule. Measuring the momenta of the ionic fragments in coincidence after explosion allows for a reconstruction of the initial atomic coordination.

Not only destructive, but also non-destructive spectroscopic techniques are available. They utilize the detection of the energy and wave vector of scattered photons. A whole class of measurement schemes has been developed by the synchrotron community employing scattering of soft and hard x-rays. These techniques have also been transferred to free-electron lasers as well to profit from the FEL's temporal resolution and brilliance. Resonant inelastic x-ray scattering (RIXS) [384, 385] is one example where vibrational and electronic dynamics are elucidated at the same time. In this technique, x-ray photons (typically with photon energies around an absorption edge of an atomic species in the molecule) inelastically scatter off the molecular structure. Conceptually, RIXS can be described as a resonant x-ray Raman process. The electronic and vibrational excitations that are induced in the target lead to a corresponding reduction in energy of the scattered photon as well as a potential

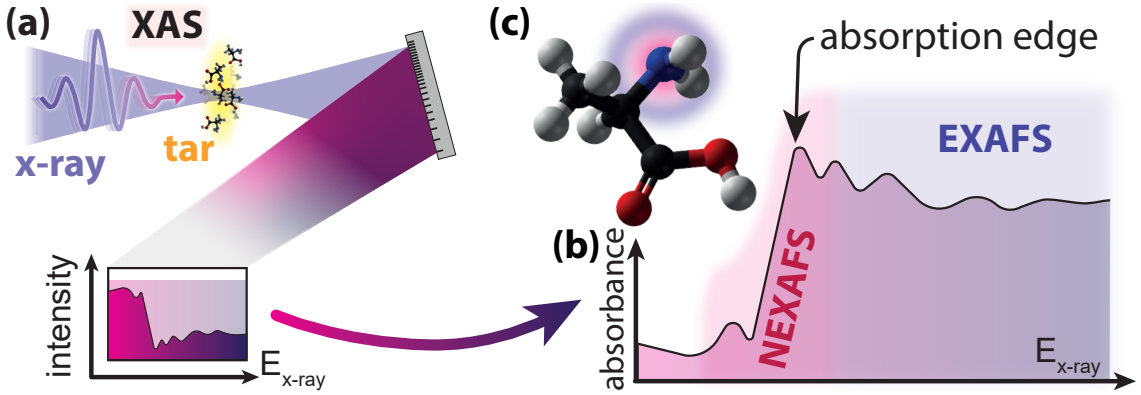

Figure 5.4.: X-ray absorption spectroscopy methods for investigating molecular structural dynamics. **(a)** XAS experimental scheme. **(b)** resulting absorbance with indicated (N)EXAFS regions around the absorption edge. **(c)** Exemplary molecule with indicated regions of NEXAFS (directly surrounding the absorber atom; *pink*) and EXAFS (first coordination shell around absorber atom; *violet*).

deflection due to momentum transfer. These changes are quantified with special high-resolution x-ray spectrometers [386–388]. Time-resolved versions of RIXS have also become available [389].

In contrast to the schemes which measure off-axis scattered x-ray photons, x-ray absorption spectroscopy (XAS) techniques spectrally characterize the x-rays after sample transmission. As connotated by the name, XAS methods rely on analysing the absorption line shapes of transitions from core-level orbitals. Due to the chemical bonding within the molecule, the energy and structure of the respective atomic resonances are altered compared to unbound atoms. This chemical shift in the transition energy can be quantified. Besides a shift in photon energy, further information is included in the absorption structure which appears near an absorption edge (near-edge x-ray absorption fine structure – NEXAFS[1]) [390] or far above the absorption edge (extended x-ray absorption fine structure – EXAFS) [391]. An illustration of the different XAS regions is presented in figure 5.4. The main criterium that differentiates NEXAFS from EXAFS is the energy of the ejected photoelectron. If the de-Broglie wavelength of the photoelectron becomes smaller than the internuclear distance within the molecule, the interactions of the photoelectron with the molecular structure can be approximated as single scattering events off the atomic constituents. This condition is often fulfilled in a region more than 100 eV above the absorption edge. The photon-energy region near the absorption edge, however, is dominated by transitions to (quasi-)bound states that have a very short lifetime. Hence, NEXAFS

[1] A synonym for NEXAFS is *x-ray absorption near-edge structure* (XANES).

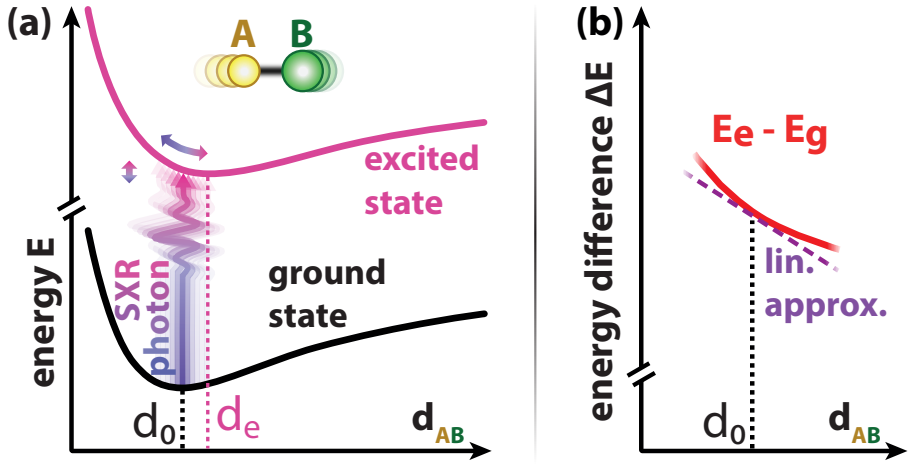

Figure 5.5.: Mapping vibrational dynamics with TR-XAS. **(a)** Electronic potential energy curves of an exemplary molecule AB. The overall molecular energy E over the internuclear distance d is shown. The ground- and an excited-electronic-state's PEC are dipole-coupled by an x-ray photon. **(b)** A dipole-transition from a different internuclear distance results in an alteration of the transition energy and thus x-ray photon energy. In general, the two PECs have different equilibrium distances (PEC minima) d_0 and d_e, respectively. In addition, they may differ in shape/width. Thus, there is a direct mapping of the transition energy in respect to the internuclear distance around the ground state's equilibrium distance d_0. Around d_0, the mapping can be approximated linearly.

provides information about the direct surrounding of the absorbing atom (e.g., bond distance and angle), while the signal of the EXAFS region is dominated by the first coordination shell of atoms around the absorbing atom. With the development of HHG-based sources in the soft x-ray region, covering multiple K, L, and M absorption edges, (N)EXAFS is becoming evermore available for table-top experiments [290, 392]. A comprehensive review of XAS is given in [74].

5.2. Vibrational metrology scheme based on TR-XAS

After the general introduction to XAS in the previous section, a more specific view on the application of XAS to elucidate molecular vibrational dynamics is given: By combining the XAS scheme with an intense, time-delayed optical pulse (e.g., in the IR spectral region), vibrational dynamics can be initiated and their time-resolved measurement is possible. In TR-XAS, the x-ray pulse probes the system via a transition from a core-level orbital. This can be described in a many-body picture as a dipole transition from the electronic ground-state PEC to an excited-state PEC as shown in figure 5.5(a). Here, the excited-state PEC is very general: it can be a (quasi-)bound electronic state or even a dissociative PEC of the ionized molecule. The

PECs of the ground and excited state have different minima positions (equilibrium bond-lengths d_0 and d_e, respectively) and vary in their general shapes and widths. Thus, the energy difference of the two PECs ΔE is not constant over the bond length d. Now, this energy difference relation $\Delta E(d)$ is mapped with x-ray photons according to the ground-state's time-dependent population distribution. This mapping is illustrated in figure 5.5(b). A linear approximation of ΔE works very well in close proximity to d_0.
The sensitivity of transient absorption spectroscopy to vibrational signatures has been exploited in multiple recent experiments in the XUV and SXR spectral regions [231, 291, 393–396]. Up to now, the smallest reported spatially resolved vibrational feature of a gas-phase molecule has been 0.6 pm [397]. In solid-state systems, few-femtometer resolution of structural changes has already been achieved with different spectroscopic and diffractive techniques [398–401] with the potential of even breaking the femtometer frontier [402, 403]. So far, though, the quantification of molecular vibrational dynamics in a time-resolved manner has remained on the picometer level or just below. Thus, the question arises, what the spatial resolution-limit of TR-XAS for characterizing molecular vibrations is. In addition, this is linked to the question how small a vibrational amplitude in an ensemble of molecules can become.

5.3. TR-XAS measurement in SF_6

To answer these questions concerning perturbative limits of molecular vibrational dynamics, a TR-XAS experiment is conducted in SF_6.

5.3.1. TR-XAS of SF_6 – the experiment

For this experiment, the SWIR few-cycle source and its configuration as well as the HHG process and the target parameters are the same as for the SWIR-intensity-dependent experiment (see section 4.2.2.1). Another similarity is the focus of the TR-XAS measurement on the S $2p$ ($2t_{1u}$) to LUMO ($6a_{1g}$) transition. Further details on the electronic structure of SF_6 are presented in figure 2.11 in the theory chapter. The vacuum beamline is set to time-delay configuration (see section 3.3.4) for the TR-XAS experiment. Overall, two separate TR-XAS measurement campaigns are conducted with slightly different settings (see table 5.1). The second measurement further explores the available parameter space by looking at an extended SWIR-first

Table 5.1.: Overview of the parameters of the two TR-XAS measurements campaigns *m#1* and *m#2*: measurement campaign number (*camp. #*), SXR-SWIR temporal overlap position within the available delay range t_0, SWIR peak intensity in the target focus I_{SWIR}, metal filter configuration after HHG, CCD integration time t_{int}^{m} during the measurement and for the HHG reference t_{int}^{ref}, the number of measurement cycles (*# cycles*) and overall measurement time t_m.

camp. #	t_0	I_{SWIR}	filter (HHG)	t_{int}^{m}	t_{int}^{ref}	*# cycles*	t_m
m#1	119.5 fs	9 TW/cm^2	1×200 nm Zr	17 s	9 s	27	16 h
m#2	63.7 fs	26 TW/cm^2	2×200 nm Zr	30 s	30 s	39	41 h

temporal region and perturbing the molecular system with a higher SWIR intensity.

The aim of the first measurement campaign is to elucidate the smallest resolvable vibrational dynamics in SF_6. Similar to the measurement protocol of the previous experiment (see section 4.2.2.3), each campaign consists of HHG-reference measurements without target, the measurement itself with a constant backing pressure of 16 mbar of SF_6 in the target cell, as well as respective dark spectra with shuttered SWIR beam. Both measurement campaigns, *m#1* and *m#2*, share further parameters: For both measurements, the time delay is scanned over a range of 232 fs with a time-step of 1.86 fs which corresponds to a 2 µm position increment of the SWIR-mirror of the split-and-delay assembly. The different time-delay positions within a scan are randomized to exclude any potential effects of drifts in laser and beamline parameters. One spectrum is acquired for each time-delay position and the randomized time-delay scan is cycled multiple times. Furthermore, 2×200 nm Zr metallic full filters are inserted in front of the SXR spectrometer for both campaigns. The SXR spectrometer CCD is set to spectral output mode (hardware-based binning) analogue to the XAS experiment in chapter 4.
The temporal SXR-SWIR overlap of the first measurement campaign (*m#1*) is set close to the middle of the overall delay range. Furthermore, the SWIR peak intensity of the focus in the target volume is reduced by setting the height of the Zr half filter after HHG such that a larger portion of the IR beam mode is covered by the half filter. This is illustrated in figure 5.6(b). Thus, the transmitted beam energy is accordingly reduced. Furthermore, the focal spot is spatially broadened in one dimension due to the Fourier-character of the target focal plane. These two factors result in a significantly reduced peak intensity of *m#1*. In the second measurement campaign *m#2*, the time-delay range is set to earlier times with the SXR mirror of

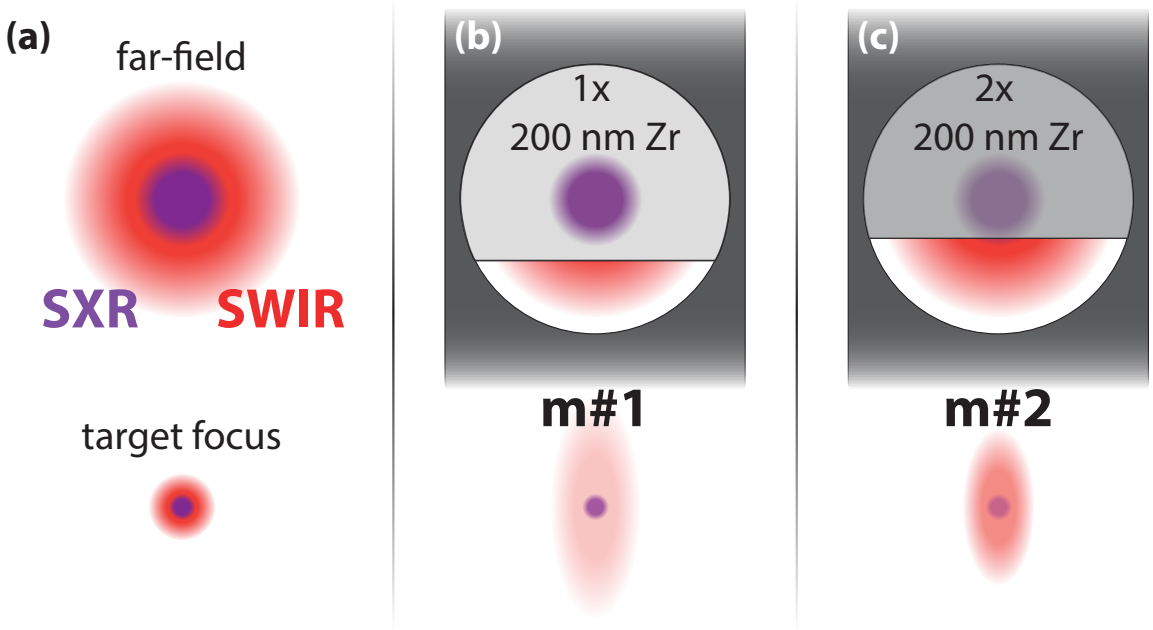

Figure 5.6.: Settings of the metallic Zr half filters for SXR/SWIR beam separation after HHG. **(a)** Unperturbed SXR and SWIR beam modes in the far field (top) and the target focus plane (bottom). **(b)** Setting of the 200 nm thick Zr half filter during the measurement campaign *m#1* with corresponding effects in the target focus plane. **(c)** Setting of the 2×200 nm thin Zr half filters during the measurement campaign *m#2* with corresponding effects in the target focus plane.

the split-and-delay mirror assembly. The SXR/SWIR spatial overlap is preserved by slightly tilting the SWIR mirror and checked with the target camera (compare figure 3.25 in the 'experimental setup' chapter). In addition, the post-HHG metallic filter assembly is changed to a double-filter to guarantee an SXR beam with no residual SWIR contamination due to micro-holes in the metallic filters. This, however, reduces the SXR flux around 170 eV by about 50% [404]. Moreover, the Zr half-filter positions are modified to allow for a higher SWIR intensity at the target as schematically shown in figure 5.6(c). Details on the determination of the SXR-SWIR time-overlap t_0, as well as on the SWIR intensity calibration of the two measurements, are given in the following paragraphs.

5.3.1.1. Temporal overlap determination

To experimentally determine the temporal overlap, the in-vacuum silicon CMOS chip (see figure B.13 in the appendix) is moved to the position of the target cell and a time-delay scan is conducted with an attenuated SWIR beam and without the Zr half filter. The resulting interferometric autocorrelation (IAC) data for both measurement campaigns, *m#1* and *m#2* are shown in figure 5.7. The fits in the plots

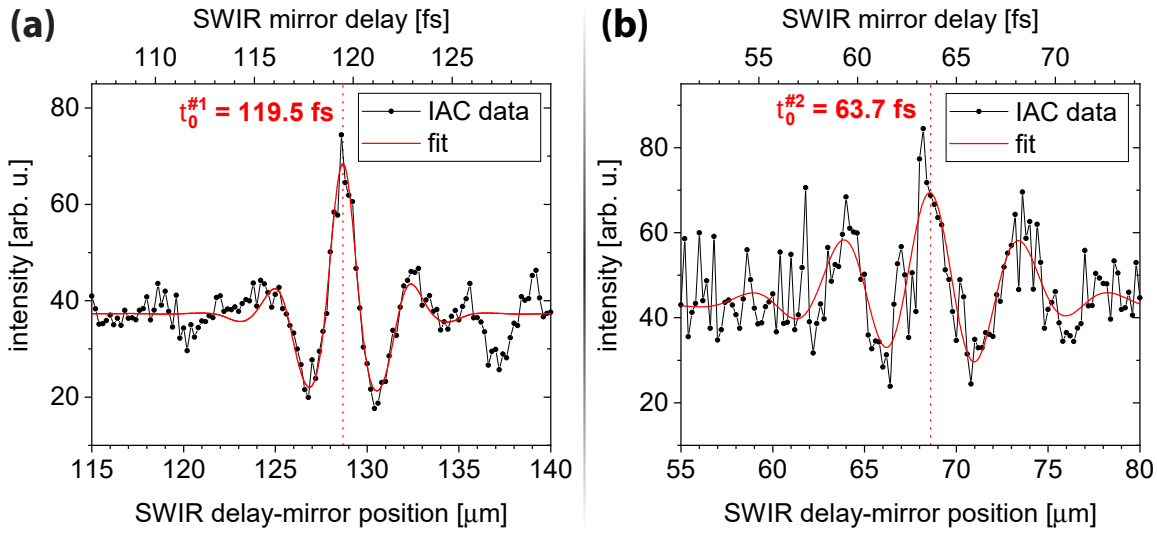

Figure 5.7.: Experimental determination of the SXR-SWIR temporal overlap position for the two TR-XAS measurement campaigns *m#1*/*m#2*, in **(a)** and **(b)**, respectively. The measurements are interferometric autocorrelation traces using the attenuated SWIR beam. This is enabled by the intrinsic TPA nonlinearity of the silicon CMOS.

show that SXR and SWIR are in temporal overlap at an SWIR-mirror position of 128.7 µm for *m#1* and 68.6 µm for *m#2*. Thus, using the position-to-time conversion of 1 µm ≙ 928.5 as (see equation (3.8) in the setup section 3.3.4), these position values translate to time-overlap values of 119.5 fs and 63.7 fs, respectively. In contrast to this SWIR-only IAC measurements, Zr half filters are inserted during the TR-XAS measurements. The additional SXR group delay of the filters can be calculated with equations (2.11) and (2.12) in the theory section 2.1.2.3 and the refractive index of Zr [405]. For one or two 200 nm-thick filters, however, this additional delay is only 19 as and 38 as, respectively, and is thus negligible here.

5.3.1.2. SWIR intensity calibration of TR-XAS

The different SWIR peak intensities at the target focus for the two measurement campaigns are determined by the energy shift of the $6a_{1g}$ doublet in SXR-SWIR temporal overlap. Here, the data set and the 5×5-Hamiltonian toy model (equation (4.3) in section 4.1.3.2) of the SWIR-intensity-dependent measurement are used as a reference. The resulting SWIR-intensity calibration plot is shown in figure 5.8. As the basic toy model only takes four excited many-body states into consideration, it deviates from the data for SWIR intensities $> 5 \times 10^{13}\,\mathrm{W/cm^2}$. This high-intensity regime, however, is not relevant for *m#1* and *m#2*. With shifts of $\Delta E_c^{\#1}$ = -27 meV and $\Delta E_c^{\#2}$ = -70 meV of *m#1* and *m#2*, respectively, this results in field strengths of

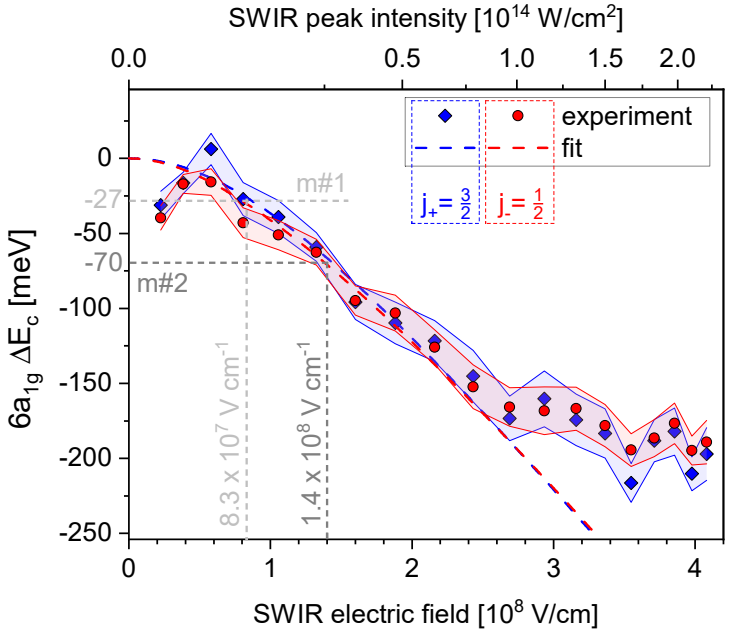

Figure 5.8.: SWIR-intensity calibration of TR-XAS measurements *m#1* and *m#2* in SF_6 by comparing the $6a_{1g}$ absorbance shifts in SXR-SWIR time overlap with the data and fit model of the SWIR-intensity scan of section 4.1.3.2 . The SWIR peak intensities used in the time-delay scans are obtained by comparison to the $6a_{1g}$ absorbance peak center $E_c(j_{+/-})$ shifts (red/blue circles/diamonds) in SXR-SWIR time overlap (compare figure 4.12). The dashed lines represent a fit based on the quantum-mechanical toy model Hamiltonian (4.3) in section 4.1.3.2. For the two TR-XAS measurements, the SWIR intensities for the data sets *m#1/m#2* are determined: The lower-intensity measurement (*m#1*) has a time-zero shift of $\Delta E_c^{\#1}$ = -27 meV which translates to an electric field strength of $\mathcal{E}_{IR}^{\#1} = 8.3 \times 10^7$ V/cm. The second, higher-intensity data set (*m#2*) shows a time-zero offset of $\Delta E_c^{\#2}$ = -70 meV. Consequently, the peak field strength is determined to be $\mathcal{E}_{IR}^{\#2} = 1.4 \times 10^8$ V/cm.

$\mathcal{E}_{IR}^{\#1} = 8.3 \times 10^7$ V/cm and $\mathcal{E}_{IR}^{\#2} = 1.4 \times 10^8$ V/cm. Thus, the IR peak intensities are calculated to be $I_{IR}^{\#1} = 9.1 \times 10^{12}$ W/cm^2 and $I_{IR}^{\#2} = 2.6 \times 10^{13}$ W/cm^2.

5.3.2. TR-XAS data and evaluation

5.3.2.1. TR-XAS raw data processing

The raw data processing is conducted in a manner similar to the previous experiment (see section 4.2.3.1): First, all spectra are dark-image corrected. To make sure that the TR-XAS measurement is free from any systematic artifacts due to the mechanical mirror movement of the time-delay scan itself, the reference data are acquired with a time-delay scan routine as well. A global third-order polynomial fit is applied to the non-resonant background. As no time-dependent effect on the non-resonant absorption below the S $L_{2,3}$ edge is found, the spectra are normalized to this region.

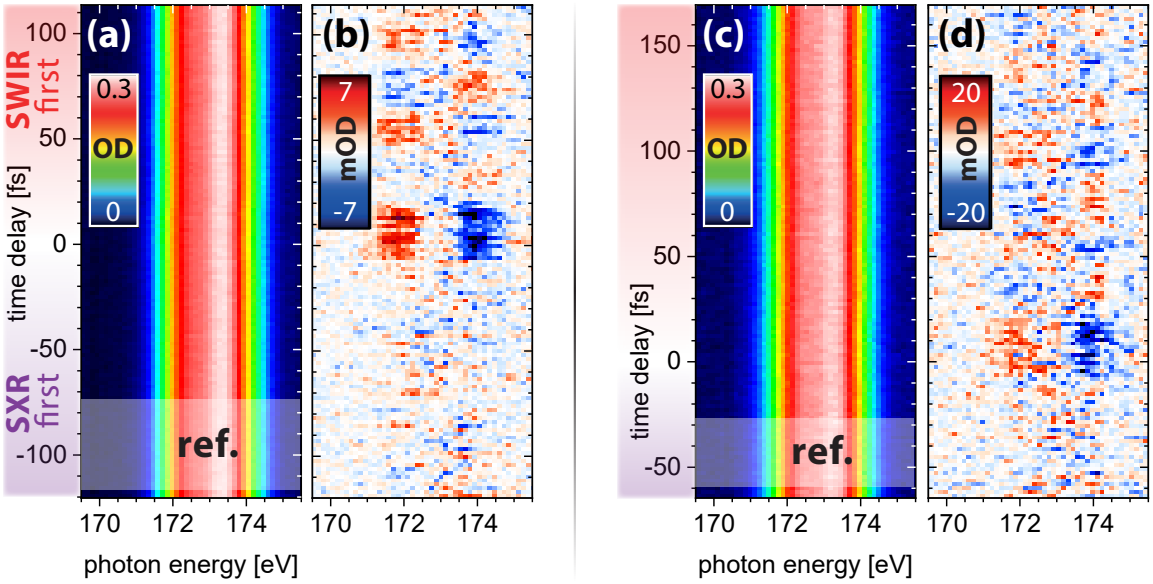

Figure 5.9.: TR-XAS (differential) absorbance data of the $6a_{1g}$ doublet resonance in SF_6. **(a)** Resonant absorbance over SXR-SWIR time-delay for measurement campaign *m#1* ($I_{SWIR}^{m\#1} = 9\,\mathrm{TW/cm^2}$). **(b)** Differential absorbance of *m#1* by subtracting the absorbance mean of the indicated reference region (*ref.*). **(c)** Resonant absorbance over SXR-SWIR time-delay for measurement campaign *m#2* ($I_{SWIR}^{m\#2} = 26\,\mathrm{TW/cm^2}$).**(d)** Differential absorbance of (c) by subtracting the absorbance mean of the indicated reference region (*ref.*).

A normalization factor based on an averaged static absorption measurement is used. The small differences in SXR counts are caused by variations in the SXR flux. Now, for all TR-XAS spectra, the OD is calculated using equation (2.48). The spectra are time-delay sorted by employing the position value of the SWIR-mirror-actuator feedback of the 4SM assembly. Finally, all absorbances in the same time-delay bin are averaged. Due to the additional post-HHG Zr filter and the reduced integration time and number of spectra at each data point compared to the SWIR-intensity measurement, the signal-to-noise ratio in the TR-XAS measurements is only sufficient for a physical interpretation of the $6a_{1g}$ spin-split doublet region. Thus, the higher-energy $L_{2,3}$-edge associated resonances (e.g., $2t_{2g}$) cannot be analyzed. The resulting $\mathrm{OD}(\omega, \tau)$ traces around the $6a_{1g}$ resonance are presented for both measurement campaigns *m#1*/*m#2* in subfigures 5.9(a) and 5.9(c), respectively. There, no time-dependent signature is visible by eye. Hence, to unveil any SWIR-induced dynamics, differential absorbance spectra $\Delta\mathrm{OD}(\omega, \tau)$ are calculated by taking the SXR-first time-delay region as reference. The respective spectral reference is calculated by a mean over $\mathrm{OD}(\omega, -115.8 \leq \tau \leq -74.9\,\mathrm{fs})$ for *m#1* and $\mathrm{OD}(\omega, -59.9 \leq \tau \leq -28.4\,\mathrm{fs})$ for *m#2*. Subfigures 5.9(b) and 5.9(d) present the resulting differential absorbances

of *m#1* and *m#2*. A clear time-dependent oscillatory signature is visible in the differential absorbance traces for the SWIR-first region. Looking at the relative scales of (differential) ODs explains their invisibility in the absorbance plots: While the maximum resonant absorbance is around 0.3 OD, the changes in OD are in the low milli-OD regime.

5.3.2.2. Denoising using singular value decomposition

Due to the small relative dynamical signatures, a denoising of the data is conducted to enhance the SNR. This denoising is based on the fact that the investigated resonances and their differences are comparably broad in photon energy. Also, the dynamical features are expected to be on the time scale of the pulse or longer[2]. Among the common denoising techniques are Fourier-based methods [60, 406] and techniques that use principle component analysis [407] or singular value decomposition (SVD) [408]. Here, the SVD approach is applied. In short, SVD factorizes a two-dimensional $(m \times n)$ matrix Y (e.g., $\Delta OD(\omega, \tau)$):

$$Y = U\,S\,V^T\ , \tag{5.1}$$

with U $(m \times n)$ containing the left singular vectors $\{\vec{u_k}\}$ as its columns. The matrix S $(n \times n$, diagonal) is composed of the singular values s_k sorted from highest to lowest value and the matrix V^T comprises the right singular vectors $\{\vec{v_k}\}$ as rows. Now, the rank-l matrix that best approximates Y at reduced complexity is given by

$$Y^{(l)} = \sum_{k=1}^{l} \vec{u_k}\, s_k\, \vec{v_k}^T\ . \tag{5.2}$$

Thus, by only including certain principle components, an effective disentanglement between signature patterns and noise can be achieved. For the TR-XAS data, the SVD components $2 < k < 50$ are used for extracting the denoised signal. This selection of principle components proved to be most efficient in filtering out broad, stripe-like fluctuations as well as pixel-sized noise. Figure 5.10 shows a comparison of the differential absorbance for the *m#1* data set. More mathematical details of SVD with scientific applications can be found in [409].

[2] Here, no SWIR sub-cycle effects are resolved in the measurement. The CEP is not stabilized and thus effectively averaged during the experiment [100].

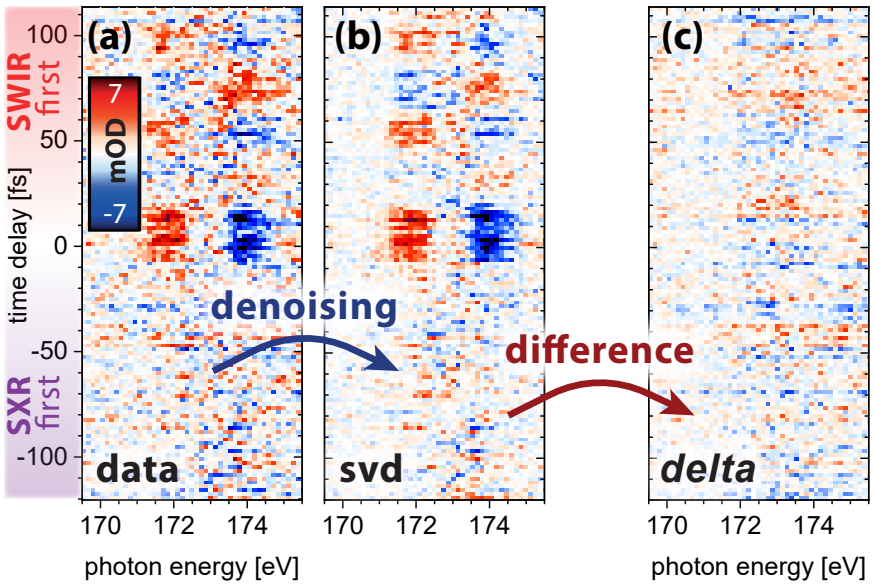

Figure 5.10.: Denoising of the TR-XAS data sets using SVD. **(a)** ΔOD of *m#1* from the raw data (compare figure 5.9). **(b)** ΔOD of *m#1* after SVD denoising. **(c)** Difference of the denoised ΔOD data and the raw ΔOD data.

5.3.2.3. Resonance fit procedure for TR-XAS data

For a further analysis of the time-dependent signatures in the differential absorbances in subfigures 5.9(b) and 5.9(d), fits of the $6a_{1g}$ absorbance data (subfigures 5.9(a) and 5.9(c)) are conducted. The same Voigt-fit model as in the SWIR-dependent measurement is used (see section 4.2.3.2). Here, however, the challenge is to correlate the small low-SNR absorbance differences with specific fit parameters. While a fit with all parameters of the Voigt model being unrestricted results in a precise description of the data, the physical insights are limited as no clear trend in any fit parameter is visible. Thus, the approach is to investigate which of the Voigt fit parameters (peak area, width or resonance position), is able to describe the measured data best on its own. A comparison of the $\Delta OD(\omega, \tau)$ resulting from the data fit procedure is depicted in figure 5.11. Besides visual agreement between the differential absorbances of the experiment and the fits, another quantifiable distinction criterium is the deviation of the fit from the data. This is given by the so-called *residual sum of squares* (RSS). Here, the RSS definition from [340] is utilized:

$$\mathrm{RSS} = \sum_{k=1}^{n} (O_k - E_k)^2 \tag{5.3}$$

with the number of pixels n, the measured spectral intensity at the k-th pixel O_k and

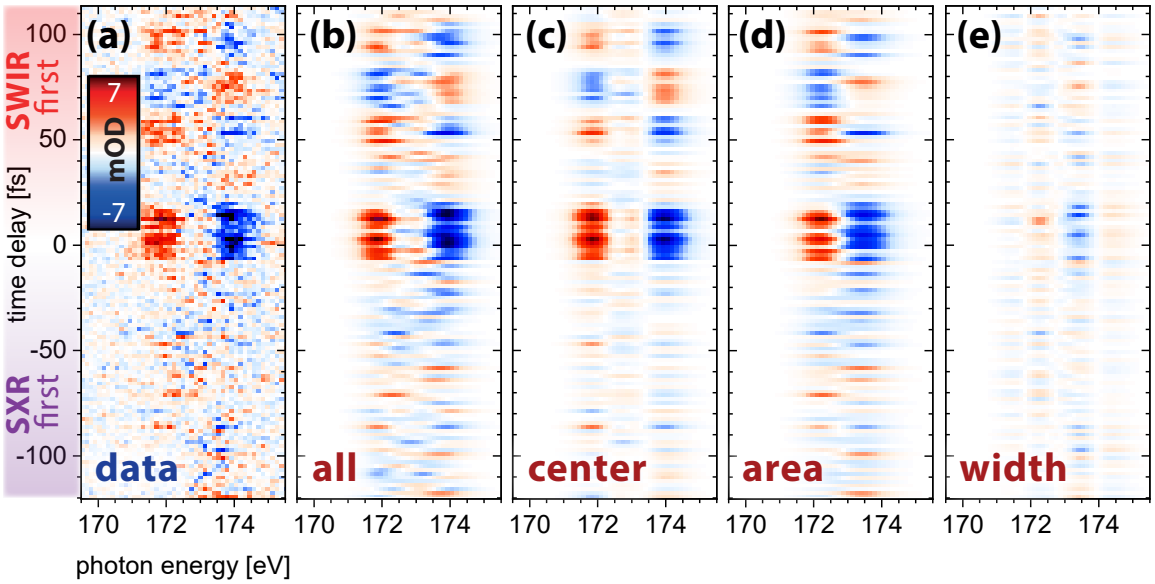

Figure 5.11.: Differential absorbance of the $6a_{1g}$ absorbance doublet in SF_6 over SXR-SWIR time delay for different free parameters of the Voigt fit. **(a)** Differential absorbance of the measured *m#1* data set for comparison. Differential absorbance resulting by a fit with **(b)** all parameters, **(c)** the peak centers, **(d)** the peak areas, **(e)** the peak widths being unrestricted.

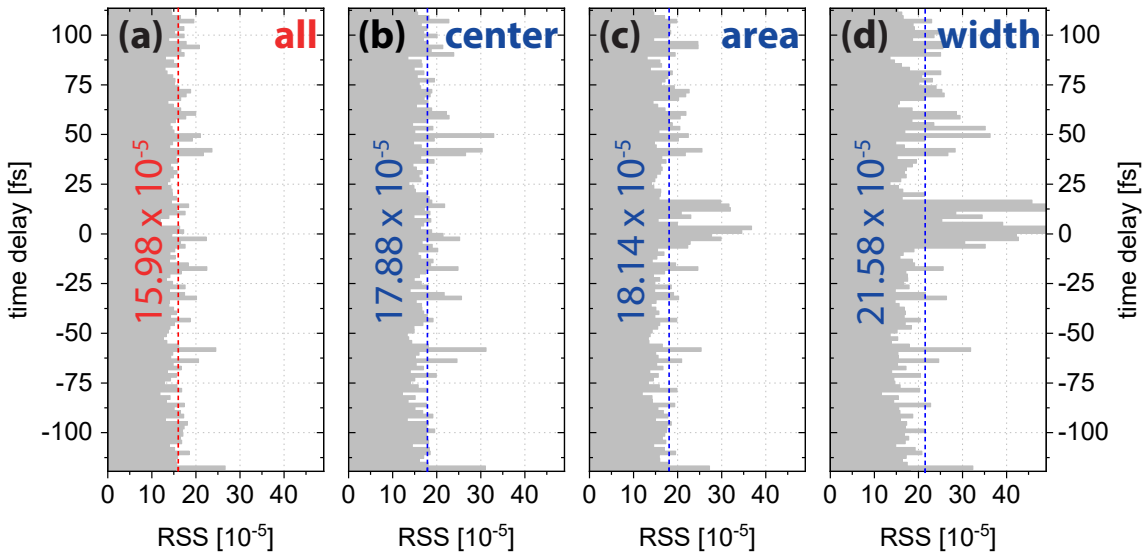

Figure 5.12.: Voigt fit RSS for different unrestricted fit parameters. The mean RSS is shown as dashed vertical line and the mean value is given for **(a)** all parameters, **(b)** peak positions, **(c)** peak areas, **(d)** peak widths as free fit parameters.

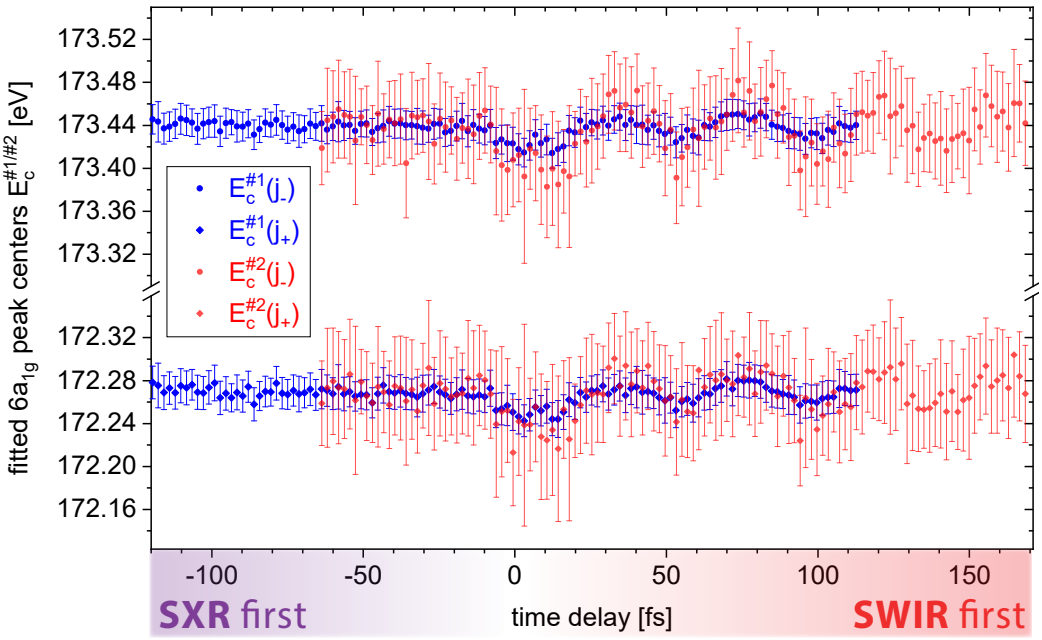

Figure 5.13.: Voigt-fit results of the $6a_{1g}$ spin-orbit split resonance center energies E_c for both $6a_{1g}(j_{\pm})$ doublet peaks and both measurement campaigns *m#1* and *m#2*.

the respective fit value E_k. The RSS values for each fitted absorbance time-step and all free-fit-parameter variations are depicted in figure 5.12. The delay-time-averaged RSS is given in the plots as well. The visual differential absorbance comparison in figure 5.11 shows that the resonance position as free fit parameter can best describe the measured signatures. In contrast to the 'peak area' and the 'width' case, the position parameter is even capable of emulating the measured differential absorbance around the time-overlap region. This is quantitatively supported by the RSS analysis in figure 5.12. The peak-position parameter shows a relatively constant RSS over the whole time-delay range and has the lowest mean RSS, which is even close to the completely unrestricted Voigt fit. Based on this analysis of the Voigt fit, all following physical conclusions will be drawn from fits with unrestricted peak center positions.

5.3.2.4. $6a_{1g}$ resonance shifts in SWIR-perturbed SF_6

As a consequence, the Voigt-fit model with the center positions of $6a_{1g}$ doublet peaks as free parameters is applied to both data sets *m#1* and *m#2*. The resulting resonance energies E_c for each campaign and each spin-orbit absorbance peak are shown in figure 5.13. Notably, the calculated peak-energy differences ΔE_c of the two peaks within the absorbance doublet, as well as the two measurement campaigns can be matched very well as shown in figure 5.14. Only the y-axis had to be scaled in

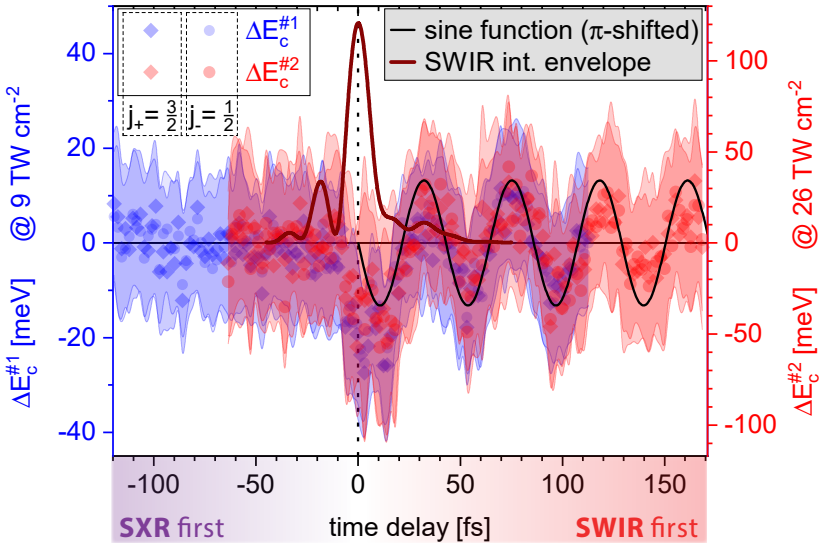

Figure 5.14.: Comparing $6a_{1g}$-peak shift dynamics $\Delta E_c^{\#1/\#2}(\tau)$ of the TR-XAS experiments to a π-shifted sinusoidal function (black line) with a period of 43 fs. The center-position differences ΔE_c from both spin-split peaks $j_\pm$ of the two measurements, *m#1* (left, blue y-axis) and *m#2* (right, red y-axis), are merged into one graph. Details on the experimental data can be found in figure 5.13.

figure 5.14 to account for the different oscillation amplitudes of the two different SWIR-intensities of *m#1* and *m#2*. The larger uncertainties in the fit results of *m#2* in figure 5.13 are due to the reduced SXR flux which is caused by the additional Zr half filter. As one can see in the relative resonance energies for the SXR-first temporal range of *m#1* (see figure 5.13), though, there is no quantifiable impact of potential SWIR leakage due to micro-holes in the single Zr half filter of measurement *m#1*. Hence, the results of *m#1* and *m#2* are very well comparable and can be matched without problems. Notably, the absorbance shifts especially of the low-SWIR-intensity campaign *m#1* are sub-10 meV. This is a fraction of the photon-energy resolution of a single pixel on the CCD of the SXR spectrometer (130 meV per pixel at 173 eV). That emphasizes the importance of the high statistics of this measurement, enabled by the long overall measurement duration under stable laser and beamline conditions.

5.3.3. Discussion and comparison with theory

Looking heuristically at figure 5.14, one can differentiate two distinct signatures over the time-delay range: For larger time-delays $\tau \gg 0$ fs, a damped sinusoidal oscillation is visible. In contrast, a distinct shift to lower photon energies is observed around the time overlap $\tau = 0$ fs. As a first step to extract more information about the oscillatory feature, a comparison with a sinusoidal function is conducted as shown in

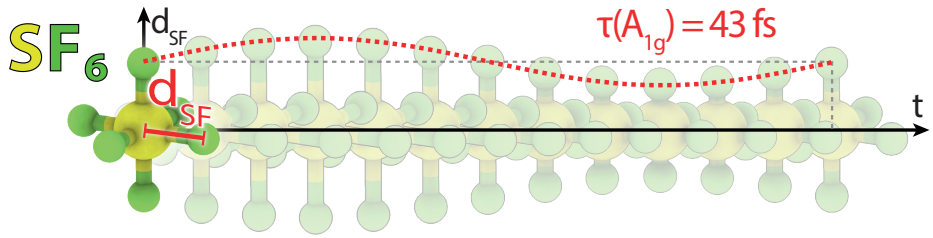

Figure 5.15.: Illustration of the first symmetric breathing mode A_{1g} in SF_6 (for an overview of the normal modes, see figure 2.12 in the theory chapter). The period duration is $\tau(A_{1g}) = 43\,\text{fs}$.

figure 5.14. Multiple physical insights are revealed from this basic comparison: First, the oscillation period is $(43 \pm 2)\,\text{fs}$, this translates to a wavenumber of $(776 \pm 36)\,\text{cm}^{-1}$. As the oscillatory signature is only measured for SWIR-first delays, this is a hint towards SWIR-induced vibrational dynamics. Comparing the oscillatory signatures with the known vibrational normal modes of SF_6 shown in figure 2.12 in the theory section 2.6, it is evident that the oscillatory period matches the one of the Raman-active first symmetric breathing mode A_{1g} [102, 410]. The A_{1g} vibrational mode is illustrated in figure 5.15. Furthermore, figure 5.14 shows that the oscillatory behavior can be well described by a π-shifted sine function. As pointed out by Wei *et al.* [397], this is a clear sign that the observed vibrational dynamics indeed originate from a Raman-excitation process. Also, no phase shift for the two different SWIR-intensity measurements *m#1/m#2* is observed, indicating that solely Raman-induced dynamics take place. To analyze the deviations of the $E_c^{m\#1,2}$ around the temporal overlap $\tau = 0\,\text{fs}$, figure 5.14 also shows the SWIR pulse intensity envelope, that is measured right before the experiment (see figure 4.6 in the experimental section 4.2.2.1). Here, the correlation between the SWIR intensity and the $E_c^{m\#1,2}(\tau)$ deviation from the sinusoidal function is striking. This is a strong indication of a transient shift of the electronic structure due to the SWIR field. Such transient energy alterations are induced by AC Stark shifts as described in the theory section 2.4.2. Furthermore, the SWIR intensity calibration plot (figure 5.8) already quantified this shift for the SXR-SWIR time-overlap in figure 5.8. The theory that is used for this plot (compare section 4.2.3.3) only includes electronic states and properties, but no explicit structural information of the molecule. Figure 5.16 revisits the calibration plot and clearly shows that the TR-XAS measurements are in the quadratic AC Stark regime. Thus, the corresponding shift to lower photon energies is SWIR-intensity dependent. This heuristic analysis already shows that the signatures in the TR-XAS measurements can be clearly separated into electronic and vibrational ones. While the electronic

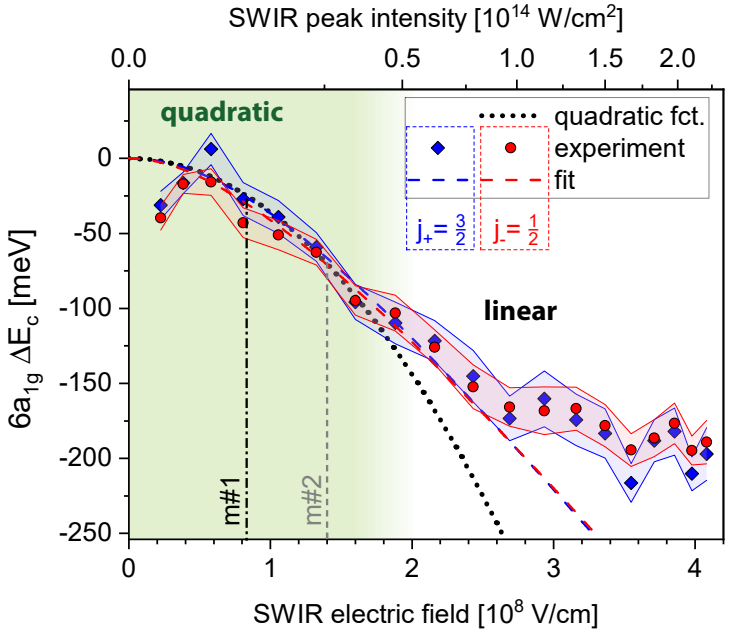

Figure 5.16.: Resonance shifts due to laser-dressed electronic many-body states. Shifts in the resonance energies of the $6a_{1g}$ doublet in time overlap τ = 0 fs from the SWIR intensity-scan (see figure 5.8 and figure 4.12). Here, a clear transition from the low-intensity, quadratic AC Stark effect to the linear AC Stark effect around $5 \times 10^{14}\,\mathrm{W/cm^2}$ is visible (compare theory section 2.4.2). The region of the quadratic AC Stark is illustrated in light green. As the black, dotted quadratic guide to the eye shows, the TR-XAS experiments are well within the quadratic AC Stark regime.

features are only transiently visible in the presence of the SWIR pulse, the vibrational signatures are much longer lived and dynamically originate from the highest SWIR peak intensity. These observations can be viewed as examples for Born-Oppenheimer dynamics (see section 2.5.1). The aim of the TR-XAS measurements in SF_6, though, is to target a physical understanding way beyond these simple pictures. Further questions arise, for example:

- How exactly are the vibrational dynamics initiated?
- What is the role of electron-vibrational coupling dynamics?
- Can we quantify and microscopically understand the electronic and vibrational dynamics?

5.3.3.1. Combined many-body quantum-mechanical and classical simulation

To address these questions, a more thorough approach is needed. For this purpose, the many-body quantum-mechanical simulation that is used for elucidating the

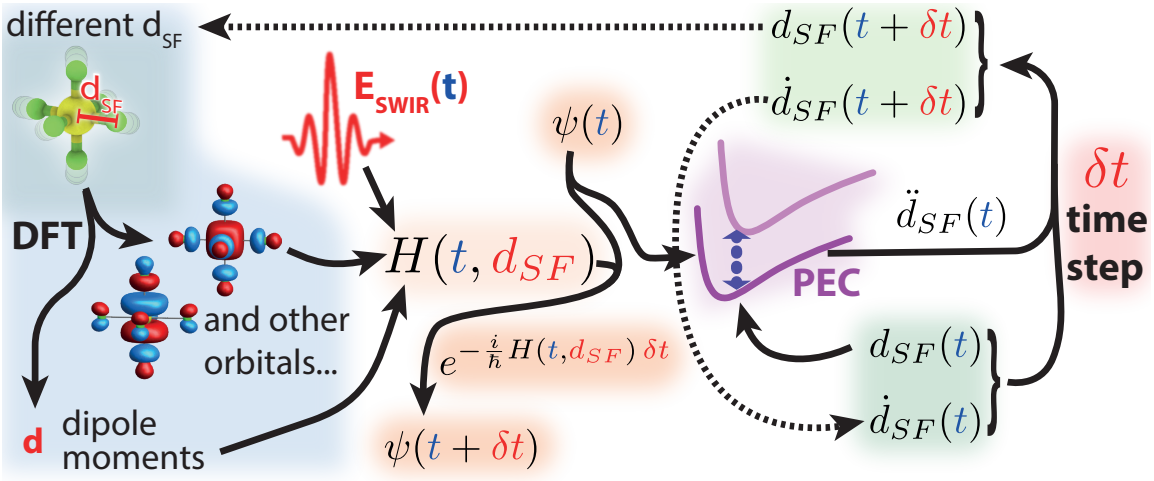

Figure 5.17.: Procedure of the combined many-body quantum-mechanical and classical simulation. First, molecular orbitals and dipole moments are calculated for different internuclear distances d_{SF} via DFT. The DFT results in combination with the SWIR electric field $E_{SWIR}(t)$ serve as input for the Hamiltonian matrix $H(t, d_{SF})$. The electronic wave function of the system $\psi(t)$ is propagated in time with H as input for the TDSE. The ground- and excited-state PECs are derived from $\psi(t)$ for time t. Afterwards, the SXR absorption spectrum at time t is determined by a dipole coupling of the two PECs at internuclear distance d_{SF}. For propagating the nuclear dynamics in time as well, the force on the nuclei can be calculated from the PEC's gradient at d_{SF}. This force leads to an acceleration $\ddot{d}_{SF}(t)$. From the position d_{SF}, the velocity $\dot{d}_{SF}(t)$ and the acceleration $\ddot{d}_{SF}(t)$, the new position and velocity after a time step δt can be calculated, $d_{SF}(t + \delta t)$ and $\dot{d}_{SF}(t + \delta t)$, respectively. Now, with the updated $d_{SF}(t + \delta t)$, an interpolation of the pre-calculated DFT results acts together with $\dot{d}_{SF}(t + \delta t)$ and $\psi(t + \delta t)$ as input for the simulation of the next time step.

electronic dynamics of the SWIR-intensity scan (see section 4.2.4.2) is extended. It is complemented with a classical force approach to include nuclear dynamics as well. Figure 5.17 schematically shows the procedure of this simulation which was conducted by Dr. Simon Heinze and Prof. Dr. Maurits Haverkort from Heidelberg University. First, properties of the electronic structure of SF_6 for different d_{SF} interatomic distances are calculated via the DFT code FPLO [343, 344]. The resulting MOs up to the $6a_{1g}$ LUMO and dipole moments as well as the SWIR electric field $E_{SWIR}(t)$ are used as input for the Hamiltonian matrix H. Then, $H(t, d_{SF})$ is used to propagate the electronic wave function of the system, $\psi(t)$ in time via the time-dependent Schrödinger equation. The propagated $\psi(t + \delta t)$ is used in the next time-step iteration of the simulation. The ground- and core-level excited PECs are derived from $\psi(t)$ and the corresponding absorption spectrum at time t is determined as the PECs' energy difference at internuclear position $d_{SF}(t)$. Now, the simulation switches to a classical perspective to propagate the nuclear dynamics in time as well: The fluorine nuclei are approximated as classical particles and the PEC gradient at the position of the fluorine

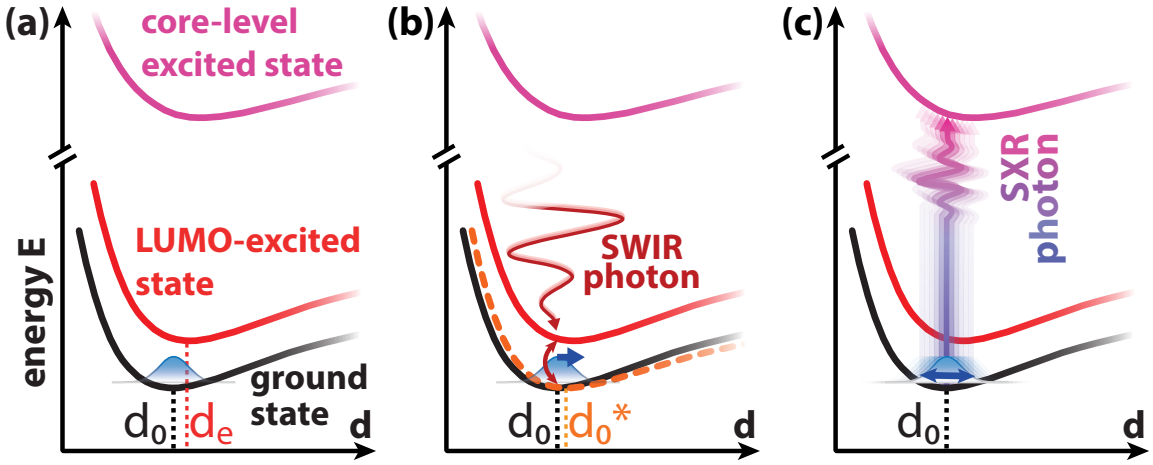

Figure 5.18.: A mixing of the electronic many-body ground state with the HOMO-LUMO excited state results in a laser-dressed ground-state PEC. As the laser-dressed PEC typically has a lower dissociation energy, this mechanism is called bond softening. **(a)** Unperturbed ground-state PEC with nuclear wave-function probability density situated around the equilibrium distance d_0. **(b)** Bond softening in the presence of the SWIR pulse. Now, the nuclei are not located at the laser-dressed PEC's minimum d_0^* any more. Thus, according to the PEC's slope, a force acts upon the nuclei. **(c)** The PEC returns to its initial, unperturbed form after the full duration of the SWIR pulse. The nuclear wave packet oscillates in the PEC. This illustrates the initiation of a Raman-active vibration via bond softening. The vibrational wave packet is probed by SXR photons (see also figure 5.5).

atoms results in a force and respective acceleration of the nuclei, $\ddot{d}_{SF}(t)$. Taking current position, velocity and acceleration of the fluorine atoms into consideration, a new position $d_{SF}(t + \delta t)$ and velocity $\dot{d}_{SF}(t + \delta t)$ after a time step δt are calculated. These values act as inputs for the calculation of the next time step iteration, as the electronic structure follows the nuclei immediately within the BOA. The time propagation as well as the extraction of simulated absorbances $\mathrm{OD}(\omega, t)$ is conducted with the QUANTY code [345, 346].

The Hamiltonian gives insights into the origin of the Raman vibrational excitation process itself (see figure 5.18): The dipole coupling of the electronic ground state with the first excited electronic states is necessary to induce vibrational dynamics. In the many-body picture, these low-energy electronic excited states are populated via off-resonant HOMO to LUMO dipole couplings by the SWIR field. As illustrated in figure 5.18(b), this alters the effective ground-state PEC and shifts the PEC's minimum. This is known as bond softening [397, 411–413], as it usually leads to a distortion of the PEC that lowers the dissociation energy. Now, the nuclear wave packet is not located around the PEC's minimum any more and hence feels the PEC's gradient and a respective force and acceleration. The bond-softening only occurs transiently in the presence of the SWIR pulse and initiates the molecular

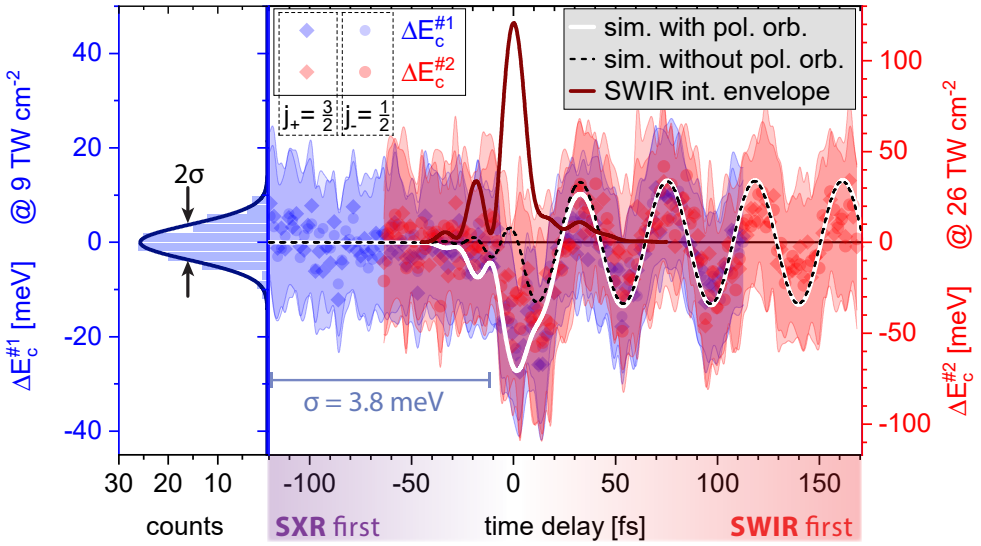

Figure 5.19.: Comparison of experimental differential absorbance resonance shifts $\Delta E_c^{\#1/\#2}$ (as shown in figure 5.14) with simulation results. Here, the simulation results without the polarizing orbitals (black dotted) are shown as well as the simulation results that include the polarizing orbitals (solid white line). The SWIR-pulse intensity envelope is depicted as solid dark red line. Furthermore, the experimental statistics for the SXR-first region of the *m#1* data is given as a histogram on the left-hand side. A standard deviation of σ = 3.8 meV can be extracted from the distribution.

vibration. Afterwards, the ground-state PEC returns to its original shape and the nuclei-dynamics evolve according to a damped harmonic oscillator. The damping comes into play due to the dephasing of the nuclear wave packet. This dephasing can be caused by anharmonicity of the PEC [414]. While the anharmonicity of the potential is included in the simulation, only A_{1g} vibrations are accounted for in the simulation and hence the damping is neglected.

The peak positions are determined from the numerically calculated TR-XAS simulation absorbances. Figure 5.19 shows the resonance shift ΔE_c for the experimental conditions of the lower SWIR-intensity measurement campaign *m#1*. The black-dashed line in figure 5.19 represents the simulation that takes the measured SWIR profile (solid red line) into consideration. The region of longer time delays $\tau \gg 0$ fs with its oscillatory shifts is well reproduced besides its damping. In this experiment, the nuclear wave packet dephasing is not at the center of interest. Therefore, the damping of the oscillatory signatures is not included in the simulation and remains subject for future experimental investigations ideally with an accessible time-delay range of picoseconds. The region close to time overlap τ = 0 fs, however, shows major discrepancies in comparison to the experimental data. As noted earlier, transient electronic signatures are expected in the region of the SXR temporal overlap with

the SWIR. To include these AC Stark shifts, a dipole coupling of the LUMO to higher unoccupied states is added to the theory. This is equal to the polarizing-orbital (see figure 4.5) approach in the SWIR-intensity-scan section 4.2.1. Finally, including the polarizing orbitals in the simulation (white solid line in figure 5.19) leads to a precise agreement with the experimental data. To summarize, this combined quantum-mechanical and classical theoretical approach can replicate the electronic and vibrational signatures of the measured data. Moreover, it provides a basis for understanding the electronic-vibrational coupling dynamics that initiate the molecular vibrations.

5.3.3.2. Perturbative vibrational excitation

After ensuring that the simulation matches the experimental observations as depicted in figure 5.19, further analysis reveals deeper physical insights into the initiated vibrational dynamics within this small molecular quantum system. Here, information about the nuclear wave functions and their dynamics are an interesting aspect. One parameter which is closely linked to nuclear wave functions is the population of individual vibrational basis states, which is given by the absolute square of the wave function's prefactor. To get a feeling for nuclear wave functions and populations, a two-level vibrational toy model of a harmonic oscillator is considered. This scenario is depicted in figure 5.20(a). In very good approximation, the electronic PEC can be assumed as a harmonic potential for the ground- and first excited vibrational state. The resulting solutions of the quantum-mechanical harmonic oscillator are given in section 2.2.1. With the ground- and first-vibrationally-excited states, $|\psi_0\rangle$ and $|\psi_1\rangle$, respectively, one can formulate the mixed wave function $|\psi\rangle$ to be

$$|\psi\rangle = \sqrt{1 - |a|^2}\ |\psi_0\rangle + a\ |\psi_1\rangle\ , \tag{5.4}$$

with the population coefficient a ($0 \leq |a|^2 \leq 1$). To get an idea for the expected nuclear wave-function dynamics, figures 5.20(b)-(e) show the time-dependent probability density $\left|\psi(t,d)\right|^2$ over the internuclear distance d and time t. Counter-intuitively to a classical vibration, the quantum-mechanical probability density does not show any dynamics for the extreme case of a fully populated excited state ($|a|^2 = 100\%$) in figure 5.20(b). It exhibits that the probability to find the nuclei left or right of d_0 is equally high, but zero to find the fluorine nuclei at their original equilibrium position d_0. For a population transfer of $|a|^2 = 50\%$, a distinct dynamical evolution

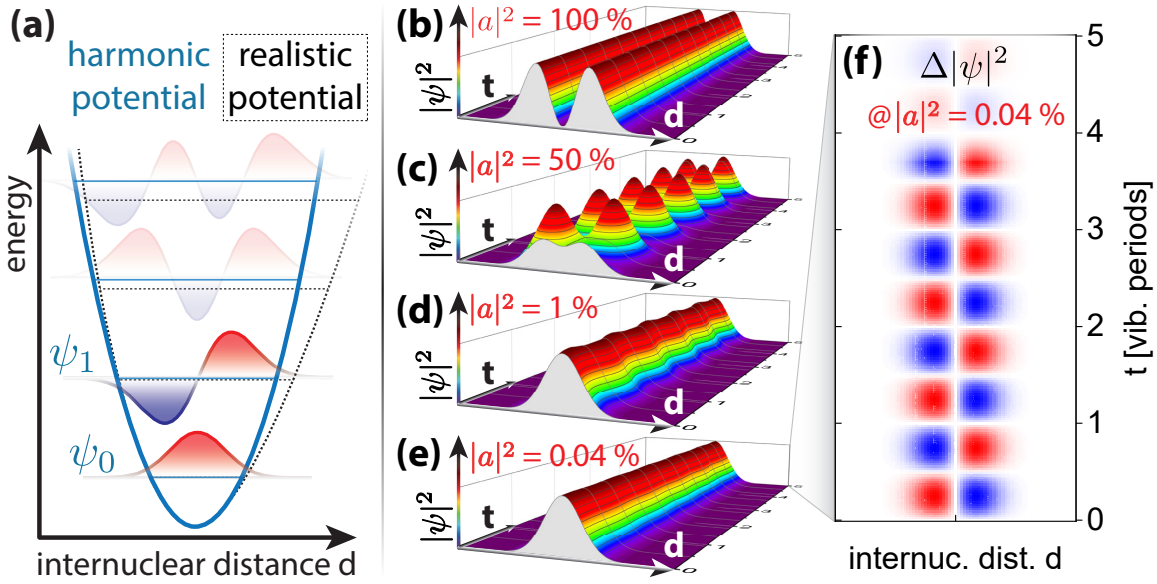

Figure 5.20.: Nuclear wave functions and populations of a two-level quantum-mechanical harmonic oscillator. **(a)** Scheme of a harmonically approximated PEC with the ground and first-excited nuclear wave function, ψ_0 and ψ_1, respectively. (b)-(e) Probability-density dynamics of the mixed nuclear wave function ψ for an excited-state population of **(b)** $|a|^2$ = 100%, **(c)** $|a|^2$ = 50%, **(d)** $|a|^2$ = 1% and **(e)** $|a|^2$ = 0.04%. **(f)** Differential probability density map for a population of $|a|^2$ = 0.04%.

of the probability density is observed in figure 5.20(c). Here, a clear alteration of the peak in the probability density can be seen every half vibrational period. This *quantum-hopping* behavior has no classical equivalent. Going towards small, perturbative excitations, figure 5.20(d) illustrates the case $|a|^2$ = 1%. In contrast to the previously discussed non-perturbative $|a|^2$ = 50% case, there is no distinct probability-density-amplitude modification visible anymore. Only a periodic shift of a ground-state-like probability density can be observed. Thus, in the perturbative excitation limit, quantum mechanical vibrations show a quasi-classical behavior. For even smaller excitations like $|a|^2$ = 0.04%, significant dynamics of the probability density can no longer be visually observed in figure 5.20(e). Plotting the differential probability density as in figure 5.20(f), though, transforms the marginal shifts into a clearly visible oscillatory signature.

Now, with the knowledge of the expected probability density dynamics induced by a certain amount of vibrational excitation, the excited-state population which results from the simulation is discussed. Figure 5.21 shows the calculated population dynamics for the lower SWIR-intensity measurement *m#1* in combination with the SWIR pulse shape. While one would expect an error-function-like behavior of the excited-state population for a Gaussian excitation pulse, the calculation includes the measured SWIR

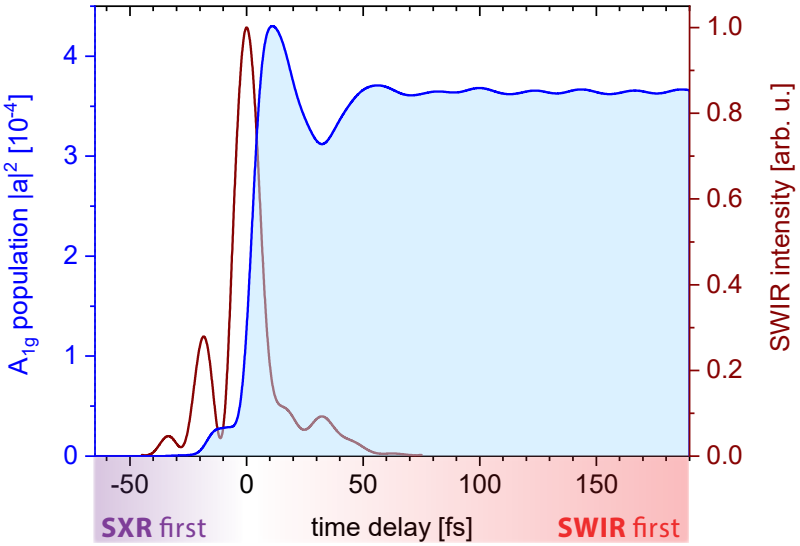

Figure 5.21.: Excited vibrational state population dynamics $|a|^2(\tau)$ extracted from the simulation for the *m#1* TR-XAS data set. After perturbative excitation via the SWIR pulse, the coherent population (blue solid line) of the A_{1g} vibrational mode converges to $|a|^2 \approx 0.035\%$. The SWIR intensity envelope is shown as well (dark red solid line).

pulse structure and thus shows additional wiggles in figure 5.21. This demonstrates that the presented TR-XAS measurement *m#1* indeed populates the symmetric breathing mode in the perturbative limit (compare figure 5.20). Interestingly, this impulsive-stimulated-Raman-excitation-related vibrational population turns out to be much smaller than the thermal population at room temperature (around 300 K). Using the Boltzmann distribution (equation (2.59) in the theory chapter) the thermally-induced A_{1g} population calculates to $|a|^2_{300K} = 2.4\%$. A visual comparison between the ISRE-induced and the thermal population is presented in figure 5.22(c). The key to resolve a vibrational excitation which is 60-times smaller than the statistical population at room temperature is the coherent character of the ISRE. Thus, the ISRE-induced signature can be separated from the incoherent thermal vibrational background.

5.3.3.3. Femtometer-scale vibrations

As mentioned in the introduction of this chapter, the main aim is to precisely measure and quantify smallest molecular vibrations. Using the DFT-based PECs of A_g-symmetric vibrations in SF_6, the respective mapping curve which links the SXR transition energy shift to the dynamics in atomic structural coordination is calculated. The basis thereof has been established in the previous figure 5.5 in the

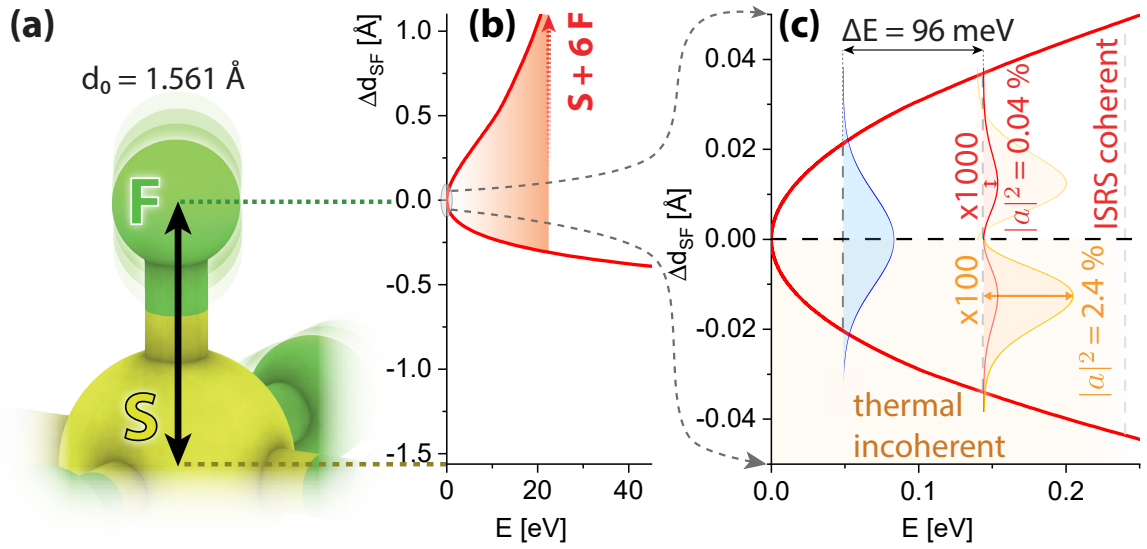

Figure 5.22.: Perturbative vibrational excitation versus thermally-induced population in SF_6. **(a)** Visualization of a single S–F chemical bond vibrating around the equilibrium distance d_0 = 1.561 Å[99]. **(b)** Calculated ground-state PEC for symmetric-breathing-mode vibrations A_g. The dissociation limit around 22.4 eV from [415] is indicated. **(c)** Zoomed-in view of the PEC around d_0 including the first two vibrational levels. A comparison to the 100-times magnified (in comparison to the vibrational ground state) view of the thermally (at 300 K) induced probability density of the A_{1g} state (lower half) with the coherently excited 1000-times zoomed-in coherent population induced by ISRE (upper half).

introduction of this chapter. Figure B.16 in the appendix shows the resulting plot using the electronic ground-state PEC in combination with the core-to-LUMO-excited many-body PEC. A slope value of 0.27 eV/pm is extracted for a linear approximation of the mapping. To put this into perspective, Hosler *et al.* [393] report a slope value of 0.14 eV/pm for a transition from the electronic ground state of Br_2 to the $3d^{-1}\sigma^{*1}$ state around 68 eV. While SF_6 and Br_2 are vastly different molecules and the respective core-level transitions differ significantly, the slope values are still in the same order of magnitude. The mapping-curve in figure B.16 is essential for connecting the measured oscillatory features of the $6a_{1g}$ resonance in SF_6 (see figure 5.19) to the S–F bond-length dynamics as presented in figure 5.23. This demonstrates that a SWIR pulse in the 1×10^{13} W/cm^2 intensity range leads to a resolvable vibrational amplitude of only 50 fm in SF_6. Comparing this value to other literature sources, the vibrational amplitude is an order of magnitude smaller than previously resolved features linked to gas-phase molecular structural dynamics (0.6 pm in [397]). Moreover, the d_{SF}-precision in the *m#1* data is significantly lower than the measured amplitude: With the statistics of *m#1* for the SXR-first range (see figure 5.19), resulting in a standard deviation of σ = 3.8 meV and the slope value of 0.27 eV/pm, vibration

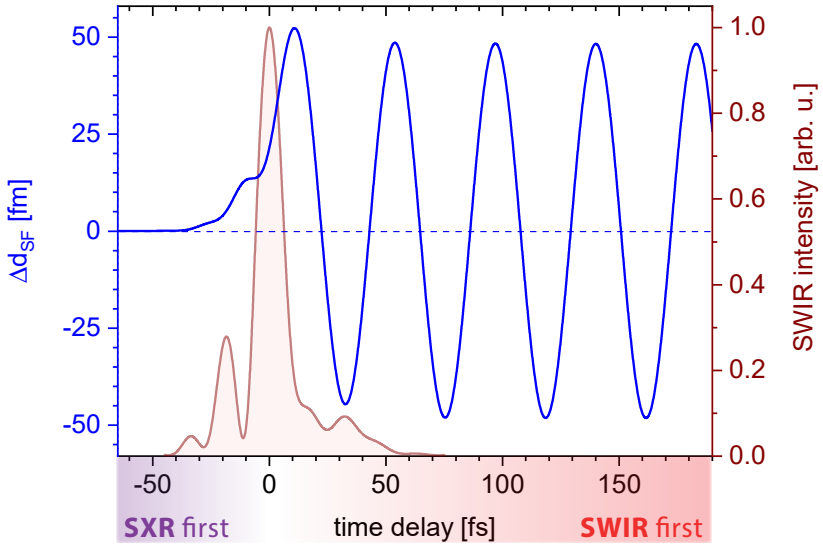

Figure 5.23.: S–F bond-distance dynamics extracted from the simulation using the parameters of the TR-XAS measurement *m#1*. The nuclear dynamics are given as the blue solid line and the SWIR intensity envelope is depicted as the solid dark red line. The maximum A_{1g} vibrational amplitude is around 50 fm.

amplitudes as small as 14 fm can be differentiated from the noise. This is equivalent to roughly double the diameter (d_S = 6.5 fm [416]) of the sulfur nucleus. Also, this precision translates to a relative bond-length change of 10^{-4}.

5.3.3.4. Comparison with classical differential equation

As discussed in the previous chapters, the combined electronic and vibrational dynamics are fully understood by employing the combined quantum-mechanical many-body/classical simulation described in section 5.3.3.1. Another heuristic perspective on the qualitative bond-length dynamics is given by the classical model that describes the vibrational amplitude of a Raman excitation as discussed in the theory section 2.5.3.2. Applying the laser parameters λ_c and τ_{FWHM} as well as the A_{1g} vibrational frequency ω to the second-order differential equation (2.61) results in figure 5.24(a). The damped oscillatory behavior with the A_{1g} eigenfrequency of SF_6 visualizes that the vibration is driven in the fully impulsive regime as expected. To numerically confirm the intensity-dependence of the ISRE process, equation (2.61) is solved for an ensemble of different electric-field strengths of the ISRE-driving pulse. The clear quadratic field dependence is shown in figure 5.24(b). This explains, why the different measurement campaigns *m#1*/*m#2* can be matched in figure 5.19 by a scaling of the resonance shift ΔE_c: Both components, the transient electronic aspects being the quadratic

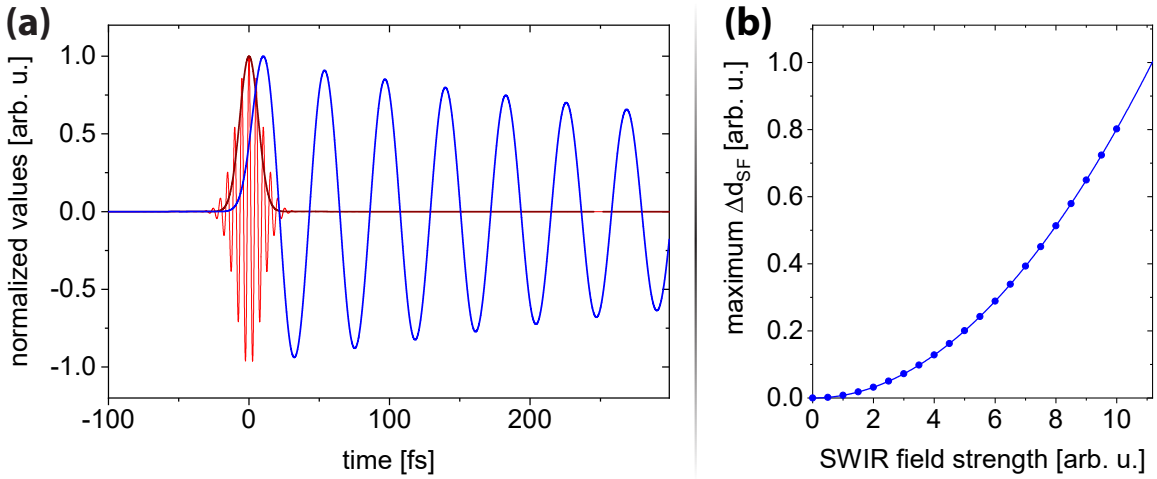

Figure 5.24.: Fully classical simulation of the ISRE process exciting the A_{1g} mode in SF_6 based on the differential equation (2.61) which was introduced in the theory chapter. **(a)** Bond-length change Δd_{SF} (solid blue line) for a λ_c = 1535 nm laser SWIR pulse (field: solid red line; intensity envelope: dark red line) with a three-optical cycle (15 fs) FWHM duration. **(b)** Quadratic scaling of the maximum Δd_{SF} with the SWIR field amplitude (blue dots: numerical simulation; blue solid line: quadratic fit).

AC Stark effect and the ISRE vibrational component scale with the square of the SWIR field and thus linearly with the intensity. Hence, the intensity ratio of the two measurement campaigns $I_{IR}^{\#2} / I_{IR}^{\#1}$ represents the necessary $\Delta E_c^{\#2} / \Delta E_c^{\#1}$ scaling.

5.4. Vibrational precision metrology with TR-XAS – an outlook

To sum up, this chapter showed that coherent vibrations can be perturbatively induced and effectively quantified with TR-XAS. Smallest vibrational amplitudes around 50 fm of the first vibrational breathing mode A_{1g} in SF_6 are excited in an ISRE process by a few-cycle SWIR pulse. The induced nuclear and vibrational dynamics manifest in an SXR transition energy shift that is quantified by fitting the $6a_{1g}$ absorbance doublet with Voigt profiles. Two TR-XAS measurement campaigns with different SWIR energies are conducted and reveal that both, the electronic component and the vibrational signatures scale with the intensity of the pulse for the used experimental conditions. A model based on the electronic ground state and core-level excited state links the determined absorbance shift to bond-length changes. By employing a combined quantum-mechanical many-body and classical simulation, the quadratic AC Stark shift, the initiation of the vibration via HOMO-LUMO mixing (also called

bond softening) and the further vibrational dynamics are reproduced. As a result, a population transfer to the excited vibrational state of less than 0.04% and a corresponding vibrational amplitude of around 50 fm are extracted from the simulation that reproduces the ΔE_c-signatures of the TR-XAS measurement with an SWIR intensity of $9\,\mathrm{TW/cm^2}$. In this case, an experimental precision of 14 fm is achieved, which translates to a relative change in the S–F bond length of 10^{-4}. Employing a fully-classical calculation, it is verified that not only the AC Stark effect but also the ISRE-induced vibrational amplitude scales linearly with the SWIR intensity for the conducted measurements.

These TR-XAS measurements in SF_6 and their corresponding analysis provide the basis for future experiments to make full use of the vibrational-metrology capabilities of TR-XAS. As these investigations with TR-XAS represent an ensemble measurement of the target molecules, there is no immediate physical limitation concerning the realizable vibrational bond-length precision. By further laser-source and beamline optimizations and by employing a high-resolution SXR spectrometer[3] [386, 387, 417] one can expect a further push of the precision to the *sub-femtometer* regime. The SWIR vibrational excitation mechanism allows for inducing such extremely small structural alterations: ISRE is widely applicable with the prerequisite of the existence of a Raman-active vibrational mode. With its nonresonant excitation scheme, it can be applied to many different electronic structures of vastly different molecules. Furthermore, the nonlinear character of Raman processes enables a well-controllable vibrational excitation that is easily scalable to smaller internuclear oscillatory amplitudes. In addition, the coherently excited nuclear wave packet is well distinguishable from the incoherent thermal vibrational background. The presented TR-XAS measurement *m#1* resulted in a A_{1g} population 60 times smaller than the corresponding vibrational population at room temperature. Moreover, vibrational metrology with TR-XAS does not rely on molecular alignment or orientation. Furthermore, TR-XAS provides the possibility for detailed investigations into electronic-nuclear coupling dynamics.

Based upon these findings, many more studies are envisioned to deepen our understanding of ultrafast chemical dynamics:

- The time-resolved approach with sub-femtosecond precision will allow to easily quantify nuclear decoherence or vibrational dissipation effects in the future.

[3] The resolution of the used SXR spectrometer is about $\lambda/\Delta\lambda \approx 300$ at $\lambda = 7\,\mathrm{nm}$ (177 eV) due to the diffractive grating which is optimized for the XUV spectral region.

Time-delays up to the picosecond regime might enable investigating nuclear wave-packet revivals [414, 418].

- TR-XAS experiments with higher SWIR intensity will draw a complete picture of the perturbative excitation with classical analogy to the pure quantum-mechanical regime including quantum-hopping behavior of the nuclear probability density to the dissociative limit.
- Looking at different core-excited state symmetries at the same time, e.g., not only $6a_{1g}$, but also $2t_{2g}$ in SF_6, will enable studies to test the point symmetry considerations [89] within the dipole picture.
- With its element-specificity, TR-XAS enables looking at vibrations from the point-of-view of different reporter atoms within the molecule. This will contribute to a better understanding of vibrational dissipation within a large molecule.
- Reaching the carbon, oxygen and nitrogen K-edges will enable extending this metrology scheme to biologically relevant, organic molecules [287].
- The perturbative vibrational-excitation scheme will be applied to enhance/control chemical reactivity of neutral molecules precisely.

These examples illustrate that a manifold of potential research directions are unlocked with implications from fundamental quantum physics over physical chemistry up to ultrafast dynamics of proteins.

6. Summary and future directions

The idea of transiently altering the *chemistry within a molecule* on an ultrashort timescale is at the heart of this work. Two different aspects of ultrafast molecular quantum control have been targeted:

Firstly, the focus was on the *electronic structure* of the molecule. Here, for the first time, solely quantum properties of the electron–electron interaction were manipulated without any mediation through nuclear motion or significant charge transfer. This was demonstrated in an x-ray absorption experiment in which sulfur hexafluoride molecules were perturbed by infrared pulses with variable intensity. The observed changes in the absorbance of a core-level, spin-orbit-split doublet resonance were linked to a laser-dressing of the molecular valence orbital by employing a basic toy model. Here, the alteration in the symmetry of this mixed valence state led to an increase of the electron–electron exchange energy by up to 50%. These results were confirmed by an *ab-initio* quantum many-body simulation. The laser-based, transient exchange-energy manipulation as demonstrated in this work hence expands the toolbox for ultrafast molecular control.

Secondly, the limits of inducing and measuring smallest *vibrational dynamics* in the perturbative limit were elucidated. In the respective experiment, an infrared pulse of only three-optical-cycle duration excited a breathing-mode vibration in SF_6 via a nonresonant, impulsive Raman process. Subsequent electronic and nuclear dynamics were probed by a time-delayed x-ray pulse from an electronic core level. The electronic and vibrational contributions of the signatures in the transmitted x-ray spectrum were disentangled with a combined classical/quantum-mechanical simulation. As a result, a vibrational amplitude of only 50 fm at a measurement precision of 14 fm was extracted. This is an improvement of the precision by more than one order of magnitude in comparison to previous reports [397] and establishes time-resolved x-ray absorption spectroscopy as an ideal tool for vibrational metrology of molecular systems on the femtometer level.

These measurements were enabled by a laser source of few-cycle, wavelength-tunable

pulses in the 1 µm to 2 µm spectral region. This source was built from scratch in the recently established *Laser Laboratory 2* of the *Quantum Dynamics and Control* division at the *Max Planck Institute for Nuclear Physics* in Heidelberg. With its unique combination of millijoule-level pulse energies, wavelength-tunability, few-cycle pulse durations and an uninterrupted, stable operation over one week, this optical laser source provides ideal conditions for complex measurement campaigns on quantum dynamics within molecules. In combination with a flexible transient-absorption beamline, a large variety of x-ray photon energies, infrared-pulse intensities and inter-pulse time delays with sub-femtosecond resolution are accessible.
While specific outlooks have already been given in sections 3.4, 4.3 and 5.4 at the end of the respective chapters, here, the big picture of future experiments is discussed:

- How will the next generation of “ultrafast quantum microscopes" look like?
- Which physical and chemical targets and science questions are in reach?
- Which research questions will be answered by employing the next-generation technology on novel targets?

The first vision is the merger of different *timescales*: Up to now, experiments targeting the electronic processes on the atto- to femtosecond timescale have been rather separated from studies involving the atomic structure of molecules in the femto- to picosecond regime. The cases, however, where the Born-Oppenheimer approximation breaks down and thus electronic and nuclear dynamics cannot be separated any longer, turn out to be of great interest and relevance for chemistry [82, 291, 394] and even biology [419, 420]. With the availability of high-repetition-rate (around 100 kHz) sources [172, 421, 422] with ultrastable properties, the task seems feasible to reach attosecond-precision [423] within a picosecond measurement range. Employing carrier-envelope-phase-stabilization [47, 424] of the laser pulse unlocks the potential to monitor sub-cycle electronic effects [425–427] together with nuclear dynamics. Such a control-scheme can be understood as an extension of the tailored light pulses previously used for chemical quantum control [313, 428–430]. Hence, this addresses research questions such as: Can picosecond-related effects such as vibrational and rotational wave-packet revivals [414, 418, 431] impact the electronic dynamics on the femto- to attosecond timescale and vice versa?
Not only the timescales but also the *spectral domain* has been separated into different regimes so far: Here, the idea is to probe the system in many different wavelength

regimes at once. In the experiments presented in this thesis, the molecular system is probed in the x-ray regime, while the perturbing SWIR pulse remains spectrally unresolved after target transmission. Adding weak, few-cycle pulses in the ultraviolet to far-infrared region to the experimental scheme enables the observation of core-level, valence and vibrational/rotational dynamics simultaneously in the same experiment. This provides the opportunity to gain a complete picture of the dynamics of the system rather than relying on assumptions during data interpretation.

Experimental techniques suitable for disentangling the dynamics of complex systems are another future direction. In this context, the key is to introduce new experimental variables and hence expand the dimensions of the acquired data sets. Two initial steps in this direction are already possible with the current experimental setup described in this thesis: Combined time-delay/intensity scans will become the standard measurement scheme in the future and will allow for time-resolving different effects (ionization-related phenomena versus transient, light-dressed states) in their natural field-strength/intensity regimes in the same system and within one measurement. Furthermore, the described few-cycle SWIR source provides wavelength tunability which helps to disentangle the laser-mediated coupling of states in a complex quantum system as indicated in first measurements on helium in the section 3.3.5.2. Another perspective is the transition towards multi-pulse schemes. In the simplest case, a pulse sequence can orient or even align molecules [377, 432–435] and thus grant access to geometrical effects. More generally speaking, a pulse sequence with well-defined time delays will bring multi-dimensional spectroscopy to the x-ray regime [436, 437]. This is highly anticipated, as populations and coherences of a quantum system are disentangled [438, 439] in such measurements which will be key to the interpretation of core-level spectroscopy of complex molecules. This is linked to scientific problems such as: Is the ultrafast controllability of a molecule ultimately limited by its size?

Measurements on biologically related molecules are of great relevance particularly if they are conducted in the natural environment of the respective molecule. In living matter, this is usually the liquid phase. Employing in-vacuum experiments on solvated molecules, though, imposes major technical challenges. Recently, significant progress has been made concerning sample delivery in ultrathin liquid jets in vacuum [224, 230, 440, 441]. This key technology in combination with x-ray attosecond pulses spectrally covering the absorption edges of carbon, oxygen and nitrogen [106–108, 287, 396, 421, 442] will provide new perspectives on ultrafast processes in a biological context.

These progresses of molecular quantum control will be further accelerated by an ever advancing laser technology. Without doubt, laser sources based on Ytterbium-doped gain media which provide few-cycle pulses with high repetition rates in the 100 kHz regime, millijoule-level pulse energies and average powers up to 1 kW will be readily available for scientific experiments in the future [119–121, 443]. Utilizing nonlinear optical processes, the laser-pulse generation from the x-ray up to the terahertz regime is feasible with such sources [444–446]. Besides the optical source developments, the next-generation vacuum beamline for x-ray absorption spectroscopy will be based on grazing-incidence optics for maximum spectral bandwidth as also employed by the beamline described in this thesis. A significant extension concerning flexibility will be achieved by a small-legged in-vacuum interferometric beam-splitting [234, 238], which combines a high time-delay stability with the possibility to further alter the recycled HHG-driving pulse, e.g., by wavelength conversion or polarization rotation.
Now, with the femto- and attosecond science coming of age, many scientific breakthroughs have already been accomplished [104, 447–454]. In the future, innovative approaches will offer new opportunities and ensure continuous progress of the research on new fundamental ultrafast phenomena: The upcoming laser technologies and large-data processing scalability will lead to an era of systematic investigations of entire classes of small quantum systems. Here, the idea is to employ a high degree of automation with 24/7-running measurement campaigns. In these campaigns, the complete parameter space concerning time-delays from atto- to picoseconds, perturbing pulse wavelengths and intensities as well as probing wavelengths from the far infrared to the hard x-ray regime will be exploited. Subsequently, the data will be benchmarked against standard quantum-chemical theory methods with statistical methods and the support of artificial intelligence [455–457]. The data with the most severe discrepancies to standard theory contain thus the most promising results with the potential for new scientifically-relevant effects. Theory will also benefit from such an approach with its enormous amount of measured data as a test field for new theoretical models and codes. This is analogue to the well-established high-throughput screening process in pharmaceutical science [458].
Overall, the spectroscopic future for investigating molecules on a quantum level shines now brighter than ever.

A. Abbreviations

4SM	four split mirror
BBO	beta barium borate
BOA	Born-Oppenheimer approximation
CDI	coherent diffractive imaging
CEP	carrier envelope phase
CPA	chirped pulse amplification
cw	continuous wave
DBS	dichroic beamsplitter
EXAFS	extended x-ray absorption fine structure
FEL	free-electron laser
FROG	frequency-resolved optical gating
FWHM	full width at half maximum
GDD	group delay dispersion
GVD	group velocity dispersion
HCF	hollow-core fiber
HF	Hartree-Fock (method)
HHG	high-order harmonic generation
HHS	high-harmonic spectroscopy
HOMO	highest occupied molecular orbital
IAC	interferometric autocorrelation
IR	infrared
ISRE	impulsive stimulated Raman excitation
LIED	laser-induced electron diffraction
LIS	light-induced state
LL2	Laser Laboratory 2
LUMO	lowest unoccupied molecular orbital
MO	molecular orbital
MPIK	Max Planck Institute for Nuclear Physics

NEXAFS	near-edge x-ray absorption fine structure
OD	optical density
OPA	optical parametric amplifier
OPCPA	optical parametric chirped-pulse amplification
PEC	potential energy curve
PES	photoelectron spectroscopy
Regen	regenerative amplifier
RIXS	resonant inelastic x-ray scattering
RSS	residual sum of squares
SF_6	sulfur hexafluoride
SF-HCF	stretched flexible hollow-core fiber
SNR	signal-to-noise ratio
SPA	single-pass amplifier
SPM	self-phase modulation
SWIR	short-wavelength infrared
SXR	soft x-ray
TAS	transient absorption spectroscopy
TDSE	time-dependent Schrödinger equation
TG	transient grating
THG	third-harmonic generation
Ti:Sa	titanium-doped sapphire
TOD	third-order dispersion
TPA	two-photon absorption
TR-XAS	time-resolved x-ray absorption spectroscopy
UED	ultrafast electron diffraction
VLS	variable line-spacing (grating)
XAS	x-ray absorption spectroscopy
XUV	extreme ultraviolet

B. Appendix

B.1. Photos – Laser Laboratory 2

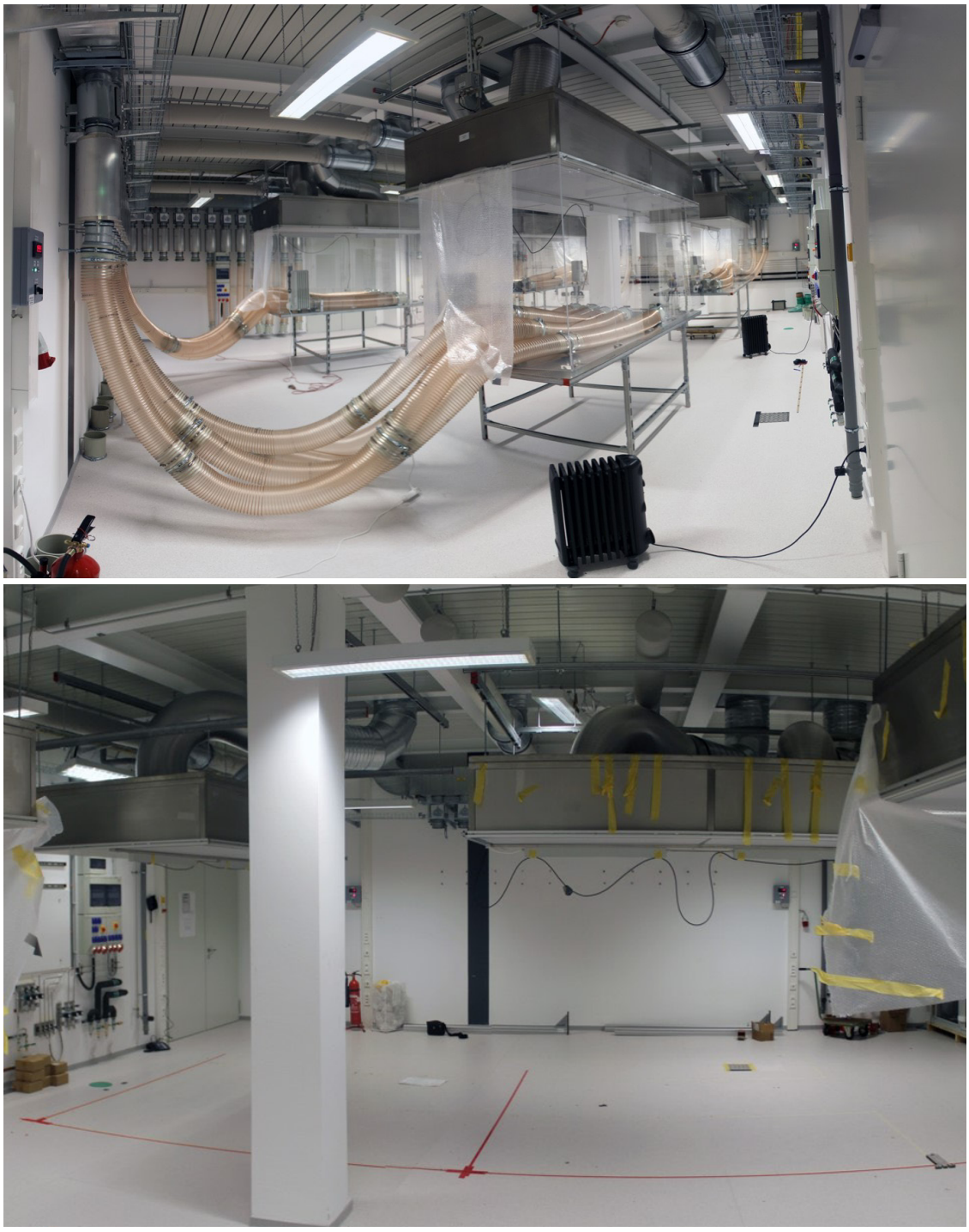

Figure B.1.: Initial status of the *Laser Laboratory 2* and prepared for optical table delivery.

Figure B.2.: Optical table delivery and installation in the *Laser Laboratory 2*.

Figure B.3.: Laser housing setup and final status.

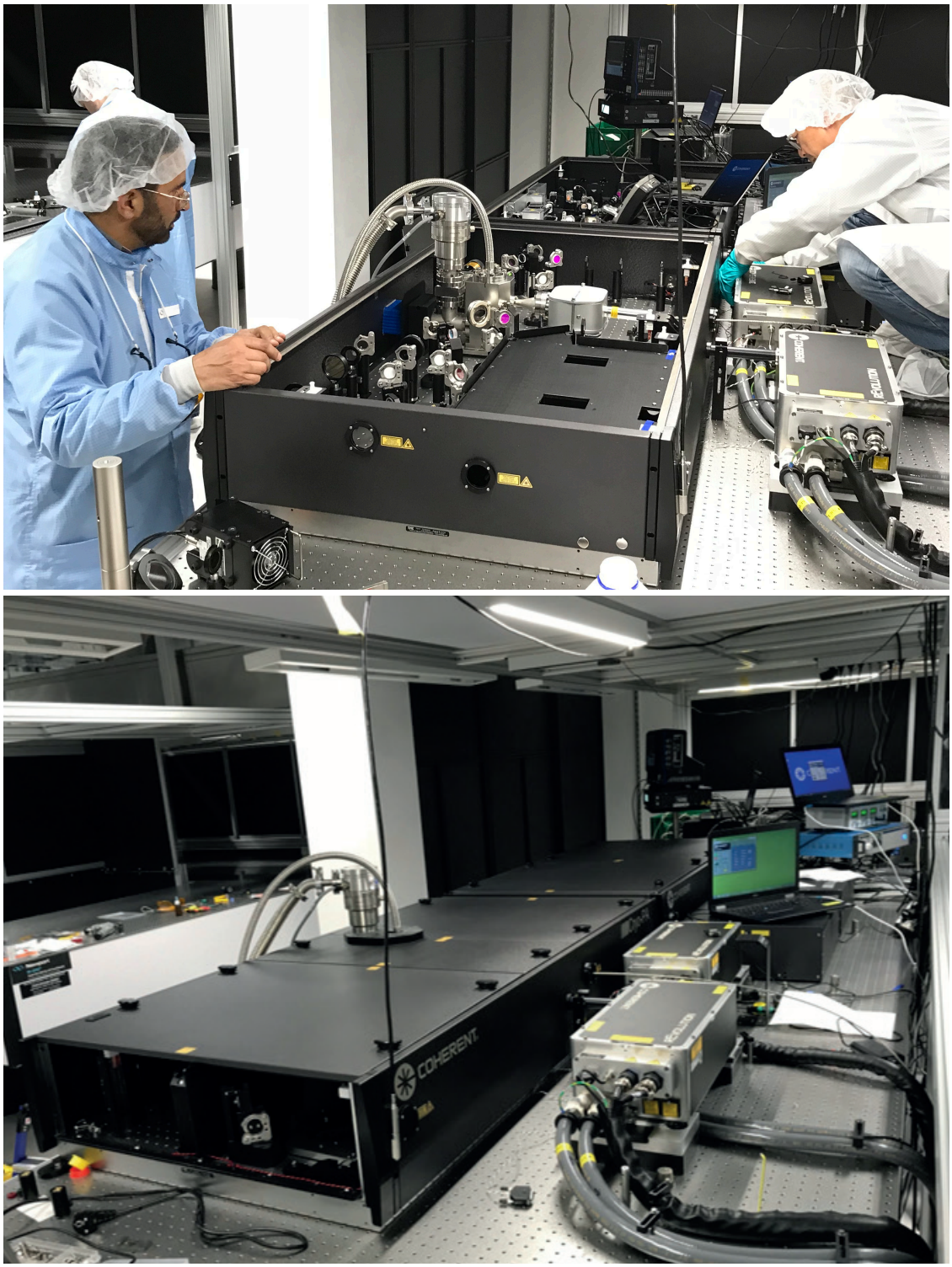

Figure B.4.: Laser system installation.

Figure B.5.: Laser system – current status.

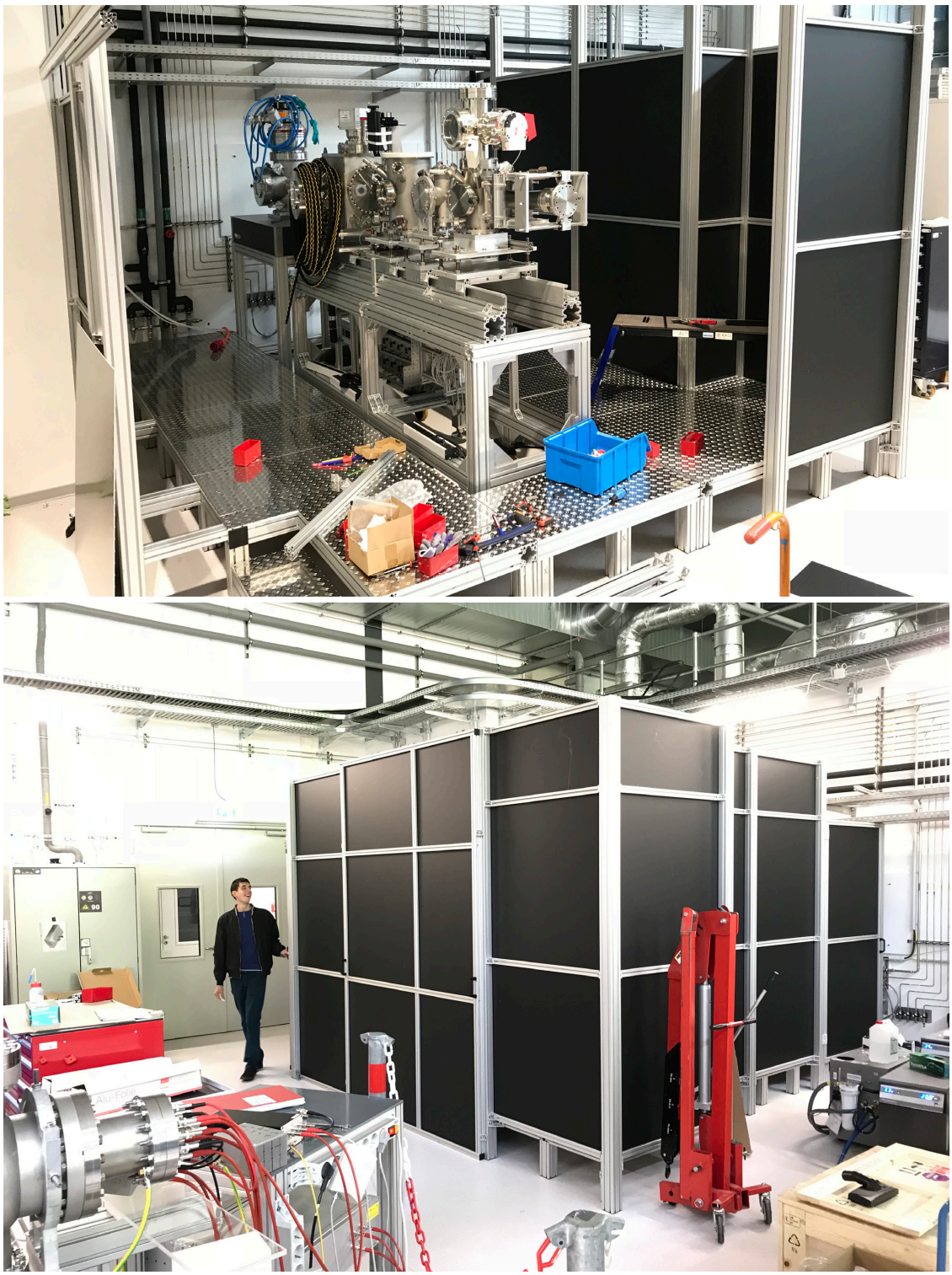

Figure B.6.: Laser hutch including the beamline in the *Experimental Hall*.

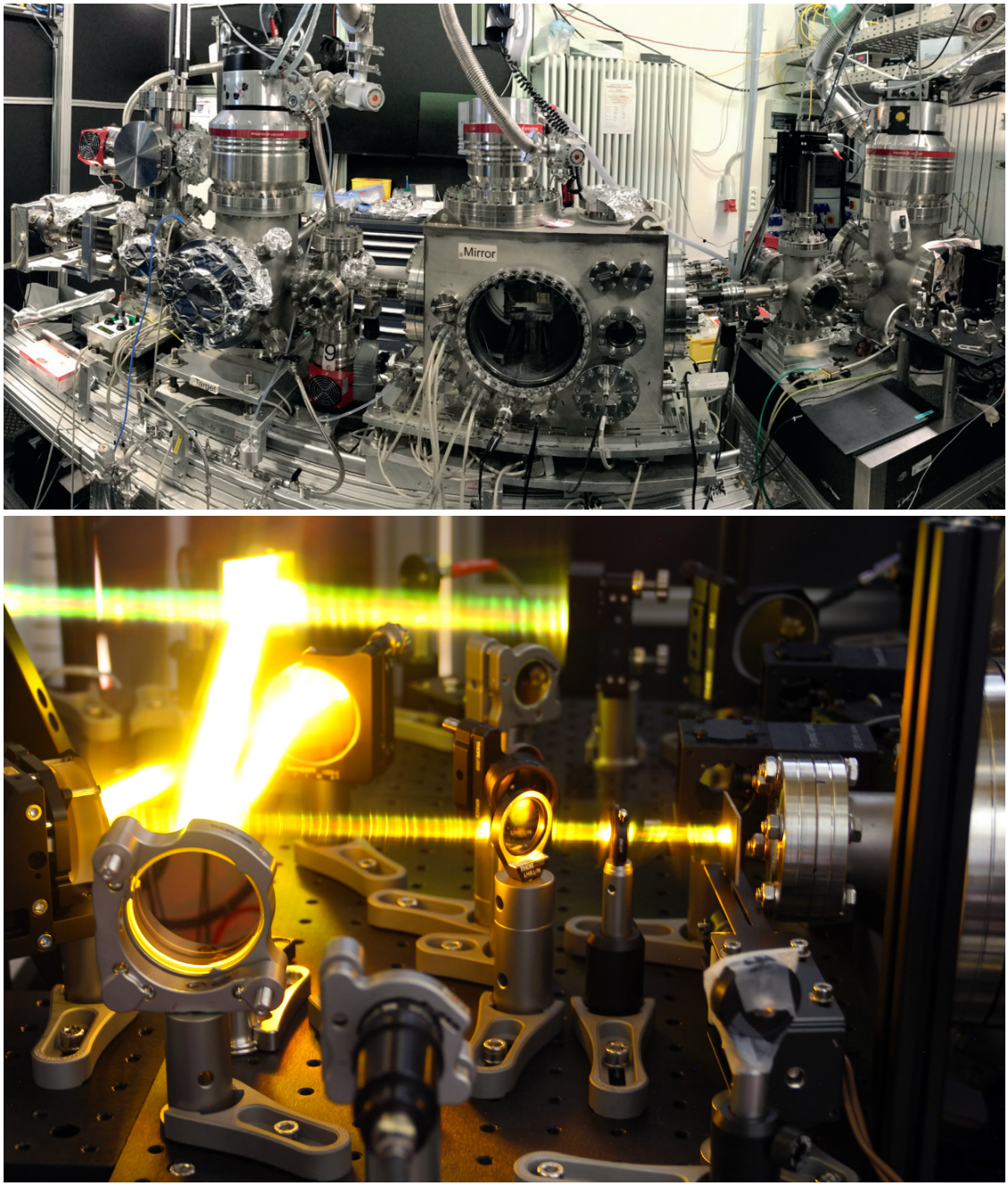

Figure B.7.: Beamline overview and visualized pre-beamline optical beampath.

B.2. Experimental setup – details

B.2.1. Optical setup – details

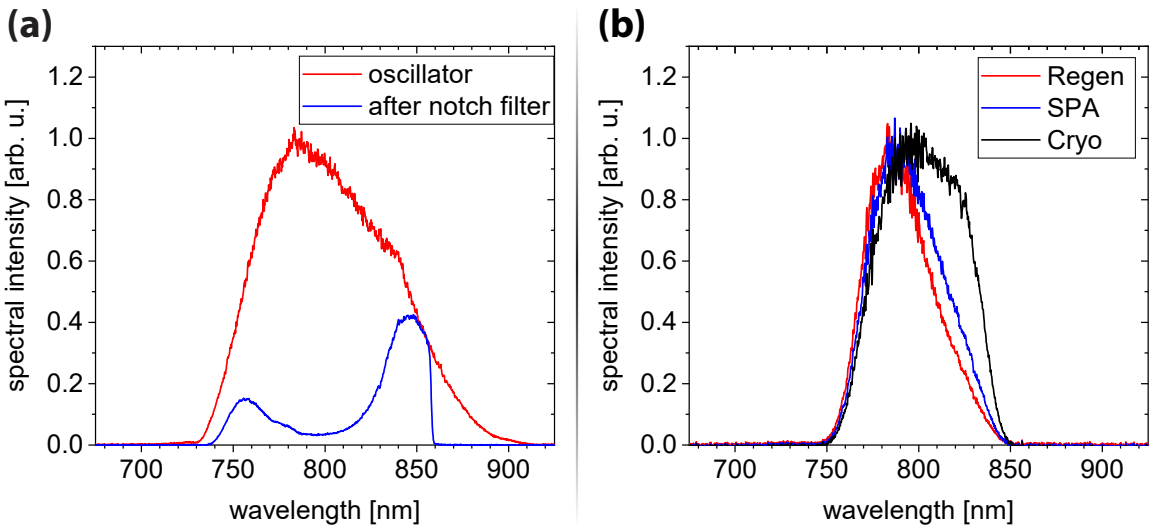

Figure B.8.: Spectra of the Ti:Sa amplification stages. **(a)** Spectrum after the oscillator (blue) and after the notch filter (red). **(b)** spectra after the first (Regen; red), second (SPA; blue) and third (Cryo; black) amplification stages.

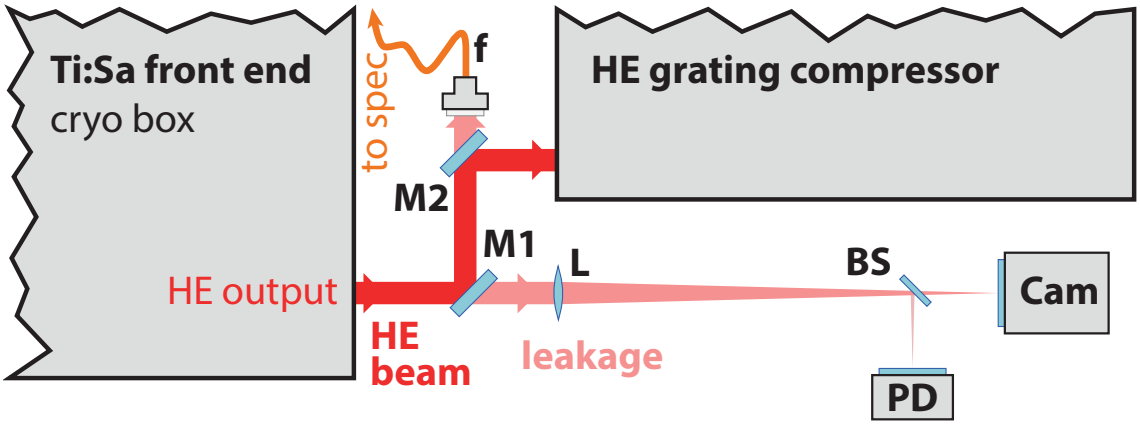

Figure B.9.: Logging setup for the Ti:Sa front end. The *HE output* beam of the *Ti:Sa front end* is routed to the external *HE grating compressor* via the two flat, dielectric mirrors *M1* and *M2*. The leakage of M1 is used and focused with a lens (*L*). A camera (*Cam*) is placed in the focal plane to track the beam-pointing and average power drift, while a beamsplitter (*BS*) provides a fraction of the focused beam to a photodiode (*PD*) which is connected to an oscilloscope for logging shot-to-shot pulse-energy fluctuations. The leakage of the second routing mirror is used for logging the spectrum: It impinges on a diffuser and subsequently the tip of a multimode fiber (*f*) which is connected to a spectrometer.

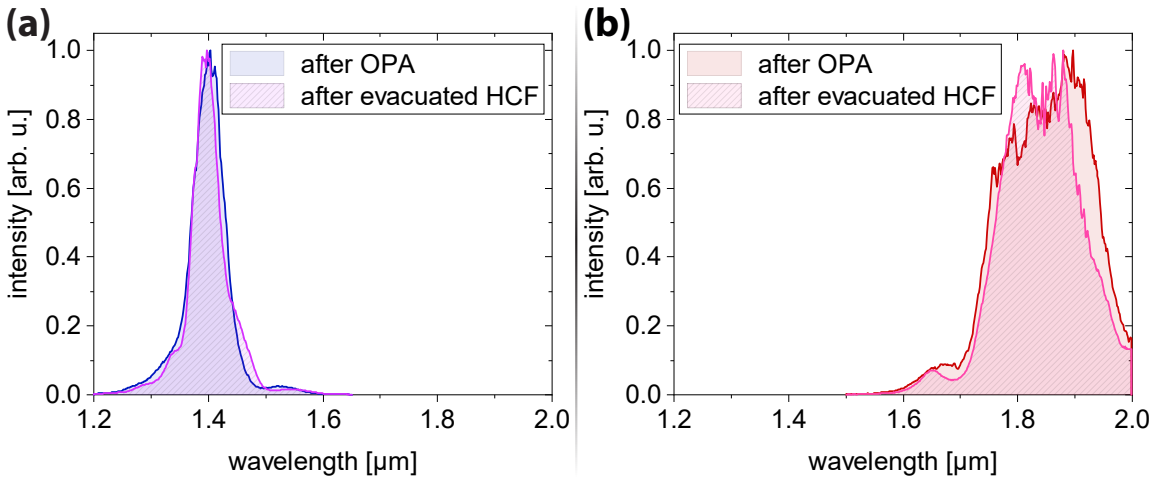

Figure B.10.: Input vs. output spectra of the evacuated HCF the investigate spectral filtering due to chromatic aberrations in the SWIR focus. **(a)** OPA signal wavelength example (λ_c = 1400 nm). **(b)** OPA idler wavelength example (λ_c = 1850 nm).

Table B.1.: Lens telescope components for focusing the OPA output into the SF-HCF. Lens *l1* is the first, defocusing 1" diameter lens, whereas *l2* refers to the second, focusing lens with 2" diameter. The respective radius of curvature (ROC) is given by *ROC#1* and *ROC#2*. The beampath is shown in figure 3.10 in the setup chapter.

λ region [nm]	material of *l1*	*ROC#1* [cm]	material of (*l2*)	*ROC#2* [cm]
1150 - 1800	UVFS	35	UVFS	-19
1800 - 2150	CaF_2	20	CaF_2	-15

Table B.2.: SF-HCF setting for optimal broadening and bulk compression material and thickness for different center wavelengths λ_c. Here, *FS* stands for fused silica.

λ_c [nm]	gas	p_{gas} [mbar]	disp. mat.	$d_{disp.}$ [mm]
1150	Ne	1500	ADP	2.5
1350	Ne	1350	KDP	1
1750	Ar	275	FS	2
2100	Ar	900	NaCl	3

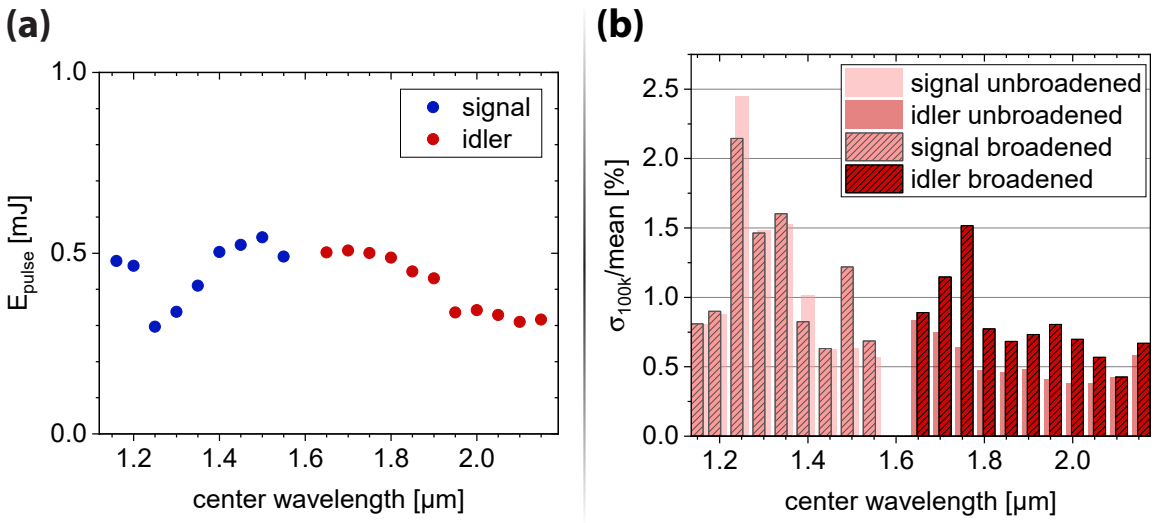

Figure B.11.: SF-HCF transmission and stability. **(a)** Transmission through the SF-HCF for different center wavelengths λ_c. **(b)** Shot-to-shot stability after the SF-HCF with and without gas/broadening in the HCF.

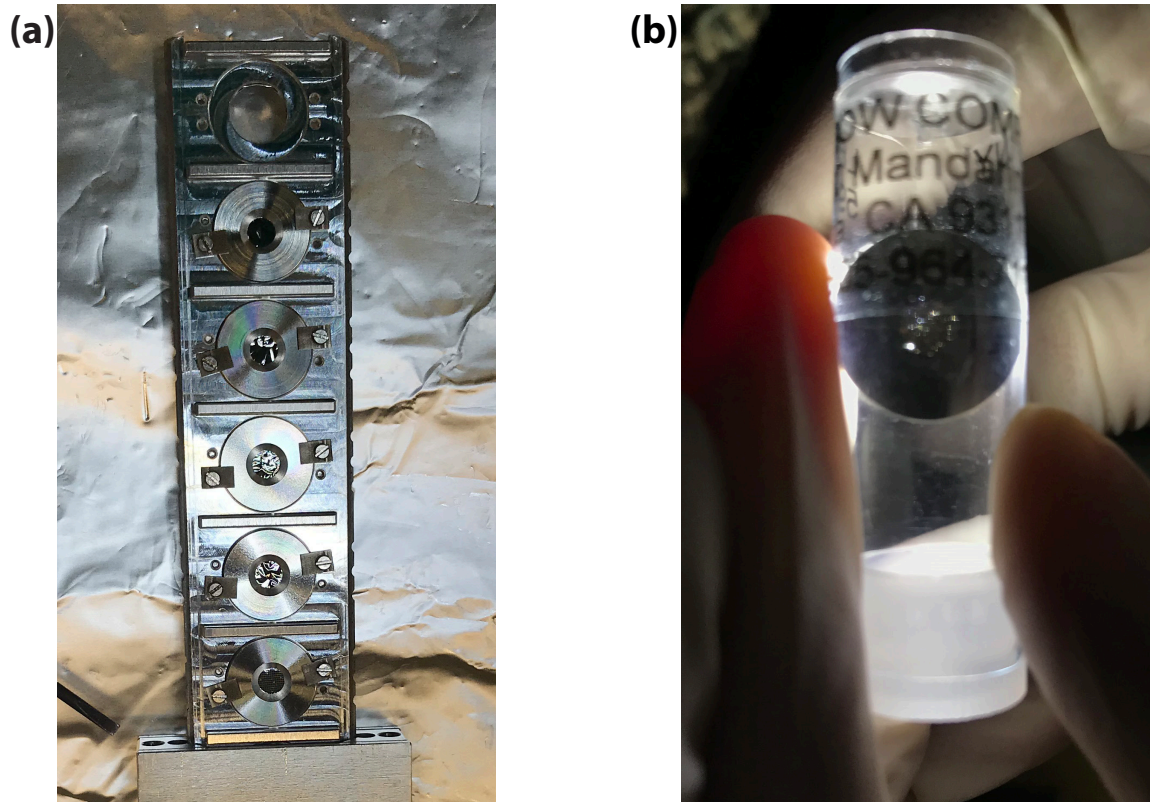

Figure B.12.: Photos of the thin metallic filters. **(a)** SXR-spectrometer filter box with 2×8 slots for filters. **(b)** Exemplary picture of the microholes in a thin metallic filter.

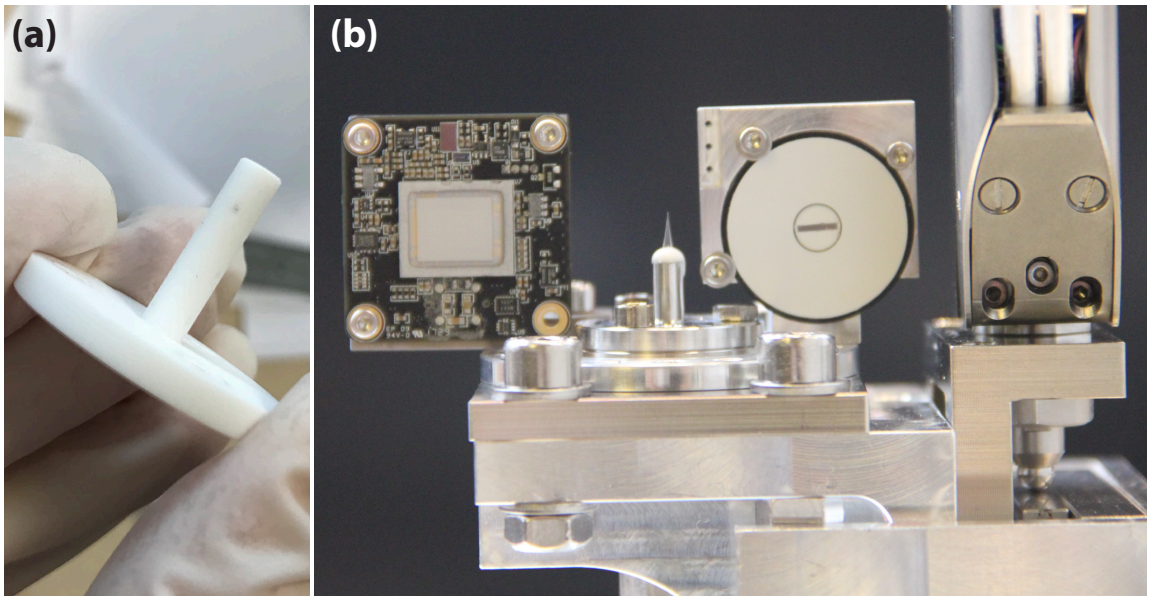

Figure B.13.: Target cell assembly. **(a)** Target cell made from Macor ceramic. **(b)** Target assembly (here with nozzle instead of cell) including in-vacuum CMOS chip on the left-hand side.

B.2.2. Spectrometer calibration

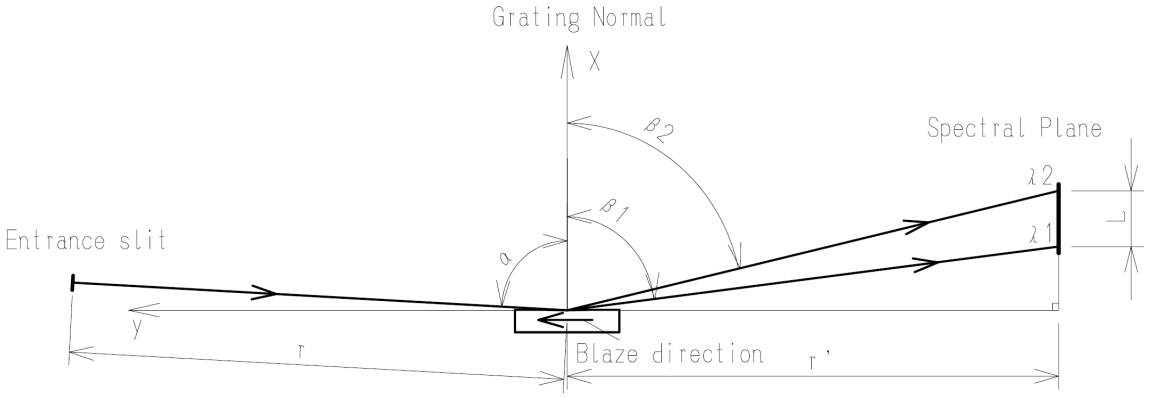

Figure B.14.: Sketch of the VLS reflective grating geometry. Reprinted from [255].

The wavelength λ at the k-th pixel is given by

$$\lambda(k) = \frac{1}{\rho_g}\left[\sin(\Theta_{in}) - \sin\left(\arctan\left(\frac{d_{gCCD}}{\Delta d_p\,(k_0 - k)}\right)\right)\right] \tag{B.1}$$

with the groove density ρ_g, the angle of incidence Θ_{in}, the distance of the grating to the CCD d_{gCCD} and the spectral pixel offset k_0.

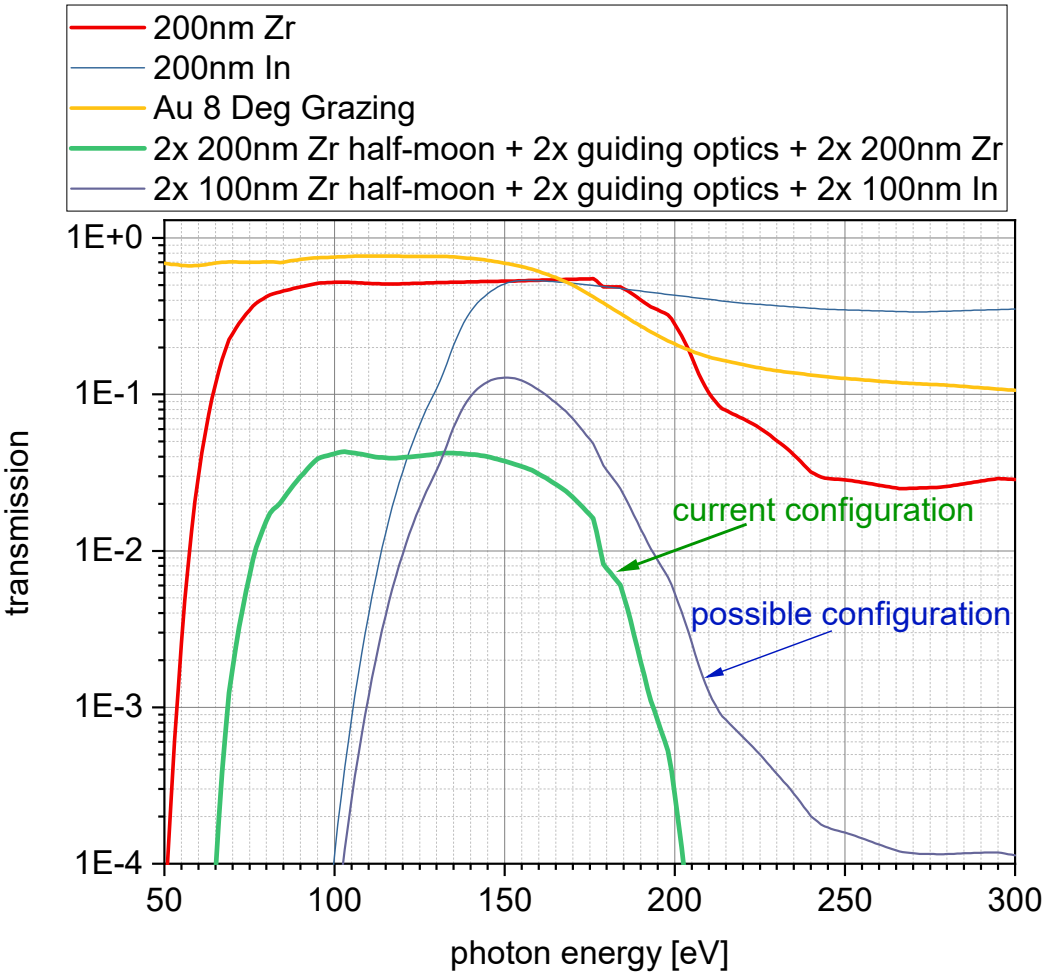

Figure B.15.: Transmission of the beamline (only reflectance of mirrors and transmission of filters taken into account). By employing thinner filters and a different material (In instead of Zr), a higher transmission in the $>200\,\mathrm{eV}$ photon-energy region is achieved. Furthermore, an idler driver wavelength will increase the HHG cutoff and may result in a higher flux at the 200 eV region. Thus, an extension towards 300 eV seems feasible.

B.3. SF_6 (TR-)XAS experiments – details

B.3.1. SF_6 bond-elongation to photon-energy mapping

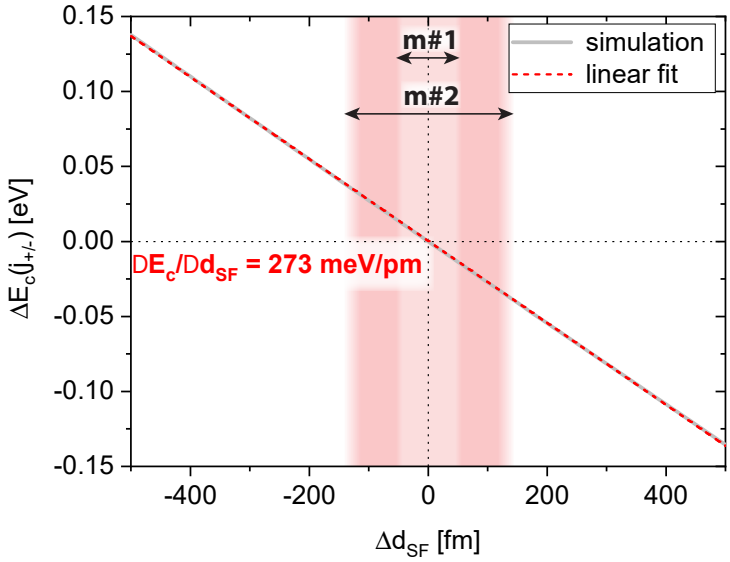

Figure B.16.: Calculated mapping curve for SXR vibrational A_{1g} metrology in SF_6. A schematic view on the role of such mapping curves for vibrational metrology is given in figure 5.5 in the main text. The change of the transition energy over the difference from the equilibrium S–F length d_0 is shown (grey solid line). Around d_0, the curve can be linearly approximated (dashed red line) leading to a slope value of 0.27 eV/pm. Also, the regions of bond-length change for the two measurement campaigns *m#1* and *m#2* are indicated.

Bibliography

[1] P. Rupprecht, L. Aufleger, S. Heinze, A. Magunia, T. Ding, M. Rebholz, S. Amberg, N. Mollov, F. Henrich, M. W. Haverkort, C. Ott, and T. Pfeifer. Laser Control of Electronic Exchange Interaction within a Molecule. *Physical Review Letters*, 128(15):153001, 2022.

[2] P. Rupprecht, L. Aufleger, S. Heinze, A. Magunia, T. Ding, M. Rebholz, S. Amberg, N. Mollov, F. Henrich, M. W. Haverkort, C. Ott, and T. Pfeifer. Resolving Vibrations in a Polyatomic Molecule with Femtometer Precision. *Physical Review Letters* (manuscript under peer review), 2022.

[3] L. Aufleger, P. Friebel, P. Rupprecht, A. Magunia, T. Ding, M. Rebholz, M. Hartmann, C. Ott, and T. Pfeifer. Line-shape broadening of an autoionizing state in helium at high XUV intensity. *New Journal of Physics*, 24(1):013014, 2022.

[4] M. Rebholz, T. Ding, L. Aufleger, M. Hartmann, K. Meyer, V. Stooß, A. Magunia, D. Wachs, P. Birk, Y. Mi, G. D. Borisova, C. da Costa Castanheira, P. Rupprecht, M. Magrakvelidze, U. Thumm, S. Roling, M. Butz, H. Zacharias, S. Düsterer, R. Treusch, G. Brenner, C. Ott, and T. Pfeifer. XUV-Initiated Dissociation Dynamics of Molecular Oxygen (O_2). *The Journal of Physical Chemistry A*, 125(47):10138–10143, 2021.

[5] M. Ilchen, P. Schmidt, N. M. Novikovskiy, et al. Site-specific interrogation of an ionic chiral fragment during photolysis using an X-ray free-electron laser. *Communications Chemistry*, 4(1):119, 2021.

[6] M. Rebholz, T. Ding, V. Despré, et al. All-XUV Pump-Probe Transient Absorption Spectroscopy of the Structural Molecular Dynamics of Di-iodomethane. *Physical Review X*, 11(3):031001, 2021.

[7] T. Ding, M. Rebholz, L. Aufleger, M. Hartmann, V. Stooß, A. Magunia, P. Birk,

G. D. Borisova, D. Wachs, C. da Costa Castanheira, P. Rupprecht, Y. Mi, A. R. Attar, T. Gaumnitz, Z.-H. Loh, S. Roling, M. Butz, H. Zacharias, S. Düsterer, R. Treusch, A. Eislage, S. M. Cavaletto, C. Ott, and T. Pfeifer. Measuring the frequency chirp of extreme-ultraviolet free-electron laser pulses by transient absorption spectroscopy. *Nature Communications*, 12(1):643, 2021.

[8] L. Aufleger, P. Friebel, P. Rupprecht, A. Magunia, T. Ding, M. Rebholz, M. Hartmann, V. Stooß, C. Ott, and T. Pfeifer. Pulse length effects on autoionizing states under the influence of intense SASE XUV fields. *Journal of Physics B: Atomic, Molecular and Optical Physics*, 53(23):234002, 2020.

[9] T. Ding, M. Rebholz, L. Aufleger, M. Hartmann, V. Stooß, A. Magunia, P. Birk, G. D. Borisova, C. da Costa Castanheira, P. Rupprecht, Y. Mi, T. Gaumnitz, Z.-H. Loh, S. Roling, M. Butz, H. Zacharias, S. Düsterer, R. Treusch, C. Ott, and T. Pfeifer. XUV pump–XUV probe transient absorption spectroscopy at FELs. *Faraday Discussions*, 228:519–536, 2021.

[10] A. Magunia, L. Aufleger, T. Ding, P. Rupprecht, M. Rebholz, C. Ott, and T. Pfeifer. Bound-State Electron Dynamics Driven by Near-Resonantly Detuned Intense and Ultrashort Pulsed XUV Fields. *Applied Sciences*, 10(18):6153, 2020.

[11] C. Ott, L. Aufleger, T. Ding, M. Rebholz, A. Magunia, M. Hartmann, V. Stooß, D. Wachs, P. Birk, G. D. Borisova, K. Meyer, P. Rupprecht, C. da Costa Castanheira, R. Moshammer, A. R. Attar, T. Gaumnitz, Z.-H. Loh, S. Düsterer, R. Treusch, J. Ullrich, Y. Jiang, M. Meyer, P. Lambropoulos, and T. Pfeifer. Strong-Field Extreme-Ultraviolet Dressing of Atomic Double Excitation. *Physical Review Letters*, 123(16):163201, 2019.

[12] T. Ding, M. Rebholz, L. Aufleger, M. Hartmann, K. Meyer, V. Stooß, A. Magunia, D. Wachs, P. Birk, Y. Mi, G. D. Borisova, C. d. C. Castanheira, P. Rupprecht, Z.-H. Loh, A. R. Attar, T. Gaumnitz, S. Roling, M. Butz, H. Zacharias, S. Düsterer, R. Treusch, S. M. Cavaletto, C. Ott, and T. Pfeifer. Nonlinear Coherence Effects in Transient-Absorption Ion Spectroscopy with Stochastic Extreme-Ultraviolet Free-Electron Laser Pulses. *Physical Review Letters*, 123 (10):103001, 2019.

[13] M. Ilchen, G. Hartmann, P. Rupprecht, A. N. Artemyev, R. N. Coffee, Z. Li, H. Ohldag, H. Ogasawara, T. Osipov, D. Ray, P. Schmidt, T. J. A. Wolf,

A. Ehresmann, S. Moeller, A. Knie, and P. V. Demekhin. Emitter-site-selective photoelectron circular dichroism of trifluoromethyloxirane. *Physical Review A*, 95(5):053423, 2017.

[14] W. Pauli. Über den Zusammenhang des Abschlusses der Elektronengruppen im Atom mit der Komplexstruktur der Spektren. *Zeitschrift für Physik*, 31(1): 765–783, 1925.

[15] L. Pauling. Moderne Strukturchemie Nobel-Vortrag Dezember 1954. *Angewandte Chemie*, 67(9-10):241–244, 1955.

[16] R. S. Mulliken. Spectroscopy, Molecular Orbitals, and Chemical Bonding. *Science*, 157(3784):13–24, 1967.

[17] K. Fukui. The Role of Frontier Orbitals in Chemical Reactions (Nobel Lecture). *Angewandte Chemie International Edition in English*, 21(11):801–809, 1982.

[18] R. Hoffmann. Building Bridges Between Inorganic and Organic Chemistry (Nobel Lecture). *Angewandte Chemie International Edition in English*, 21(10): 711–724, 1982.

[19] W. Kohn. Nobel lecture: Electronic structure of matter - Wave functions and density functional. *Reviews of Modern Physics*, 71(5):1253–1266, 1999.

[20] J. A. Pople. Nobel Lecture: Quantum chemical models. *Reviews of Modern Physics*, 71(5):1267–1274, 1999.

[21] M. Karplus. Development of Multiscale Models for Complex Chemical Systems: From H+H_2 to Biomolecules (Nobel Lecture). *Angewandte Chemie International Edition*, 53(38):9992–10005, 2014.

[22] G. V. Marr. *Handbook on Synchrotron Radiation: Vacuum Ultraviolet and Soft X-ray Processes*. Handbook on Synchrotron Radiation. Elsevier Science, 2013.

[23] B. Wu and A. Kumar. Extreme ultraviolet lithography: A review. *Journal of Vacuum Science and Technology B: Microelectronics and Nanometer Structures*, 25(6):1743, 2007.

[24] J. C. Diels, W. Rudolph, P. F. Liao, and P. Kelley. *Ultrashort Laser Pulse Phenomena*. Optics and photonics. Elsevier Science, 2006.

[25] P. Russbueldt, T. Mans, D. Hoffmann, and S. Schippel. High-Average Power Ultrafast Yb:Innoslab-Amplifier. In *Springer Series in Optical Sciences*, volume 195, pages 117–134. 2016.

[26] G. P. Agrawal. *Fiber-Optic Communication Systems*. Wiley, 2021.

[27] K. F. Palmer and D. Williams. Optical properties of water in the near infrared. *Journal of the Optical Society of America*, 64(8):1107, 1974.

[28] W. Heisenberg. Über quantentheoretische Umdeutung kinematischer und mechanischer Beziehungen. *Zeitschrift für Physik*, 33(1):879–893, 1925.

[29] M. Padgett. On the focussing of light, as limited by the uncertainty principle. *Journal of Modern Optics*, 55(18):3083–3089, 2008.

[30] B. E. A. Saleh and M. C. Teich. *Fundamentals of Photonics*. Wiley Series in Pure and Applied Optics. John Wiley & Sons, Inc., New York, USA, 1991.

[31] G. D. Gillen, C. M. Seck, and S. Guha. Analytical beam propagation model for clipped focused-Gaussian beams using vector diffraction theory. *Optics Express*, 18(5):4023, 2010.

[32] W. von Sellmeier. Zur Erklärung der abnormen Farbenfolge im Spectrum einiger Substanzen. *Annalen der Physik und Chemie*, 219(6):272–282, 1871.

[33] M. N. Polyanskiy. Refractive index database. `https://refractiveindex.info/`, accessed on 27 Mar. 2022.

[34] Light Conversion. Optics Toolbox - Refractive Index. `http://toolbox.lightcon.com/tools/refractiveindex/`, accessed on 27 Mar. 2022.

[35] T. H. Maiman. Stimulated Optical Radiation in Ruby. *Nature*, 187(4736): 493–494, 1960.

[36] J. A. Armstrong. Measurement of picosecond laser pulse widths. *Applied Physics Letters*, 10(1):16–18, 1967.

[37] J. A. Giordmaine, P. M. Rentzepis, S. L. Shapiro, and K. W. Wecht. Two-photon excitation of fluorescence by picosecond light pulses. *Applied Physics Letters*, 11 (7):216–218, 1967.

[38] J. Hecht. A short history of laser development. *Applied Optics*, 49(25):F99,

2010.

[39] R. W. Boyd. *Nonlinear Optics*. Elsevier Science, 2008.

[40] P. B. Corkum. Plasma perspective on strong field multiphoton ionization. *Physical Review Letters*, 71(13):1994–1997, 1993.

[41] K. J. Schafer, B. Yang, L. F. DiMauro, and K. C. Kulander. Above threshold ionization beyond the high harmonic cutoff. *Physical Review Letters*, 70(11): 1599–1602, 1993.

[42] J. Li, J. Lu, A. Chew, S. Han, J. Li, Y. Wu, H. Wang, S. Ghimire, and Z. Chang. Attosecond science based on high harmonic generation from gases and solids. *Nature Communications*, 11(1):2748, 2020.

[43] B. Shan and Z. Chang. Dramatic extension of the high-order harmonic cutoff by using a long-wavelength driving field. *Physical Review A - Atomic, Molecular, and Optical Physics*, 65(1):4, 2002.

[44] A. D. Shiner, C. Trallero-Herrero, N. Kajumba, H.-C. Bandulet, D. Comtois, F. Légaré, M. Giguère, J.-C. Kieffer, P. B. Corkum, and D. M. Villeneuve. Wavelength Scaling of High Harmonic Generation Efficiency. *Physical Review Letters*, 103(7):073902, 2009.

[45] J. Tate, T. Auguste, H. G. Muller, P. Salières, P. Agostini, and L. F. DiMauro. Scaling of Wave-Packet Dynamics in an Intense Midinfrared Field. *Physical Review Letters*, 98(1):013901, 2007.

[46] C. Winterfeldt, C. Spielmann, and G. Gerber. Colloquium : Optimal control of high-harmonic generation. *Reviews of Modern Physics*, 80(1):117–140, 2008.

[47] F. Krausz and M. Ivanov. Attosecond physics. *Reviews of Modern Physics*, 81 (1):163–234, 2009.

[48] D. R. Hartree and H. C. W. P. P. Fund. *The calculation of atomic structures*. J. Wiley, 1957.

[49] J. C. Slater. The Theory of Complex Spectra. *Physical Review*, 34(10):1293–1322, 1929.

[50] B. H. Bransden and C. J. Joachain. *Physics of atoms and molecules*. Pearson

Education, 2003.

[51] R. Jenkins, R. Manne, R. Robin, and C. Senemaud. Nomenclature, symbols, units and their usage in spectrochemical analysis - VIII. Nomenclature system for X-ray spectroscopy (Recommendations 1991). *Pure and Applied Chemistry*, 63(5):735–746, 1991.

[52] D. J. Griffiths and D. F. Schroeter. *Introduction to Quantum Mechanics*. Cambridge University Press, 2018.

[53] A. Einstein. Über einen die Erzeugung und Verwandlung des Lichtes betreffenden heuristischen Gesichtspunkt. *Annalen der Physik*, 322(6):132–148, 1905.

[54] L. Meitner. Über die β-Strahl-Spektra und ihren Zusammenhang mit der γ-Strahlung. *Zeitschrift für Physik*, 11(1):35–54, 1922.

[55] P. Auger. Sur les rayons β secondaires produits dans un gaz par des rayons X. *CR Acad. Sci.(F)*, 177:169, 1923.

[56] A. Kotani and S. Shin. Resonant inelastic x-ray scattering spectra for electrons in solids. *Reviews of Modern Physics*, 73(1):203–246, 2001.

[57] J. Als-Nielsen and D. McMorrow. *Elements of Modern X-ray Physics*. John Wiley & Sons, Inc., Hoboken, NJ, USA, 2011.

[58] S. H. Autler and C. H. Townes. Stark Effect in Rapidly Varying Fields. *Physical Review*, 100(2):703–722, 1955.

[59] J. Bakos. AC stark effect and multiphoton processes in atoms. *Physics Reports*, 31(3):209–235, 1977.

[60] C. Ott. *Attosecond multidimensional interferometry of single and two correlated electrons in atoms*. PhD thesis, Ruperto-Carola-University of Heidelberg, 2012.

[61] L. Keldysh. Ionization in the field of a strong electromagnetic wave. *Sov. Phys. JETP*, 20(5):1307–1314, 1965.

[62] L. Zandee and R. B. Bernstein. Resonance-enhanced multiphoton ionization and fragmentation of molecular beams: NO, I_2, benzene, and butadiene. *The Journal of Chemical Physics*, 71(3):1359–1371, 1979.

[63] R. R. Freeman, P. H. Bucksbaum, H. Milchberg, S. Darack, D. Schumacher,

and M. E. Geusic. Above-threshold ionization with subpicosecond laser pulses. *Physical Review Letters*, 59(10):1092–1095, 1987.

[64] M. Y. Ivanov, M. Spanner, and O. Smirnova. Anatomy of strong field ionization. *Journal of Modern Optics*, 52(2-3):165–184, 2005.

[65] V. S. Popov. Tunnel and multiphoton ionization of atoms and ions in a strong laser field (Keldysh theory). *Physics-Uspekhi*, 47(9):855–885, 2004.

[66] G. Mainfray and G. Manus. Multiphoton ionization of atoms. *Reports on Progress in Physics*, 54(10):1333–1372, 1991.

[67] G. L. Yudin and M. Y. Ivanov. Nonadiabatic tunnel ionization: Looking inside a laser cycle. *Physical Review A*, 64(1):013409, 2001.

[68] M. Bartelmann. *Theoretical Astrophysics: An Introduction*. Heidelberg University Publishing, Heidelberg, 2021.

[69] J. Fraunhofer. Bestimmung des Brechungs- und des Farbenzerstreungs-Vermögens verschiedener Glasarten, in Bezug auf die Vervollkommnung achromatischer Fernröhre. *Annalen der Physik*, 56(7):264–313, 1817.

[70] G. Kirchhoff and R. Bunsen. Chemische Analyse durch Spectralbeobachtungen. *Annalen der Physik und Chemie*, 189(7):337–381, 1861.

[71] K. Siegbahn. Electron spectroscopy for atoms, molecules, and condensed matter. *Reviews of Modern Physics*, 54(3):709–728, 1982.

[72] F. de Groot and A. Kotani. *Core Level Spectroscopy of Solids*. CRC Press, 2008.

[73] F. de Groot. High-Resolution X-ray Emission and X-ray Absorption Spectroscopy. *Chemical Reviews*, 101(6):1779–1808, 2001.

[74] C. Bressler and M. Chergui. Molecular Structural Dynamics Probed by Ultrafast X-Ray Absorption Spectroscopy. *Annual Review of Physical Chemistry*, 61(1): 263–282, 2010.

[75] V. Stooß. *Strong-Field Spectroscopy: From Absorption to Time-Resolved Dynamics in Strong Fields*. PhD thesis, Ruperto-Carola-University of Heidelberg, 2018.

[76] M. Hartmann. *Attosecond dynamics of strong-field generated ions*. PhD thesis,

Ruperto-Carola-University of Heidelberg, 2021.

[77] W. Demtröder. *Laser Spectroscopy 1*. Springer, Berlin, Heidelberg, 2014.

[78] P. M. Morse. Diatomic Molecules According to the Wave Mechanics. II. Vibrational Levels. *Physical Review*, 34(1):57–64, 1929.

[79] J. E. Jones. On the determination of molecular fields.—I. From the variation of the viscosity of a gas with temperature. *Proceedings of the Royal Society of London. Series A, Containing Papers of a Mathematical and Physical Character*, 106(738):441–462, 1924.

[80] J. E. Jones. On the determination of molecular fields. —II. From the equation of state of a gas. *Proceedings of the Royal Society of London. Series A, Containing Papers of a Mathematical and Physical Character*, 106(738):463–477, 1924.

[81] X. Wang, S. Ramírez-Hinestrosa, J. Dobnikar, and D. Frenkel. The Lennard-Jones potential: When (not) to use it. *Physical Chemistry Chemical Physics*, 22(19):10624–10633, 2020.

[82] G. A. Worth and L. S. Cederbaum. Beyond Born-Oppenheimer: Molecular Dynamics Through a Conical Intersection. *Annual Review of Physical Chemistry*, 55(1):127–158, 2004.

[83] D. R. Yarkony. Diabolical conical intersections. *Reviews of Modern Physics*, 68 (4):985–1013, 1996.

[84] M. S. Schuurman and A. Stolow. Dynamics at Conical Intersections. *Annual Review of Physical Chemistry*, 69:427–450, 2018.

[85] J. J. Nash. Vibrational Modes of Small Molecules. `https://www.chem.purdue.edu/jmol/vibs/index.html`, accessed on 27 Mar. 2022.

[86] C. V. Raman and K. S. Krishnan. A New Type of Secondary Radiation. *Nature*, 121(3048):501–502, 1928.

[87] R. Bartels, S. Backus, M. Murnane, and H. Kapteyn. Impulsive stimulated Raman scattering of molecular vibrations using nonlinear pulse shaping. *Chemical Physics Letters*, 374(3-4):326–333, 2003.

[88] Y. R. Shen and N. Bloembergen. Theory of Stimulated Brillouin and Raman

Scattering. *Physical Review*, 137(6A):A1787–A1805, 1965.

[89] F. A. Cotton. *Chemical Applications of Group Theory*. Wiley, 1991.

[90] S. G. Lias. Ionization energy evaluation. *NIST Chemistry WebBook, NIST Standard Reference Database*, 69, 2005.

[91] L. G. Christophorou and J. K. Olthoff. Electron Interactions With SF_6. *Journal of Physical and Chemical Reference Data*, 29(3):267–330, 2000.

[92] S. Menk, S. Das, K. Blaum, M. W. Froese, M. Lange, M. Mukherjee, R. Repnow, D. Schwalm, R. von Hahn, and A. Wolf. Vibrational autodetachment of sulfur hexafluoride anions at its long-lifetime limit. *Physical Review A*, 89(2):022502, 2014.

[93] L. G. Christophorou, J. K. Olthoff, and D. Green. Gases for electrical insulation and arc interruption: Possible Present and Future Alternatives to Pure SF_6. Technical report, 1997.

[94] M. Rabie and C. M. Franck. Assessment of Eco-friendly Gases for Electrical Insulation to Replace the Most Potent Industrial Greenhouse Gas SF_6. *Environmental Science and Technology*, 52(2):369–380, 2018.

[95] R. D'Agostino and D. L. Flamm. Plasma etching of Si and SiO_2 in SF_6–O_2 mixtures. *Journal of Applied Physics*, 52(1):162–167, 1981.

[96] S. Cashion, N. Ricketts, and P. Hayes. Characterisation of protective surface films formed on molten magnesium protected by air/SF_6 atmospheres. *Journal of Light Metals*, 2(1):37–42, 2002.

[97] M. K. W. Ko, N. D. Sze, W.-C. Wang, G. Shia, A. Goldman, F. J. Murcray, D. G. Murcray, and C. P. Rinsland. Atmospheric sulfur hexafluoride: Sources, sinks and greenhouse warming. *Journal of Geophysical Research*, 98(D6):10499, 1993.

[98] G. Herzberg. *Electronic Spectra and Electronic Structure of Polyatomic Molecules*. Molecular spectra and molecular structure. Van Nostrand, 1966.

[99] L. Bartell and S. Doun. Structures of hexacoordinate compounds of main-group elements: Part III. An electron diffraction study of SF_6. *Journal of Molecular Structure*, 43(2):245–249, 1978.

[100] S. Heinze. *Material-specific Simulations of many-body Electron Dynamics*. PhD thesis, Ruperto-Carola-University of Heidelberg„ 2021.

[101] E. Hudson, D. A. Shirley, M. Domke, G. Remmers, A. Puschmann, T. Mandel, C. Xue, and G. Kaindl. High-resolution measurements of near-edge resonances in the core-level photoionization spectra of SF_6. *Physical Review A*, 47(1): 361–373, 1993.

[102] N. L. Wagner, A. Wuest, I. P. Christov, T. Popmintchev, X. Zhou, M. M. Murnane, and H. C. Kapteyn. Monitoring molecular dynamics using coherent electrons from high harmonic generation. *Proceedings of the National Academy of Sciences*, 103(36):13279–13285, 2006.

[103] T. Brabec and F. Krausz. Intense few-cycle laser fields: Frontiers of nonlinear optics. *Reviews of Modern Physics*, 72(2):545–591, 2000.

[104] L. Gallmann, C. Cirelli, and U. Keller. Attosecond science: Recent highlights and future trends.

[105] B. Wolter, M. G. Pullen, M. Baudisch, M. Sclafani, M. Hemmer, A. Senftleben, C. D. Schröter, J. Ullrich, R. Moshammer, and J. Biegert. Strong-Field Physics with Mid-IR Fields. *Physical Review X*, 5(2):021034, 2015.

[106] S. M. Teichmann, F. Silva, S. L. Cousin, M. Hemmer, and J. Biegert. 0.5-keV Soft X-ray attosecond continua. *Nature Communications*, 7(1):11493, 2016.

[107] Y. Fu, K. Nishimura, R. Shao, A. Suda, K. Midorikawa, P. Lan, and E. J. Takahashi. High efficiency ultrafast water-window harmonic generation for single-shot soft X-ray spectroscopy. *Communications Physics*, 3(1):92, 2020.

[108] T. Popmintchev, M.-C. Chen, D. Popmintchev, P. Arpin, S. Brown, S. Ališauskas, G. Andriukaitis, T. Balciunas, O. D. Mücke, A. Pugzlys, A. Baltuska, B. Shim, S. E. Schrauth, A. Gaeta, C. Hernández-García, L. Plaja, A. Becker, A. Jaron-Becker, M. M. Murnane, and H. C. Kapteyn. Bright coherent ultrahigh harmonics in the keV x-ray regime from mid-infrared femtosecond lasers. *Science*, 336(6086):1287–91, 2012.

[109] Private communication with Claus Dieter Schröter.

[110] K. Konig. Multiphoton microscopy in life sciences. *Journal of Microscopy*, 200

(2):83–104, 2000.

[111] W. R. Zipfel, R. M. Williams, and W. W. Webb. Nonlinear magic: Multiphoton microscopy in the biosciences. *Nature Biotechnology*, 21(11):1369–1377, 2003.

[112] A. Diaspro, P. Bianchini, G. Vicidomini, M. Faretta, P. Ramoino, and C. Usai. Multi-photon excitation microscopy. *BioMedical Engineering OnLine*, 5(1):36, 2006.

[113] R. R. Gattass and E. Mazur. Femtosecond laser micromachining in transparent materials. *Nature Photonics*, 2(4):219–225, 2008.

[114] R. E. Russo. Laser Ablation. *Applied Spectroscopy*, 49(9):14A–28A, 1995.

[115] D. E. Spence, P. N. Kean, and W. Sibbett. 60-fsec pulse generation from a self-mode-locked Ti:sapphire laser. *Optics Letters*, 16(1):42, 1991.

[116] S. Backus, C. G. Durfee, M. M. Murnane, and H. C. Kapteyn. High power ultrafast lasers. *Review of Scientific Instruments*, 69(3):1207–1223, 1998.

[117] D. M. Gaudiosi, A. L. Lytle, P. Kohl, M. M. Murnane, H. C. Kapteyn, and S. Backus. 11-W average power Ti:sapphire amplifier system using downchirped pulse amplification. *Optics Letters*, 29(22):2665, 2004.

[118] I. Matsushima, H. Yashiro, and T. Tomie. 10 kHz 40 W Ti:sapphire regenerative ring amplifier. *Optics Letters*, 31(13):2066, 2006.

[119] C. J. Saraceno, D. Sutter, T. Metzger, and M. Abdou Ahmed. The amazing progress of high-power ultrafast thin-disk lasers. *Journal of the European Optical Society-Rapid Publications*, 15(1):15, 2019.

[120] P. Russbueldt, T. Mans, J. Weitenberg, H. D. Hoffmann, and R. Poprawe. Compact diode-pumped 1.1 kW Yb:YAG Innoslab femtosecond amplifier. *Optics Letters*, 35(24):4169, 2010.

[121] H. Stark, J. Buldt, M. Müller, A. Klenke, and J. Limpert. 1 kW, 10 mJ, 120 fs coherently combined fiber CPA laser system. *Optics Letters*, 46(5):969, 2021.

[122] Light Conversion. Orpheus OPCPA - Compact, Few-cycle, CEP-stable OPCPA Systems. `https://lightcon.com/product/orpheus-opcpa/`, accessed on 27 Mar. 2022.

[123] Class 5 Photonics GmbH. Supernova OPCPA. `https://www.class5photonics.com/supernova.html`, accessed 27 Mar. 2022.

[124] Laser Quantum GmbH. Venteon OPCPA. `https://www.laserquantum.com/blog/wp-content/uploads/2017/01/OPCPA-VA2.1.pdf`, accessed on 20 Jan. 2022.

[125] H. Fattahi, H. G. Barros, M. Gorjan, et al. Third-generation femtosecond technology. *Optica*, 1(1):45, 2014.

[126] M. Schultze, T. Binhammer, A. Steinmann, G. Palmer, M. Emons, and U. Morgner. Few-cycle OPCPA system at 143 kHz with more than 1 μJ of pulse energy. In *Lasers, Sources and Related Photonic Devices*, volume 94, page APDP5, Washington, D.C., 2010. OSA.

[127] J. Rothhardt, S. Demmler, S. Hädrich, J. Limpert, and A. Tünnermann. Octave-spanning OPCPA system delivering CEP-stable few-cycle pulses and 22 W of average power at 1 MHz repetition rate. *Optics Express*, 20(10):10870, 2012.

[128] C.-H. Lu, Y.-J. Tsou, H.-Y. Chen, B.-H. Chen, Y.-C. Cheng, S.-D. Yang, M.-C. Chen, C.-C. Hsu, and A. H. Kung. Generation of intense supercontinuum in condensed media. *Optica*, 1(6):400, 2014.

[129] R. Budriūnas, D. Kučinskas, and A. Varanavičius. High-energy continuum generation in an array of thin plates pumped by tunable femtosecond IR pulses. *Applied Physics B*, 123(7):212, 2017.

[130] T. Balciunas, C. Fourcade-Dutin, G. Fan, T. Witting, A. A. Voronin, A. M. Zheltikov, F. Gerome, G. G. Paulus, A. Baltuska, and F. Benabid. A strong-field driver in the single-cycle regime based on self-compression in a kagome fibre. *Nature Communications*, 6(1):6117, 2015.

[131] P. S. J. Russell, P. Hölzer, W. Chang, A. Abdolvand, and J. C. Travers. Hollow-core photonic crystal fibres for gas-based nonlinear optics. *Nature Photonics*, 8 (4):278–286, 2014.

[132] J. Schulte, T. Sartorius, J. Weitenberg, A. Vernaleken, and P. Russbueldt. Nonlinear pulse compression in a multi-pass cell. *Optics Letters*, 41(19):4511, 2016.

[133] A.-L. Viotti, M. Seidel, E. Escoto, S. Rajhans, W. P. Leemans, I. Hartl, and C. M. Heyl. Multi-pass cells for post-compression of ultrashort laser pulses. *Optica*, 9(2):197, 2022.

[134] T. Nagy, P. Simon, and L. Veisz. High-energy few-cycle pulses: post-compression techniques. *Advances in Physics: X*, 6(1), 2021.

[135] M. Kaumanns, D. Kormin, T. Nubbemeyer, V. Pervak, and S. Karsch. Spectral broadening of 112 mJ, 13 ps pulses at 5 kHz in a LG_{10} multipass cell with compressibility to 37 fs. *Optics Letters*, 46(5):929, 2021.

[136] S. L. Chin. *Femtosecond Laser Filamentation*, volume 55 of *Springer Series on Atomic, Optical, and Plasma Physics*. Springer New York, New York, NY, 2010.

[137] C. Hauri, W. Kornelis, F. Helbing, A. Heinrich, A. Couairon, A. Mysyrowicz, J. Biegert, and U. Keller. Generation of intense, carrier-envelope phase-locked few-cycle laser pulses through filamentation. *Applied Physics B*, 79(6):673–677, 2004.

[138] M. Nisoli, S. De Silvestri, and O. Svelto. Generation of high energy 10 fs pulses by a new pulse compression technique. *Applied Physics Letters*, 68(20): 2793–2795, 1996.

[139] A. L. Cavalieri, E. Goulielmakis, B. Horvath, W. Helml, M. Schultze, M. Fieß, V. Pervak, L. Veisz, V. S. Yakovlev, M. Uiberacker, A. Apolonski, F. Krausz, and R. Kienberger. Intense 1.5-cycle near infrared laser waveforms and their use for the generation of ultra-broadband soft-x-ray harmonic continua. *New Journal of Physics*, 9(7):242–242, 2007.

[140] A. Wirth, M. T. Hassan, I. Grguras, J. Gagnon, A. Moulet, T. T. Luu, S. Pabst, R. Santra, Z. A. Alahmed, A. M. Azzeer, V. S. Yakovlev, V. Pervak, F. Krausz, and E. Goulielmakis. Synthesized light transients. *Science (New York, N.Y.)*, 334(6053):195–200, 2011.

[141] S. Hädrich, M. Kienel, M. Müller, A. Klenke, J. Rothhardt, R. Klas, T. Gottschall, T. Eidam, A. Drozdy, P. Jójárt, Z. Várallyay, E. Cormier, K. Osvay, A. Tünnermann, and J. Limpert. Energetic sub-2-cycle laser with 216 W average power. *Optics Letters*, 41(18):4332, 2016.

[142] G. Fan, P. A. Carpeggiani, Z. Tao, G. Coccia, R. Safaei, E. Kaksis, A. Pugzlys,

F. Légaré, B. E. Schmidt, and A. Baltuška. 70 mJ nonlinear compression and scaling route for an Yb amplifier using large-core hollow fibers. *Optics Letters*, 46(4):896, 2021.

[143] G. Fan, T. Balčiūnas, T. Kanai, T. Flöry, G. Andriukaitis, B. E. Schmidt, F. Légaré, and A. Baltuška. Hollow-core-waveguide compression of multi-millijoule CEP-stable 32 μm pulses. *Optica*, 3(12):1308, 2016.

[144] Y.-G. Jeong, R. Piccoli, D. Ferachou, V. Cardin, M. Chini, S. Hädrich, J. Limpert, R. Morandotti, F. Légaré, B. E. Schmidt, and L. Razzari. Direct compression of 170-fs 50-cycle pulses down to 1.5 cycles with 70% transmission. *Scientific Reports*, 8(1):11794, 2018.

[145] E. Conejero Jarque, J. San Roman, F. Silva, R. Romero, W. Holgado, M. A. Gonzalez-Galicia, B. Alonso, I. J. Sola, and H. Crespo. Universal route to optimal few- to single-cycle pulse generation in hollow-core fiber compressors. *Scientific Reports*, 8(1):2256, 2018.

[146] P. A. Carpeggiani, G. Coccia, G. Fan, E. Kaksis, A. Pugžlys, A. Baltuška, R. Piccoli, Y.-G. Jeong, A. Rovere, R. Morandotti, L. Razzari, B. E. Schmidt, A. A. Voronin, and A. M. Zheltikov. Extreme Raman red shift: ultrafast multimode nonlinear space-time dynamics, pulse compression, and broadly tunable frequency conversion. *Optica*, 7(10):1349, 2020.

[147] T. Nagy, L. von Grafenstein, D. Ueberschaer, and U. Griebner. Femtosecond multi-10-mJ pulses at 2 µm wavelength by compression in a hollow-core fiber. *Optics Letters*, 46(13):3033, 2021.

[148] TEM Messtechnik GmbH. Aligna - automatic beam alignment and stabilization. `http://www.tem-messtechnik.de/aligna.htm`, accessed on 27 Mar. 2022.

[149] Coherent Inc. Vitara - Automated, Hands-Free Ultrashort Pulse Ti:Sapphire Oscillator Family. `https://www.coherent.com/content/dam/coherent/site/en/resources/datasheet/lasers/COHR_Vitara_DS_0520_3.pdf`, accessed on 27 Mar. 2022.

[150] Coherent Inc. Verdi G -Series - High-Power Pumps for Ti:Sapphire Lasers and Amplifiers. `https://www.coherent.com/content/dam/coherent/site/en/resources/datasheet/lasers/COHR_Verdi_G-Series_DS_0220_1.pdf`, ac-

cessed on 27 Mar. 2022.

[151] D. Strickland and G. Mourou. Compression of amplified chirped optical pulses. *Optics Communications*, 56(3):219–221, 1985.

[152] D. Strickland. Nobel Lecture: Generating high-intensity ultrashort optical pulses. *Reviews of Modern Physics*, 91(3):030502, 2019.

[153] G. Mourou. Nobel Lecture: Extreme light physics and application. *Reviews of Modern Physics*, 91(3):030501, 2019.

[154] J. E. Murray and W. H. Lowdermilk. Nd:YAG regenerative amplifier. *Journal of Applied Physics*, 51(7):3548–3556, 1980.

[155] G. Vaillancourt, T. B. Norris, J. S. Coe, P. Bado, and G. A. Mourou. Operation of a 1-kHz pulse-pumped Ti:sapphire regenerative amplifier. *Optics Letters*, 15 (6):317, 1990.

[156] Coherent Inc. Revolution - Family of High Energy, kHz, Pulsed Green Lasers. `https://www.coherent.com/content/dam/coherent/site/en/resources/datasheet/lasers/COHR_Revolution_DS_1019_4.pdf`, accessed on 10 Mar. 2022.

[157] CryoSpectra. CryoCooler - low-vibration cryocooler. `https://www.cryospectra.com/cryocooler/`, accessed on 10 Mar. 2022.

[158] APE Angewandte Physik und Elektronik GmbH. Compact LX Spider - The Compact Choice for the Ti:Sa Wavelength Range. `https://www.ape-berlin.de/en/spider-spectral-phase-interferometry-for-direct-electric-field-reconstruction/compact-lx-spider/`, accessed on 10 Mar. 2022.

[159] Light Conversion. TOPAS Prime HE - High Energy Optical Parametric Amplifier. `https://lightcon.com/product/topas-prime-high-energy-opa/`, accessed on 27 Mar. 2022.

[160] D. N. Nikogosyan. Beta barium borate (BBO). *Applied Physics A Solids and Surfaces*, 52(6):359–368, 1991.

[161] A. Dubietis, G. Jonušauskas, and A. Piskarskas. Powerful femtosecond pulse generation by chirped and stretched pulse parametric amplification in BBO

crystal. *Optics Communications*, 88(4-6):437–440, 1992.

[162] Ocean Insight. Preconfigured NIRQuest+ spectrometers. `https://www.oceaninsight.com/products/spectrometers/near-infrared/preconfigured-nirquest-spectrometers/`, accessed on 27 Mar. 2022.

[163] S. Amberg. *Setup and characterization of a hollow-core fiber waveguide for transient absorption experiments with short-wavelength infrared pulses*. BSc thesis, Ruperto-Carola-University of Heidelberg, 2019.

[164] E. A. J. Marcatili and R. A. Schmeltzer. Hollow Metallic and Dielectric Waveguides for Long Distance Optical Transmission and Lasers. *Bell System Technical Journal*, 43(4):1783–1809, 1964.

[165] R. Abrams. Coupling losses in hollow waveguide laser resonators. *IEEE Journal of Quantum Electronics*, 8(11):838–843, 1972.

[166] T. Pfeifer. *Propagation of high Intensity Light through Gas-Filled Hollow-Core Capillaries*. Ma thesis, University of Texas at Austin, 2000.

[167] C. Vozzi, M. Nisoli, G. Sansone, S. Stagira, and S. De Silvestri. Optimal spectral broadening in hollow-fiber compressor systems. *Applied Physics B*, 80 (3):285–289, 2005.

[168] G.-J. Nijsse. *Linear motion systems; a modular approach for improved straightness performance*. PhD thesis, Delft University, 2001.

[169] A. G. Ewing, R. A. Wallingford, and T. M. Olefirowicz. Capillary Electrophoresis. *Analytical Chemistry*, 61(4):292A–303A, 1989.

[170] Polymicro Technologies. The book on the technologies of Polymicro. `https://www.molex.com/mx_upload/superfamily/polymicro/theBOOK.pdf`, accessed on 27 Mar. 2022.

[171] T. Nagy, M. Forster, and P. Simon. Flexible hollow fiber for pulse compressors. *Applied Optics*, 47(18):3264, 2008.

[172] T. Nagy, S. Hädrich, P. Simon, A. Blumenstein, N. Walther, R. Klas, J. Buldt, H. Stark, S. Breitkopf, P. Jójárt, I. Seres, Z. Várallyay, T. Eidam, and J. Limpert. Generation of three-cycle multi-millijoule laser pulses at 318 W average power. *Optica*, 6(11):1423, 2019.

[173] Molex LLC. Polymicro Flexible Fused Silica Capillary Tubing. `https://www.molex.com/molex/products/part-detail/capillary_tubing/1068150028`, accessed on 27 Mar. 2022.

[174] Lenox Laser. Alumina Ceramic Aperture. `https://lenoxlaser.com/shop/optical-apertures/high-power-apertures/ceramic-aperture/`, accessed on 27 Mar. 2022.

[175] Princeton Instruments. Quantum efficiency of CCD sensors - educational notes. `https://www.princetoninstruments.com/learn/camera-fundamentals/quantum-efficiency`, accessed 27 Mar. 2022.

[176] J. H. Bechtel and W. L. Smith. Two-photon absorption in semiconductors with picosecond laser pulses. *Physical Review B*, 13(8):3515–3522, 1976.

[177] A. D. Bristow, N. Rotenberg, and H. M. van Driel. Two-photon absorption and Kerr coefficients of silicon for 850–2200nm. *Applied Physics Letters*, 90(19): 191104, 2007.

[178] P. G. Chua, Y. Tanaka, M. Takeda, and T. Kurokawa. Infra-red image detection with a Si-CCD image sensor due to the two-photon absorption process. In *Pacific Rim Conference on Lasers and Electro-Optics, CLEO - Technical Digest*, volume 1, pages I–482–I–483. IEEE, 2001.

[179] A. Suda, M. Hatayama, K. Nagasaka, and K. Midorikawa. Generation of sub-10-fs, 5-mJ-optical pulses using a hollow fiber with a pressure gradient. *Applied Physics Letters*, 86(11):111116, 2005.

[180] T. Nagy, V. Pervak, and P. Simon. Optimal pulse compression in long hollow fibers. *Optics Letters*, 36(22):4422, 2011.

[181] S. Bohman, A. Suda, T. Kanai, S. Yamaguchi, and K. Midorikawa. Generation of 50~fs, 50~mJ pulses at 1~kHz using hollow-fiber pulse compression. *Optics Letters*, 35(11):1887, 2010.

[182] D. Wang, Y. Leng, and Z. Xu. Measurement of nonlinear refractive index coefficient of inert gases with hollow-core fiber. *Applied Physics B*, 111(3): 447–452, 2013.

[183] I. A. Walmsley and C. Dorrer. Characterization of ultrashort electromagnetic

pulses. *Advances in Optics and Photonics*, 1(2):308, 2009.

[184] Y. Cai, Z. Chen, X. Zeng, H. Shangguan, X. Lu, Q. Song, Y. Ai, S. Xu, and J. Li. The Development of the Temporal Measurements for Ultrashort Laser Pulses. *Applied Sciences*, 10(21):7401, 2020.

[185] C. Iaconis and I. A. Walmsley. Spectral phase interferometry for direct electric-field reconstruction of ultrashort optical pulses. *Optics Letters*, 23(10):792, 1998.

[186] J. R. Birge, R. Ell, and F. X. Kärtner. Two-dimensional spectral shearing interferometry for few-cycle pulse characterization. *Optics Letters*, 31(13):2063, 2006.

[187] V. V. Lozovoy, I. Pastirk, and M. Dantus. Multiphoton intrapulse interference IV Ultrashort laser pulse spectral phase characterization and compensation. *Optics Letters*, 29(7):775, 2004.

[188] M. Miranda, T. Fordell, C. Arnold, A. L'Huillier, and H. Crespo. Simultaneous compression and characterization of ultrashort laser pulses using chirped mirrors and glass wedges. *Optics Express*, 20(1):688, 2012.

[189] D. Spangenberg, E. Rohwer, M. H. Brügmann, and T. Feurer. Ptychographic ultrafast pulse reconstruction. *Optics Letters*, 40(6):1002, 2015.

[190] R. Trebino and D. J. Kane. Using phase retrieval to measure the intensity and phase of ultrashort pulses: frequency-resolved optical gating. *Journal of the Optical Society of America A*, 10(5):1101, 1993.

[191] R. Trebino, K. W. DeLong, D. N. Fittinghoff, J. N. Sweetser, M. a. Krumbügel, B. a. Richman, and D. J. Kane. Measuring ultrashort laser pulses in the time-frequency domain using frequency-resolved optical gating. *Review of Scientific Instruments*, 68(9):3277–3295, 1997.

[192] J.-C. M. Diels, J. J. Fontaine, I. C. McMichael, and F. Simoni. Control and measurement of ultrashort pulse shapes (in amplitude and phase) with femtosecond accuracy. *Applied Optics*, 24(9):1270, 1985.

[193] D. J. Kane and R. Trebino. Single-shot measurement of the intensity and phase of an arbitrary ultrashort pulse by using frequency-resolved optical gating.

Optics Letters, 18(10):823, 1993.

[194] J. N. Sweetser, D. N. Fittinghoff, and R. Trebino. Transient-grating frequency-resolved optical gating. *Optics Letters*, 22(8):519, 1997.

[195] T. Tsang, M. A. Krumbügel, K. W. DeLong, D. N. Fittinghoff, and R. Trebino. Frequency-resolved optical-gating measurements of ultrashort pulses using surface third-harmonic generation. *Optics Letters*, 21(17):1381, 1996.

[196] M. V. Klibanov, P. E. Sacks, and A. V. Tikhonravov. The phase retrieval problem. *Inverse Problems*, 11(1):1–28, 1995.

[197] T. Latychevskaia. Iterative phase retrieval in coherent diffractive imaging: practical issues. *Applied Optics*, 57(25):7187, 2018.

[198] D. J. Kane. Principal components generalized projections: a review. *Journal of the Optical Society of America B*, 25(6):A120, 2008.

[199] P. Sidorenko, O. Lahav, Z. Avnat, and O. Cohen. Ptychographic reconstruction algorithm for frequency-resolved optical gating: super-resolution and supreme robustness. *Optica*, 3(12):1320, 2016.

[200] T. Zahavy, A. Dikopoltsev, D. Moss, G. I. Haham, O. Cohen, S. Mannor, and M. Segev. Deep learning reconstruction of ultrashort pulses. *Optica*, 5(5):666, 2018.

[201] N. C. Geib, M. Zilk, T. Pertsch, and F. Eilenberger. Common pulse retrieval algorithm: a fast and universal method to retrieve ultrashort pulses. *Optica*, 6 (4):495, 2019.

[202] M. Li, J. P. Nibarger, C. Guo, and G. N. Gibson. Dispersion-free transient-grating frequency-resolved optical gating. *Applied Optics*, 38(24):5250, 1999.

[203] A. C. Eckbreth. BOXCARS: Crossed-beam phase-matched CARS generation in gases. *Applied Physics Letters*, 32(7):421–423, 1978.

[204] Ocean FX extended range spectrometer. `https://www.oceaninsight.com/products/spectrometers/high-speed-acquisition/ocean-fx/ocean-fx-extended-range/`, accessed on 10 Mar. 2022.

[205] SmarAct GmbH. CLS-3232 - Linear Stage with EDU. `https://www.smaract.`

`com/linear-stages/product/cls-3232-linear-stage-with-edu`, accessed on 12 Mar. 2022.

[206] E. Treacy. Optical pulse compression with diffraction gratings. *IEEE Journal of Quantum Electronics*, 5(9):454–458, 1969.

[207] O. E. Martinez. Grating and prism compressors in the case of finite beam size. *Journal of the Optical Society of America B*, 3(7):929, 1986.

[208] S. Akturk, X. Gu, M. Kimmel, and R. Trebino. Extremely simple single-prism ultrashort- pulse compressor. *Optics Express*, 14(21):10101, 2006.

[209] R. Szipöcs, C. Spielmann, F. Krausz, and K. Ferencz. Chirped multilayer coatings for broadband dispersion control in femtosecond lasers. *Optics Letters*, 19(3):201, 1994.

[210] Light Conversion. Optics Toolbox - Material Dispersion. `http://toolbox.lightcon.com/tools/dispersionparameters/`, accessed on 27 Mar. 2022.

[211] D. M. Carey and G. M. Korenowski. Measurement of the Raman spectrum of liquid water. *The Journal of Chemical Physics*, 108(7):2669–2675, 1998.

[212] P. Béjot, B. E. Schmidt, J. Kasparian, J.-P. Wolf, and F. Legaré. Mechanism of hollow-core-fiber infrared-supercontinuum compression with bulk material. *Physical Review A*, 81(6):063828, 2010.

[213] S. L. Cousin, F. Silva, S. Teichmann, M. Hemmer, B. Buades, and J. Biegert. High-flux table-top soft x-ray source driven by sub-2-cycle, CEP stable, 185-μm 1-kHz pulses for carbon K-edge spectroscopy. *Optics Letters*, 39(18):5383, 2014.

[214] F. Silva, M. Miranda, B. Alonso, J. Rauschenberger, V. Pervak, and H. Crespo. Simultaneous compression, characterization and phase stabilization of GW-level 14 cycle VIS-NIR femtosecond pulses using a single dispersion-scan setup. *Optics Express*, 22(9):10181, 2014.

[215] H. Timmers, Y. Kobayashi, K. F. Chang, M. Reduzzi, D. M. Neumark, and S. R. Leone. Generating high-contrast, near single-cycle waveforms with third-order dispersion compensation. *Optics Letters*, 42(4):811, 2017.

[216] M. Miranda, J. Penedones, C. Guo, A. Harth, M. Louisy, L. Neoričić, A. L'Huillier, and C. L. Arnold. Fast iterative retrieval algorithm for ultrashort

pulse characterization using dispersion scans. *Journal of the Optical Society of America B*, 34(1):190, 2017.

[217] H. Wende. Recent advances in x-ray absorption spectroscopy. *Reports on Progress in Physics*, 67(12):2105–2181, 2004.

[218] E. Fonda, A. Rochet, M. Ribbens, L. Barthe, S. Belin, and V. Briois. The SAMBA quick-EXAFS monochromator: XAS with edge jumping. *Journal of Synchrotron Radiation*, 19(3):417–424, 2012.

[219] S. Diaz-Moreno, S. Hayama, M. Amboage, A. Freeman, J. Sutter, and G. Duller. I20; the Versatile X-ray Absorption spectroscopy beamline at Diamond Light Source. *Journal of Physics: Conference Series*, 190:012038, 2009.

[220] A.-M. Flank, G. Cauchon, P. Lagarde, S. Bac, M. Janousch, R. Wetter, J.-M. Dubuisson, M. Idir, F. Langlois, T. Moreno, and D. Vantelon. LUCIA, a microfocus soft XAS beamline. *Nuclear Instruments and Methods in Physics Research Section B: Beam Interactions with Materials and Atoms*, 246(1):269–274, 2006.

[221] E. A. Seddon, J. A. Clarke, D. J. Dunning, C. Masciovecchio, C. J. Milne, F. Parmigiani, D. Rugg, J. C. H. Spence, N. R. Thompson, K. Ueda, S. M. Vinko, J. S. Wark, and W. Wurth. Short-wavelength free-electron laser sources and science: a review. *Reports on Progress in Physics*, 80(11):115901, 2017.

[222] A. S. Johnson, D. Wood, D. R. Austin, C. Brahms, A. Gregory, K. B. Holzner, S. Jarosch, E. W. Larsen, S. Parker, C. Strüber, P. Ye, J. W. G. Tisch, and J. P. Marangos. Apparatus for soft x-ray table-top high harmonic generation. *Review of Scientific Instruments*, 89(8):083110, 2018.

[223] K. Nishimura, Y. Fu, A. Suda, K. Midorikawa, and E. J. Takahashi. Apparatus for generation of nanojoule-class water-window high-order harmonics. *Review of Scientific Instruments*, 92(6):063001, 2021.

[224] C. Kleine, M. Ekimova, G. Goldsztejn, S. Raabe, C. Strüber, J. Ludwig, S. Yarlagadda, S. Eisebitt, M. J. J. Vrakking, T. Elsaesser, E. T. J. Nibbering, and A. Rouzée. Soft X-ray Absorption Spectroscopy of Aqueous Solutions Using a Table-Top Femtosecond Soft X-ray Source. *The Journal of Physical Chemistry Letters*, 10(1):52–58, 2019.

[225] P. Wachulak, M. Duda, T. Fok, A. Bartnik, Z. Wang, Q. Huang, A. Sarzyński, A. Jancarek, and H. Fiedorowicz. Single-Shot near Edge X-ray Fine Structure (NEXAFS) Spectroscopy Using a Laboratory Laser-Plasma Light Source. *Materials*, 11(8):1303, 2018.

[226] J. Holburg, M. Müller, K. Mann, P. Wild, K. Eusterhues, and J. Thieme. High-Resolution Table-Top NEXAFS Spectroscopy. *Analytical Chemistry*, 94 (8):3510–3516, 2022.

[227] L. Zehnder. Ein neuer Interferenzrefraktor. *Zeitschrift für Instrumentenkunde*, 11(7):275–285, 1891.

[228] L. Mach. Ueber einen interferenzrefraktor. *Zeitschrift für Instrumentenkunde*, 12(3):89–93, 1892.

[229] L. Barreau, A. D. Ross, S. Garg, P. M. Kraus, D. M. Neumark, and S. R. Leone. Efficient table-top dual-wavelength beamline for ultrafast transient absorption spectroscopy in the soft X-ray region. *Scientific Reports*, 10(1):5773, 2020.

[230] A. D. Smith, T. Balčiunas, Y.-P. Chang, C. Schmidt, K. Zinchenko, F. B. Nunes, E. Rossi, V. Svoboda, Z. Yin, J.-P. Wolf, and H. J. Wörner. Femtosecond Soft-X-ray Absorption Spectroscopy of Liquids with a Water-Window High-Harmonic Source. *The Journal of Physical Chemistry Letters*, 11(6):1981–1988, 2020.

[231] Y. Pertot, C. Schmidt, M. Matthews, A. Chauvet, M. Huppert, V. Svoboda, A. von Conta, A. Tehlar, D. Baykusheva, J.-P. Wolf, and H. J. Wörner. Time-resolved x-ray absorption spectroscopy with a water window high-harmonic source. *Science*, 355(6322):264–267, 2017.

[232] N. Saito, H. Sannohe, N. Ishii, T. Kanai, N. Kosugi, Y. Wu, A. Chew, S. Han, Z. Chang, and J. Itatani. Real-time observation of electronic, vibrational, and rotational dynamics in nitric oxide with attosecond soft x-ray pulses at 400 eV: supplementary material. *Optica*, 6(12):1542, 2019.

[233] A. R. Attar, A. Bhattacherjee, C. D. Pemmaraju, K. Schnorr, K. D. Closser, D. Prendergast, and S. R. Leone. Femtosecond x-ray spectroscopy of an electrocyclic ring-opening reaction. *Science (New York, N.Y.)*, 356(6333):54–59, 2017.

[234] M. Huppert, I. Jordan, and H. J. Wörner. Attosecond beamline with actively stabilized and spatially separated beam paths. *Review of Scientific Instruments*, 86(12):123106, 2015.

[235] M. Luttmann, D. Bresteau, J.-F. Hergott, O. Tcherbakoff, and T. Ruchon. In Situ Sub-50-Attosecond Active Stabilization of the Delay Between Infrared and Extreme-Ultraviolet Light Pulses. *Physical Review Applied*, 15(3):034036, 2021.

[236] K. Hütten, M. Mittermair, S. O. Stock, R. Beerwerth, V. Shirvanyan, J. Riemensberger, A. Duensing, R. Heider, M. S. Wagner, A. Guggenmos, S. Fritzsche, N. M. Kabachnik, R. Kienberger, and B. Bernhardt. Ultrafast quantum control of ionization dynamics in krypton. *Nature Communications*, 9(1):719, 2018.

[237] V. Stooß, M. Hartmann, P. Birk, G. D. Borisova, T. Ding, A. Blättermann, C. Ott, and T. Pfeifer. XUV-beamline for attosecond transient absorption measurements featuring a broadband common beam-path time-delay unit and in situ reference spectrometer for high stability and sensitivity. *Review of Scientific Instruments*, 90(5):053108, 2019.

[238] M. Fieß, M. Schultze, E. Goulielmakis, B. Dennhardt, J. Gagnon, M. Hofstetter, R. Kienberger, and F. Krausz. Versatile apparatus for attosecond metrology and spectroscopy. *Review of Scientific Instruments*, 81(9):093103, 2010.

[239] T. Ding. *Quantum dynamics in weak and strong fields measured by XUV nonlinear spectroscopy*. PhD thesis, Ruperto-Carola-University of Heidelberg, 2018.

[240] M. Rebholz. *All-XUV pump-probe transient absorption spectroscopy on the dissociation dynamics of small molecules*. PhD thesis, Ruperto-Carola-University of Heidelberg, 2020.

[241] L. Aufleger. *Nonlinear spectroscopy on an autoionizing two-electron resonance in intense, extreme ultraviolet fields at a free-electron laser*. PhD thesis, Ruperto-Carola-University of Heidelberg, 2022.

[242] Corning Inc. MACOR Machinable Glass Ceramic. `https://www.corning.com/emea/de/products/advanced-optics/product-materials/specialty-glass-and-glass-ceramics/glass-ceramics/macor.html`, accessed on 12 Mar. 2022.

[243] M. Chini, K. Zhao, and Z. Chang. The generation, characterization and applications of broadband isolated attosecond pulses. *Nature Photonics*, 8(3): 178–186, 2014.

[244] P. Antoine, A. L'Huillier, and M. Lewenstein. Attosecond Pulse Trains Using High–Order Harmonics. *Physical Review Letters*, 77(7):1234–1237, 1996.

[245] P. Agostini and L. F. DiMauro. The physics of attosecond light pulses. *Reports on Progress in Physics*, 67(6):813–855, 2004.

[246] A. S. Johnson, D. R. Austin, D. A. Wood, C. Brahms, A. Gregory, K. B. Holzner, S. Jarosch, E. W. Larsen, S. Parker, C. S. Strüber, P. Ye, J. W. G. Tisch, and J. P. Marangos. High-flux soft x-ray harmonic generation from ionization-shaped few-cycle laser pulses. *Science Advances*, 4(5), 2018.

[247] J. Schötz, B. Förg, W. Schweinberger, I. Liontos, H. A. Masood, A. M. Kamal, C. Jakubeit, N. G. Kling, T. Paasch-Colberg, S. Biswas, M. Högner, I. Pupeza, M. Alharbi, A. M. Azzeer, and M. F. Kling. Phase-Matching for Generation of Isolated Attosecond XUV and Soft-X-Ray Pulses with Few-Cycle Drivers. *Physical Review X*, 10(4):041011, 2020.

[248] M. B. Gaarde, F. Salin, E. Constant, P. Balcou, K. J. Schafer, K. C. Kulander, and A. L'Huillier. Spatiotemporal separation of high harmonic radiation into two quantum path components. *Physical Review A*, 59(2):1367–1373, 1999.

[249] S. Roscam Abbing, F. Campi, F. S. Sajjadian, N. Lin, P. Smorenburg, and P. M. Kraus. Divergence Control of High-Harmonic Generation. *Physical Review Applied*, 13(5):054029, 2020.

[250] P. Salières, A. L'Huillier, and M. Lewenstein. Coherence Control of High-Order Harmonics. *Physical Review Letters*, 74(19):3776–3779, 1995.

[251] SmarAct GmbH. SID-5714-ID-22 - Iris Diaphragm. `https://www.smaract.com/opto-mechanics/product/xsid-5714-id-22-218`, accessed on 14 Mar. 2022.

[252] optiX fab GmbH. optiX fab - EUV optics. `http://www.optixfab.com/index.html`, accessed 27 Mar. 2022.

[253] M. Rebholz. *Design and construction of an experimental setup for multidi-*

mensional spectroscopy in the XUV/soft-X-ray spectral region. MSc thesis, Ruperto-Carola-University of Heidelberg, 2015.

[254] T. Ding, C. Ott, A. Kaldun, A. Blättermann, K. Meyer, V. Stooss, M. Rebholz, P. Birk, M. Hartmann, A. Brown, H. Van Der Hart, and T. Pfeifer. Time-resolved four-wave-mixing spectroscopy for inner-valence transitions. *Optics Letters*, 41(4):709, 2016.

[255] Hitachi High Technologies America Inc. Aberration-Corrected Concave Gratings for Flat-Field Spectrographs. `https://www.hitachi-hightech.com/products/images/9797/ana-grating_05.pdf`, accessed 15 Mar. 2022.

[256] Teledyne Princeton Instruments. PIXIS-XO: 400B. `https://www.princetoninstruments.com/wp-content/uploads/2020/04/PIXIS-XO_400B_datasheet.pdf`, accessed on 27 Mar. 2022.

[257] T. Kita, T. Harada, N. Nakano, and H. Kuroda. Mechanically ruled aberration-corrected concave gratings for a flat-field grazing-incidence spectrograph. *Applied Optics*, 22(4):512, 1983.

[258] H. A. Rowland. XXIX. On concave gratings for optical purposes. *The London, Edinburgh, and Dublin Philosophical Magazine and Journal of Science*, 16(99): 197–210, 1883.

[259] Physik Instrumente GmbH. PIHera Linear Precision Positioner. `https://www.physikinstrumente.com/en/products/nanopositioning-piezo-flexure-stages/linear-piezo-flexure-stages/p-6201-p-6291-pihera-linear-precision-positioner-202300/`, accessed on 16 Mar. 2022.

[260] Physik Instrumente GmbH. S-325 Piezo Z/Tip/Tilt Platform. `https://www.physikinstrumente.com/en/products/nanopositioning-piezo-flexure-stages/piezo-flexure-tilting-mirrors/s-325-piezo-z-tip-tilt-platform-300650/`, accessed on 16 Mar. 2022.

[261] Physik Instrumente GmbH. H-811.I2V Vacuum-Compatible 6-Axis Miniature Hexapod. `https://www.physikinstrumente.com/en/products/parallel-kinematic-hexapods/h-811i2v-vacuum-compatible-6-axis-miniature-hexapod-412418499/`, accessed on 16 Mar. 2022.

[262] K. Schulz, M. Domke, R. Püttner, A. Gutiérrez, G. Kaindl, G. Miecznik, and

C. H. Greene. High-resolution experimental and theoretical study of singly and doubly excited resonances in ground-state photoionization of neon. *Physical Review A*, 54(4):3095–3112, 1996.

[263] K. Codling, R. P. Madden, and D. L. Ederer. Resonances in the Photo-Ionization Continuum of Ne I (20-150 eV). *Physical Review*, 155(1):26–37, 1967.

[264] E. B. Saloman and C. J. Sansonetti. Wavelengths, Energy Level Classifications, and Energy Levels for the Spectrum of Neutral Neon. *Journal of Physical and Chemical Reference Data*, 33(4):1113–1158, 2004.

[265] V. Kaufman and L. Minnhagen. Accurate Ground-Term Combinations in Ne I. *Journal of the Optical Society of America*, 62(1):92, 1972.

[266] W. Persson. The Spectrum of Singly Ionized Neon, Ne II. *Physica Scripta*, 3 (3-4):133–155, 1971.

[267] F. Henrich. *An investigation into experimental transient absorption measurements of neon by a few-level simulation*. BSc thesis, Ruperto-Carola-University of Heidelberg, 2020.

[268] M. Domke, K. Schulz, G. Remmers, G. Kaindl, and D. Wintgen. High-resolution study of $^1P^0$ double-excitation states in helium. *Physical Review A*, 53(3): 1424–1438, 1996.

[269] C. Ott, A. Kaldun, P. Raith, K. Meyer, M. Laux, J. Evers, C. H. Keitel, C. H. Greene, and T. Pfeifer. Lorentz meets Fano in spectral line shapes: a universal phase and its laser control. *Science*, 340(6133):716–20, 2013.

[270] C. Ott, A. Kaldun, L. Argenti, P. Raith, K. Meyer, M. Laux, Y. Zhang, A. Blättermann, S. Hagstotz, T. Ding, R. Heck, J. Madroñero, F. Martín, and T. Pfeifer. Reconstruction and control of a time-dependent two-electron wave packet. *Nature*, 516(7531):374–378, 2014.

[271] A. Kaldun, A. Blättermann, V. Stooß, S. Donsa, H. Wei, R. Pazourek, S. Nagele, C. Ott, C. D. Lin, J. Burgdörfer, and T. Pfeifer. Observing the ultrafast buildup of a Fano resonance in the time domain. *Science*, 354(6313):738–741, 2016.

[272] N. Harkema, J. E. Bækhøj, C.-T. Liao, M. B. Gaarde, K. J. Schafer, and A. Sandhu. Controlling attosecond transient absorption with tunable, non-

commensurate light fields. *Optics Letters*, 43(14):3357, 2018.

[273] N. Harkema, C. Cariker, E. Lindroth, L. Argenti, and A. Sandhu. Autoionizing Polaritons in Attosecond Atomic Ionization. *Physical Review Letters*, 127(2): 023202, 2021.

[274] S. Chen, M. J. Bell, A. R. Beck, H. Mashiko, M. Wu, A. N. Pfeiffer, M. B. Gaarde, D. M. Neumark, S. R. Leone, and K. J. Schafer. Light-induced states in attosecond transient absorption spectra of laser-dressed helium. *Physical Review A*, 86(6):063408, 2012.

[275] M. Chini, X. Wang, Y. Cheng, Y. Wu, D. Zhao, D. A. Telnov, S.-I. Chu, and Z. Chang. Sub-cycle Oscillations in Virtual States Brought to Light. *Scientific Reports*, 3(1):1105, 2013.

[276] M. J. Bell, A. R. Beck, H. Mashiko, D. M. Neumark, and S. R. Leone. Intensity dependence of light-induced states in transient absorption of laser-dressed helium measured with isolated attosecond pulses. *Journal of Modern Optics*, 60(17): 1506–1516, 2013.

[277] M. Reduzzi, J. Hummert, A. Dubrouil, F. Calegari, M. Nisoli, F. Frassetto, L. Poletto, S. Chen, M. Wu, M. B. Gaarde, K. Schafer, and G. Sansone. Polarization control of absorption of virtual dressed states in helium. *Physical Review A*, 92(3):033408, 2015.

[278] X. Wu, S. Zhang, and D. Ye. Clocking the buildup dynamics of light-induced states through attosecond transient absorption spectrum. *Journal of Physics B: Atomic, Molecular and Optical Physics*, 54(20):205602, 2021.

[279] M. Wu, S. Chen, S. Camp, K. J. Schafer, and M. B. Gaarde. Theory of strong-field attosecond transient absorption. *Journal of Physics B: Atomic, Molecular and Optical Physics*, 49(6):062003, 2016.

[280] C. Shannon. Communication in the Presence of Noise. *Proceedings of the IRE*, 37(1):10–21, 1949.

[281] I. Sanchez, H. Bachau, and E. Cormier. Theory of two-photon spectroscopy of autoionizing states in helium and beryllium. *Journal of Physics B: Atomic, Molecular and Optical Physics*, 28(12):2367–2384, 1995.

[282] C. da Costa Castanheira. *Towards multidimensional spectroscopy experiments in the XUV*. MSc thesis, Ruperto-Carola-University of Heidelberg, 2018.

[283] S. Takezawa. Absorption Spectrum of H_2 in the Vacuum-UV Region. I. Rydberg States and Ionization Energies. *The Journal of Chemical Physics*, 52(5):2575–2590, 1970.

[284] Y. Cheng, M. Chini, X. Wang, A. González-Castrillo, A. Palacios, L. Argenti, F. Martín, and Z. Chang. Reconstruction of an excited-state molecular wave packet with attosecond transient absorption spectroscopy. *Physical Review A*, 94(2):023403, 2016.

[285] D. Holland, D. Shaw, S. McSweeney, M. MacDonald, A. Hopkirk, and M. Hayes. A study of the absolute photoabsorption, photoionization and photodissociation cross sections and the photoionization quantum efficiency of oxygen from the ionization threshold to 490 Å. *Chemical Physics*, 173(2):315–331, 1993.

[286] C.-T. Liao, X. Li, D. J. Haxton, T. N. Rescigno, R. R. Lucchese, C. W. McCurdy, and A. Sandhu. Probing autoionizing states of molecular oxygen with XUV transient absorption: Electronic-symmetry-dependent line shapes and laser-induced modifications. *Physical Review A*, 95(4):043427, 2017.

[287] X. Ren, J. Li, Y. Yin, K. Zhao, A. Chew, Y. Wang, S. Hu, Y. Cheng, E. Cunningham, Y. Wu, M. Chini, and Z. Chang. Attosecond light sources in the water window. *Journal of Optics*, 20(2):023001, 2018.

[288] J. Li, X. Ren, Y. Yin, K. Zhao, A. Chew, Y. Cheng, E. Cunningham, Y. Wang, S. Hu, Y. Wu, M. Chini, and Z. Chang. 53-attosecond X-ray pulses reach the carbon K-edge. *Nature Communications*, 8(1):186, 2017.

[289] J. Pupeikis, P.-A. Chevreuil, N. Bigler, L. Gallmann, C. R. Phillips, and U. Keller. Water window soft x-ray source enabled by a 25 W few-cycle 22 µm OPCPA at 100 kHz. *Optica*, 7(2):168, 2020.

[290] D. Popmintchev, B. R. Galloway, M.-C. Chen, F. Dollar, C. A. Mancuso, A. Hankla, L. Miaja-Avila, G. O'Neil, J. M. Shaw, G. Fan, S. Ališauskas, G. Andriukaitis, T. Balčiunas, O. D. Mücke, A. Pugzlys, A. Baltuška, H. C. Kapteyn, T. Popmintchev, and M. M. Murnane. Near- and Extended-Edge X-Ray-Absorption Fine-Structure Spectroscopy Using Ultrafast Coherent High-

Order Harmonic Supercontinua. *Physical Review Letters*, 120(9):093002, 2018.

[291] K. S. Zinchenko, F. Ardana-Lamas, I. Seidu, S. P. Neville, J. van der Veen, V. U. Lanfaloni, M. S. Schuurman, and H. J. Wörner. Sub-7-femtosecond conical-intersection dynamics probed at the carbon K-edge. *Science*, 371(6528): 489–494, 2021.

[292] X. He, L. Fusti-Molnar, G. Cui, and K. M. Merz. Importance of Dispersion and Electron Correlation in ab Initio Protein Folding. *The Journal of Physical Chemistry B*, 113(15):5290–5300, 2009.

[293] S. Tanaka, Y. Mochizuki, Y. Komeiji, Y. Okiyama, and K. Fukuzawa. Electron-correlated fragment-molecular-orbital calculations for biomolecular and nano systems. *Phys. Chem. Chem. Phys.*, 16(22):10310–10344, 2014.

[294] L. Pauling. The nature of the chemical bond. Application of results obtained from the quantum mechanics and from a theory of paramagnetic susceptibility to the structure of molecules. *Journal of the American Chemical Society*, 53(4): 1367–1400, 1931.

[295] R. S. Mulliken. Electronic Population Analysis on LCAO–MO Molecular Wave Functions. I. *The Journal of Chemical Physics*, 23(10):1833–1840, 1955.

[296] D. R. Hartree. The Wave Mechanics of an Atom with a Non-Coulomb Central Field. Part I. Theory and Methods. *Mathematical Proceedings of the Cambridge Philosophical Society*, 24(1):89–110, 1928.

[297] J. C. Slater. The Self Consistent Field and the Structure of Atoms. *Physical Review*, 32(3):339–348, 1928.

[298] V. Fock. Näherungsmethode zur Lösung des quantenmechanischen Mehrkörperproblems. *Zeitschrift für Physik*, 61(1-2):126–148, 1930.

[299] P. Hohenberg and W. Kohn. Inhomogeneous Electron Gas. *Physical Review*, 136(3B):B864–B871, 1964.

[300] W. Kohn and L. J. Sham. Self-Consistent Equations Including Exchange and Correlation Effects. *Physical Review*, 140(4A):A1133–A1138, 1965.

[301] R. K. Nesbet. Configuration interaction in orbital theories. *Proceedings of the Royal Society of London. Series A. Mathematical and Physical Sciences*, 230

(1182):312–321, 1955.

[302] H. D. Meyer, U. Manthe, and L. S. Cederbaum. The multi-configurational time-dependent Hartree approach. *Chemical Physics Letters*, 165(1):73–78, 1990.

[303] M. Nest, T. Klamroth, and P. Saalfrank. The multiconfiguration time-dependent Hartree–Fock method for quantum chemical calculations. *The Journal of Chemical Physics*, 122(12):124102, 2005.

[304] R. J. Bartlett and J. F. Stanton. Applications of Post-Hartree-Fock Methods: A Tutorial. In *Reviews in Computational Chemistry*, volume 5, pages 65–169. 2007.

[305] K. G. Wilson. The renormalization group: Critical phenomena and the Kondo problem. *Reviews of Modern Physics*, 47(4):773–840, 1975.

[306] A. H. Zewail. Laser femtochemistry. *Science*, 242(4886):1645–53, 1988.

[307] A. H. Zewail. Femtochemistry: Atomic-Scale Dynamics of the Chemical Bond Using Ultrafast Lasers. *Angewandte Chemie International Edition*, 39(15): 2586–2631, 2000.

[308] R. N. Zare. Laser control of chemical reactions. *Science*, 279(5358):1875–9, 1998.

[309] V. Engel, H. Metiu, R. Almeida, R. Marcus, and A. H. Zewail. Molecular state evolution after excitation with an ultra-short laser pulse: A quantum analysis of NaI and NaBr dissociation. *Chemical Physics Letters*, 152(1):1–7, 1988.

[310] T. Baumert, M. Grosser, R. Thalweiser, and G. Gerber. Femtosecond time-resolved molecular multiphoton ionization: The Na_2 system. *Physical Review Letters*, 67(27):3753–3756, 1991.

[311] B. J. Sussman, D. Townsend, M. Y. Ivanov, and A. Stolow. Dynamic stark control of photochemical processes. *Science*, 314(5797):278–81, 2006.

[312] M. Dantus, M. J. Rosker, and A. H. Zewail. Real-time femtosecond probing of "transition states" in chemical reactions. *The Journal of Chemical Physics*, 87 (4):2395–2397, 1987.

[313] A. Assion, T. Baumert, M. Bergt, T. Brixner, B. Kiefer, V. Seyfried, M. Strehle, and G. Gerber. Control of Chemical Reactions by Feedback-Optimized Phase-Shaped Femtosecond Laser Pulses. *Science*, 282(5390):919–922, 1998.

[314] E. T. Karamatskos, S. Raabe, T. Mullins, A. Trabattoni, P. Stammer, G. Goldsztejn, R. R. Johansen, K. Długołecki, H. Stapelfeldt, M. J. J. Vrakking, S. Trippel, A. Rouzée, and J. Küpper. Molecular movie of ultrafast coherent rotational dynamics of OCS. *Nature Communications*, 10(1):3364, 2019.

[315] J. L. Herek, W. Wohlleben, R. J. Cogdell, D. Zeidler, and M. Motzkus. Quantum control of energy flow in light harvesting. *Nature*, 417(6888):533–535, 2002.

[316] T. Brixner, J. Stenger, H. M. Vaswani, M. Cho, R. E. Blankenship, and G. R. Fleming. Two-dimensional spectroscopy of electronic couplings in photosynthesis. *Nature*, 434(7033):625–628, 2005.

[317] R. R. Subkhangulov, A. B. Henriques, P. H. Rappl, E. Abramof, T. Rasing, and A. V. Kimel. All-optical manipulation and probing of the d-f exchange interaction in EuTe. *Scientific Reports*, 4(1):4368, 2015.

[318] F. Siegrist, J. A. Gessner, M. Ossiander, C. Denker, Y. P. Chang, M. C. Schröder, A. Guggenmos, Y. Cui, J. Walowski, U. Martens, J. K. Dewhurst, U. Kleineberg, M. Münzenberg, S. Sharma, and M. Schultze. Light-wave dynamic control of magnetism. *Nature*, 571(7764):240–244, 2019.

[319] D. Fausti, R. I. Tobey, N. Dean, S. Kaiser, A. Dienst, M. C. Hoffmann, S. Pyon, T. Takayama, H. Takagi, and A. Cavalleri. Light-induced superconductivity in a stripe-ordered cuprate. *Science*, 331(6014):189–91, 2011.

[320] N. V. Vitanov, A. A. Rangelov, B. W. Shore, and K. Bergmann. Stimulated Raman adiabatic passage in physics, chemistry, and beyond. *Reviews of Modern Physics*, 89(1):015006, 2017.

[321] O. Smirnova, Y. Mairesse, S. Patchkovskii, N. Dudovich, D. Villeneuve, P. Corkum, and M. Y. Ivanov. High harmonic interferometry of multi-electron dynamics in molecules. *Nature*, 460(7258):972–977, 2009.

[322] A. Marciniak, S. Marcantoni, F. Giusti, F. Glerean, G. Sparapassi, T. Nova, A. Cartella, S. Latini, F. Valiera, A. Rubio, J. van den Brink, F. Benatti, and D. Fausti. Vibrational coherent control of localized d–d electronic excitation.

Nature Physics, 17(3):368–373, 2021.

[323] J. F. Moulder, W. F. Stickle, P. E. Sobol, and K. D. Bomben. *Handbook of X-ray Photoelectron Spectroscopy Edited by*. Physical Electronics Division, Perkin-Elmer Corporation, 1992.

[324] F. M. de Groot, H. Elnaggar, F. Frati, et al. 2p x-ray absorption spectroscopy of 3d transition metal systems. *Journal of Electron Spectroscopy and Related Phenomena*, 249:147061, 2021.

[325] B. T. Thole and G. van der Laan. Branching ratio in x-ray absorption spectroscopy. *Physical Review B*, 38(5):3158–3171, 1988.

[326] M. Kadek, L. Konecny, B. Gao, M. Repisky, and K. Ruud. X-ray absorption resonances near $L_{2,3}$-edges from real-time propagation of the Dirac–Kohn–Sham density matrix. *Physical Chemistry Chemical Physics*, 17(35):22566–22570, 2015.

[327] Y. Onodera and Y. Toyozawa. Excitons in alkali halides. *Journal of the Physical Society of Japan*, 22(3):833–844, 1967.

[328] P. A. M. Dirac. The quantum theory of the emission and absorption of radiation. *Proceedings of the Royal Society of London. Series A, Containing Papers of a Mathematical and Physical Character*, 114(767):243–265, 1927.

[329] J. L. Dehmer. Evidence of Effective Potential Barriers in the X-Ray Absorption Spectra of Molecules. *The Journal of Chemical Physics*, 56(9):4496–4504, 1972.

[330] Y. Sato, K. Ueda, H. Chiba, E. Shigemasa, and A. Yagishita. Auger-electron—photoion and photoion—photoion coincidence studies on ionic fragmentation of SF_6 following the S L-shell excitation. *Chemical Physics Letters*, 196(5):475–480, 1992.

[331] M. Coville and T. D. Thomas. Molecular effects on inner-shell lifetimes: Possible test of the one-center model of Auger decay. *Physical Review A*, 43(11):6053–6056, 1991.

[332] M. Drescher, M. Hentschel, R. Kienberger, M. Uiberacker, V. Yakovlev, A. Scrinzi, T. Westerwalbesloh, U. Kleineberg, U. Heinzmann, and F. Krausz. Time-resolved atomic inner-shell spectroscopy. *Nature*, 419(6909):803–807, 2002.

[333] D. C. Haynes, M. Wurzer, A. Schletter, et al. Clocking Auger electrons. *Nature Physics*, 17(4):512–518, 2021.

[334] Private communication with manufacturer *SmarAct*.

[335] W. Voigt. Über das Gesetz der Intensitätsverteilung innerhalb der Linien eines Gasspektrums. *Sitzungsberichte Königliche Bayerische Akademie der Wissenschaften*, 42:603–620, 1912.

[336] W. J. Thompson. Numerous Neat Algorithms for the Voigt Profile Function. *Computers in Physics*, 7(6):627, 1993.

[337] V. N. Faddeeva and N. M. Terent'ev. Tables of values of the function $w(z) = exp(-z^2)(1 + 2i/\sqrt{\pi} \int_0^z exp(t^2)dt)$ for complex argument.

[338] The SciPy Community. SciPy nonlinear curve fit algorithm. `https://docs.scipy.org/doc/scipy/reference/generated/scipy.optimize.curve_fit.html`, accessed on 27 Mar. 2022.

[339] J. Olivero and R. Longbothum. Empirical fits to the Voigt line width: A brief review. *Journal of Quantitative Spectroscopy and Radiative Transfer*, 17(2): 233–236, 1977.

[340] J. R. Taylor. *An Introduction to Error Analysis: The Study of Uncertainties in Physical Measurements*. University Science Books, 1997.

[341] The SciPy Community. SciPy differential evolution algorithm. `https://docs.scipy.org/doc/scipy/reference/generated/scipy.optimize.differential_evolution.html`, accessed on 27 Mar. 2022.

[342] R. Storn and K. Price. Differential Evolution - A Simple and Efficient Heuristic for Global Optimization over Continuous Spaces. *Journal of Global Optimization*, 11(4):341–359, 1997.

[343] K. Koepernik and H. Eschrig. Full-potential nonorthogonal local-orbital minimum-basis band-structure scheme. *Physical Review B*, 59(3):1743–1757, 1999.

[344] K. Koepernik. FPLO website. `https://www.fplo.de/`, accessed on 27 Mar. 2022.

[345] M. W. Haverkort, M. Zwierzycki, and O. K. Andersen. Multiplet ligand-field theory using Wannier orbitals. *Physical Review B*, 85(16):165113, 2012.

[346] M. W. Haverkort. QUANTY website. `http://quanty.org/`, accessed 27 Mar. 2022.

[347] J. Réhault, R. Borrego-Varillas, A. Oriana, C. Manzoni, C. P. Hauri, J. Helbing, and G. Cerullo. Fourier transform spectroscopy in the vibrational fingerprint region with a birefringent interferometer. *Optics Express*, 25(4):4403, 2017.

[348] H. Timmers, A. Kowligy, A. Lind, F. C. Cruz, N. Nader, M. Silfies, G. Ycas, T. K. Allison, P. G. Schunemann, S. B. Papp, and S. A. Diddams. Molecular fingerprinting with bright, broadband infrared frequency combs. *Optica*, 5(6): 727, 2018.

[349] I. Pupeza, M. Huber, M. Trubetskov, W. Schweinberger, S. A. Hussain, C. Hofer, K. Fritsch, M. Poetzlberger, L. Vamos, E. Fill, T. Amotchkina, K. V. Kepesidis, A. Apolonski, N. Karpowicz, V. Pervak, O. Pronin, F. Fleischmann, A. Azzeer, M. Žigman, and F. Krausz. Field-resolved infrared spectroscopy of biological systems. *Nature*, 577(7788):52–59, 2020.

[350] A. W. Chao, K. H. Mess, M. Tigner, and F. Zimmermann. *Handbook of Accelerator Physics and Engineering*. World Scientific, 2013.

[351] E. Esarey, C. B. Schroeder, and W. P. Leemans. Physics of laser-driven plasma-based electron accelerators. *Reviews of Modern Physics*, 81(3):1229–1285, 2009.

[352] R. Srinivasan, V. A. Lobastov, C.-Y. Ruan, and A. H. Zewail. Ultrafast Electron Diffraction (UED). *Helvetica Chimica Acta*, 86(6):1761–1799, 2003.

[353] G. Sciaini and R. J. D. Miller. Femtosecond electron diffraction: heralding the era of atomically resolved dynamics. *Reports on Progress in Physics*, 74(9): 096101, 2011.

[354] X. Shen, J. P. F. Nunes, J. Yang, R. K. Jobe, R. K. Li, M.-F. Lin, B. Moore, M. Niebuhr, S. P. Weathersby, T. J. A. Wolf, C. Yoneda, M. Guehr, M. Centurion, and X. J. Wang. Femtosecond gas-phase mega-electron-volt ultrafast electron diffraction. *Structural Dynamics*, 6(5):054305, 2019.

[355] E. G. Champenois, D. M. Sanchez, J. Yang, J. P. Figueira Nunes, A. Attar,

M. Centurion, R. Forbes, M. Gühr, K. Hegazy, F. Ji, S. K. Saha, Y. Liu, M.-F. Lin, D. Luo, B. Moore, X. Shen, M. R. Ware, X. J. Wang, T. J. Martínez, and T. J. A. Wolf. Conformer-specific photochemistry imaged in real space and time. *Science*, 374(6564):178–182, 2021.

[356] M. Centurion, T. J. A. Wolf, and J. Yang. Ultrafast Imaging of Molecules with Electron Diffraction. *Annual review of physical chemistry*, 49(6):062002, 2021.

[357] C. Kealhofer, W. Schneider, D. Ehberger, A. Ryabov, F. Krausz, and P. Baum. All-optical control and metrology of electron pulses. *Science*, 352(6284):429–33, 2016.

[358] S. Tokita, M. Hashida, S. Inoue, T. Nishoji, K. Otani, and S. Sakabe. Single-Shot Femtosecond Electron Diffraction with Laser-Accelerated Electrons: Experimental Demonstration of Electron Pulse Compression. *Physical Review Letters*, 105 (21):215004, 2010.

[359] A. Feist, K. E. Echternkamp, J. Schauss, S. V. Yalunin, S. Schäfer, and C. Ropers. Quantum coherent optical phase modulation in an ultrafast transmission electron microscope. *Nature*, 521(7551):200–203, 2015.

[360] R. Srinivasan, J. S. Feenstra, S. T. Park, S. Xu, and A. H. Zewail. Dark structures in molecular radiationless transitions determined by ultrafast diffraction. *Science*, 307(5709):558–63, 2005.

[361] A. H. Zewail. Four-dimensional electron microscopy. *Science*, 328(5975):187–93, 2010.

[362] C. I. Blaga, J. Xu, A. D. DiChiara, E. Sistrunk, K. Zhang, P. Agostini, T. A. Miller, L. F. DiMauro, and C. D. Lin. Imaging ultrafast molecular dynamics with laser-induced electron diffraction. *Nature*, 483(7388):194–197, 2012.

[363] A. Sanchez, K. Amini, S.-J. Wang, T. Steinle, B. Belsa, J. Danek, A. T. Le, X. Liu, R. Moshammer, T. Pfeifer, M. Richter, J. Ullrich, S. Gräfe, C. D. Lin, and J. Biegert. Molecular structure retrieval directly from laboratory-frame photoelectron spectra in laser-induced electron diffraction. *Nature Communications*, 12(1):1520, 2021.

[364] B. Wolter, M. G. Pullen, A.-T. Le, M. Baudisch, K. Doblhoff-Dier, A. Senftleben, M. Hemmer, C. D. Schröter, J. Ullrich, T. Pfeifer, R. Moshammer, S. Gräfe,

O. Vendrell, C. D. Lin, and J. Biegert. Ultrafast electron diffraction imaging of bond breaking in di-ionized acetylene. *Science*, 354(6310):308–312, 2016.

[365] M. Kreitmeir, G. Heusel, H. Bertagnolli, K. Tödheide, C. J. Mundy, and G. J. Cuello. Structure of dense hydrogen fluoride gas from neutron diffraction and molecular dynamics simulations. *The Journal of Chemical Physics*, 122(15): 154511, 2005.

[366] B. Jacrot. The study of biological structures by neutron scattering from solution. *Reports on Progress in Physics*, 39(10):911–953, 1976.

[367] S. F. Parker, D. Lennon, and P. W. Albers. Vibrational Spectroscopy with Neutrons: A Review of New Directions. *Applied Spectroscopy*, 65(12):1325–1341, 2011.

[368] I. Pomerantz, E. McCary, A. R. Meadows, A. Arefiev, A. C. Bernstein, C. Chester, J. Cortez, M. E. Donovan, G. Dyer, E. W. Gaul, D. Hamilton, D. Kuk, A. C. Lestrade, C. Wang, T. Ditmire, and B. M. Hegelich. Ultrashort Pulsed Neutron Source. *Physical Review Letters*, 113(18):184801, 2014.

[369] A. Macchi. A femtosecond neutron source. *Applied Physics B*, 82(3):337–340, 2006.

[370] B. E. Warren. *X-ray Diffraction*. Addison-Wesley series in metallurgy and materials engineering. Dover Publications, 1990.

[371] H. Ihee, M. Lorenc, T. K. Kim, Q. Y. Kong, M. Cammarata, J. H. Lee, S. Bratos, and M. Wulff. Ultrafast x-ray diffraction of transient molecular structures in solution. *Science*, 309(5738):1223–7, 2005.

[372] G. Ingold, P. Beaud, S. L. Johnson, D. Grolimund, V. Schlott, T. Schmidt, and A. Streun. Technical Report: FEMTO: A Sub-ps Tunable Hard X-ray Undulator Source for Laser/X-ray Pump-Probe Experiments at the SLS. *Synchrotron Radiation News*, 20(5):35–39, 2007.

[373] M. J. Bogan, W. H. Benner, S. Boutet, U. Rohner, M. Frank, A. Barty, M. M. Seibert, F. Maia, S. Marchesini, S. Bajt, B. Woods, V. Riot, S. P. Hau-Riege, M. Svenda, E. Marklund, E. Spiller, J. Hajdu, and H. N. Chapman. Single Particle X-ray Diffractive Imaging. *Nano Letters*, 8(1):310–316, 2008.

[374] J. Miao, T. Ishikawa, I. K. Robinson, and M. M. Murnane. Beyond crystallography: diffractive imaging using coherent x-ray light sources. *Science*, 348(6234): 530–5, 2015.

[375] J. M. Glownia, A. Natan, J. P. Cryan, R. Hartsock, M. Kozina, M. P. Minitti, S. Nelson, J. Robinson, T. Sato, T. van Driel, G. Welch, C. Weninger, D. Zhu, and P. H. Bucksbaum. Self-Referenced Coherent Diffraction X-Ray Movie of Ångstrom- and Femtosecond-Scale Atomic Motion. *Physical Review Letters*, 117 (15):153003, 2016.

[376] B. Eliasson and C. S. Liu. An electromagnetic gamma-ray free electron laser. *Journal of Plasma Physics*, 79(6):995–998, 2013.

[377] P. M. Kraus and H. J. Wörner. Perspectives of Attosecond Spectroscopy for the Understanding of Fundamental Electron Correlations. *Angewandte Chemie International Edition*, 57(19):5228–5247, 2018.

[378] S. Baker, J. S. Robinson, C. A. Haworth, H. Teng, R. A. Smith, C. C. Chirila, M. Lein, J. W. G. Tisch, and J. P. Marangos. Probing proton dynamics in molecules on an attosecond time scale. *Science*, 312(5772):424–7, 2006.

[379] P. Peng, C. Marceau, and D. M. Villeneuve. Attosecond imaging of molecules using high harmonic spectroscopy. *Nature Reviews Physics*, 1(2):144–155, 2019.

[380] W. C. Price. Photoelectron Spectroscopy and Molecular Structure. *International Reviews in Physical Chemistry*, 1(1):1–30, 1981.

[381] G. Greczynski and L. Hultman. X-ray photoelectron spectroscopy: Towards reliable binding energy referencing. *Progress in Materials Science*, 107(April 2019):100591, 2020.

[382] T. Ergler, A. Rudenko, B. Feuerstein, K. Zrost, C. D. Schröter, R. Moshammer, and J. Ullrich. Ultrafast mapping of H_2^+ (D_2^+) nuclear wave packets using time-resolved Coulomb explosion imaging. *Journal of Physics B: Atomic, Molecular and Optical Physics*, 39(13):S493–S501, 2006.

[383] X. Li, A. Rudenko, M. S. Schöffler, et al. Coulomb explosion imaging of small polyatomic molecules with ultrashort x-ray pulses. *Physical Review Research*, 4 (1):013029, 2022.

[384] W. Schuelke. *Electron dynamics by inelastic X-ray scattering*. Oxford University Press, 2007.

[385] L. J. P. Ament, M. van Veenendaal, T. P. Devereaux, J. P. Hill, and J. van den Brink. Resonant inelastic x-ray scattering studies of elementary excitations. *Reviews of Modern Physics*, 83(2):705–767, 2011.

[386] Y. Harada, M. Kobayashi, H. Niwa, Y. Senba, H. Ohashi, T. Tokushima, Y. Horikawa, S. Shin, and M. Oshima. Ultrahigh resolution soft x-ray emission spectrometer at BL07LSU in SPring-8. *Review of Scientific Instruments*, 83(1): 013116, 2012.

[387] S. G. Chiuzbăian, C. F. Hague, A. Avila, R. Delaunay, N. Jaouen, M. Sacchi, F. Polack, M. Thomasset, B. Lagarde, A. Nicolaou, S. Brignolo, C. Baumier, J. Lüning, and J.-M. Mariot. Design and performance of AERHA, a high acceptance high resolution soft x-ray spectrometer. *Review of Scientific Instruments*, 85(4):043108, 2014.

[388] R. Qiao, Q. Li, Z. Zhuo, S. Sallis, O. Fuchs, M. Blum, L. Weinhardt, C. Heske, J. Pepper, M. Jones, A. Brown, A. Spucces, K. Chow, B. Smith, P.-A. Glans, Y. Chen, S. Yan, F. Pan, L. F. J. Piper, J. Denlinger, J. Guo, Z. Hussain, Y.-D. Chuang, and W. Yang. High-efficiency in situ resonant inelastic x-ray scattering (iRIXS) endstation at the Advanced Light Source. *Review of Scientific Instruments*, 88(3):033106, 2017.

[389] M. Beye, P. Wernet, C. Schüßler-Langeheine, and A. Föhlisch. Time resolved resonant inelastic X-ray scattering: A supreme tool to understand dynamics in solids and molecules. *Journal of Electron Spectroscopy and Related Phenomena*, 188:172–182, 2013.

[390] J. Stöhr. *NEXAFS Spectroscopy*, volume 25 of *Springer Series in Surface Sciences*. Springer, Berlin, Heidelberg, 1992.

[391] P. A. Lee, P. H. Citrin, P. Eisenberger, and B. M. Kincaid. Extended x-ray absorption fine structure—its strengths and limitations as a structural tool. *Reviews of Modern Physics*, 53(4):769–806, 1981.

[392] B. Buades, D. Moonshiram, T. P. H. Sidiropoulos, I. León, P. Schmidt, I. Pi, N. Di Palo, S. L. Cousin, A. Picón, F. Koppens, and J. Biegert. Dispersive

soft x-ray absorption fine-structure spectroscopy in graphite with an attosecond pulse. *Optica*, 5(5):502, 2018.

[393] E. R. Hosler and S. R. Leone. Characterization of vibrational wave packets by core-level high-harmonic transient absorption spectroscopy. *Physical Review A*, 88(2):023420, 2013.

[394] H. Timmers, X. Zhu, Z. Li, Y. Kobayashi, M. Sabbar, M. Hollstein, M. Reduzzi, T. J. Martínez, D. M. Neumark, and S. R. Leone. Disentangling conical intersection and coherent molecular dynamics in methyl bromide with attosecond transient absorption spectroscopy. *Nature Communications*, 10(1):3133, 2019.

[395] Y. Kobayashi, K. F. Chang, S. M. Poullain, V. Scutelnic, T. Zeng, D. M. Neumark, and S. R. Leone. Coherent electronic-vibrational dynamics in deuterium bromide probed via attosecond transient-absorption spectroscopy. *Physical Review A*, 101(6):063414, 2020.

[396] N. Saito, H. Sannohe, N. Ishii, T. Kanai, N. Kosugi, Y. Wu, A. Chew, S. Han, Z. Chang, and J. Itatani. Real-time observation of electronic, vibrational, and rotational dynamics in nitric oxide with attosecond soft x-ray pulses at 400 eV. *Optica*, 6(12):1542, 2019.

[397] Z. Wei, J. Li, L. Wang, S. T. See, M. H. Jhon, Y. Zhang, F. Shi, M. Yang, and Z.-H. Loh. Elucidating the origins of multimode vibrational coherences of polyatomic molecules induced by intense laser fields. *Nature Communications*, 8(1):735, 2017.

[398] R. F. Pettifer, O. Mathon, S. Pascarelli, M. D. Cooke, and M. R. J. Gibbs. Measurement of femtometre-scale atomic displacements by X-ray absorption spectroscopy. *Nature*, 435(7038):78–81, 2005.

[399] J. Weisshaupt, A. Rouzée, M. Woerner, M. J. J. Vrakking, T. Elsaesser, E. L. Shirley, and A. Borgschulte. Ultrafast modulation of electronic structure by coherent phonon excitations. *Physical Review B*, 95(8):081101, 2017.

[400] W. Jo, E. C. Landahl, A. D. DiChiara, D. A. Walko, and S. Lee. Measuring femtometer lattice displacements driven by free carrier diffusion in a polycrystalline semiconductor using time-resolved x-ray scattering. *Applied Physics Letters*, 113(3):032107, 2018.

[401] B. K. De, V. Dwij, R. Misawa, T. Kimura, and V. G. Sathe. Femtometer atomic displacement, the root cause for multiferroic behavior of CuO unearthed through polarized Raman spectroscopy. *Journal of Physics: Condensed Matter*, 33(12): 12LT01, 2021.

[402] M. Kozina, T. Hu, J. S. Wittenberg, E. Szilagyi, M. Trigo, T. A. Miller, C. Uher, A. Damodaran, L. Martin, A. Mehta, J. Corbett, J. Safranek, D. A. Reis, and A. M. Lindenberg. Measurement of transient atomic displacements in thin films with picosecond and femtometer resolution. *Structural Dynamics*, 1(3):034301, 2014.

[403] Z. Wu, L. Zhang, M. Zhang, I. L. Li, H. Su, H. Zhao, S. Ruan, and H. Liang. Graphene Plasmon Resonances for Electrically-Tunable Sub-Femtometer Dimensional Resolution. *Nanomaterials*, 10(7):1381, 2020.

[404] Center for X-Ray Optics. Filter transmission. `https://henke.lbl.gov/optical_constants/filter2.html`, accessed 27 Mar. 2022.

[405] Center for X-Ray Optics. Index of Refraction. `https://henke.lbl.gov/optical_constants/getdb2.html`, accessed on 27 Mar. 2022.

[406] M. Holler, F. Schapper, L. Gallmann, and U. Keller. Attosecond Electron Wave-Packet Interference Observed by Transient Absorption. *Physical Review Letters*, 106(12):123601, 2011.

[407] D. Faccialà, B. W. Toulson, and O. Gessner. Removal of correlated background in a high-order harmonic transient absorption spectra with principal component regression. *Optics Express*, 29(22):35135, 2021.

[408] L. Drescher, G. Reitsma, T. Witting, S. Patchkovskii, J. Mikosch, and M. J. J. Vrakking. State-Resolved Probing of Attosecond Timescale Molecular Dipoles. *The Journal of Physical Chemistry Letters*, 10(2):265–269, 2019.

[409] M. E. Wall, A. Rechtsteiner, and L. M. Rocha. Singular Value Decomposition and Principal Component Analysis. In *A Practical Approach to Microarray Data Analysis*, pages 91–109. Kluwer Academic Publishers, Boston, 2002.

[410] A. Aboumajd, H. Berger, and R. Saint-Loup. Analysis of the Raman spectrum of SF_6. *Journal of Molecular Spectroscopy*, 78(3):486–492, 1979.

[411] P. H. Bucksbaum, A. Zavriyev, H. G. Muller, and D. W. Schumacher. Softening of the H_2^+ molecular bond in intense laser fields. *Physical Review Letters*, 64 (16):1883–1886, 1990.

[412] A. Saenz. Enhanced ionization of molecular hydrogen in very strong fields. *Physical Review A*, 61(5):051402, 2000.

[413] T. Ergler, B. Feuerstein, A. Rudenko, K. Zrost, C. D. Schröter, R. Moshammer, and J. Ullrich. Quantum-Phase Resolved Mapping of Ground-State Vibrational D_2 Wave Packets via Selective Depletion in Intense Laser Pulses. *Physical Review Letters*, 97(10):103004, 2006.

[414] T. Ergler, A. Rudenko, B. Feuerstein, K. Zrost, C. D. Schröter, R. Moshammer, and J. Ullrich. Spatiotemporal Imaging of Ultrafast Molecular Motion: Collapse and Revival of the D_2^+ Nuclear Wave Packet. *Physical Review Letters*, 97(19): 193001, 2006.

[415] V. H. Dibeler and F. L. Mohler. Dissociation of SF_6, CF_4, and SiF_4 by electron impact. *Journal of Research of the National Bureau of Standards*, 40(1):25, 1948.

[416] L. A. Schaller, D. A. Barandao, P. Bergem, M. Boschung, T. Q. Phan, G. Piller, A. Rüetschi, L. Schellenberg, H. Schneuwly, G. Fricke, G. Mallot, and H. G. Sieberling. Nuclear charge radii of the even sulphur isotopes ^{32}S, ^{34}S, and ^{36}S and of ^{31}P using muonic atoms. *Physical Review C*, 31(3):1007–1011, 1985.

[417] C. Kleine, M. Ekimova, M.-O. Winghart, S. Eckert, O. Reichel, H. Löchel, J. Probst, C. Braig, C. Seifert, A. Erko, A. Sokolov, M. J. J. Vrakking, E. T. J. Nibbering, and A. Rouzée. Highly efficient soft x-ray spectrometer for transient absorption spectroscopy with broadband table-top high harmonic sources. *Structural Dynamics*, 8(3):034302, 2021.

[418] R. Robinett. Quantum wave packet revivals. *Physics Reports*, 392(1-2):1–119, 2004.

[419] D. Polli, P. Altoè, O. Weingart, K. M. Spillane, C. Manzoni, D. Brida, G. Tomasello, G. Orlandi, P. Kukura, R. A. Mathies, M. Garavelli, and G. Cerullo. Conical intersection dynamics of the primary photoisomerization event in vision. *Nature*, 467(7314):440–443, 2010.

[420] A. Hosseinizadeh, N. Breckwoldt, R. Fung, R. Sepehr, M. Schmidt, P. Schwander, R. Santra, and A. Ourmazd. Few-fs resolution of a photoactive protein traversing a conical intersection. *Nature*, 599(7886):697–701, 2021.

[421] P.-A. Chevreuil, F. Brunner, S. Hrisafov, J. Pupeikis, C. R. Phillips, U. Keller, and L. Gallmann. Water-window high harmonic generation with 0.8-µm and 2.2-µm OPCPAs at 100 kHz. *Optics Express*, 29(21):32996, 2021.

[422] T. Witting, M. Osolodkov, F. Schell, F. Morales, S. Patchkovskii, P. Šušnjar, F. H. M. Cavalcante, C. S. Menoni, C. P. Schulz, F. J. Furch, and M. J. J. Vrakking. Generation and characterization of isolated attosecond pulses at 100 kHz repetition rate. *Optica*, 9(2):145, 2022.

[423] A. Mandal, M. S. Sidhu, J. M. Rost, T. Pfeifer, and K. P. Singh. Attosecond delay lines: design, characterization and applications. *The European Physical Journal Special Topics*, 230(23):4195–4213, 2021.

[424] D. J. Jones, S. A. Diddams, J. K. Ranka, A. Stentz, R. S. Windeler, J. L. Hall, and S. T. Cundiff. Carrier-Envelope Phase Control of Femtosecond Mode-Locked Lasers and Direct Optical Frequency Synthesis. *Science*, 288(5466):635–639, 2000.

[425] M. Sabbar, H. Timmers, Y.-j. Chen, A. K. Pymer, Z.-H. Loh, S. G. Sayres, S. Pabst, R. Santra, and S. R. Leone. State-resolved attosecond reversible and irreversible dynamics in strong optical fields. *Nature Physics*, 13(5):472–478, 2017.

[426] Q. Zhang, H. Xie, G. Li, X. Wang, H. Lei, J. Zhao, Z. Chen, J. Yao, Y. Cheng, and Z. Zhao. Sub-cycle coherent control of ionic dynamics via transient ionization injection. *Communications Physics*, 3(1):50, 2020.

[427] M. Spanner, S. Gräfe, S. Chelkowski, D. Pavičić, M. Meckel, D. Zeidler, A. B. Bardon, B. Ulrich, A. D. Bandrauk, D. M. Villeneuve, R. Dörner, P. B. Corkum, and A. Staudte. Coulomb asymmetry and sub-cycle electron dynamics in multiphoton multiple ionization of H 2. *Journal of Physics B: Atomic, Molecular and Optical Physics*, 45(19):194011, 2012.

[428] H. Rabitz. Shaped laser pulses as reagents. *Science*, 299(5606):525–7, 2003.

[429] S. J. Glaser, U. Boscain, T. Calarco, C. P. Koch, W. Köckenberger, R. Kosloff,

I. Kuprov, B. Luy, S. Schirmer, T. Schulte-Herbrüggen, D. Sugny, and F. K. Wilhelm. Training Schrödinger's cat: quantum optimal control. *The European Physical Journal D*, 69(12):279, 2015.

[430] D. Keefer and R. de Vivie-Riedle. Pathways to New Applications for Quantum Control. *Accounts of Chemical Research*, 51(9):2279–2286, 2018.

[431] T. Seideman. Revival Structure of Aligned Rotational Wave Packets. *Physical Review Letters*, 83(24):4971–4974, 1999.

[432] M. Leibscher, I. S. Averbukh, and H. Rabitz. Molecular Alignment by Trains of Short Laser Pulses. *Physical Review Letters*, 90(21):213001, 2003.

[433] C. Z. Bisgaard, M. D. Poulsen, E. Péronne, S. S. Viftrup, and H. Stapelfeldt. Observation of Enhanced Field-Free Molecular Alignment by Two Laser Pulses. *Physical Review Letters*, 92(17):173004, 2004.

[434] J. P. Cryan, P. H. Bucksbaum, and R. N. Coffee. Field-free alignment in repetitively kicked nitrogen gas. *Physical Review A*, 80(6):2–6, 2009.

[435] P. Peng, Y. Mi, M. Lytova, M. Britton, X. Ding, A. Y. Naumov, P. B. Corkum, and D. M. Villeneuve. Coherent control of ultrafast extreme ultraviolet transient absorption. *Nature Photonics*, 16(1):45–51, 2022.

[436] I. V. Schweigert and S. Mukamel. Coherent Ultrafast Core-Hole Correlation Spectroscopy: X-Ray Analogues of Multidimensional NMR. *Physical Review Letters*, 99(16):163001, 2007.

[437] S. Mukamel, D. Healion, Y. Zhang, and J. D. Biggs. Multidimensional attosecond resonant X-ray spectroscopy of molecules: Lessons from the optical regime. *Annual Review of Physical Chemistry*, 64:101–127, 2013.

[438] M. Cho. *Coherent Multidimensional Spectroscopy*, volume 226 of *Springer Series in Optical Sciences*. Springer Singapore, Singapore, 2019.

[439] M. Kowalewski, K. Bennett, K. E. Dorfman, and S. Mukamel. Catching Conical Intersections in the Act: Monitoring Transient Electronic Coherences by Attosecond Stimulated X-Ray Raman Signals. *Physical Review Letters*, 115 (19):193003, 2015.

[440] J. D. Koralek, J. B. Kim, P. Brůža, C. B. Curry, Z. Chen, H. A. Bechtel, A. A.

Cordones, P. Sperling, S. Toleikis, J. F. Kern, S. P. Moeller, S. H. Glenzer, and D. P. DePonte. Generation and characterization of ultrathin free-flowing liquid sheets. *Nature Communications*, 9(1):1353, 2018.

[441] S. Menzi, G. Knopp, A. Al Haddad, S. Augustin, C. Borca, D. Gashi, T. Huthwelker, D. James, J. Jin, G. Pamfilidis, K. Schnorr, Z. Sun, R. Wetter, Q. Zhang, and C. Cirelli. Generation and simple characterization of flat, liquid jets. *Review of Scientific Instruments*, 91(10):105109, 2020.

[442] A. S. Johnson, T. Avni, E. W. Larsen, D. R. Austin, and J. P. Marangos. Attosecond soft X-ray high harmonic generation. *Philosophical Transactions of the Royal Society A: Mathematical, Physical and Engineering Sciences*, 377 (2145):20170468, 2019.

[443] S. Kühn, M. Dumergue, S. Kahaly, et al. The ELI-ALPS facility: the next generation of attosecond sources. *Journal of Physics B: Atomic, Molecular and Optical Physics*, 50(13):132002, 2017.

[444] C. P. Hauri, C. Ruchert, C. Vicario, and F. Ardana. Strong-field single-cycle THz pulses generated in an organic crystal. *Applied Physics Letters*, 99(16): 161116, 2011.

[445] A. Gragossian, D. V. Seletskiy, and M. Sheik-Bahae. Classical trajectories in polar-asymmetric laser fields: Synchronous THz and XUV emission. *Scientific Reports*, 6(September):1–8, 2016.

[446] C. J. Saraceno. Mode-locked thin-disk lasers and their potential application for high-power terahertz generation. *Journal of Optics*, 20(4):044010, 2018.

[447] P. B. Corkum and F. Krausz. Attosecond science. *Nature Physics*, 3(6):381–387, 2007.

[448] F. Calegari, G. Sansone, S. Stagira, C. Vozzi, and M. Nisoli. Advances in attosecond science. *Journal of Physics B: Atomic, Molecular and Optical Physics*, 49(6):062001, 2016.

[449] L. Young, K. Ueda, M. Gühr, et al. Roadmap of ultrafast x-ray atomic and molecular physics. *Journal of Physics B: Atomic, Molecular and Optical Physics*, 51(3):032003, 2018.

[450] P. M. Kraus, M. Zürch, S. K. Cushing, D. M. Neumark, and S. R. Leone. The ultrafast X-ray spectroscopic revolution in chemical dynamics. *Nature Reviews Chemistry*, 2(6):82–94, 2018.

[451] M. Chergui and A. H. Zewail. Electron and X-Ray Methods of Ultrafast Structural Dynamics: Advances and Applications. *ChemPhysChem*, 10(1): 28–43, 2009.

[452] Z.-H. Loh. Studies of Ultrafast Molecular Dynamics by Femtosecond Extreme Ultraviolet Absorption Spectroscopy. *Chemistry Letters*, 50(5):965–973, 2021.

[453] C. Milne, T. Penfold, and M. Chergui. Recent experimental and theoretical developments in time-resolved X-ray spectroscopies. *Coordination Chemistry Reviews*, 277-278(February):44–68, 2014.

[454] S. R. Leone, C. W. McCurdy, J. Burgdörfer, L. S. Cederbaum, Z. Chang, N. Dudovich, J. Feist, C. H. Greene, M. Ivanov, R. Kienberger, U. Keller, M. F. Kling, Z.-H. Loh, T. Pfeifer, A. N. Pfeiffer, R. Santra, K. Schafer, A. Stolow, U. Thumm, and M. J. J. Vrakking. What will it take to observe processes in 'real time'? *Nature Photonics*, 8(3):162–166, 2014.

[455] F. Noé, A. Tkatchenko, K. R. Müller, and C. Clementi. Machine learning for molecular simulation. *Annual Review of Physical Chemistry*, 71:361–390, 2020.

[456] T. Zubatiuk and O. Isayev. Development of Multimodal Machine Learning Potentials: Toward a Physics-Aware Artificial Intelligence. *Accounts of Chemical Research*, 54(7):1575–1585, 2021.

[457] J. Terry, M. L. Lau, J. Sun, C. Xu, B. Hendricks, J. Kise, M. Lnu, S. Bagade, S. Shah, P. Makhijani, A. Karantha, T. Boltz, M. Oellien, M. Adas, S. Argamon, M. Long, and D. P. Guillen. Analysis of extended X-ray absorption fine structure (EXAFS) data using artificial intelligence techniques. *Applied Surface Science*, 547:149059, 2021.

[458] L. M. Mayr and D. Bojanic. Novel trends in high-throughput screening. *Current Opinion in Pharmacology*, 9(5):580–588, 2009.

Danksagung

Dass ich überhaupt für meine Doktorarbeit in Heidelberg gelandet bin, habe ich **Prof. Dr. Thomas Pfeifer** zu verdanken. Sein Enthusiasmus während meines initialen Besuchs in Heidelberg hat meinen festen Vorsatz, nach meiner Masterarbeit *nicht* mehr etwas in großem Maßstab neu aufzubauen Makulatur werden lassen. Zu großem Dank bin ich ihm auch für die wissenschaftlichen Ideen und Denkanstöße verpflichtet, die so manch ein Projekt dieser Doktorarbeit erst ins Rollen gebracht haben, sowie für seine positive Grundhaltung.
Mein Dank gilt des Weiteren **Prof. Dr. Andreas Wolf** für die Übernahme des Zweitgutachtens und **Prof. Dr. André Butz**, sowie **Prof. Dr. Maurits Haverkort** für die Vervollstädigung des Prüfungskommitees.
Auch möchte ich meinem Arbeitsgruppenleiter **Dr. Christian Ott** danken, dass ich in seiner Gruppe starten und meine Ideen einbringen durfte.
Das Labor und die beschriebenen Experimente würde es so nicht ohne meinen Kollegen und Freund **Dr. Lennart Aufleger** geben. We shared a vision, fought for it and it became reality. Danke auch dafür, dass du mich in den richtigen Momenten angetrieben hast – dein "egal, wir machen das jetzt", nachdem wir am Freitag-Abend am 18 Uhr festgestellt haben, dass die Messung jetzt sieben Stunden dauern wird. Und nicht zuletzt für die Erfahrung der gemeinsamen Strahlzeiten in Hamburg *#schmarterPfahl*. Und auch für alles außerhalb der Arbeit.
Eine der interessantesten Personen, die ich auf dieser Reise, die sich Doktorarbeit nennt, kennenlernen durfte ist "mein Theoretiker" und Freund **Dr. Simon Heinze**. Zusammen haben wir SF_6 gebändigt (oder sowas in der Art) und den ein oder anderen Laufkilometer zurück gelegt. Du bist mein Lieblings-Physik-Erklärer. Außerdem vielen Dank für die Salzbrezel.
Eine weitere glückliche Fügung war, dass **Felix Henrich** seinen Weg ans MPIK gefunden hat... the rest is history. Ich hätte nie gedacht, dass ich einmal eine Theorie-Arbeit betreuen würde (war ja auch nicht ganz freiwillig dank Corona), aber hat ja dank dir ganz gut geklappt. Danke auch für deine kulinarischen Einflüsse und nach

wie vor Kudos, dass du dir das Krönchen bei der Hirschgasse geholt hast!
Mein Mitstreiter und Büro-Kollege **Alexander Magunia** hat all die Höhen und Tiefen miterlebt und zum Teil mitdurchlebt. Sei es im Labor oder bei Strahlzeiten. Vielen Dank, Alex, für deine Anteilnahme (im wahrsten Sinne des Wortes)!
Des Weiteren gilt mein Dank dem ganzen Interatto und X-MuSIC Team und hier insbesondere **Gergana Borisova** und **Dr. Marc Rebholz**.
Furthermore, many thanks to the students and interns that I had the pleasure to supervise and potentially impact them science-wise (*#forTheLoveOfLasers*): my MSc student **Alex**, my BSc students **Stefano Amberg** and **Felix**, my interns **Yoonsoo Kim**, **Alisa Danilenko** and **Paul Stark** and my HiWi **Marcel Kern**.
Even though the cause was never pleasant, the presence of **Dr. Alexander Podlipenski** in the lab was for sure! Thank you for your laser magic and for getting this final (as it turned out) cryo system to work – actually to work very decently after all. I should count again how many service visits you have spent for this system in Heidelberg...
Another person that significantly contributed to all laser-related things is **Nikola Mollov**. It was a blessing to have someone like you as a support and a colleague and really sad to see you go. (The laser system was definitely mourning as well...)
Ganz herzlich danken möchte ich allen, die Teile dieser Arbeit Korrektur gelesen haben: **Lennart**, **Simon**, **Alex**, **Gergana**, **Felix**, **Patrick Friebel**, **Christian**, **Marc**, **Dr. Max Hartmann** und **Simon Rupprecht**. Das war klasse!
Dieser Labor-Neuaufbau wäre nicht ohne technische Unterstützung möglich gewesen. Danke, **Dr. Claus Dieter Schröter** für den Gesamtüberblick und die vielen Tipps. Außerdem geht mein Dank an **Alexander von der Dellen**, sowie **Christian Kaiser** und seine Kollegen. Wenn man tatkräftige Unterstüzung braucht, kann man sich auf euch zählen. Vielen Dank auch an **Peter Gahn** von der Konstruktiion.
Ohne meine Eltern, **Ingrid** und **Gerhard Rupprecht**, würde es weder mich, noch diese Arbeit geben. Danke, dass ihr immer für mich da ward und seid und mich immer unterstützt habt. Ohne euren Zuspruch, euer Zuhören und eure Aufmunterungs-Versuche ist diese Arbeit nicht vorstellbar. Großen Einsatz als Motivator zeigte auch mein Bruder **Simon Rupprecht** – diese Motivation hat mich immer angetrieben. Vielen Dank dafür. Danke auch an meinen Bruder **Markus Rupprecht** für seine Neugierde und sein Interesse.
Zu guter Letzt möchte ich allen Freunden danken, die in den letzten Jahren ein offenes Ohr (auch aus der Ferne) für mich hatten und mir eine andere Perspektive gaben.

Erklärung/*Declaration*

Ich versichere hiermit, dass ich diese Arbeit selbstständig verfasst, und keine anderen als die angegebenen Quellen und Hilfsmittel verwendet habe.
I hereby certify, that this thesis is entirely my own original work except where indicated otherwise.

Heidelberg, den 28. März 2022 .....